Construction of biocompatible and electrically conductive coatings consisting of carbon nanotubes and polyelectrolytes

Inauguraldissertation

zur

Erlangung des akademischen Grades

Doktor der Naturwissenschaften (Dr. rer. nat.)

der

Mathematisch-Naturwissenschaftlichen Fakultät

der

Universität Greifswald

vorgelegt von

Sven Neuber

Greifswald, 27. Oktober 2023

Table of Contents

1   Introduction

Biological tissues in the body stop functioning at certain times due to aging, sickness, trauma, degeneration, and accidents.[1] In particular, bone defects due to fractures, infections, or tumor resections are often responsible for disability, especially in an aging society, which results in a loss of quality of life.[2, 3] In the past decades, biomaterials in various applications have been used as a remedy in the medical and dental fields. Particularly, in modern orthopedy, which opened up a lot of therapy possibilities including the usage of modified implants. In most cases, the basic material for such implants is titanium due to its good mechanical properties, chemical stability, and biocompatibility.[4, 5] To further improve the bioactivity of these titanium-based implants, i.e., increasing cell-surface interactions, an additional physical or chemical modification of their respective surface needs to be done.

Thin organic films coated on surfaces are of increasing importance when it comes to material functionalization.[6-8] First, they have to be highly biocompatible, due to their components, and second, their properties can be tuned through film composition in a targeted manner. Understanding these fundamentals from a scientific and engineering standpoint is highly interesting. Especially, regarding the needs of cell adhesion and proliferation. Therefore, it is necessary to understand and eventually control the film parameters such as topography, thickness, roughness, and electrical behavior to provide cells with a suitable and stable implant surface.

When it comes to well-studied and widely used biocompatible thin films, polyelectrolyte multilayers (PEMs) are often used. They are formed through polyelectrolytes (PE), polymers whose repeating units bear a charged functional group. To prepare them on solid surfaces in a controlled way, sequential adsorption of oppositely charged PEs is often used.[9, 10] When it comes to the preparation of PEMs, the now well-known Layer-by-Layer (LbL) technique[11, 12] plays an important role. This adsorption technique offers an easy and inexpensive process for multilayer formation and allows a variety of nano-materials to be incorporated within the film structure. Regarding tunable implant surfaces, the incorporation of different materials is interesting from an engineering standpoint. The literature shows, that for example cell adhesion and proliferation can be improved by stimulation with an electrical field.[13, 14] Pure PEMs are mostly not able to provide this kind of film characteristic or to be precise not in the desired and stable capacity.

By incorporating additional materials, such as carbon nanotubes (CNTs), into the film, electrical capability can be gained. These tubes made out of carbon can be produced in single- and multi-walled conformations with diameters of 1 nm up to less than 100 nm. One of their advantages is remarkable electrical conductivity,[15, 16] exceptional tensile strength, and thermal conductivity.[17, 18] All of them are bonded to their nanostructure and the strength of the bonds between carbon atoms. Additionally, CNTs can be chemically modified, which opens up the opportunity to use them as macroions in the preparation of LbL films.

To understand the build-up of such films consisting of PEs and CNTs for implant surfaces, binding mechanisms, and a variety of other parameters (e.g., solubility, surface alignment, roughness, molecular weight, and electrical properties) need to be investigated and analyzed.

Preparing electrically conductive multilayers is nothing new. There are multiple examples of such composite materials.[19-21] However, when it comes to implant surfaces, biocompatibility, and an electrically conductive surface are the main focuses.[22, 23] The question that arises is: Is it possible to create/prepare such films with the LbL technique in combination with PEs and CNTs and control their topographic and electrical characteristics?

Article 1 engaged with this challenge. Films prepared with a strong linear polycation poly(diallyldimethylammonium chloride) (PDADMA) and chemically modified single-/multi-walled CNTs, as negatively charged macroions, were investigated and analyzed. Used were PDADMA with high and low molecular weights and CNT suspensions with different concentrations. Thus, a variation of preparation conditions and film compositions was established. CNT modification, the addition of functional groups, was analyzed with X-ray photoelectron spectroscopy (XPS). Film growth, like thickness and roughness as a function of deposited PDADMA/CNT bilayers, was observed with Atomic Force Microscopy (AFM) and Ellipsometry. The surface coverage was analyzed with the Vis-NIR absorption spectroscopy (Vis-NIR). Electrical properties were measured with a multimeter. This allowed an understanding of the interaction between positively charged PEs and negatively charged CNTs. It also gave insights into the film topography including CNT surface orientation, film roughness, PE/CNT coverage rate, and electrical film parameters (resistance R, sheet resistance R_s, conductivity σ) in air. Thereby, all characteristics can be influenced and controlled by the number of deposited layer pairs and thus the film thickness.

Since the preparation of stable electrically conductive thin films in combination with PDADMA and CNTs, in a controlled way, now was possible, we started to investigate the film behavior regarding its implementation as implant coating for medical applications.[24, 25] Under normal circumstances, implants, which are used for i.e., bone or jaw fractures are often surrounded by an aqueous medium (i.e., blood or saliva) when inserted into the human body. In PEMs, the molecules are bound through electrostatic forces of the repeating units. These units/ions tend to hydrate in aqueous environments. If this effect occurs, the ions are surrounded by a hydration shell. This results in film swelling and thereby in the reduction of CNT/CNT contact points which highly influences and reduces the film conductivity.[20] To prevent the effect, it is necessary to suppress the swelling and with it the ion hydration. The question is: Are films prepared with PDADMA and CNTs stable and controllable when immersed in a biological aqueous environment regarding their characteristics and is there a hydration/swelling effect? To answer this question, we immersed our coated samples in three different media (solutions) and compared the results with their respective dry state (in-air, ambient conditions), represented in **Article 2**.

A Phosphate-buffered saline solution (PBS), which is commonly applied in biological research was used to match the osmolarity and ion concentration of the human body.

To simulate a pure cell growth environment, Dulbecco's Modified Eagle's Medium (DMEM), a widely used basal medium for supporting the growth of many different mammalian cells was applied. As a comparison, the saline solution of sodium chloride was used. Investigated was the behavior of the immersed films regarding cohesion, PE swelling, and electrostatic attraction between oppositely charged functional groups of PDADMA and CNTs via AFM, Vis-NIR, Ellipsometry, and a multimeter. The results were correlated with their respective electrical properties, like resistance R, sheet resistance R_s, and electrical conductivity σ in dependence on the number of deposited PDADMA/CNT bilayers. Being able to prepare stable and cohesive films (in air and aqueous solutions) with tunable topographies and electrical characteristics (**Article 1** and **Article 2**) opened up new modification possibilities when it comes to biocompatibility.

The literature showed that uncovered carbon nanotubes tend to be cytotoxic when they come into direct contact with cells.[26-28] Therefore, we consider films prepared with PEs and CNTs mentioned in the first two articles as a base layer, which needs an additional one to cover the CNTs completely to prevent direct cell contact. This begs the question: Is it possible to create a biocompatible surface film with a potential preferential lateral topography for an improvement in cell adhesion and proliferation with the help of PEMs?

Under normal circumstances, cells prefer a rather rough and structured surface.[29] PEM films are not just biocompatible but have also a roughness that could promote cell adhesion and proliferation.[30, 31] Thus, they could be used as a top layer for the previously mentioned PE/CNT base layer. In **Article 3** the lateral morphology of PEMs is investigated to create a tunable and controllable surface structure. To be exact the self-patterning of polyelectrolyte multilayers consisting of PDADMA and poly(styrene sulfonate) sodium salt (PSS) is investigated. Self-patterning of the polymer film surfaces can be modified via i.e., external fields,[32] or through the use of self-assembly.[33-35] Investigated was the second case, an increased roughness due to pattern formation during the film build-up. Tanaka et al showed for freshly prepared gel films that patterning only occurred during the drying phase. Also, a decrease in the film volume due to asymmetric stress (films could only shrink vertically and not laterally) was observed. He also concluded that the formation of the surface pattern of drying gels was enabled by the movement of water molecules.[36] In LBL films, the asymmetric stress is dictated by the conformation of the adsorbed PEs. These films also can only expand in the direction perpendicular to the substrate during the preparation, just like a drying gel.

To find out whether the same physical laws of drying gel films apply to LBL film, films were built with the LbL technique with a mobile species in the form of a polyelectrolyte. During the preparation, the film traverses through different growth regimes.[37]

The behaviors at each state regarding the topographic structure and rearrangements were monitored via AFM in air and water, X-ray reflectometry (X-ray), and Scanning Electron Microscopy (SEM). The results are presented as a function of deposited PDADMA/PSS bilayers. Also, for both PEs a high and low molecular weight was used to get insight into their possible mobility and structural influence.

Not only the surface structure influences cell adhesion and proliferation, but above all the surface charge is an important factor, when it comes to biocompatibility.[38, 39] It is one of the main reasons for cells to attach and stay on a surface or not. Therefore, it is desirable to be able to tune and be flexible with these charges, because different cells favor different surface characteristics.[40, 41] Being able to tune the topographic structure described in **Article 3**, the next question is: Is it possible to create surface charges, that are suitable for cells, and are PEMs an alternative and suitable system?

To answer the question, PEM conformation, and their respective surface charges were investigated in **Article 4**. Using the LbL technique, films are prepared from strong polyelectrolytes with a low (PDADMA) and a high (PSS) linear charge density solved in 0.1 molar NaCl with respect to the monomer concentration. Film topography was observed with AFM. We additionally performed force measurements with the Colloidal Probe technique (CP) in the asymmetric conformation. Here, a PEM-covered surface is pressed against a silica nanoparticle, freshly cleaned, and negatively charged or covered with positively charged poly(ethylenimine) (PEI), a branched polyelectrolyte that adsorbs flatly. PEM and CP are immersed in a solution, starting with deionized water, then the solution is enriched up to 1 M NaCl to modify the electrostatic force between PEM and CP. The deflection from the cantilever in combination with Hooke's law, the force acting on the CP can be determined. With the DLVO theory, developed by Derjaguin B.V., Landau L.D. (1941)[42] and Vervey E.J.K., Overbeek J.T.G. (1948),[43] considering the NaCl concentration, the surface potential can be deduced. Based on this potential, according to the Graham equation, the surface charge density can be calculated. Additionally, it can be determined if the polyelectrolyte chains are tightly bonded to the film surface or protrude into the solution. In the latter case, the theory of PE brushes applies.[44, 45] Thereby, PE brushes are assemblies of charged polymer chains tethered or grafted by one of their extremities to a surface or to a backbone of another polymer chain. The latter is also referred as the bottle brush polymer.[46]

After getting information about the surface charge behavior of PEMs at different conditions, we can now investigate if they have the same or similar influence on cells, given cell adhesion and proliferation. As mentioned before, cells prefer a variety of different surface charges, which have to be determined specifically for each cell type.[47-49] Through a variation of PEM compositions different surface conditions and charges can be created.
The question is: Are these surface conditions provided by PEMs sufficient and in a range that affects cells positively when it comes to cell adhesion and proliferation?

Therefore, in **<u>Article 5</u>** we investigated the possibility of an enhancement of intracellular calcium ion mobilization, which correlates with cell activity. A variety of different surface coatings was employed to modify titan (Ti) surfaces to achieve different surface charges. These were created through extracellular matrix (ECM) proteins (Collage I, Matrigel), a peptide sequence of Arginyl-Glycyl-Aspartic (RGD), amino polymers (plasma polymerized allylamine (PPAAm), poly(ethylene imine) (PEI), poly(propylene imine) dendrimer generation 4 (PPI-G4), (3-aminopropyl)triethoxysilan (APTES)), and PEM prepared with PDADMA and PSS. Surface characteristics were investigated via the streaming potential for the surface zeta potential, the sessile drop method for wettability, null ellipsometry for layer thicknesses, and X-ray photoelectron spectroscopy (XPS) for the elemental composition. The investigation of the cell biology was done with Scanning Electron Microscopy (SEM) for cell morphology, fluorescence microscopic images were used for cell circularity, an MTS assay for cell viability, and the intracellular Ca^{2+} mobilization was specified via adenosine 5'-triphosphate (ATP) concentration. Results were statistically evaluated through non-parametric Kruskal-Wallis followed by Dunn's multiple comparisons tests or non-parametric Wilcoxon matched-pairs signed-rank test.

The achieved results could answer the questions previously mentioned. In the last section, further experiments and projects which are currently under development are described. These additional results will further clarify if a combination of a CNT/PDADMA film as a bottom layer, providing electrical stimulation, and PEMs as the top layer, providing surface structure and surface charge, is suitable for implant surfaces. In the next section, the theoretical background and methods are described in more detail.
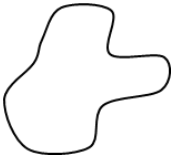
2 Theoretical background and methods

2.1 Theoretical background

2.1.1 Polymers: structure, synthesis, and characteristics

Since life began, polymers existed in natural forms, such as DNA, RNA, proteins, and polysaccharides which play crucial roles in plant and animal life. From the beginning, naturally occurring polymers have been exploited as materials for eating, clothing, decoration, shelter, tools, writing materials, and other requirements.[50] In modern-day, especially in science, a polymer is a substance or material that consists of large macromolecules, which are multiples of simpler chemical units called monomers, low-molecular and reactive molecules.[50] They can occur in a linear, cyclic, branched, or network structure (c.f. Table 1). One of their main advantages is their broad spectrum of properties that allows them to play essential and ubiquitous roles in everyday life.[51]

Table 1. Representative structure of linear, cyclic, branched, and network-forming polymers.

Linear	Cyclic	Branched	Network

To synthesize such large macromolecules a process called polymerization is necessary. Here, monomer molecules are combined in a chemical reaction to form chains or three-dimensional networks. There are multiple types of polymerizations i.e., step-growth, chain-growth, or photopolymerization.[50, 52, 53] One of the most common and industrial used ones is chain-growth polymerization, especially the free radical one.[54] This is a technique where unsaturated monomer molecules sequentially attach to the active site of a growing polymer chain.[55] The process itself involves 3 types of reactions: Initiation, Propagation, and Termination.

Here, a free radical is used as an intermediate that can continue the reaction by chain propagation. In the beginning, the chain will be seen as an addition of a radical $R^{\cdot}$ onto a monomer M, which then leads to an $R-M_1^{\cdot}$ radical.

$$R^{\cdot} + M \rightarrow R - M_1^{\cdot}$$
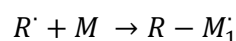
For the initiation there are two possibilities for addition:

$$R^{\cdot} + CH_2{=}CHX \rightarrow R\text{-}CH_2\text{-}\dot{C}HX \qquad \text{(I)}$$

$$\rightarrow R\text{-}CHX\text{-}\dot{C}H_2 \qquad \text{(II)}$$
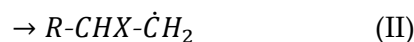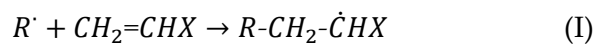
Following the initiation, the next step is propagation. The chain growth starts/continues through the addition of more monomers on a $R - M_1^{\cdot}$ radical:

$$R - M_1^{\cdot} + M \;\rightarrow\; R - M_2^{\cdot}$$

or, more general $R - M_i^{\cdot} + M \rightarrow R - M_{i+1}^{\cdot}$
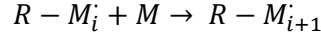
with M_i number of monomers within the radical. The average growth rate is approximately one addition per millisecond. Here, again are two forms of addition:

$$R\text{-}CH_2\text{-}\dot{C}HX + CH_2\text{=}CHX \rightarrow R\text{-}CH_2\text{-}CHX\text{-}CH_2\text{-}\dot{C}HX \tag{I}$$

$$\rightarrow R\text{-}CH_2\text{-}CHX\text{-}CHX\text{-}\dot{C}H_2 \;. \tag{II}$$
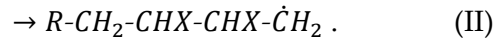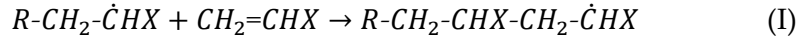
The final process is termination, which can take place by recombination (a) or disproportionation (b):

$$\text{\textasciitilde\textasciitilde\textasciitilde} CH_2\text{-}\dot{C}HX + \dot{C}HX\text{-}CH_2\text{\textasciitilde\textasciitilde} \quad\rightarrow\quad \text{\textasciitilde\textasciitilde\textasciitilde}CH_2\text{-}CHX\text{-}CHX\text{-}CH_2\text{\textasciitilde\textasciitilde} \tag{a}$$

$$\text{\textasciitilde\textasciitilde\textasciitilde} CH_2\text{-}\dot{C}HX + \dot{C}HX\text{-}CH_2\text{\textasciitilde\textasciitilde} \quad\rightarrow\quad \text{\textasciitilde\textasciitilde\textasciitilde}CH_2\text{-}CH_2X + CHX\text{=}CH\text{\textasciitilde\textasciitilde} \;. \tag{b}$$
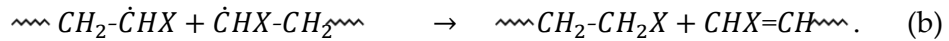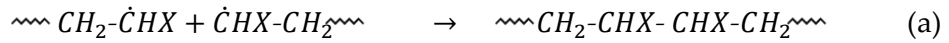
In the end, free-radical chain-growth polymerization is a cheap technique that allows the production of polymers with large variations in chain length. Therefore, the main ways to change and tune the properties of polymers lie in the processing conditions. These are i.e., temperature, pressure, the solvent in which the polymer is polymerized, type of monomer units used, the concentration of monomers in the reaction, the reagent to initiate the polymerization, and how they are collected. Additional classification of polymers takes place according to their structural arrangement and number of monomer units. Here, the characteristics of a polymer regarding the number-average molecular weight M_n and weight-average molecular weight M_w are used. They are defined as followed

$$M_n = \frac{\sum_i n_i M_i}{\sum_i n_i}$$

$$M_w = \frac{\sum_i n_i M_i^2}{\sum_i n_i M_i} \;.$$

Thereby, M_i is the molecular weight of a chain, n_i is the number of chains of molecular weight M_i, and i is the number of monomers.[56] Knowing these two molecule characteristics allows to define the number of monomer units in a polymer after their synthesis. The number is defined as the degree of polymerization X. For a homopolymer, X can be calculated as number-average X_n or weight-average X_w degree of polymerization as followed

$$X_n = \frac{M_n}{M_0}$$

$$X_w = \frac{M_w}{M_0} \;,$$

with M_0 the molecular weight of the repeating unit or monomer.[54] Additionally, polydisperse systems provide information of the heterogeneity of a sample based on size.

Polydispersity occurs due to size distribution in a sample, agglomeration, or aggregation of the sample during isolation or analysis.

With the help of Dynamic Light Scattering (DLS), the Polydispersity Index (PDI) can be obtained. It provides the broadness of molecular weight distribution and is defined as

$$PDI = \frac{M_w}{M_n}.$$

The larger the *PDI*, the broader the molecular weight. Monodisperse polymers, where all chain lengths are the same i.e., protein, have a *PDI* of 1.[56]

Another important point in molecular physics to characterize polymers is the contour length l_{cont} (c.f. Figure 1). It describes the maximum end-to-end distance of a linear polymer chain[57] and is calculated through n (number of monomer bonds) multiplied by l (length of a single monomer unit).
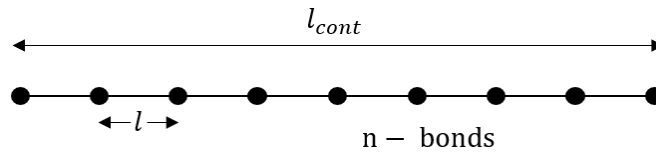
Figure 1. Description of the contour length l_{cont}.

One factor, which affects the contour length of a polymer is the bonding angle θ_{bond} between monomers (c.f. Figure 2). The maximum chain length l_{max} for a fixed bonding angle θ_{bond} can be calculated as

$$l_{max} = n \cdot l \cdot sin(\theta_{bond} / 2).$$

Is θ_{bond} arbitrary, instead of l_{cont}, the average end-to-end chain distance $\langle r^2 \rangle^{\frac{1}{2}}$ will be determined. With n segments $\langle r^2 \rangle$ is determined as

$$\langle r^2 \rangle = n \cdot l^2 .$$

Due to the entanglement, the size of the polymer is significant shortened. In this case, the average distance of all chain parts to the chain center is described through the radius of gyration $\langle s^2 \rangle^{\frac{1}{2}}$. Thereby, the relation between the average chain distance and the radius of gyrations is as follows

$$\langle r^2 \rangle^{\frac{1}{2}} = 6 \cdot \langle s^2 \rangle^{\frac{1}{2}} .$$
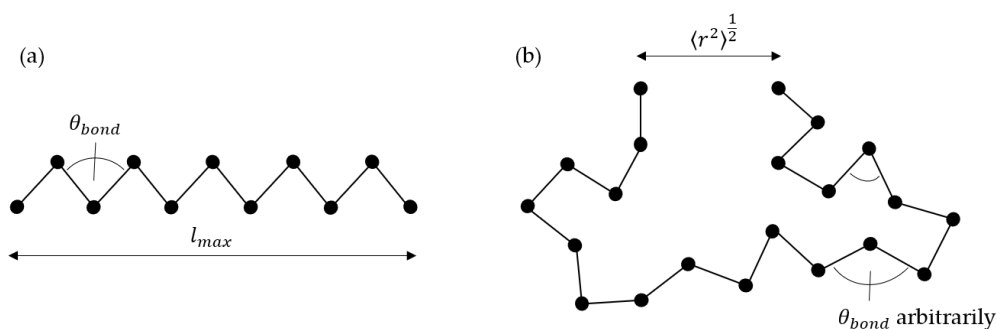
Figure 2. Description of the polymer length depending on the bond angle θ_{bond}: (a) fixed and (b) arbitrary.

This work used polyelectrolytes (PEs), polymers featuring electrolyte groups within a repeated unit structure (c.f. Table 2). They can be categorized as neutral (i.e., polypeptides), modified neutral (i.e., cellulose), and synthetic (i.e., polystyrene sulfonate (PSS)).[58] A special characteristic is the dissociation of the electrolyte groups in solution where they split into polyions and their monovalent counterions, whereby the PE chain becomes charged. These types include cationic, anionic, and zwitterionic charges, which are important for i.e., in our case, the buildup of polyelectrolyte multilayers (PEMs).[59]

Table 2. Used polyelectrolytes and characteristics: structure, polydispersity index (PDI), degree of polymerization X_n, average molecular weights M_w, and length per monomer.

	PDADMA	PSS	PEI
Structure			
	Linear	Linear	Branched
M_w / kDa	44.3, 322	666	750
PDI	1.99, 2.19	< 1.2	> 2
X_n	274, 1992	3230	-
Monomer length / nm	0.54	0.25	-

Putting PEs into solution, it is important to understand their state of dissociation that determines the strength of the respective PE. Here, the strength of a PE is determined by the linear charge density and its dependency/independency on the pH of the solution. Usually, PEs are discriminated between weak and strong ones.

PEs with weakly acidic or basic groups, which are protonated or deprotonated depending on the pH of the surrounding medium, are described as weak. Here, the charge density depends on the pH of the surrounding medium. In contrast, a strong polyelectrolyte dissociates completely in solution for most reasonable pH values.

For example, in this case, PDADMA and PSS are considered strong PEs, whereas PEI is considered weak.[60] The dissociation of PEs in a solution, results in charged monomers. If these charges are not compensated 1:1 by their respective counterions or additionally through the ionic strength of the surrounding solution, they repel each other due to electrostatic forces. Thereby, the PE is stretched and disentangled in a low ionic density environment. Increasing the ionic strength of the solution results in a 1:1 charge compensation that causes more compact and entangled molecules (c.f. Figure 3). For the charge of individual monomers, the diffusion of counterions into solution is prevented by strong electrostatic forces.

Thus, a few counterions condensate in the immediate environment of the polymer, which leads to a reduced linear charge density of the PE and an increasing distance between two monomer charges. The Bjerrum length λ_B, the separation at which the electrostatic interaction energy between two elementary charges is comparable in magnitude to the thermal energy $k_b T$, gives insights into the range of electrostatic forces between two monovalent charges. In Gaussian units with $4\pi\varepsilon_0$ (with ε_0 the vacuum permittivity) = 1, λ_B is described as

$$\lambda_B = \frac{e^2}{\varepsilon_r k_B T},$$

where e is the elementary charge, ε_r the relative dielectric constant of the medium, k_B the Boltzmann constant, and T is the absolute temperature in Kelvin. Additionally, to electrostatic interactions, an effect called shielding occurs, when PEs dissolve in solution (i.e., salt). Here, the polycation/polyanion charges are shielded by the oppositely charged ions of the solvent. The monovalent ions form a charge-compensating cloud around the charged polyions. Thereby, the Debye length λ_D, a measure of a charge carrier's net electrostatic effect in solution and his persistence,[61] characterizes the range of this cloud of an electrolyte as followed

$$\lambda_D = \kappa^{-1} = \sqrt{\frac{\varepsilon_0 \varepsilon_r k_B T}{2N_A e^2 I_{ionic}}}$$

with k_B the Boltzmann constant, N_A the Avogadro's number, and I_{ionic} the ionic strength of the electrolyte. In this connection, λ_D primarily depends on the ionic strength of the surrounding environment, where small mobile ions are able to accumulate a charged PE chain. One distinguishes polymer sections that are bound to the surface (trains), sections that form loops, and end sections that can form dangling tails (c.f. Figure 4). Which type of adsorption occurs can be influenced by various parameters i.e., salt concentration or pH of the solution.
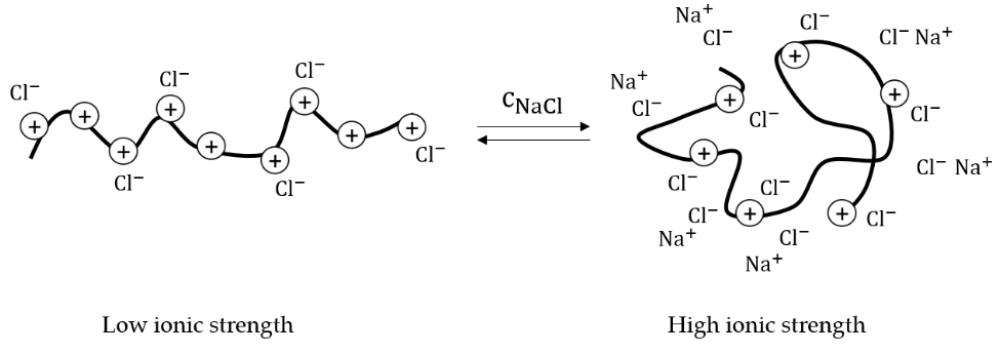
Figure 3. Polyelectrolytes in solution with low and high ionic strength.

Increasing the ionic strength of the surrounding solution causes entangled molecules, causing the PE charge carriers to be more shielded. Therefore, an increased adsorption of loops and tails takes place. Reducing the ionic strength results in more stretched PE chains due to intermolecular repulsion forces, whereby the chain adsorbs flat.
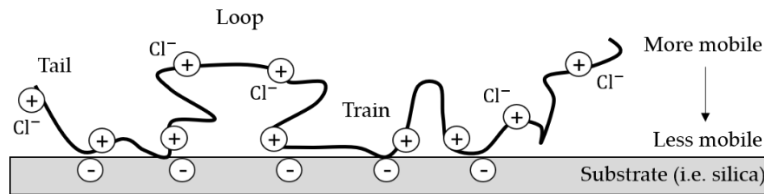
Figure 4. Adsorption of a free-moving polymer chain and its three sections: tail, loop, and train.

2.1.2   Carbon nanotubes (CNTs): structure, synthesis, properties, and chemical modification

When it comes to substrate surface modifications for biological and medical applications, the preferred coatings have to be biocompatible and electrically conductive. Both factors are important i.e., regarding cell adhesion and proliferation.[41, 62-64] In this work, biocompatibility is achieved with the help of suitable polyelectrolytes (PE) and conductivity by adding electrically conducting nanomaterial in the form of carbon nanotubes (CNTs). Due to their excellent chemical modifiability,[65] mechanical,[66] and electrical properties,[67] the combination of CNTs and PEs allows the build-up of multilayer systems that are suitable for biological or medical needs. Two kinds of carbon nanotubes are used in this work: one is a single-walled carbon nanotube (SWCNT) and the other is a multi-walled carbon nanotube (MWCNT). SWCNTs consist of one layer of graphite with three different structure types.

Depending on the chiral vector C_h, the lattice vectors a_1 and a_2, and the chiral angle θ_{chiral} the tube types differ between armchair, zigzag, and chiral (c.f. Figure 5). MWCNTs on the other side are multi-layer concentric graphite.[68] The three commonly used methods to synthesize CNTs are Arc Discharge, Laser Ablation, and Chemical Vapor Composition. Arc Discharge is a technique where the electrical breakdown of a gas to generate plasma is used.

This technique was first practiced by Iijima in 1991.[69, 70] Figure 6a shows a schematic build-up of an arc discharge chamber that consists of two horizontal or vertically mounted electrodes. Thereby, the anode is filled with powdered carbon precursor along with a catalyst, whereas the cathode is normally a pure graphite rod. The chamber itself is submerged inside a liquid environment or filled with gas.
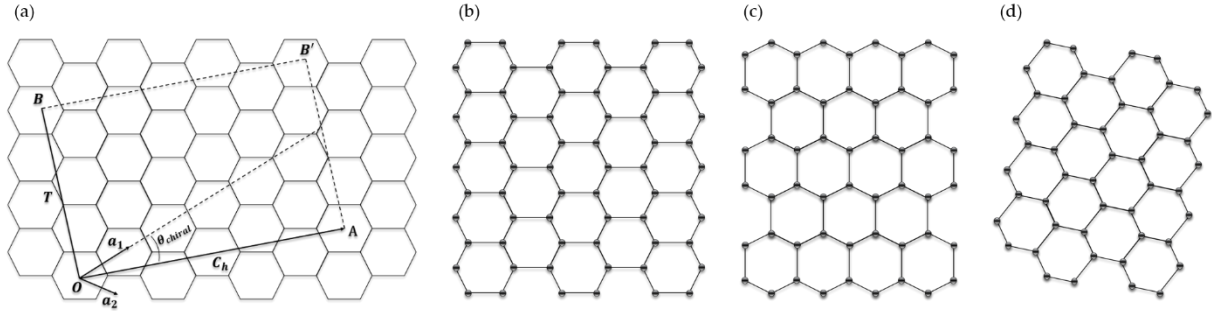
Figure 5. Schematic construction of a single-walled carbon nanotube by rolling up an infinite strip of graphite sheet. (a) Connection of two lattice points $O_{lattice}$ and $A_{lattice}$ on a graphene sheet via the chiral vector $C_h = na_1 + ma_2$. Perpendicular to the chiral vector an infinity strip is cut through these two points. The strip then can be rolled up into a seamless cylinder. T is the primitive translation vector of the nanotube. The nanotube is uniquely specified by the pair of integer numbers n, m or by its radius $R = C_h/2\pi$ and chiral angle θ_{chiral} which is the angle between C_h and the nearest zigzag of C–C bonds. (b) Structure of an armchair tube (n, n) with $\theta_{chiral} = 30°$, (c) structure of a zigzag tube $(n, 0)$ with $\theta_{chiral} = 0°$, and (d) structure of a chiral tube.[71]

Using a power supply of alternating current (AC) or direct current (DC) (c.f. Figure 6b - d), the electrodes are brought together to generate an arc. To obtain a steady discharge they are kept at an intermitted gap of $1 - 2$ mm. It is important to maintain a constant current to obtain a non-fluctuating arc, otherwise, in the case of a fluctuant one, the quality of the product (CNTs) is strongly influenced.
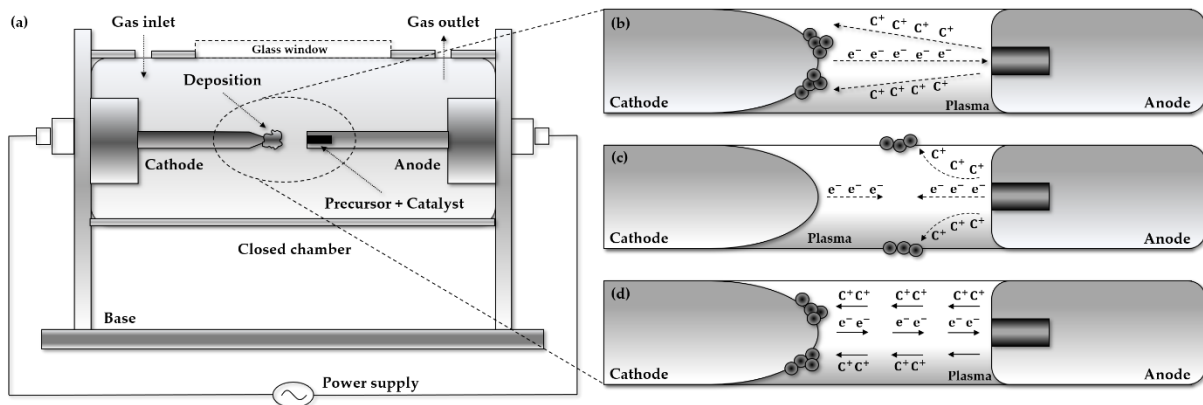
Figure 6. Schematic setup of an Arc Discharge (a) and the formation of CNTs using different power supplies (b – d): (b) DC Arc Discharge of a continuous movement of ions and electrodes within a plasma and deposition on the cathode, (c) AC Arc Discharge with changing polarity of the electrodes after every cycle, and (d) Pulse Arc Discharge where accelerating electrons are discharged from the cathode in short pulses with time intervals between micro and millisecond. (adapted from Arora, N., 2014)[69]

The plasma generated through the arc current reaches temperatures between ~ 4000 – 6000 K. This sublimes the carbon precursor filled inside the anode. The evolving carbon vapor aggregates in the gas phase and moves towards the cathode where it cools down due to the temperature gradient. The applied arc duration time is a few minutes, then the discharge is stopped and the CNTs with the soot can be collected from the chamber walls.

Laser Ablation is another method to produce CNTs with high quality and purity (c.f. Figure 7) and was introduced by Guo et al. 1995.[72] Here, the principle and mechanism are similar to the arc discharge method. CNTs produced with this technique exhibit a relatively high crystallinity and straightness. Here the energy is generated by hitting a graphite target containing catalytic materials (i.e., nickel (Ni) or cobalt (Co)) with a specific laser wavelength.[73]
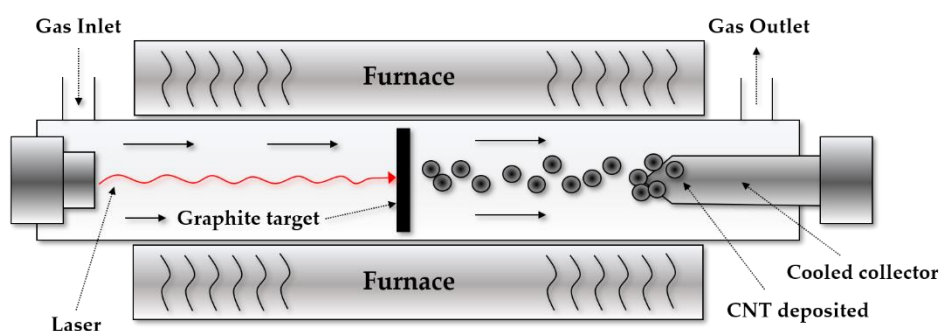
Figure 7. Schematic CNT formation process with laser ablation. (adapted from Lu Z. et al. 2019)[74]

Transition metals like Co or Ni are firstly doped as a catalyst into the graphite target and placed in the reactor. After reaching a reaction temperature of ~ 2300 K under the protection of an inert gas, the target is then bombarded with the laser.
The formed gaseous carbon and catalyst particles are then transferred from the high-temperature zone into the low-temperature zone with the help of the gas flow. During this time the gaseous carbon collides with each other and forms CNTs in the carrier gas under the action of the catalyst.

Thereby, the performance of CNTs produced with this method is dependent on the laser parameters (i.e., energy fluence, peak power, pulse wave, repetition rate, etc.), pressure and material composition of the combustion chamber, structure and chemical composition of the target material, flow and pressure of the buffer gas, spacing between the target material and matrix, and the temperature of matrix and ambient.[75]

Both Arc Discharge and Laser Ablation are methods where the crystallinity and straightness are high, however, these methods suffer from low yield. On the contrary, Chemical Vapor Deposition (CVD) is a method that reaches industrial production.[74] Here, the carbon source is a hydrocarbon substance that is cleaved into carbon clusters on the surface of a catalyst particle through thermal dehydrogenation.

Then, these clusters are regrouped when the carbon source gas is in contact with the catalyst in the quartz tube at a suitable temperature (c.f. Figure 8). As a catalyst, transition metals like iron (Fe), cobalt (Co), nickel (Ni), molybdenum (Mo), niobium (Nb), or tantalum (Ta) are normally used. The advantages of this method are low costs, high yields, and an easy to control CNT production. The downside is the quality of the CNTs which is lower than CNTs synthesized with Arc Discharge or Laser Ablation.[68] The properties of CNTs synthesized by such methods depend mostly on the atomic arrangement, tube diameter, tube length, morphology, or nanostructure.
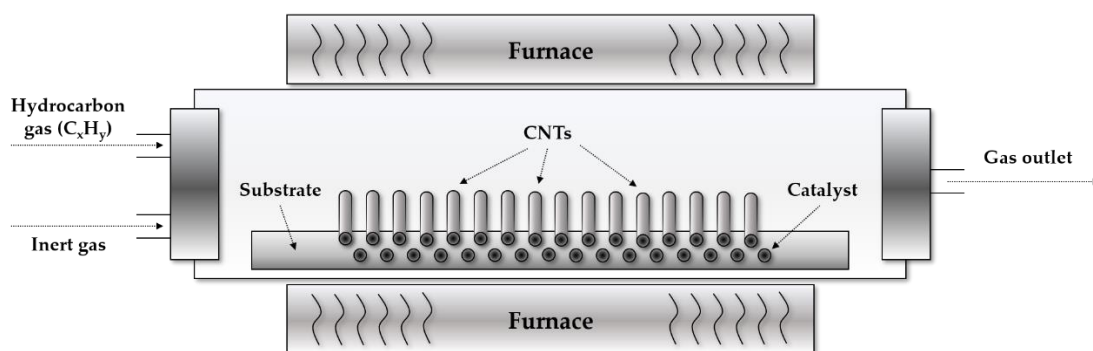
Figure 8. Schematic process of a chemical vapor deposition (CVD, adapted from Olga Zaytseva, 2016).[76]

However, the overall cage-like shape of carbon of CNTs showed exceptional material properties that are the consequence of the symmetric structure. They can be subclassified in electrical, mechanical, and thermal properties.

As demonstrated by many researchers CNTs display extraordinary electrical conductivity. SWCNTs show metallic behavior with an electrical resistivity between 5.1×10^{-6} to 1.2×10^{-4} Ω cm.[77] In combination with a known surface size the specific resistance ρ can be calculated and thus with its inverse $1/\rho$ the conductivity. Also, each carbon atom is arranged in a hexagonal lattice covalently bonded to three adjacent carbon atoms through sp^2 orbitals. This allows the fourth valence electron to remain free in each unit. These free electrons are delocalized on all atoms which allows them to contribute to the electrical conductivity of the CNT.

Depending on the type of chirality, CNTs can be considered conductive or semi-conductive.[77, 78] When it comes to the mechanical properties CNTs are considered as some of the strongest material in nature due to the C-C bonds observed in graphite. Especially, in their axial direction CNTs are considered extremely strong.[79] Its Young's modulus is between 270 and 950 GPa with a tensile strength between 11 and 63 GPa.[68] Also, their radial elasticity is an important factor when it comes to the formation of CNT nanocomposites. This allows CNT applications i.e., in multilayer films for surface coatings. Here, they can be embedded and form a composite structure so the coating film can be functionalized to the scope of application.

Additionally, all CNTs are expected to be good thermal conductors along the tube and exhibit a property known as ballistic conduction.[80]

This refers to the unimpeded flow of charge carriers (i.e., electrons), or energy-carrying particles over a relatively long distance in a material. SWCNTs at room temperature have a thermal conductivity along its axis of ~ 3500 W m^{-1} K^{-1},[81] whereas the thermal conductivity of i.e., copper as a metal known for its good thermal conductivity, is 385 W m^{-1} K^{-1}. The stability of CNTs regarding the temperature is estimated up to ~ 3000 K in vacuum and ~ 1000 K in air.[82]

In this work, a mixture of SWCNTs/MWCNTs is used. This mixture is hydrophobic. For film build-up (described in part 2.2.2), the CNTs must be dissolved in water. Therefore, a chemical modification/functionalization was necessary. Following the procedure described in Lopez-Oyama et al. (2014),[83] the CNTs were treated with a mixture of concentrated H_2SO_4 and HNO_3 acid. During the process, the CNT walls are attacked by the acid mixture which creates defects where functional groups could be added. The outcome was a mixture of slightly negatively charged SWCNTs and MWCNTS with an increased dispersion in water which was necessary for the film preparation.

2.2   Methods

2.2.1   X-ray Photoelectron Spectroscopy (XPS)

Due to the necessity of a chemical functionalization process of the carbon nanotubes (CNTs), mentioned in section 2.1.2, it is essential to know the nature of the CNTs functionalization i.e., which parts of the PEs and CNTs are able to react or bond with each other for multilayer film preparation. X-ray photoelectron spectroscopy (XPS) is a quantitative technique for measuring the elemental composition of the surface of a material, and it also identifies the binding states of the elements.[84, 85]
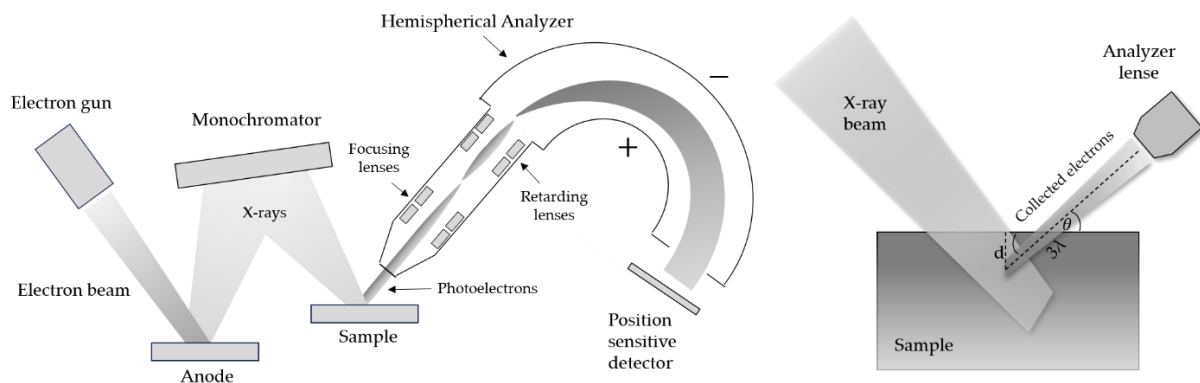
Figure 9. Schematic representation of an XPS system (left) and photoelectron emission from a sample surface (right), with d the depth of analysis, θ the take-off angle, and λ the mean free path of an electron. (adapted from Cushman 2016)[86]

The XPS process (cf. Figure 9) is an application of the photoelectric effect. Here, electrons are emitted from atoms in response to impinging electromagnetic radiation. 1905 Albert Einstein explained the appearance of photoelectrons, produced from a material when the energy of impinging photons exceeds the binding energy of electrons in the material. Thereby, the energy is proportional to the frequency (v) not the intensity or duration of exposure to the incident electromagnetic radiation. Also, the kinetic energy ($E_{kinetic}$) of an emitted electron is related to its binding energy ($E_{binding}$). $E_{binding}$ is well known for the electrons of a specific atom.[87] Because atoms have multiple orbitals at different energy states, the resulting response will be a range of emitted electrons with different binding energies which results in the XPS spectrum. The relations can be described as follows

$$E_{kinetic} = E_{photon\,(hv)} - E_{binding} - \varphi_{work} \,,$$

where $E_{kinetic}$ is the kinetic energy of the photoelectrons measured by the instrument, $E_{photon\,(hv)}$ is the energy of the incident photon (monochromatic X-ray in this case), $E_{binding}$ is the binding energy of a given electron, and φ_{work} is the work function, the energy difference between the vacuum energy (E_v) level and the Fermi (E_f) level of a solid used in the experimental set-up.[88]

The energy source is a monochromatic beam of soft X-rays in an ultrahigh vacuum environment. Electrons are emitted from the sample and their kinetic energy and number are simultaneously measured by detectors. The difference between the photon energy, the sum of the electron kinetic energy, and the work function determines the electron binding energy.

The work function depends on both the spectrometer and the material, so it is often treated as an adjustable instrumental correction factor.

The resulting XPS spectrum shows the number of detected photoelectrons as a function of the binding energy. At binding energies at characteristics for the specific state of an element, a peak appears. The binding energies are affected by the formal oxidation state, and the local bonding environment such as the identity of the nearest-neighbor atoms, bonding hybridization to the nearest-neighbor atoms, etc. Therefore, XPS is sensitive to the chemical bonds of the materials and enables us to determine the chemical structure.[89]

2.2.2   Carbon nanotube / Polyelectrolyte multilayer – buildup

There are multiple techniques like spin-coating, solution casting, thermal deposition, or chemical self-assembly to prepare multilayers. A common one to prepare PEMs is the layer–by–layer (LbL) method, invented by the group of Gero Decher.[11, 90] It is a simple and robust method that does not require sophisticated equipment, precise stoichiometry, or complicated chemical reactions to deposit successive layers.[91]

In general, oppositely charged PEs (polycations/polyanions) are used which are able to build multilayers in a sequential adsorption process in combination with a dipping device (c.f. Figure 10). The build-up itself is driven by electrostatic attraction between the oppositely charged constituents.[92]
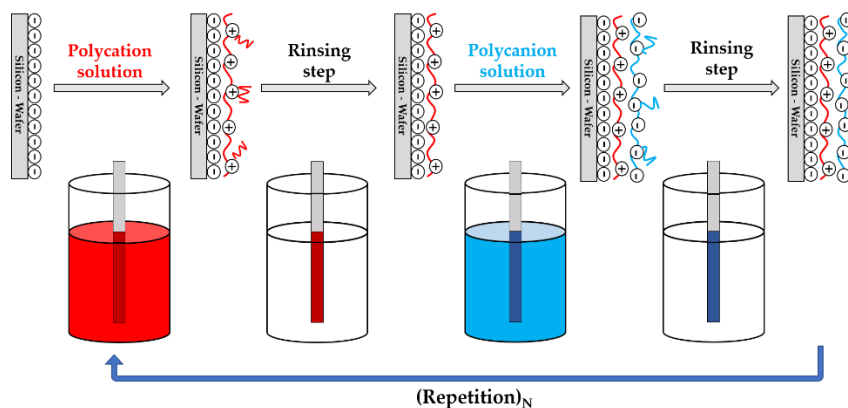
Figure 10. Schematic illustration of the layer-by-layer method using a dipping device.

However, hydrogen bonding, hydrophobic interactions, and van der Waals forces may be exploited to assemble LbL systems or influence the stability, morphology, and thickness of the films, particle/molecule depositions, and permeation properties of the film.[91]

One of the main advantages of the LbL method is the incorporation of nano-particles as long as they are adequately charged and sized. This includes colloidal particles (i.e. gold)[20, 93] or other nano-materials like modified CNTs[94, 95] to produce multifunctional hybrid carrier systems or films. Therefore, the LbL technique met all of our needs and allowed us, after an initial anchor-layer (bilayer of PEI and PSS), to prepare functionalized multilayers. Using modified CNTs
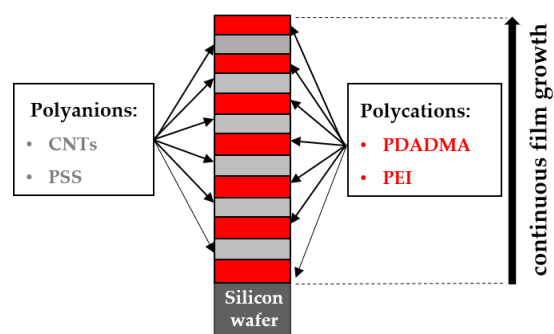
Figure 11. Schematic build-up of a CNT/PDADMA film.

(polyanion) and PDADMA (polycation) allowed the preparation of a stable netstructure, which enables the film to be electrically conductive, in a controlled way. Figure 11 illustrates a build-up of such a multilayer film. By varying the preparation conditions, film properties like thickness, roughness, or conductivity can be influenced, additionally.

2.2.3   Atomic Force Microscopy (AFM) – a technique to characterize surface topography, roughness, and on a microscopic level static electric charge

To investigate surface structures with high resolution and accuracy Atomic Force Microscopy (AFM) is one of the most suitable techniques. It is a type of Scanning Probe Microscopy (SPM) and can provide imaging on the scale of fractions of a nanometer vertically and down to a few

nanometers laterally.[96] Another advantage is that this technique can be applied to nearly every sample without drastically changing the surrounding environment (i.e., vacuum or low temperatures). Choosing the right AFM setup, hard surfaces, such as ceramic materials,[97] dispersions of nanomaterials,[98] or soft surfaces, like polymers, or individual molecules of DNA can be imaged.[99] Therefore, using AFM allows us to gather detailed information about our coatings' surface topography, roughness, and electrical surface charges.
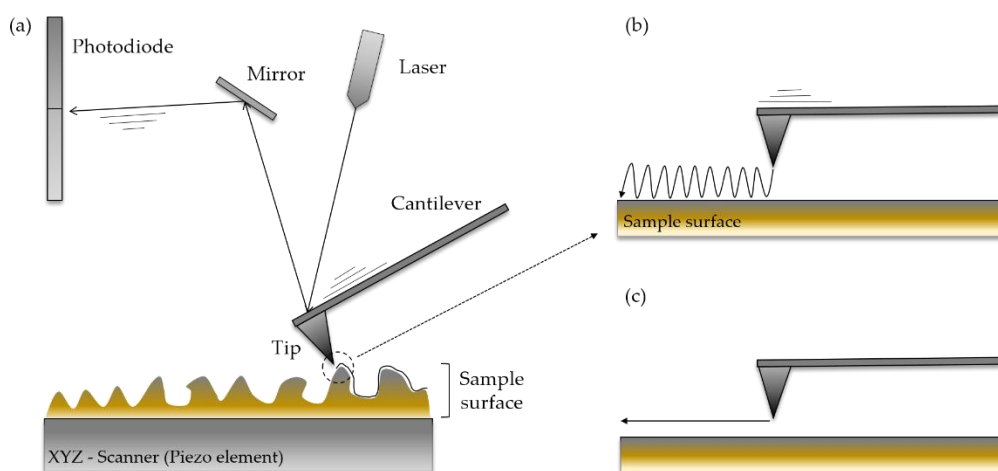
Figure 12. Schema of an AFM in tapping mode (a), and actual movement of the cantilever with respect to the sample surface in standard tapping mode (b) and contact mode (c).

To avoid the destruction or deformation of the fragile structure of our sample surfaces during topographic and roughness measurements, AFM in tapping mode was used (c.f. Figure 12a and b).[100] Here, the cantilever vibrates slightly above its resonance frequency. At the end of the cantilever, where the tip is located, the vibration amplitude is typically $1 - 10$ nm. While the vibrating cantilever is approaching the sample surface, at one point the amplitude will decrease due to the contact of the tip with the surface. The scanning follows the constant reduction of the vibrating amplitude instead of scanning at a constant deflection or height (i.e., contact mode). Thus, the cantilever is most of the scanning time not actually in contact with the sample. It only touches the surface for a very short time with a small force ($\approx$ pN).

Monitored are the amplitude, the frequency, and their shifts through a laser and its reflection (cf. Figure 12a). With the help of a mirror, the reflection is guided to a photodiode. Here, the incoming laser beam converts into electrical signals which then are evaluated and transferred into a topographic and phase image. Compared to other AFM modes, (i.e., contact mode c.f. Figure 12c) the tapping mode is less destructive due to the small applied force ($\approx$ pN), and the very short contact time, which additionally prevents shear.

Beyond topography and roughness, surface forces at the multilayer/water interface under in situ conditions are also of high interest. To obtain insights into surface forces normal AFM techniques like tapping- or contact-mode are not suitable, due to the high variation of the tip geometry.

However, defined interaction geometries can still be obtained for AFM by the so-called colloidal probe (CP) technique.[101] Here, a micrometer-sized colloidal particle is attached to a cantilever surface (c.f. Figure 13a and b). The technique also allows a combination of electrochemistry and direct force measurements.[102, 103]
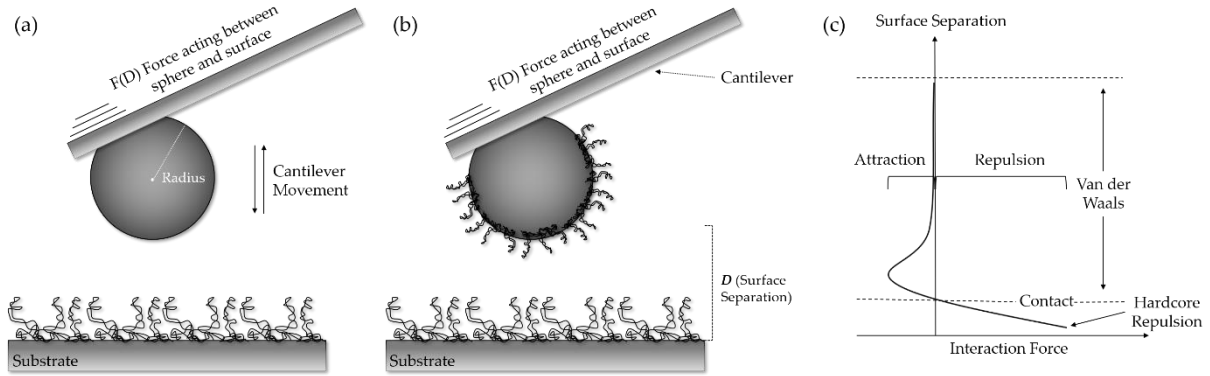
Figure 13. Schematic illustration of a colloidal probe technique for direct force measurements. (a) Uncoated sphere interacting with a flat coated surface and (b) coated sphere interacting with a coated surface. (c) Attractive van der Waals forces and hardcore repulsion between a colloidal sphere and a flat surface as a function of the surface separation.

It is experimentally easier to measure the interaction force between macroscopic bodies than their interaction potential.[104] In 1934, Derjaguin[105] introduced an approximation for the relationship between interaction energy and surface force $F(D)$ that holds when the distance D (or surface separation) between two spherical surfaces is much smaller than their radius of curvature (c.f. Figure 13c). The interaction energy per unit area $W(D)$ can easily be calculated theoretically.[106] The approximation is mainly suitable for the AFM CP technique. Given two spheres with radii R_1 and R_2, the interaction force between them is

$$F(D) = 2\pi \, \frac{R_1 R_2}{R_1 + R_2} \, W(D).$$

Regarding a sphere ($R_1 = R$) interacting with a surface ($R_2 = \infty$), it is convenient to normalize the force in the CP technique to R. Than the interaction force is

$$F(D) = 2\pi \, R \, W(D).$$

Using the interaction force $F(D)$ in dependency of the surface separation D, electrostatic and steric forces, can be investigated.

Steric forces are interaction forces that arise from the spatial arrangement of atoms. They arise from repulsion of groups or atoms (e.g., within a molecule) when they are too close to each other (simplest example are just two gas molecules at sufficient small inter-molecular

distances). In order to decrease this interaction, groups or atoms will move apart from the contact area. Generally, this will require stretching or bending of bonds with a related increase in energy. The final configuration is the configuration of minimum energy which will be the result of a compromise between the short range repulsion of molecules or atoms and the elastically deformation.[107]

Electrostatic forces are characterized by the surface charge density and the electrostatic potential at the surface. Counterions are attracted to the surface (the so-called electrical double layer) and lead to a repulsive force between surfaces of the same charge. However, electrostatic interactions between two surfaces, considered individually, do not describe every experiment. Derjaguin, Landau, Verwey, and Overbeek further extended the theory of electrostatic forces and included additional van der Waals (vdW) interaction in aqueous dispersions.[42, 43, 108] The theory, in short DLVO, is explained by the interplay of two forces: the attractive van der Waals force and the repulsive electrostatic double-layer force.[100] It describes the coagulation of dispersed particles. Here, van der Waal forces promote coagulation while the double-layer force stabilizes the dispersion. When two surfaces approach each other, the overlap between the electrical double layers rises, and the coulomb repulsion increases. Also, the dispersion (or vdW) attraction increases. Therefore, the combination of the energies of the arising of the electrostatic interactions and the dispersion can be summed up to

$$W(D) = W_{van\ der\ Waals(vdW)}(D) + W_{double\ layer\ (dl)}(D)$$

With $W_{dl}(D)$ is the interaction energy (per unit area) due to the electric double layer and $W_{vdW}(D)$ is the attractive interaction energy (per unit area) resulting from the van der Waals interactions. In general, van der Waals forces always act due to the consequence of interactions of the fluctuating electrical dipoles of atoms and molecules. Compared to electrostatic interactions, the vdW potential largely is not sensitive to variations in salt concentration or pH. At small enough distances, the vdW attraction always exceeds the double-layer repulsion and is described as follows

$$W_{vdW}(D) = -\frac{H}{12\pi D^2}.$$

Here, H is the Hamaker constant and in most cases positive which results in an attractive vdW force.

Importantly, DLVO theory is applied to describe the interaction forces between polymer brushes. Polymer chains are a brush-like configuration when grafted or localized at an interface (solid-liquid or liquid-liquid) and the distance between grafting points is way lower than the diameter of the free polymer coil. The proximity then triggers a special type of interaction between the neighboring polymer molecules, forcing them to stretch orthogonally to the graft interface, instead of a random coil arrangement.

Polyelectrolyte (PE) brushes are a special class of polymer brushes that contain charges. The electrostatic interaction between the charges of the polymer chains makes them far more repulsive than uncharged ones. A key factor of any PE brush is a strong confinement of counterions within the brush layer. To maintain electroneutrality counterions are confined to the brush at a high entropic cost. This leads to strong repulsion between segments and electrostatic interactions that are not present in uncharged brushes.[46]

2.2.4   Streaming potential – a method to characterize the dynamic electrical surface zeta potential on a macroscopic level

The Colloidal Probe (CP) technique is suitable for the measurement of electrical surface charge density and surface potential. However, the colloidal probe technique is a static technique, always equilibrium forces are measured. Therefore, another method has to be applied to determine the electrical surface charges when flow occurs.

The Streaming Potential (SP) is an electrokinetic technique commonly used to study the surface charge density of biological membranes. When both electrodes are held at the same potential, the streaming current is measured directly as the electric current flowing through the electrodes. The streaming potential is the potential difference produced by the convective flow of electrolyte solution due to a pressure gradient (i.e., liquid flow) through a capillary, membrane, plug, or diaphragm when the electrodes on either side of the fluidic geometry are set to the same potential[109, 110] (c.f. Figure 14). If the chamber surface is charged (i.e., through sample material), an electrical double layer next to the surface exhibits a local increase in counterion concentration. The application of the flow engenders, due to the transport of the mobile charges in the double layer, a streaming current, leading to a potential difference between the two electrodes, the streaming potential ΔU.[111]

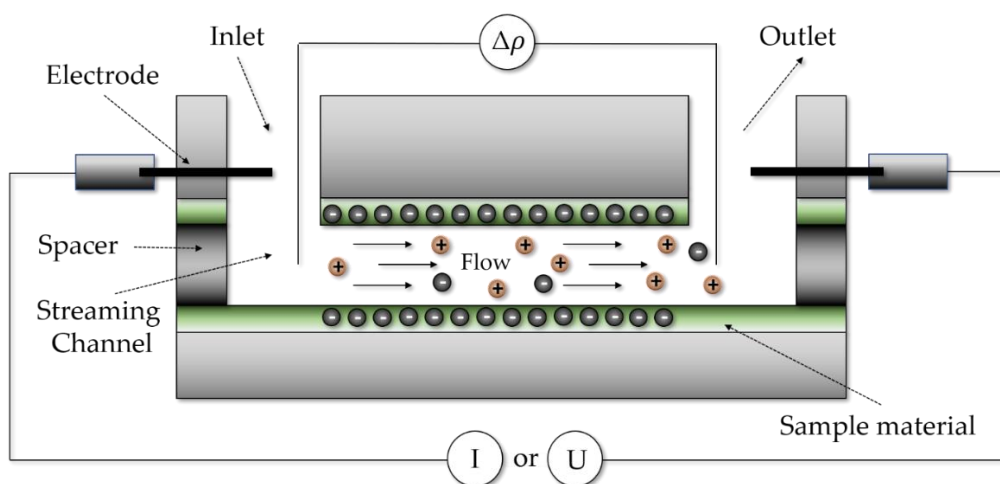
Figure 14. Schematic setup for a Streaming Potential process. Measured is the pressure difference $\Delta\rho$, the current I, and the voltage drop (ΔU).

There are two forms the SP can take. One is the transversal SP where the flow is through a porous plug of material (i.e., membrane pores). The other one is the tangential SP.

Here, the flow is across the surface of the membrane through a channel formed by two plates (c.f. Figure 14). In both cases, the accumulation of counter-charges downstream generates an SP across the capillary and causes a conduction current through the capillary in the reverse direction. This opposes the mechanical transfer of charge, causing back-conduction by ion diffusion and electro-osmotic flow.

The charge transfer originating from the two processes is called leak current. After reaching equilibrium conditions, the streaming current cancels the leak current where the occurring potential difference is the SP.

The SP can be calculated experimentally by plotting the voltage difference across the membrane over a range of flow rates. Thus, a linear relation should be obtained. To calculate the zeta potential ζ, a parameter for dynamic surface potentials, the gradient of the best fit linear line in combination with the Helmholtz-Smoluchowski equation is used.

$$\zeta = \frac{\Delta U}{\Delta P} \frac{\eta \kappa}{\varepsilon \varepsilon_0}$$

Here, $\Delta U/\Delta P$ is the ratio of electrical streaming potential ΔU to pressure drop ΔP, κ is the conductivity of the electrolyte solution, η the dynamic viscosity, ε the relative permittivity of the liquid, and ε_0 the electrical permittivity of vacuum.

2.2.5   Ellipsometry – a method to determine film thickness

In modern science, thin film or coating systems are often used for surface modifications. Especially, in nanotechnology,[112] microelectronics,[113] or optoelectronics,[114] ultrathin films, or coatings play an important role. Therefore, it is necessary to have experimental methods to analyze and characterize such film systems. A very basic property of any coating is its thickness (e.g., film thickness).[115] One of the most used optical techniques to efficiently characterize these complex thin film systems (e.g., PEMs) is Ellipsometry. A linearly polarized monochromatic light is used in the incident beam. Then, a change in polarization and intensity as light reflects from a thin film is measured. This change is represented as an amplitude ratio, Ψ, and the phase, Δ. The measured response depends on the optical properties and thickness of thin layers. Ellipsometry is primarily used to determine film thickness in the range of 1 nm up to 1 µm which makes the technique suitable for the analysis of our carbon nanotube (CNT) / polyelectrolyte (PE) film.

Polarization of light (elliptic)

Light can be described as an electromagnetic wave that travels through space. The orientation of the wave's electric field in space and time is known as polarization. The electric field vector $\vec{E}$ of a wave is always orthogonal to the propagation direction $\vec{z}$ and can be described by its x- and y-components. Since the wave is transverse, the electric-field intensity vector processes along an elliptic trajectory in any plane perpendicular to the direction of propagation. Here, in one period of $2\pi/\omega$ one revolution is achieved which can be described as a superposition of harmonic vibrations along two perpendicular axes. If the vibrations are shifted in phase the resulting trajectory is elliptic shown in Figure 15.

The wave propagates along the z-axis of the right-handed cartesian coordinate system x-y-z. X and Y are the amplitudes in the x and y directions, real, and non-negative quantities. Dependent on time the electric field vector $\vec{E}(t)$ in the plane $z = 0$ can be written as follows

$$\vec{E}(t) = \begin{bmatrix} E_x(t) \\ E_y(t) \end{bmatrix} = Re\left\{ \begin{bmatrix} Xe^{i\Phi} \\ Y \end{bmatrix} e^{i\omega(t-t_0)} \right\} .$$

Here, $E_x(t)$ and $E_y(t)$ are the complex amplitudes of $\vec{E}(t)$ along the x- and y-axis, $Re\{f\}$ is the real and $Im\{f\}$ is the imaginary part of the complex quantity f, Φ is the relative phase, ω the angular frequency, and t the time.

At the initial time $t = t_0$, the y component is at its maximum as indicated with the dashed arrow in Figure 15. The x component reaches its maximum after the time interval of Φ/ω (dotted arrow). Thereby, the angle Ψ is related to the relative phase Δ of the vibration along x- and y-directions. Are the values of Φ positive, the sense of precession is clockwise, and the polarization is called right-handed. If Φ is negative, the polarization ellipse goes counter-clockwise and is called left-handed. The values of Φ are usually limited to the interval from zero to 2π, or from $-\pi$ to π.

Figure 15. Polarization ellipse of light, described by the ellipsometric angles Ψ and Δ. The polarized wave propagates in the positive sense of the z axis, which points towards the reader.

The state of the elliptic polarization is also described by the amplitudes X and Y alongside the phase shift Φ. To be precise, only the relative amplitude X/Y is relevant. It can be expressed with the help of the angle Ψ shown in Figure 15 which is given as $\tan\Psi = X/Y$, varying from zero to $\pi/2$. With the help of the two real angles Ψ and Φ the *Jones vector*

$$\begin{bmatrix} sin\,\Psi e^{i\Phi} \\ cos\,\Psi \end{bmatrix}$$

can be written as a representation of the elliptic polarization. An important notion in dealing with polarization is that of the orthogonality of polarization states. Two states are called orthogonal when their Jones vectors are orthogonal in the usual sense of vector algebra. The polarization orthogonal to the Jones vector therefore is

$$\begin{bmatrix} -cos\,\Psi e^{i\Phi} \\ sin\,\Psi \end{bmatrix} = \begin{bmatrix} sin(\pi/2 - \Psi)\,e^{i(\Phi \pm \pi)} \\ cos(\pi/2 - \Psi) \end{bmatrix} .$$

There are three different polarization states: linear, circular, and elliptical. Thereby, the most general polarization of a monochromatic light wave is elliptic.

The ellipsometric technique is based on a suitable manipulation of the polarization state by auxiliary polarizing elements and the measured samples. Thereby, a basic configuration of polarizer-compensator-sample-analyzer (PCSA, c.f. Figure 16) can be used to determine the two ellipsometric parameters of the sample. The process consists of finding component settings for extinguishing the light at the detector. The azimuth of the polarizer (P_0) and compensator (C_0) are adjusted so that the resulting elliptically polarized light is reflected as linear polarized from the sample. Thus, the reflected beam is extinguished by a suitable adjusted analyzer azimuth (A_0).
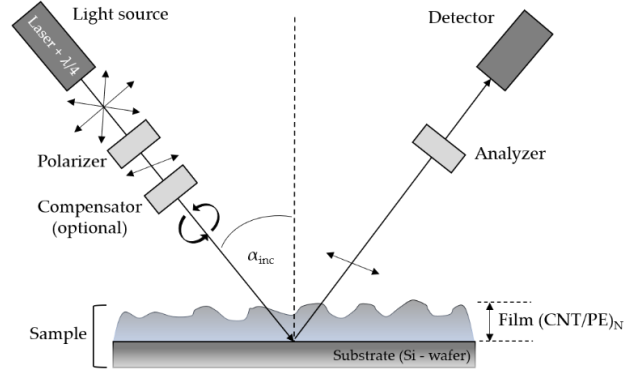
Figure 16. Principal set-up of a polarizer-compensator-sample-analyzer (PCSA) configuration.

Setting the azimuth of the complex amplitude zero, the linear equation of the complex reflectance ratio can be obtained as follows

$$\rho = \frac{\tau_c \, tan(P_0 - C_0) + tan \, C_0}{tan(P_0 - C_0) \, tan \, C_0 - 1} \, tan \, A_0 \ .$$

Thereby, τ_c is the complex transmittance ratio of the compensator. It is defined as

$$\tau_c = tan \, \Psi_c e^{i\Delta_c} \ ,$$

and can be expressed in terms of the angles Ψ_c and Δ_c. There is a significant simplification for results of a quarter-wave ($\tau_c = i$) compensator set at the azimuth of $C_0 = \pi/4$. Here, the output intensity is extingguished for two settings P_1, A_1 and P_2, A_2 related by $P_2 = \pm P_1, A_2 = -A_1$ (P_x - state of polarization, A_x - analyzer azimuths). In addition, these azimuths are related to the measured ellipsometric angles

$$\Psi = A_1, \qquad \Delta = 2P_1 + \pi/2, \qquad for \ A_1 \geq 0.$$

Using this simple setup with a laser source, high-quality polarizing elements, and mountings, highly precise and accurate measurements are achievable. To calibrate the instruments the usual way consists of multiple-zone (P_1, A_1 and P_2, A_2) measurements to determine and correct unavoidable errors in the zero positions of P, C, A, and the retardation angle of the compensator.

In this work null ellipsometric measurements are used to determine the film thickness d and the refractive index $\bar{n}$ of the adsorbed CNT/PE film (c.f. Figure 17). This is done by a numerical data evaluation of the experimentally determined ellipsometric angles Ψ_{exp} and Δ_{exp} as a function of the angle of incidence α_{inc}.

For a two-layer system (Si/SiO₂/Coating/Air) and with the help of a self-programmed algorithm of Dr. Peter Nestler, the refractive index profile perpendicular to the sample surface is given by four slaps ($n_{air} = 1$, $n_{SiO_2} = 1.457$, and $n_{Si} = 3.882 - 0.019i$).[116]
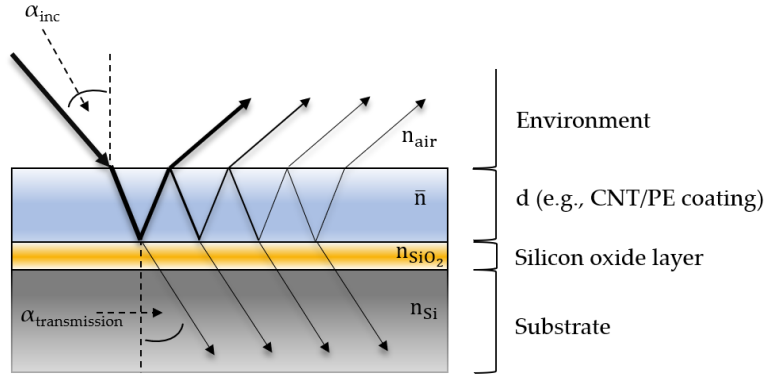
Figure 17. Representation of an incoming electromagnetic wave, its multiple reflections (due to the complexity pictured for just one layer), and transmissions through a sample with different refractive indexes n (n_{air} refractive index of the environment (e.g. air or water), $\bar{n}$ refractive index of the coated film, n_{SiO_2} refraction index of the silicon oxide layer, and n_{Si} refraction index of silicon).

Given a pair of values $(d, \bar{n})$, both r_p and r_s (complex reflection coefficients of p- and s-polarization) can be calculated with the help of the *Airy equation* given by

$$r_p = \frac{r_{p,1} + r_{p,2} \cdot e^{-i\varphi}}{1 + r_{p,1}r_{p,2} \cdot e^{-i\varphi}} \qquad r_s = \frac{r_{s,1} + r_{s,2} \cdot e^{i\varphi}}{1 + r_{s,1}r_{s,2} \cdot e^{i\varphi}} \quad ,$$

with $r_{p,1}$ the Fresnel coefficient of the p-polarized component at the environment / coating interface and $r_{p,2}$ as the component at the coating / substrate interface. This applies analogously for the s-polarized components $r_{s,1}$ and $r_{s,2}$. Also, the phase shift φ, given by

$$\varphi = 2\bar{n} \cos \alpha \cdot \frac{2\pi d}{\lambda} \quad ,$$

describes the phase change of the beam reflected at the film substrate interface compared to the air film interface. The propagation direction of the light with the wave length λ inside the coating is represented by the angle α. Therefore, the layer thickness changes the reflection coefficient via the relative phase φ.

However, the ellipsometric measurement only gives information about the complex reflectance ratio ρ with $\rho = r_p/r_s$. Due to its complexity, ρ provides a complex number consisting of a real part $Re(\rho)$ and an imaginary part $iIm(\rho)$. Through the measurement of the ellipsometric angles Ψ and Δ the complex number of ρ can be given in this polar form as $\rho = \tan \Psi \cdot e^{i\Delta}$. With the help of the *Airy equation*, the ratio $\rho = r_p/r_s$ can be calculated and fitted to the experimental values $\rho = \tan \Psi \cdot e^{i\Delta}$ by varying the parameters d and $\bar{n}$, which we want to know. Using one set of d and $\bar{n}$, for several ellipsometric measurements there are differences between calculated and measured angles. The mean square difference at all incident angles is defined as follows

$$X(d, \bar{n}) = \sqrt{\frac{1}{N^\circ} \sum_{i=1}^{N^\circ} \left(\left(\Delta_i^{exp} - \Delta_i^{calc} \right)^2 + \left(\Psi_i^{exp} - \Psi_i^{calc} \right)^2 \right)} \, .$$

Here, N° is the number of individual measurements at different angles of incidence. The minimization of $X(d, \bar{n})$ provides the values of d and $\bar{n}$ which describe the properties of the coating at best.[36, 117]

2.2.6   UV-Vis-NIR spectroscopy – a method to determine CNT surface coverage

The Ultra-Violet – Visible Near-Infrared (UV/VIS/NIR) spectroscopy is a powerful analytical technique to determine optical properties i.e., transmittance, reflectance, and absorbance of liquids and solids.[118, 119] It can be applied to characterize semiconductor materials, coatings, glass, and many other research and manufacturing materials, which makes it suitable for the optical characterization of our coatings. The operation range of UV/VIS/NIR spectroscopy lies between 175 nm to 3300 nm. Figure 18 shows the principal mode of operation.
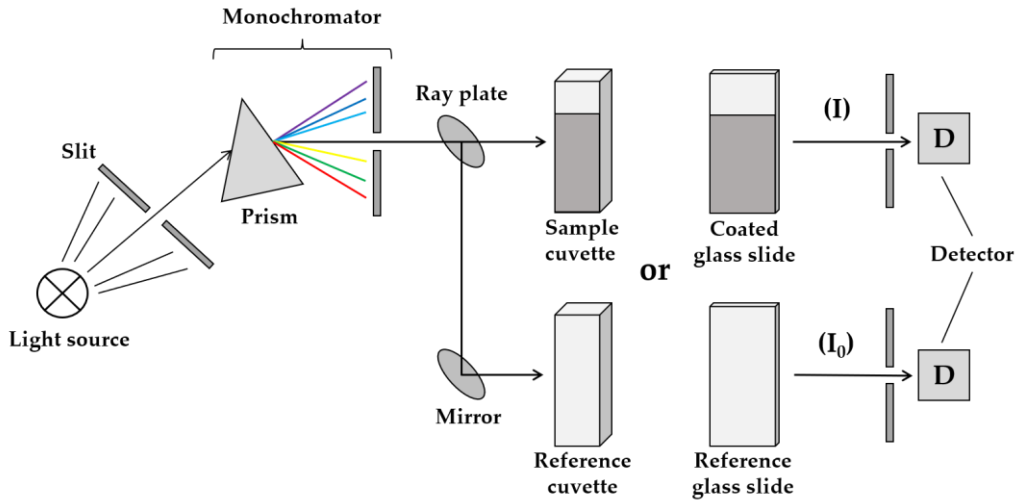
Figure 18. UV/VIS/NIR spectroscopy: Principal mode of operation.

Considering the absorption spectra of unsorted CNTs,[120] especially the Vis-NIR scope is of great interest when it comes to the optical characterization of our coatings with modified CNTs. According to the Beer-Lambert-law, the Extinction E_λ is defined as

$$E_\lambda = log_{10} \left(\frac{I_0}{I_1} \right) = \varepsilon_\lambda \cdot c \cdot l$$

with I_0 the incident light intensity, I_1 the intensity of the light transmitted through the sample, ε_λ molar absorption coefficient in M^{-1}cm^{-1}, c molar concentration in M, and l the optical path length. Knowing the concentration c of our CNTs in the suspension, the optical path length i.e., the thickness of the cuvette, and the measured absorbance A(λ), which is defined as

$$A(\lambda) = log_{10} \left(\frac{I_0}{I_1} \right)$$

we are able to determine the extinction coefficient ε_λ. Thereby, ε_λ is specific for our CNTs. This also allows the calculation of the CNT surface coverage of our coatings.

Here, we use the Beer-Lambert-law as follows

$$E_\lambda = log_{10}\left(\frac{I_0}{I_1}\right) = \varepsilon_\lambda \cdot c_{CNT} \cdot d_{film} \, .$$

Instead of the cuvette thickness l, we use d_{film} (film thickness, measured with ellipsometry) as optical path length. This allows the estimation of the CNT concentration c_{CNT} of our coated surfaces, thus the calculation of the surface coverage.

2.2.7 Characterization of electrical properties of CNT/PE multilayer films

The characterization of the CNT/PE surface coatings regarding their electrical properties took place in terms of electrical resistance R, resistivity ρ_{ris}, and electrical conductivity σ. Due to the ohmic behavior of the coated films the electrical resistance can be simply calculated as

$$R = \frac{U}{I} \, ,$$

with U the applied voltage over the electrical conductor and I the current that flows through the conductor. Knowing the sample size and the thickness d (from ellipsometric measurements) of our coatings, the resistivity ρ_{ris} can be calculated according to

$$\rho_{ris} = R \cdot \frac{A_{el}}{L} = R \cdot \frac{W}{L} \cdot d \, .$$

Here, A_{el} is the cross-sectional area of the coating, L the length and W the width of the coating (c.f. Figure 19). The conductivity σ is the inverse of ρ_{ris}

$$\sigma = \frac{1}{\rho_{ris}} \, .$$
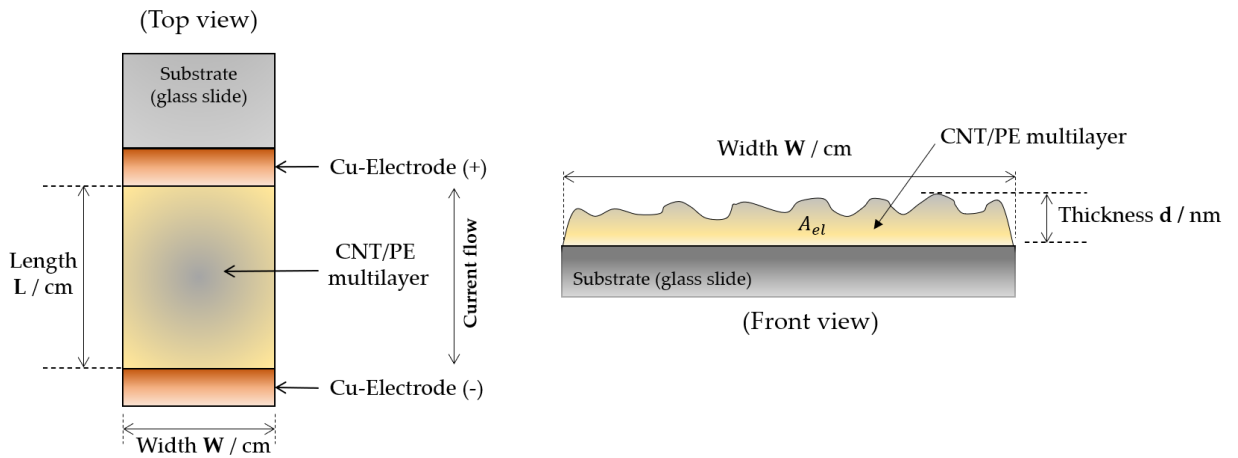
Figure 19. Schematic representation of the electrical measurement setup.

3   Article conclusions

3.1   **Neuber, S.**, Sill, A., Efthimiopoulos, I., Nestler, P., Fricke, K., & Helm, C. A. (2022). Influence of molecular weight of polycation polydimethyldiallylammonium and carbon nanotube content on the electric conductivity of layer-by-layer films. Thin Solid Films, 745, 139103.

The creation of biocompatible and highly electrically conductive nm-thin multilayer films has gained more and more interest in the field of implant surface applications. To create such films the layer-by-layer method, in combination with poly(diallyldimethylammonium chloride) (PDADMA) and modified carbon nanotubes (CNTs), was used. Different PDADMA molecular weights (322 and 44 kDa) and CNT concentrations, in the deposition suspension (0.15 and 0.25 mg/ml), enabled tunable film compositions and thereby tunable film properties i.e., film thickness or sheet resistance. By using chemically modified and therefore charged CNTs the adsorption process and thus the CNT surface coverage was improved.

After four deposited CNT/PDADMA bilayers a percolation transition occurred. At this point, the film, or more precisely the deposited CNTs, forms a lateral homogeneous net structure that resembles fallen jackstraws with now multiple CNT crossing points and nods. This enhanced the electron transport significantly. As a result, the film sheet resistance decreased by a factor of 3. By adding additional CNT/PDADMA bilayers after the percolation transit, the film thickness and surface coverage increase linearly with a constant conductivity of up to 4 kS/m. Increasing the molecular weight of PDADMA resulted in reduced film/air roughness, whereas film thickness and electrical conductivity were not affected. However, increasing the CNT concentration of the suspension up to 0.25 mg/ml raised the thickness per CNT/PDADMA bilayer. Simultaneously, the higher bilayer thickness is accompanied by a decreased electrical conductivity, which is attributed to an increased PDADMA/CNT ratio.

3.2   **Neuber, S.**, Sill, A., Ahrens, H., Quade, A., & Helm, C. A. Influence of Different Solutions on Electrically Conductive Films Composed of Carbon Nanotubes and Polydimethyldiallylammonium. ACS Applied Engineering Materials 2023 1 (6), 1493-1503

In our previous work, it is shown, that the preparation of stable electrically conductive nm-thin films from poly(dimethyldiallylammonium chloride) (PDADMA) and modified carbon nanotubes (CNTs), in a controlled way in air are possible. These films have to be stable and tunable not only at ambient but also at aqueous conditions, regarding implementation as an implant coating for medical applications. Layer-by-layer (LbL) coatings are mostly based on electrostatic interactions. However, since many synthetic polymers consist of a hydrophobic backbone, it is also interesting to understand the role of hydrophobic interactions within LbL films. Therefore, multilayer films built of PDADMA and oxidized CNTs, with a low linear charge density, were investigated in three different solutions.

In an aqueous environment, the CNT/PDADMA multilayer cohesion is due to the electrostatic attractions between oppositely charged functional groups of PDADMA and modified CNTs as well as through the hydrophobic attraction of the PDADMA backbone and the non-functionalized CNT atoms. The latter also affects the swelling behavior of the film. The hydrophobic attraction also ensures, additionally, that the films do not swell, as always observed previously for polyelectrolyte multilayers (PEMs). In fact, the CNT/PDADMA film shrinks or retains its thickness. It appears, that not only a high CNT: PDADMA ratio within the film, but also a generally thinner CNT/PDADMA multilayer (1 – 2 nm) are responsible for higher film conductivities (up to 13.4 kS/m). Thus, due to the tuning of interpolyelectrolyte forces film swelling can be prevented, which otherwise would negatively influence the electrical film properties. Overall, the films were stable, and on immersion into biologically relevant solutions, the electrical conductivity increased at ambient conditions.

3.3   Azinfar, A., **Neuber, S.,** Vancova, M., Sterba, J., Stranak, V., & Helm, C. A. (2021). Self-Patterning Polyelectrolyte Multilayer Films: Influence of Deposition Steps and Drying in a Vacuum. Langmuir, 37(35), 10490-10498.

Cell adhesion and proliferation on modified surfaces not only depend on the surface charge. Also, the lateral morphology of the surface itself is an important factor. Here, the self-patterning of polyelectrolyte multilayers consisting of PDADMA and PSS is investigated. Due to its higher mobility, a low molecular weight of PSS (M_w(PSS$_{short}$) = 10.7 kDa) was used. Monitored via AFM was the film self-pattering in air and water as a function of the number of deposited PDADMA/PSS bilayers.

When films were built with immobile high molecular weight polyelectrolytes no self-patterning was observed. However, after seven deposited PDADMA/PSS$_{short}$ bilayers, films built from PSS$_{short}$ started to begin the process of self-patterning shown via AFM images. With each additionally deposited PDADMA/PSS$_{short}$ bilayer, the lateral structure started changing from surface grooves, then stripes, and at the end to the point of circular domains. It appeared that the mean distance between the surface structures increased monotonously with the film thickness. Additional SEM images showed that films exposed to a vacuum resulted in a decrease in the film thickness, while the mean distance between the film domains increased. It also revealed a different film behavior depending on whether the film was PSS$_{short}$ – or PDADMA-terminated. Films terminated with PSS$_{short}$ were vertically thinner while the mean distance between domains slightly increased. This is attributed to the adaptation to the elastic modulus caused by dehydration during the exposure of the film to a vacuum. PDADMA-terminated films showed tall pillars and an increase in distance between the domains by a factor of 1.4.

Thus, it turned out the self-patterning process is driven by the mobility of polymers. The average spacing between the domains can be adjusted by the number of deposited bilayers, and exposure to a vacuum, whereby the surface morphology overall can be tuned.

3.4   Mohamad, H. S., **Neuber, S.**, & Helm, C. A. (2019). Surface forces of asymmetrically grown polyelectrolyte multilayers: searching for the charges. Langmuir, 35(48), 15491-15499.

Surface charges are essential parameters when it comes to biocompatibility. Cell adhesion and proliferation are highly influenced by the surface charge density. Using the layer-by-layer technique, films were prepared from strong polyelectrolytes with a low (PDADMA) and high (PSS) linear charge density at 0.1 mol/L NaCl. To investigate the polyelectrolyte conformation and surface charge of polyelectrolyte multilayers in aqueous solution at different salt concentrations, surface forces were used.

During the preparation process, the multilayer exhibits two growth regimes. In the beginning, in a non-linear growth regime, where the thickness per bilayer increases with each deposition step, the film contains as many positive as negative monomers. After reaching about 15 deposited layer pairs a linear growth regime occurs (exact number of bilayers, at which the transition occurs, depends on the PE molecular weight). This linear growth regime is characterized by excess cationic PDADMA monomers within the PEM. Surface force measurements at preparation conditions (0.1 mol/L NaCl) showed a flat, uncharged, and partially hydrophobic film surface, which also is independent of the film composition.

Electrostatic forces were found for films terminated with PSS when the ion concentration in the test solution was decreased below 0.1 mol/L. In the non-linear regime, the surface charge density is negative, while in the linear growth regime, it is positive. Always, it is low (one charge per $200 - 400\,\text{nm}^2$) at ion concentrations below the preparation concentration. The observed reversal of surface charge density in PSS-terminated films is attributed to an excess of PDADMA monomers within the film. When the films were terminated with PDADMA also steric forces were found in measuring solutions with low ion concentrations. Here, PDADMA chains protrude into the solution and form pseudo brushes, which scale as polyelectrolyte brushes with a small anchoring density ($1900\,\text{nm}^2$ per chain). Thus, the low linear charge density polycation adsorbs with few electrostatic monomer-monomer bonds. The charges of many of its monomers are compensated by negative monovalent ions resulting in loosely bound polycation chains. These chains form a pseudo-brush on the decrease of the ionic strength. In the following polyanion adsorption step, the polyanion replaces the monovalent anions, rendering the surface neutral. In the linear growth regime, many electrostatic monomer-monomer bonds are formed during each adsorption step. Yet, there is an excess of monovalent negative anions in the multilayer. This fact does not affect the almost non-existent surface charge at preparation conditions but the composition of the multilayer.

3.5   Gruening, M., **Neuber, S.**, Nestler, P., Lehnfeld, J., Dubs, M., Fricke, K., ... & Nebe, J. B.
        (2020). Enhancement of Intracellular Calcium Ion Mobilization by Moderately but Not
        Highly Positive Material Surface Charges. Frontiers in bioengineering and
        biotechnology, 8, 1016.

To further improve the bioactivity of titanium-based implants, regarding the optimization of cell/substrate interactions, the topography of the substrate needs to be modified. This can include additional physical or chemical treatments. Surface properties will influence cellular processes at the interface. Electrostatic forces at the cell/substrate interface can significantly affect cell adhesion and function. Therefore, a variety of different surface coatings were used and characterized via zeta (ζ) potential, a parameter for surface charges.

In this work, multiple titanium surfaces were modified with amino polymers, extracellular matrix proteins/peptide motifs, and polyelectrolyte multilayers to generate ζ-potentials between - 90 mV and + 50 mV. The intracellular calcium mobilization, representing cell activity, was significantly enhanced on surfaces with a moderate positive surface ζ-potential between + 1 mV and + 10 mV compared to their negative counterparts (- 90 mV to – 3 mV). High surface ζ-potentials up to + 50 mV led to increased losses of membrane integrity, viability, cell proliferation, and cell mobilization. Overall, positive charges offer unique cues that induce an intensive cell response. However, only moderate positive ζ-potentials are necessary to significantly increase cell viability and proliferation.

4 Summary

The combination of the Layer-by-Layer (LbL) method, a nano-material such as carbon nanotubes (CNTs), and charged polyelectrolytes (PEs) is a reliable approach to produce highly functionalized surface coatings. These coatings are stable, controllable, ultra-thin, and most importantly, biocompatible. The ability to tune their properties by varying the preparation conditions and the terminating layer opens up a wide range of applications in the fields of biology and medicine. Here, the goal was to create electrically conductive coatings on which cells grow and proliferate. To achieve this goal, a coating with a stable conductive film structure, a suitable film surface topography, and suitable surface potential (and ζ-potential) must be prepared.

At the beginning of this thesis, the focus was on the fabrication of electrically conductive multilayer films, whose electrical properties should be stable and adjustable in a controlled manner (**Article 1**). The combination of chemically modified CNTs as polyanions, a strong linear polycation like poly(diallyldimethylammonium chloride) (PDADMA), and the LbL-method allowed us to prepare such films. Their characterization was carried out in air at ambient conditions. Since PDADMA is non-conductive, the charge transfer within the film and thus the electrical conductivity itself depends mainly on the CNTs and their arrangement. It was found that four CNT/PDADMA bilayers (BL) were always necessary to create a lateral network structure with multiple CNT crossing points to enable and support electron transport within the film. Moreover, additional CNT/PDADMA BL resulted in decreasing sheet resistance, while the conductivity remained constant at ≈ 4 kS/m regardless of the number of bilayers. Increasing the PDADMA molecular weight (M_w) from 44.4 kDa to 322 kDa did not affect film properties such as thickness or electrical conductivity.

However, increasing the CNT concentration from 0.15 mg/ml to 0.25 mg/ml in the deposition suspension resulted in thicker and less conductive films. This is attributed to a faster adsorption process of the CNTs leading to more adsorption sites for the polycation. We found an increased PDADMA monomer/CNT ratio compared to films prepared with the lower CNT concentration in the deposition suspension. The electrical conductivity decreased by a factor of four down to 1.1 kS/m, which can be attributed to fewer contact points between the CNTs. Overall, we were able to prepare stable and electrically conductive multilayer films. Additionally, by varying the preparation conditions tuning of the electrical conductivity is possible.

To fulfill requirements regarding i.e., medical implants, film properties not only have to be stable and controllable in a dry state (described in Article 1) but also in a biological aqueous environment. Therefore, in **Article 2** we immersed our coated samples in three different solutions usually employed in biological research and compared their properties with their dry state, respectively. Also, hydration/swelling effects that normally occur for polyelectrolyte multilayer films (PEMs) in solutions were investigated.

For the film preparation, PDADMA (M_w = 322 kDa) and a deposition suspension of modified CNTs with two different concentrations (0.15 mg/ml and 0.25 mg/ml), which aged for two years, were used. Independent of the CNT suspension concentration, it turned out that the film thickness of the samples, prepared from the aged suspension, decreased significantly compared to the film thickness previously measured in Article 1. As a cross-check a new and fresh CNT suspension was made, which allowed us to reproduce the film thickness described in Article 1.

These results indicated that something happened with the CNT suspension over a two-year period. An analysis via X-ray photoelectron spectroscopy (XPS) showed a decrease in the percentage of functional groups in the CNTs from the aged suspension. The loss of functional groups resulted in less negatively charged CNTs and thus in fewer adsorption sites for the polycation PDADMA. Consequently, the PDADMA monomer/CNT ratio decreased, which lowered the thickness per bilayer by a factor of three, compared to films prepared with a freshly prepared CNT suspension. The lower linear charge density of the aged CNTs also enhanced their hydrophobicity, which is, in combination with the electrostatic forces, another important factor for multilayer cohesion. In contrast to PEMs made from polycations and polyanions, no swelling of the films occurred when immersed in solutions. This can be attributed to the fact that the increased hydrophobicity of the CNTs and the hydrophobic nature of the PDADMA backbone prevent the incorporation of water into the multilayer film. In solution, the films slightly shrink (by ≈ 2 nm), which makes them even more compact. Yet they remain stable. The result is an increased electrical conductivity from 9.6 kS/m, in the dry state, up to 15.3 kS/m immersed in solutions. To summarize, we showed that by tuning the interpolyelectrolyte forces the swelling and the ensuing decrease of the electrical conductivity of the films can be prevented.

Regarding the application in biology and medicine, we must consider that long-term exposure of cells to nano-materials like CNTs could lead to damage and inflammation of adjacent tissue. Therefore, it is necessary to prevent direct contact between the electrically conductive multilayer, i.e., CNT/PDADMA film, and the cells. The solution to this problem is a biocompatible top film that covers the CNT/PDADMA multilayer completely and still provides a lateral surface structure that supports cell adhesion and proliferation. Additional layers consisting solely of PEs could provide such a top film.

In **Article 3** we investigated the self-patterning of PEM films as function of deposition steps. After preparation in water, the films were dried, characterized in air, and in vacuum. The films were built with high and low molecular weight PEs. PDADMA was used as polycation and poly(styrene sulfonate) sodium salt (PSS) as polyanion. The observation via Atomic Force Microscopy (AFM) showed that films prepared with high molecular weight PEs are laterally homogeneous and form no patterns, due to the chain immobility. The flat surfaces are ineligible as a substrate for cell adhesion.

In contrast, films built with a short PSS, especially at $M_{w, PSS} = 10.7$ kDa, began to self-pattern after seven deposited PDADMA/PSS bilayers. With each additionally deposited bilayer, the surface got more and more structured, from grooves over stripes to circular domains. Increasing film thickness led to an increased lateral mean distance between the surface structures. Scanning Electron Microscopy (SEM) images showed that exposure to a vacuum resulted in a decrease in the film thickness attributed to water removal, while the mean distance between the domains increased.

Thus, by using this self-pattering process we are able to prepare PEMs with a highly structured surface. By adding PDADMA/PSS bilayers, not only the CNT/PDADMA film can be covered completely, but also a suitable surface morphology for cells can be created. Controlling the number of deposited bilayers allows the preparation of suitable coatings for cells.

To further improve the interaction of the cell and coated substrate not only the lateral structure but also the interacting electrostatic forces between cells and substrate are important for the nature of cell adhesion, function, and proliferation. In **Article 4** we investigated PEMs, consisting of strong PEs with a low (PDADMA) and high (PSS) linear charge density. We performed asymmetric force measurements with the help of the colloidal probe technique (CP). Here, the forces between a PEM-covered surface and a colloidal probe (silica sphere) glued to a cantilever were investigated. The colloidal probe was either bare or covered with polycation poly(ethylenimine) (PEI). The surfaces were immersed in NaCl solutions with different ionic strengths (I_{NaCl}), starting with deionized water, then enriched up to 1 mol/L NaCl. The interaction force between a CP and the surface was measured. Thus, insight into the surface potential/charge was obtained.

During film preparation, two growth regimes (parabolic and linear) exist. These regimes and the terminating layer determine the surface force of the PEM. PEMs with a terminating PSS layer are predominantly flat and negatively charged when the ion concentration is low and the film is in the parabolic growth regime (between 1 and ≈ 15 BL). This indicates charge reversal on PSS adsorption. At the transition point between the parabolic and linear growth regimes, the ratio between polyanion and polycation monomers starts to switch and some cationic monomers are neutralized not by anionic monomers but by monovalent ions. Therefore, the surface charge density in diluted NaCl solutions changed from slightly positive near the transition to positive in the linear growth regime. At the lowest ionic strengths (I_{NaCL}) the range of the surface potential goes from -40.5 mV (9 BL, parabolic) up to $+50$ mV (19 BL, linear).

In contrast, polycation (PDADMA) terminated films are overall positive in diluted NaCl solutions. At the beginning of the parabolic growth regime, the layers are more compact and flat. However, with each additional layer deposited, the film becomes less compact and the chains begin to loosen. The now more loosely bound chains start to protrude into the solution and form pseudo-brushes. This could already be observed for 10.5 BL.

It intensifies in the linear growth regime (begin at ≈ 15 BL) and results in steric surface forces. Changing the surrounding I_{NaCl} affects this behavior and the pseudo-brushes scale as polyelectrolyte brushes.

By controlling the number of bilayers (thus the growth regime), the surrounding ionic strength, and the conformation of PEs at the PEM surface, it is possible to prepare a suitable range of surface properties i.e., for cell adhesion and proliferation. To prove that these multilayers can provide a suitable surface and have a positive effect on cell behavior, we coated in **Article 5** titanium-covered samples with PEMs. Investigated was the cell interaction with the surface at different zeta(ζ) - potentials, a parameter for dynamic surface potential. Here the cell activity is measured by the mobilization of calcium (Ca^{2+}) within the cell as a function of the ζ - potential of the substrate and the externally applied electrical potential. The cell activity indicates if the ζ - potential, provided by the sample surface, is suitable or not for the cells. The favorable interaction with the substrate is also reflected in the cell morphology and proliferation.

The results showed that highly negative ζ - potentials between - 90 and - 3 mV led to a decreasing/reduced Ca^{2+} mobilization which correlates with reduced cell activity. Nearly neutral to moderate positive surfaces (ζ - potential + 1 to + 10 mV) i.e., PSS-terminated PEMs are able to promote cell adhesion and growth as demonstrated by an increased Ca^{2+} mobilization. The access to the intracellular Ca^{2+} stores, provided by the external stimulus, is now more effective and suggests a higher cell activity. Increasing the ζ - potentials up to ≈ + 50 mV (highly positive), i.e., PDADMA - terminated PEMs with pseudo-brushes, resulted in restricted cell viability and impaired Ca^{2+} mobilization, which led to a disturbed cell morphology and proliferation. In conclusion, only surfaces, terminated with i.e., PEI, with moderate positive charges (ζ - potential + 1 to + 10 mV) are able to improve the Ca^{2+} mobilization and thus the cell activity and proliferation. PEMs with a PSS termination provide negative ζ −potentials, onto which cells adhere, and proliferate. Therefore, they are a good alternative for surface functionalization for implant surfaces.

In summary, the objective set at the beginning of the thesis is addressed within articles written as part of this thesis. It is possible to fabricate PEMs with modified CNTs to produce coatings that are electrically conductive with tunable sheet resistance, whether dry in air or immersed in an aqueous solution (Articles 1 and 2). Also, for pure PEMs, it is shown that with the right molecular weight of PEs and a certain number of bilayers, a suitable surface structure for cell adhesion can be produced (Article 3). Additional surface properties such as a suitable surface charge density can be provided by PEMs which can improve the cell activity as monitored with Ca^{2+} mobilization (Articles 4 and 5). The next step is to combine the knowledge gained from Articles 1 – 5 and link it to the application of external electrical fields to cells.

5 References

1. Abraham, A. M.; Venkatesan, S., A review on application of biomaterials for medical and dental implants. *Proceedings of the Institution of Mechanical Engineers, Part L: Journal of Materials: Design and Applications* **2023,** *237* (2), 249-273.

2. Gruening, M.; Neuber, S.; Nestler, P.; Lehnfeld, J.; Dubs, M.; Fricke, K.; Schnabelrauch, M.; Helm, C. A.; Müller, R.; Staehlke, S., Enhancement of intracellular calcium ion mobilization by moderately but not highly positive material surface charges. *Frontiers in bioengineering and biotechnology* **2020,** *8*, 1016.

3. Akter, F.; Ibanez, J., Bone and cartilage tissue engineering. In *Tissue engineering made easy*, Elsevier: 2016; pp 77-97.

4. Hanawa, T., Titanium–tissue interface reaction and its control with surface treatment. *Frontiers in bioengineering and biotechnology* **2019,** *7*, 170.

5. Brunette, D. M.; Tengvall, P.; Textor, M.; Thomsen, P., *Titanium in medicine: material science, surface science, engineering, biological responses and medical applications*. Springer: 2001.

6. Wang, N.; Yang, A.; Fu, Y.; Li, Y.; Yan, F., Functionalized organic thin film transistors for biosensing. *Accounts of chemical research* **2019,** *52* (2), 277-287.

7. Kippelen, B.; Brédas, J.-L., Organic photovoltaics. *Energy & Environmental Science* **2009,** *2* (3), 251-261.

8. Xu, Q.; Li, X.; Jin, Y.; Sun, L.; Ding, X.; Liang, L.; Wang, L.; Nan, K.; Ji, J.; Chen, H., Bacterial self-defense antibiotics release from organic–inorganic hybrid multilayer films for long-term anti-adhesion and biofilm inhibition properties. *Nanoscale* **2017,** *9* (48), 19245-19254.

9. Boudou, T.; Crouzier, T.; Ren, K.; Blin, G.; Picart, C., Multiple functionalities of polyelectrolyte multilayer films: new biomedical applications. *Advanced materials* **2010,** *22* (4), 441-467.

10. Picart, C., Polyelectrolyte multilayer films: from physico-chemical properties to the control of cellular processes. *Current medicinal chemistry* **2008,** *15* (7), 685-697.

11. Decher, G.; Hong, J., Buildup of ultrathin multilayer films by a self-assembly process: II. Consecutive adsorption of anionic and cationic bipolar amphiphiles and polyelectrolytes on charged surfaces. *Berichte der Bunsengesellschaft für physikalische Chemie* **1991,** *95* (11), 1430-1434.

12. Decher, G.; Eckle, M.; Schmitt, J.; Struth, B., Layer-by-layer assembled multicomposite films. *Current opinion in colloid & interface science* **1998,** *3* (1), 32-39.

13. Pall, M. L., Electromagnetic fields act via activation of voltage-gated calcium channels to produce beneficial or adverse effects. *Journal of cellular and molecular medicine* **2013,** *17* (8), 958-965.

14. Zhu, R.; Sun, Z.; Li, C.; Ramakrishna, S.; Chiu, K.; He, L., Electrical stimulation affects neural stem cell fate and function in vitro. *Experimental neurology* **2019,** *319*, 112963.

15. Mintmire, J. W.; Dunlap, B. I.; White, C. T., Are fullerene tubules metallic? *Physical review letters* **1992,** *68* (5), 631.

16. Tans, S. J.; Devoret, M. H.; Dai, H.; Thess, A.; Smalley, R. E.; Geerligs, L.; Dekker, C., Individual single-wall carbon nanotubes as quantum wires. *Nature* **1997,** *386* (6624), 474-477.

17. Sadri, R.; Ahmadi, G.; Togun, H.; Dahari, M.; Kazi, S. N.; Sadeghinezhad, E.; Zubir, N., An experimental study on thermal conductivity and viscosity of nanofluids containing carbon nanotubes. *Nanoscale research letters* **2014,** *9*, 1-16.

18. Kim, P.; Shi, L.; Majumdar, A.; McEuen, P. L., Thermal transport measurements of i ndividual multiwalled nanotubes. *Physical review letters* **2001,** *87* (21), 215502.

19. Li, Y.; Chen, S.; Wu, M.; Sun, J., Polyelectrolyte multilayers impart healability to highly electrically conductive films. *Advanced Materials* **2012,** *24* (33), 4578-4582.

20. Ostendorf, A.; Cramer, C.; Decher, G.; Schönhoff, M., Humidity-tunable electronic conductivity of polyelectrolyte multilayers containing gold nanoparticles. *The Journal of Physical Chemistry C* **2015,** *119* (17), 9543-9549.

21. An, H.; Habib, T.; Shah, S.; Gao, H.; Patel, A.; Echols, I.; Zhao, X.; Radovic, M.; Green, M. J.; Lutkenhaus, J. L., Water sorption in MXene/polyelectrolyte multilayers for ultrafast humidity sensing. *ACS Applied Nano Materials* **2019,** *2* (2), 948-955.

22. Lemons, J.; Natiella, J., Biomaterials, biocompatibility, and peri-implant considerations. *Dental clinics of north america* **1986,** *30* (1), 3-23.

23. Arteshi, Y.; Aghanejad, A.; Davaran, S.; Omidi, Y., Biocompatible and electroconductive polyaniline-based biomaterials for electrical stimulation. *European Polymer Journal* **2018,** *108*, 150-170.

24. Gheith, M. K.; Sinani, V. A.; Wicksted, J. P.; Matts, R. L.; Kotov, N. A., Single-walled carbon nanotube polyelectrolyte multilayers and freestanding films as a biocompatible platform for neuroprosthetic implants. *Advanced Materials* **2005,** *17* (22), 2663-2670.

25. Sabino, R. M.; Mondini, G.; Kipper, M. J.; Martins, A. F.; Popat, K. C., Tanfloc/heparin polyelectrolyte multilayers improve osteogenic differentiation of adipose-derived stem cells on titania nanotube surfaces. *Carbohydrate polymers* **2021,** *251*, 117079.

26. Li, X.; Gao, H.; Uo, M.; Sato, Y.; Akasaka, T.; Feng, Q.; Cui, F.; Liu, X.; Watari, F., Effect of carbon nanotubes on cellular functions in vitro. *Journal of Biomedical Materials Research Part A: An Official Journal of The Society for Biomaterials, The Japanese Society for*

Biomaterials, and The Australian Society for Biomaterials and the Korean Society for Biomaterials **2009,** *91* (1), 132-139.

27.   Kolosnjaj, J.; Szwarc, H.; Moussa, F., Toxicity studies of carbon nanotubes. *Bio-Applications of Nanoparticles* **2007**, 181-204.

28.   Jacobsen, N. R.; Pojana, G.; White, P.; Møller, P.; Cohn, C. A.; Smith Korsholm, K.; Vogel, U.; Marcomini, A.; Loft, S.; Wallin, H., Genotoxicity, cytotoxicity, and reactive oxygen species induced by single-walled carbon nanotubes and C60 fullerenes in the FE1-Muta™ Mouse lung epithelial cells. *Environmental and molecular mutagenesis* **2008,** *49* (6), 476-487.

29.   Harvey, A. G.; Hill, E. W.; Bayat, A., Designing implant surface topography for improved biocompatibility. *Expert review of medical devices* **2013,** *10* (2), 257-267.

30.   Rosales-Leal, J. I.; Rodríguez-Valverde, M. A.; Mazzaglia, G.; Ramón-Torregrosa, P. J.; Díaz-Rodríguez, L.; García-Martínez, O.; Vallecillo-Capilla, M.; Ruiz, C.; Cabrerizo-Vílchez, M., Effect of roughness, wettability and morphology of engineered titanium surfaces on osteoblast-like cell adhesion. *Colloids and Surfaces A: Physicochemical and Engineering Aspects* **2010,** *365* (1-3), 222-229.

31.   Ranella, A.; Barberoglou, M.; Bakogianni, S.; Fotakis, C.; Stratakis, E., Tuning cell adhesion by controlling the roughness and wettability of 3D micro/nano silicon structures. *Acta biomaterialia* **2010,** *6* (7), 2711-2720.

32.   Rodriguez-Hernandez, J., Wrinkled interfaces: Taking advantage of surface instabilities to pattern polymer surfaces. *Progress in Polymer Science* **2015,** *42*, 1-41.

33.   Bates, F. S., Polymer-polymer phase behavior. *Science* **1991,** *251* (4996), 898-905.

34.   Halperin, A.; Tirrell, M.; Lodge, T., Tethered chains in polymer microstructures. *Macromolecules: Synthesis, Order and Advanced Properties* **1992**, 31-71.

35.   Luo, M.; Epps III, T. H., Directed block copolymer thin film self-assembly: emerging trends in nanopattern fabrication. *Macromolecules* **2013,** *46* (19), 7567-7579.

36.   Nestler, P. Untersuchungen der Adsorption und Diffusion von Polyelektrolyten in Polyelektrolyt-Multischichten   mittels   in-situ   Ellipsometrie   und Neutronenreflektometrie. 2015.

37.   Tanaka, T.; Sun, S.-T.; Hirokawa, Y.; Katayama, S.; Kucera, J.; Hirose, Y.; Amiya, T., Mechanical instability of gels at the phase transition. *Nature* **1987,** *325* (6107), 796-798.

38.   Terada, A.; Okuyama, K.; Nishikawa, M.; Tsuneda, S.; Hosomi, M., The effect of s urface charge property on Escherichia coli initial adhesion and subsequent biofilm formation. *Biotechnology and bioengineering* **2012,** *109* (7), 1745-1754.

39.   Tang, L.; Thevenot, P.; Hu, W., Surface chemistry influences implant biocompatibility. *Current topics in medicinal chemistry* **2008,** *8* (4), 270-280.

40. Felgueiras, H.; Antunes, J.; Martins, M.; Barbosa, M., Fundamentals of protein and cell interactions in biomaterials. In *Peptides and proteins as biomaterials for tissue regeneration and repair*, Elsevier: 2018; pp 1-27.

41. Ferrari, M.; Cirisano, F.; Morán, M. C., Mammalian cell behavior on hydrophobic substrates: Influence of surface properties. *Colloids and Interfaces* **2019,** *3* (2), 48.

42. Derjaguin, B. V., Theory of the stability of strongly charged lyophobic sol and of the adhesion of strongly charged particles in solutions of electrolytes. *Acta phys. chim. URSS* **1941,** *14*, 633.

43. Verwey, E.; Overbeek, J. T. G., Theory of the stability of lyophobic colloids. *Journal of Colloid Science* **1955,** *10* (2), 224-225.

44. Misra, S.; Varanasi, S.; Varanasi, P., A polyelectrolyte brush theory. *Macromolecules* **1989,** *22* (11), 4173-4179.

45. Ballauff, M.; Borisov, O., Polyelectrolyte brushes. *Current Opinion in Colloid & Interface Science* **2006,** *11* (6), 316-323.

46. Das, S.; Banik, M.; Chen, G.; Sinha, S.; Mukherjee, R., Polyelectrolyte brushes: theory, modelling, synthesis and applications. *Soft Matter* **2015,** *11* (44), 8550-8583.

47. De Aza, P.; Luklinska, Z.; Santos, C.; Guitian, F.; De Aza, S., Mechanism of bone-like formation on a bioactive implant in vivo. *Biomaterials* **2003,** *24* (8), 1437-1445.

48. Fernández-Yagüe, M.; Antoñanzas, R. P.; Roa, J. J.; Biggs, M.; Gil, F. J.; Pegueroles, M., Enhanced osteoconductivity on electrically charged titanium implants treated by physicochemical surface modifications methods. *Nanomedicine: Nanotechnology, Biology and Medicine* **2019,** *18*, 1-10.

49. Staehlke, S.; Koertge, A.; Nebe, B., Intracellular calcium dynamics dependent on defined microtopographical features of titanium. *Biomaterials* **2015,** *46*, 48-57.

50. Young, R. J.; Lovell, P. A., *Introduction to polymers*. CRC press: 2011.

51. McCrum, N. G.; Buckley, C. P.; Bucknall, C. B., *Principles of polymer engineering*. Oxford University Press: 1997.

52. Yokozawa, T.; Ohta, Y., Transformation of step-growth polymerization into living chain-growth polymerization. *Chemical reviews* **2016,** *116* (4), 1950-1968.

53. Gibson, I.; Rosen, D. W.; Stucker, B.; Khorasani, M.; Rosen, D.; Stucker, B.; Khorasani, M., *Additive manufacturing technologies*. Springer: 2021; Vol. 17.

54. Tieke, B., *Makromolekulare Chemie: Eine Einführung*. John Wiley & Sons: 2014.

55. Sperling, L. H., *Introduction to physical polymer science*. John Wiley & Sons: 2005.

56. Shrivastava, A., *Introduction to plastics engineering*. William Andrew: 2018.

57. Jones, R. G.; Pure, I. U. o.; Division, A. C. P.; Wilks, E. S., *Compendium of polymer terminology and nomenclature: IUPAC recommendations, 2008*. RSC Pub.: 2009.

58.   Koetz, J.; Kosmella, S., *Polyelectrolytes*. Springer: 2007.

59.   Schanze, K. S.; Shelton, A. H., Functional polyelectrolytes. *Langmuir* **2009,** *25* (24), 13698 13702.

60.   Padeste, C.; Neuhaus, S., *Polymer micro-and nanografting*. William Andrew: 2015.

61.   Braus, M., The theory of electrolytes. I. Freezing point depression and related phenomena (Translation). **2019**.

62.   Müller, R.; Abke, J.; Schnell, E.; Scharnweber, D.; Kujat, R.; Englert, C.; Taheri, D.; Nerlich, M.; Angele, P., Influence of surface pretreatment of titanium-and cobalt-based biomaterials on covalent immobilization of fibrillar collagen. *Biomaterials* **2006,** *27* (22), 4059-4068.

63.   Chen, S.; Guo, Y.; Liu, R.; Wu, S.; Fang, J.; Huang, B.; Li, Z.; Chen, Z.; Chen, Z., Tuning surface properties of bone biomaterials to manipulate osteoblastic cell adhesion and the signaling pathways for the enhancement of early osseointegration. *Colloids and Surfaces B: Biointerfaces* **2018,** *164*, 58-69.

64.   Thrivikraman, G.; Boda, S. K.; Basu, B., Unraveling the mechanistic effects of electric field stimulation towards directing stem cell fate and function: A tissue engineering perspective. *Biomaterials* **2018,** *150*, 60-86.

65.   Yu, M.-F., Fundamental mechanical properties of carbon nanotubes: current understanding and the related experimental studies. *J. Eng. Mater. Technol.* **2004,** *126* (3), 271-278.

66.   Yakobson, B. I.; Avouris, P., Mechanical properties of carbon nanotubes. In *Carbon nanotubes: synthesis, structure, properties, and applications*, Springer: 2001; pp 287-327.

67.   Bandaru, P. R., Electrical properties and applications of carbon nanotube structures. *Journal of nanoscience and nanotechnology* **2007,** *7* (4-5), 1239-1267.

68.   Chen, J.; Wei, S.; Xie, H. In *A brief introduction of carbon nanotubes: history, synthesis, and properties*, Journal of Physics: Conference Series, IOP Publishing: 2021; p 012184.

69.   Arora, N.; Sharma, N., Arc discharge synthesis of carbon nanotubes: Comprehensive review. *Diamond and related materials* **2014,** *50*, 135-150.

70.   Iijima, S., Helical microtubules of graphitic carbon. *nature* **1991,** *354* (6348), 56-58.

71.   Popov, V. N., Carbon nanotubes: properties and application. *Materials Science and Engineering: R: Reports* **2004,** *43* (3), 61-102.

72.   Guo, T.; Nikolaev, P.; Thess, A.; Colbert, D. T.; Smalley, R. E., Catalytic growth of single-walled manotubes by laser vaporization. *Chemical physics letters* **1995,** *243* (1-2), 49-54.

73.   Guo, T.; Diener, M.; Chai, Y.; Alford, M.; Haufler, R.; McClure, S.; Ohno, T.; Weaver, J.; Scuseria, G.; Smalley, R., Uranium stabilization of C28: a tetravalent fullerene. *Science* **1992,** *257* (5077), 1661-1664.

74. Lu, Z.; Raad, R.; Safaei, F.; Xi, J.; Liu, Z.; Foroughi, J., Carbon nanotube based fiber supercapacitor as wearable energy storage. *Frontiers in Materials* **2019,** *6*, 138.

75. Ikegami, T.; Nakanishi, F.; Uchiyama, M.; Ebihara, K., Optical measurement in carbon nanotubes formation by pulsed laser ablation. *Thin Solid Films* **2004,** *457* (1), 7-11.

76. Zaytseva, O.; Neumann, G., Carbon nanomaterials: production, impact on plant development, agricultural and environmental applications. *Chemical and Biological Technologies in Agriculture* **2016,** *3* (1), 1-26.

77. Ebbesen, T.; Lezec, H.; Hiura, H.; Bennett, J.; Ghaemi, H.; Thio, T., Electrical conductivity of individual carbon nanotubes. *Nature* **1996,** *382* (6586), 54-56.

78. Dai, H.; Wong, E. W.; Lieber, C. M., Probing electrical transport in nanomaterials: conductivity of individual carbon nanotubes. *Science* **1996,** *272* (5261), 523-526.

79. Zhang, R.; Zhang, Y.; Wei, F., Controlled synthesis of ultralong carbon nanotubes with perfect structures and extraordinary properties. *Accounts of chemical research* **2017,** *50* (2), 179-189.

80. Poncharal, P.; Berger, C.; Yi, Y.; Wang, Z.; de Heer, W. A., Room temperature ballistic conduction in carbon nanotubes. ACS Publications: 2002; Vol. 106, pp 12104-12118.

81. Pop, E.; Mann, D.; Wang, Q.; Goodson, K.; Dai, H., Thermal conductance of an individual single-wall carbon nanotube above room temperature. *Nano letters* **2006,** *6* (1), 96-100.

82. Thostenson, E. T.; Li, C.; Chou, T.-W., Nanocomposites in context. *Composites science and technology* **2005,** *65* (3-4), 491-516.

83. López-Oyama, A.; Silva-Molina, R.; Ruíz-García, J.; Gámez-Corrales, R.; Guirado-López, R., Structure, electronic properties, and aggregation behavior of hydroxylated carbon nanotubes. *The Journal of Chemical Physics* **2014,** *141* (17).

84. Mather, R. R., Surface modification of textiles by plasma treatments. In *Surface modification of textiles*, Elsevier: 2009; pp 296-317.

85. Stevie, F. A.; Donley, C. L., Introduction to x-ray photoelectron spectroscopy. *Journal of Vacuum Science & Technology A* **2020,** *38* (6).

86. Cushman, C. V.; Chatterjee, S.; Major, G. H.; Smith, N. J.; Roberts, A.; Linford, M. R., Trends in Advanced XPS Instrumentation. *Vac. Technol. Coat* **2017,** *9*, 25-31.

87. Moore, C. E.; Russell, H. N., Binding energies for electrons of different types. *Journal of Research of the National Bureau of Standards* **1952,** *48* (1), 61.

88. Baer, D. R.; Artyushkova, K.; Richard Brundle, C.; Castle, J. E.; Engelhard, M. H.; Gaskell, K. J.; Grant, J. T.; Haasch, R. T.; Linford, M. R.; Powell, C. J., Practical guides for x-ray photoelectron spectroscopy: First steps in planning, conducting, and reporting XPS measurements. *Journal of Vacuum Science & Technology A* **2019,** *37* (3).

89. Omidi, M.; Fatehinya, A.; Farahani, M.; Akbari, Z.; Shahmoradi, S.; Yazdian, F.; Tahriri, M.; Moharamzadeh, K.; Tayebi, L.; Vashaee, D., Characterization of biomaterials. In *Biomaterials for oral and dental tissue engineering*, Elsevier: 2017; pp 97-115.

90. Decher, G.; Hong, J. D.; Schmitt, J., Buildup of ultrathin multilayer films by a self-assembly process: III. Consecutively alternating adsorption of anionic and cationic polyelectrolytes on charged surfaces. *Thin solid films* **1992,** *210*, 831-835.

91. De Villiers, M. M.; Otto, D. P.; Strydom, S. J.; Lvov, Y. M., Introduction to nanocoatings produced by layer-by-layer (LbL) self-assembly. *Advanced drug delivery reviews* **2011,** *63* (9), 701-715.

92. Iler, R., Multilayers of colloidal particles. *Journal of colloid and interface science* **1966,** *21* (6), 569-594.

93. Machado, G.; Feil, A. F.; Migowski, P.; Rossi, L.; Giovanela, M.; Crespo, J. d. S.; Miotti, L.; Sortica, M. A.; Grande, P. L.; Pereira, M. B., Structural control of gold nanoparticles self-assemblies by layer-by-layer process. *Nanoscale* **2011,** *3* (4), 1717-1723.

94. Du, Y.; Chen, C.; Li, B.; Zhou, M.; Wang, E.; Dong, S., Layer-by-layer electrochemical biosensor with aptamer-appended active polyelectrolyte multilayer for sensitive protein determination. *Biosensors and Bioelectronics* **2010,** *25* (8), 1902-1907.

95. Tian, Y.; Park, J. G.; Cheng, Q.; Liang, Z.; Zhang, C.; Wang, B., The fabrication of single-walled carbon nanotube/polyelectrolyte multilayer composites by layer-by-layer assembly and magnetic field assisted alignment. *Nanotechnology* **2009,** *20* (33), 335601.

96. Eaton, P.; West, P., *Atomic force microscopy*. Oxford university press: 2010.

97. Roa, J.; Oncins, G.; Díaz, J.; Capdevila, X.; Sanz, F.; Segarra, M., Study of the friction, adhesion and mechanical properties of single crystals, ceramics and ceramic coatings by AFM. *Journal of the European Ceramic Society* **2011,** *31* (4), 429-449.

98. Pratibha, R.; Park, W.; Smalyukh, I., Colloidal gold nanosphere dispersions in smectic liquid crystals and thin nanoparticle-decorated smectic films. *Journal of applied physics* **2010,** *107* (6).

99. Mangalam, A. P.; Simonsen, J.; Benight, A. S., Cellulose/DNA hybrid nanomaterials. *Biomacromolecules* **2009,** *10* (3), 497-504.

100. Butt, H.-J.; Graf, K.; Kappl, M., *Physics and chemistry of interfaces*. John Wiley & Sons: 2023.

101. Karg, A.; Rößler, T.; Mark, A.; Markus, P.; Lauster, T.; Helfricht, N.; Papastavrou, G., A versatile and simple approach to electrochemical colloidal probes for direct force measurements. *Langmuir* **2021,** *37* (46), 13537-13547.

102. Rentsch, S.; Siegenthaler, H.; Papastavrou, G., Diffuse layer properties of thiol-modified gold electrodes probed by direct force measurements. *Langmuir* **2007,** *23* (17), 9083-9091.

103.   Papastavrou, G., Combining electrochemistry and direct force measurements: from the control of surface properties towards applications. *Colloid and Polymer Science* **2010,** *288,* 1201-1214.

104.   Mohamad, H. S. Surface Forces Characterization of Polyelectrolyte Monolayers and Multilayers. 2018.

105.   Derjaguin, B., Friction and adhesion. IV. The theory of adhesion of small particles. *Kolloid Zeits* **1934,** *69,* 155-164.

106.   Israelachvili, J. N., *Intermolecular and surface forces*. Academic press: 2011.

107.   Hill, T. L., On steric effects. *The Journal of Chemical Physics* **1946,** *14* (7), 465-465.

108.   Derjaguin, B.; Kussakov, M., Anomalous properties of thin polymolecular films V. *Acta physicochim. URSS* **1939,** *10,* 25.

109.   Oatley-Radcliffe, D.; Aljohani, N.; Williams, P.; Hilal, N., Electrokinetic phenomena for membrane charge. In *Membrane Characterization*, Elsevier: 2017; pp 405-422.

110.   Peeters, J.; Mulder, M.; Strathmann, H., Streaming potential measurements as a characterization method for nanofiltration membranes. *Colloids and Surfaces A: Physicochemical and Engineering Aspects* **1999,** *150* (1-3), 247-259.

111.   West, A., Experimental methods to investigate self-assembly at interfaces. In *Interface Science and Technology*, Elsevier: 2018; Vol. 21, pp 131-241.

112.   Swaminathan, V. S.; Wei, R.; Gandy, D. W., Nanotechnology coatings for erosion protection of turbine components. **2010**.

113.   Singh, N.; Singh, K.; Pandey, A.; Kaur, D., Improved electrical transport properties in high quality nanocrystalline silicon carbide (nc-SiC) thin films for microelectronic applications. *Materials Letters* **2016,** *164,* 28-31.

114.   Chtouki, T.; El Mrabet, M.; Tarbi, A.; Goncharova, I.; Erguig, H., Comprehensive review of the morphological, linear and nonlinear optical characterization of spin-coated NiO thin films for optoelectronic applications. *Optical Materials* **2021,** *118,* 111294.

115.   Ohlídal, I.; Franta, D., 3 Ellipsometry of thin film systems. *Progess in Optics* **2000,** *41,* 181-282.

116.   Palik, E. D., *Handbook of optical constants of solids*. Academic press: 1998; Vol. 3.

117.   Sill, A. Vertical diffusion of polyelectrolytes in polyelectrolyte multilayers during film preparation and post preparation treatment. 2022.

118.   Biyada, S.; Merzouki, M.; Elkarrach, K.; Benlemlih, M., Spectroscopic characterization of organic matter transformation during composting of textile solid waste using UV–Visible spectroscopy, Infrared spectroscopy and X-ray diffraction (XRD). *Microchemical Journal* **2020,** *159,* 105314.

119.   Baka, N. A.;   Abu-Siada, A.;   Islam, S.; El-Naggar, M., A new technique to measure interfacial tension of transformer oil using UV-Vis spectroscopy. *IEEE Transactions on Dielectrics and Electrical Insulation* **2015,** *22* (2), 1275-1282.

120.   Green, A. A.; Hersam, M. C., Processing and properties of highly enriched double-wall carbon nanotubes. *Nature Nanotechnology* **2009,** *4* (1), 64-70.

6   Abbreviations

A	Analyzer
AC	Alternating Current
AFM	Atomic Force Microscopy
APTES	(3-Aminopropyl)triethoxysilan
ATP	Adenosine 5'-triphosphate
BL	Bilayer
C	Compensator
CNT	Carbon Nanotube
CP	Colloidal Probe
CVD	Chemical Vapor Deposition
DC	Direct Current
DLS	Dynamic Light Scattering
DLVO	Derjaguin, Landau, Vervey, and Overbeek
DMEM	Debecco's Modified Eagle's Medium
DNA	Deoxyribonucleic Acid
ECM	Extracellular Matrix
LBL	Layer–by–layer
MWCNT	Multi-Walled Carbon Nanotube
P	Polarizer
PBS	Phosphate-buffered Saline Solution
PCSA	Polarizer-Analyzer-Sample-Analyzer
PDADMA	Poly(diallyldimethylammonium chloride)
PDI	Polydispersity Index
PE	Polyelectrolyte
PEI	Poly(ethylenimine)
PEM	Polyelectrolyte Multilayer

pH	Potential Hydrogen
PPAAm	Plasma Polymerized Allylamine
PSS	Poly(styrene sulfonate)
RGD	Arginyl-Glycyl-Aspartic
RNA	Ribonucleic Acid
SEM	Secondary Electron Microscopy
SP	Streaming Potential
SPM	Scanning Probe Microscopy
SWCNT	Single-Walled Carbon Nanotube
Ti	Titan
UV-Vis-NIR	Ultraviolet-Visible Near-Infrared
vdW	van der Waals
XPS	X-ray Photoelectron Spectroscopy

Ca	Calcium
Co	Cobalt
Fe	Iron
H_2SO_4	Sulfuric acid
HNO_3	Nitric acid
Mo	Molybdenum
NaCl	Natrium chloride
Nb	Niobium
Ni	Nickel
Si	Silicon
SiO_2	Silicon oxide
Ta	Tantalum

7   Symbol dictionary

$A(\lambda)$	Absorbance
ε_λ	Absorption coefficient
ω	Angular frequency
$\langle r^2 \rangle^{\frac{1}{2}}$	Average end-to-end chain distance
N_A	Avogadro constant
$E_{binding}$	Binding energy
λ_B	Bjerrum length
k_B	Boltzmann constant
θ_{bond}	Bonding angle
θ_{chiral}	Chiral angle
C_h	Chiral vector
ρ	Complex reflectance ratio
r_p	Complex reflection coefficient of p-polarization
r_s	Complex reflection coefficient of s-polarization
c	Concentration
c_{CNT}	Concentration of carbon nanotubes
l_{cont}	Contour length
I	current
λ_D	Debye length
X	Degree of polymerization
η	Dynamic viscosity
σ	Electrical conductivity
ΔU	Electrical streaming potential
e	Elementary charge
Ψ, Δ	Ellipsometric angles
E_{photon}	Energy of incident photon
E_λ	Extinction
E_f	Fermi energy
$\vec{E}$	Field vector

d_{film}	Film thickness
H	Hamaka constant
I_0	Incoming light intensity
$W(D)$	Interaction energy
$W_{double\ layer\ (dl)}(D)$	Interaction energy due to the double layer
$W_{van\ der\ Waals\ (vdW)}(D)$	Interaction energy resulting from van der Waals interaction
$F(D)$	Interaction force
κ^{-1}	Inverse Debye length
I_{ionic}	Ionic strength
$E_{kinetic}$	Kinetic energy
l	Length
l_{max}	Maximum chain length
I_1	Measured light intensity
M_i	Molecular weight of a chain
M_0	Molecular weight of repeating unit/monomer
M	Monomer
n_i	Number of chains of molecular weight
n	Number of monomer bonds
$M_i^{\cdot}$	Number of monomers within the radical
X_n	Number-average degree of polymerization
M_n	Number-average molecular weight
φ	Phase shift
ΔP	Pressure drop
$\vec{z}$	Propagation direction
$R^{\cdot}$	Radical
$\langle s^2 \rangle^{\frac{1}{2}}$	Radius of gyration
n_{air}	Refractive index of air
n_{Si}	Refractive index of silicon
n_{SiO_2}	Refractive index of silicon oxide
ε_r	Relative dielectric constant

Φ	Relative phase
R	Resistance
R_s	Sheet resistance
ρ_{ris}	Specific resistance
D	Surface separation
T	Temperature
d	Thickness
E_v	Vacuum energy
ε_0	Vacuum permittivity
U	Voltage
λ	Wavelength
X_w	Weight-average degree of polymerization
M_w	Weight-average molecular weight
φ_{work}	Work function
ζ	Zeta potential

8 Author contributions

Article 1:

Neuber, S., Sill, A., Efthimiopoulos, I., Nestler, P., Fricke, K., & Helm, C. A. (2022). Influence of molecular weight of polycation polydimethyldiallylammonium and carbon nanotube content on electric conductivity of layer-by-layer films. *Thin Solid Films*, *745*, 139103.

S.N. oxidized the CNTs, built the multilayers, and characterized them. He also performed statistical analysis of the data. K.F. performed the XPS measurements and analyzed them. A.S. planned the chemical modification of the CNTs and validated it. P.N. analyzed the ellipsometric data. I.E. performed ellipsometric measurements. S.N. and C.A.H. planned the experiments. S.N., A.S., and C.A.H. wrote the manuscript.

Article 2:

Neuber, S., Sill, A., Ahrens, H., Quade, A., & Helm, C. A. (2023). Influence of Different Solutions on Electrically Conductive Films Composed of Carbon Nanotubes and Polydimethyldiallylammonium. *ACS Applied Engineering Materials*.

S.N. oxidized the CNTs, built the multilayers, characterized them, and also performed the statistical analysis of the data. A.Q. performed the XPS measurements and analyzed them. S.N. and A.S. performed the ellipsometric measurements and A.S. analyzed the ellipsometric data. H.A. helped with data analysis and provided theoretical insights. S.N. and C.A.H. planned the experiments. S.N., A.S., and C.A.H. wrote the manuscript.

Article 3:

Azinfar, A., **Neuber, S.**, Vancova, M., Sterba, J., Stranak, V., & Helm, C. A. (2021). Self-patterning polyelectrolyte multilayer films: Influence of deposition steps and drying in a vacuum. *Langmuir*, *37*(35), 10490-10498.

C.A.H. and A.A. conceived and designed the experiments. A.A. and S.N. prepared the samples. AA and S.N. performed and analyzed AFM and X-ray reflectometry experiments. A.A. performed and analyzed the ellipsometry measurements. A.A., S.N., M.V., J.S., V.S., and C.A.H. designed, performed, and analyzed SEM experiments. A.A. and C.A.H. wrote the paper.

Article 4:

Mohamad, H. S., **Neuber, S.**, & Helm, C. A. (2019). Surface forces of asymmetrically grown polyelectrolyte multilayers: searching for the charges. *Langmuir*, *35*(48), 15491-15499.

C.A.H. and H.S.M. conceived and designed the experiments. H.S.M. prepared, analyzed the samples, and performed the analysis of the data. S.N. prepared and analyzed the AFM images. H.S.M. and C.A.H. wrote the paper.

<u>Article 5:</u>

Gruening, M., **Neuber, S.**, Nestler, P., Lehnfeld, J., Dubs, M., Fricke, K., Schnabelrauch M., Helm C.A., Müller R., Staehlke S., and Nebe J. B. (2020). Enhancement of intracellular calcium ion mobilization by moderately but not highly positive material surface charges. *Frontiers in bioengineering and biotechnology, 8*, 1016.

M.G. did the conceptualization, investigation, validation, visualization, and original draft preparation. S.N. prepared the PEMs. P.N. performed layer thickness measurement including review and editing. K.F. performed XPS measurement and did the plasma polymerized allylamine (PPAAm) preparation. M.D. performed the (3-aminopropyl) triethoxysilan (APTES) and peptide sequence Arg-Gly-Asp (RGD) preparation. J.L. performed the PEI and poly(propylene imine) dendrimer generation 4 (PPI-G4) preparation with review and editing. M.S. performed visualization, review, and editing. C.A.H. and R.M. performed review, editing, and funding acquisition. S.S. performed adenosine 5′-triphosphate (ATP) receptor immunofluorescence, review, and editing. J.B.N. performed conceptualization, review and editing, project administration, and funding acquisition.

Greifswald, 27th October 2023   ………………………….   ………………………

      Location, Date   Prof. Dr. Christiane A. Helm   Sven Neuber

9 Publications

9.1 Publications published in peer-reviewed journals

Neuber, S., Sill, A., Efthimiopoulos, I., Nestler, P., Fricke, K., & Helm, C. A. (2022). Influence of molecular weight of polycation polydimethyldiallylammonium and carbon nanotube content on electric conductivity of layer-by-layer films. *Thin Solid Films*, *745*, 139103.

(Article 1, DOI: 10.1016/j.tsf.2022.139103)

Neuber, S., Sill, A., Ahrens, H., Quade, A., & Helm, C. A. (2023). Influence of Different Solutions on Electrically Conductive Films Composed of Carbon Nanotubes and Polydimethyldiallylammonium. *ACS Applied Engineering Materials*.

(Article 2, DOI: 10.1021/acsaenm.3c00085)

Azinfar, A., **Neuber, S.**, Vancova, M., Sterba, J., Stranak, V., & Helm, C. A. (2021). Self-Patterning Polyelectrolyte Multilayer Films: Influence of Deposition Steps and Drying in a Vacuum. *Langmuir*, *37*(35), 10490-10498.

(Article 3, DOI: 10.1021/acs.langmuir.1c01409)

Mohamad, H. S., **Neuber, S.**, & Helm, C. A. (2019). Surface forces of asymmetrically grown polyelectrolyte multilayers: searching for the charges. *Langmuir*, *35*(48), 15491-15499.

(Article 4, DOI: 10.1021/acs.langmuir.9b01787)

Gruening, M., **Neuber, S.**, Nestler, P., Lehnfeld, J., Dubs, M., Fricke, K., ... & Nebe, J. B. (2020). Enhancement of Intracellular Calcium Ion Mobilization by Moderately but Not Highly Positive Material Surface Charges. *Frontiers in bioengineering and biotechnology*, *8*, 1016.

(Article 5, DOI: 10.3389/fbioe.2020.01016)

Article 1

Influence of molecular weight of polycation polydimethyldiallylammonium and carbon nanotube content on electric conductivity of layer-by-layer films

Neuber, S., Sill, A., Efthimiopoulos, I., Nestler, P., Fricke, K., & Helm, C. A.

Thin Solid Films

Volume 745 (2022) 139103

Contents lists available at ScienceDirect

Thin Solid Films

journal homepage: www.elsevier.com/locate/tsf

Influence of molecular weight of polycation polydimethyldiallylammonium and carbon nanotube content on electric conductivity of layer-by-layer films

Sven Neuber [a], Annekatrin Sill [a], Ilias Efthimiopoulos [a], Peter Nestler [b], Katja Fricke [c], Christiane A. Helm [a,*]

[a] Institute of Physics, University of Greifswald, Felix-Hausdorff-Straße 6, D-17489 Greifswald, Germany
[b] ZIK-HIKE - Biomechanics, University of Greifswald, Fleischmannstr. 42, D-17489, Germany
[c] Leibniz Institute for Plasma Science and Technology, Felix-Hausdorff-Straße 2, D-17489 Greifswald, Germany

ABSTRACT

For biological and engineering applications, nm-thin films with high electrical conductivity and tunable sheet resistance are desirable. Multilayers of polydimethyldiallylammonium chloride (PDADMA) with two different molecular weights (322 and 44.3 kDa) and oxidized carbon nanotubes (CNTs) were constructed using the layer-by-layer technique. The surface coverage of the CNTs was monitored with a selected visible near infrared absorption peak. Both the film thickness and the surface coverage of the CNTs increased linearly with the number of CNT/PDADMA bilayers deposited (film thickness up to 80 nm). Atomic force microscopy images showed a predominantly surface-parallel orientation of CNTs. Ohmic behavior with constant electrical conductivity of each CNT/PDADMA film and conductivity up to $4 \cdot 10^3$ S/m was found. A change in PDADMA molecular weight by almost a factor of ten has no effect on the film thickness and electrical conductivity, only the film/air roughness is reduced. However, increasing CNT concentration in the deposition dispersion from 0.15 up to 0.25 mg/ml results in an increased thickness of a CNT/PDADMA bilayer (by a factor of three). The increased bilayer thickness is accompanied by a decreased electrical conductivity (by a factor of four). The decreased conductivity is attributed to the increased monomer/CNT ratio.

1. Introduction

Electrically active implants are often isolators covered by an electrically conducting coating [1,2]. Ultrathin organic films as coatings were investigated. For applications, the sheet resistance R_s of the coating needs to be low and adjustable. For very thin films to be sufficient, high electrical conductivity is required [3–7]. One way to reduce the sheet resistance of an organic film is to make a composite material with electrically conductive carbon nanotubes (CNTs). Electrically conductive films of carbon nanotubes have been made many different ways. However, the influence of film composition on electrical conductivity is far from clear. We used the layer-by-layer (LbL) technique and found constant electrical conductivity above a certain number of layers. With constant electrical conductivity, it is possible to tune the sheet resistance within an order of magnitude by adjusting (i) the preparation conditions and (ii) the thickness of the film.

In the LbL technique, films are prepared by the consecutive adsorption of oppositely charged polyions [8–11]. The film thickness can be controlled by the number of deposition steps. To identify the composition of the film, absorption spectra of one component can be used. At first glance, the visible and near infrared (Vis-NIR) absorption spectrum of CNTs is complicated [12]: Depending on the preparation of CNTs different absorption spectra are observed, and the correlation between CNT absorption spectrum and other physical properties of CNTs is not yet established. However, we find that for a specific preparation procedure typical absorption peaks can be identified.

Kotov and coworkers [13] showed that it is possible to form electrically conductive LbL films by using polyelectrolytes (PE) and CNTs. CNTs have interesting electrical properties: Due to freely moving electrons, the electrical conductivity of a multi-walled carbon nanotube can be large ($\sim 10^7$ S/m) [14]. Therefore, we use multi-walled nanotubes. However, even for μm-thick films consisting of CNTs only, the conductivity is reduced by a factor of 10 to 100 (up to $6.7 \cdot 10^5$ S/m) [15,16]. Between CNTs, electrons are transferred by a hopping process between touching CNTs. Compared to a single nanotube, the charge transfer between CNTs reduced the conductivty of that film by one to two orders of magnitude [3,4]. Multilayers consisting only of organic polyelectrolytes have a low elelctrically conductivity; it is fourteen to sixteen

orders of magnitude smaller than that of a CNT, 10^{-9} S/m to 10^{-7} S /m; conductivity occurs by ion transport [17]. Therefore, high electrical conductivity in LbL films can only be achieved by CNTs which touch at cross-over points and allow the electrons to hop from one CNT to the next.

For LbL film assembly, the dispersion of hydrophobic CNTs in water is necessary. In the past, this was achieved by chemically modifying the CNTs with functional groups or by wrapping them in polyanions, usually poly(styrenesulfonate sodium salt) (PSS) [18,19]. LbL films prepared from two kinds of chemically modified CNTs (one kind of CNT was positively charged, the other negatively) showed a low conductivity (200 S/m to 800 S/m), three orders of magnitude lower than found in films prepared of pure CNTs [20]. LbL films made from single-wall CNTs wrapped in PSS and a second polyelectrolyte exhibited a somewhat larger conductivity: 430 S/m with CNTs and laminin [13] or 1000 S /m with CNTs and polyvinyl alcohol [18]. We shall show that oxidation of the CNTs and close packing leads to a larger conductivity.

To complement the Vis-NIR absorption measurements, the film surface is imaged by atomic force microscopy (AFM) and the film thickness is determined by ellipsometry. We modified the CNTs (single-walled/double-walled mixture; carbon nanotubes ratio > 90%, diameter 1 to 2 nm, length 5 to 30 μm) by chemical oxidation to obtain negatively charged CNTs. To achieve a high packing density of the film, a strong linear polycation (polydimethyldiallylammonium chloride, PDADMA) was used. To adjust the CNT surface coverage per deposition step, the CNT concentration in the dispersion was varied. To influence the thickness per polycation adsorption layer, the molecular weight of PDADMA was varied by almost a factor of ten [21].

2. Materials and methods

2.1. Chemical modification of CNTs

To obtain negatively charged CNTs, they were treated with a mixture of concentrated acid. This process is necessary to reduce the hydrophobicity of the CNT sidewalls and thus, to increase the dispersion of the CNTs in water. The acid treatment presumably leads to the formation of holes and oxidative etching along the walls of the CNTs [22–24]. The acid mixture of concentrated H_2SO_4 and HNO_3 produces electrophilic groups like NO_2^+, which can attack the -C = C- double bonds. This creates new defects. In addition, the H_2SO_4 molecule can attack the created and existing defect sites. A C-OSO_2OH bond is formed which, when reacted with water, leads to a-OH bond [25].

Hydrophobic CNTs (512 mg, single-walled/double-walled mixture; CNT ratio > 90%, diameter 1 to 2 nm, length 5 to 30 μm, abcr GmbH, Karlsruhe, Germany) were treated with 50 ml of a volume/volume ratio (1:3) of a HNO_3 (60–68%)/H_2SO_4 (98%) acid mixture at 80 °C for 3.5 h according to the procedure proposed by López-Oyama [22].

The obtained dispersion was filtered under vacuum and washed with deionized water until the pH of the rinsing water became neutral. The solvent was removed with the use of a liquid nitrogen rotary evaporator and modified CNTs were dried overnight via lyophilization. After the chemical treatment, 65 mg of dry CNTs were obtained (at ambient conditions), due to addition of some negative charges. This allowed the CNTs to be used as polyanions. For a fine dispersion in water, raw CNTs were put in a solution containing 2 wt% sodium dodecyl sulfate (SDS), purchased from Carl Roth GmbH+Co. KG, Karlsruhe, Germany.

2.2. Film preparation

Single side polished silica wafer (Silicon Materials, Kaufering, Germany) and microscope slides (76 mm × 26 mm, Carl Roth GmbH + Co. KG, Karlsruhe, Germany) were cleaned according to a RCA treatment protocol [26] and used as substrate. The polyelectrolyte multilayers in combination with freshly modified CNTs were prepared by the

LbL-method [27], sequential adsorption of oppositely charged PEs and CNTs from solution with the help of a dipping robot (Riegler & Kirstein GmbH, Potsdam, Germany) and a refrigerated circulation thermostat (Carl Roth GmbH + Co. KG, Karlsruhe, Germany) at 20 °C.

As polycations poly(ethylenimine) (PEI, branched, M_w = 750kDa, PDI = 12.5) and PDADMA (M_w = 44.3kDa and 322kDa, PDI = 2.19) were used. As polyanions we used PSS (M_w = 666kDa, PDI < 1.2) and modified CNTs. PEI was purchased from Sigma Aldrich Chemie GmbH (Steinheim, Germany), PDADMA and PSS from Polymer Standards Service (Mainz, Germany). For the polyelectrolyte solutions, the composition of the adsorption solution was 1 mM PE with respect to the monomer concentration solved in 100 mM NaCl (Merck KGaA, Darmstadt, Germany). The modified CNT concentration was 0.15 mg/ml and 0.25 mg/ml suspended in ultrapure water. The adsorption time for each deposition step was 30 min with three subsequent washing steps (each step 1 min) with ultrapure water (nominal conductivity of 0.054 μS/cm, Sartorius arium advance, Göttingen, Germany, followed by Millipore purification system, Molsheim, France) to remove the loosely bond polycations or polyanions. For all films the first adsorbed layer was PEI followed by a PSS layer. Then the PDADMA and the CNTs were absorbed in an alternating sequence. Therefore, the overall film structure is PEI/PSS/PDADMA/(CNT/PDADMA)$_N$, abbreviated as CNT/PDADMA film.

2.3. Atomic force microscopy

Surface morphology was determined with a DI Multimode AFM using NanoScope IIIa software from Veeco (Santa Barbara, CA, USA). As cantilever a RTESP-300 model (BRUKER, Billerica, MA, USA) was used with a tip radius < 10 nm. All measurements were done in the AFM tapping mode with dry samples at ambient conditions. At least 3 different positions of each sample were imaged with a scan size of 5 μm × 5 μm. For data analysis, the NanoScope Analysis (version 1.90, 32 bit) software from BRUKER (Billerica, MA, USA) was used. Beside imaging AFM is also used to quantify sample surface roughness, which is calculated via root mean square (RMS) deviation from measured height profiles.

AFM scratch images for comparison with ellipsometric measurements were recorded with JPK NanoWizzard 3 (JPK Instruments, Berlin, Germany) using OMCL-AC160TS cantilever (Oxford Instruments, Wiesbaden, Germany) with measured spring constant 61.8 N/m and sensitivity 29.7 nm/V.

2.4. Vis-NIR absorption spectroscopy

Vis-NIR spectra of the dry films were recorded with a Lambda 900 UV–Vis spectrometer from Perkin-Elmer (Wiesbaden, Germany), at 30% r.h.. The films were measured directly with the microscopic slides (76 mm × 26 mm, Carl Roth GmbH + Co.KG, Karlsruhe, Germany) at ambient conditions (≈ 21°C and relative humidity ≈ 30%). The slide was covered at both sides due to preparation conditions. To obtain the absorbance of one film, the obtained values were divided by two. The determination of the extinction coefficient was done with a CNT suspension in a cuvette (Rotilabo®-single-use cells, 4 ml, Carl Roth GmbH + Co. KG, Karlsruhe, Germany). According to the Beer-Lambert law the absorbance is given by $A = -\log\left(\frac{I}{I_0}\right) = \varepsilon \cdot d \cdot c$. The incident intensity is I_0 (at a particular wavelength), I is the transmitted intensity after passing through a sample with a thickness d, containing a concentration c of the absorbing species with a wavelength-dependent extinction coefficient ε. Absorption was measured from 400 nm to 1800 nm with 5 nm/s steps and an integration time of 1 s per step.

2.5. Ellipsometry

CNT/PDADMA film thickness d_{film} was determined by null-
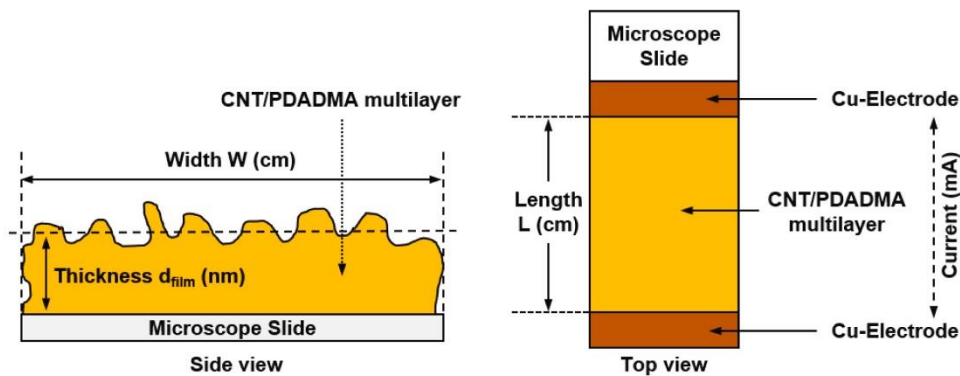
Scheme 1. Sketch of an electrically conductive film on top of a non-conductive substrate. The sheet resistance of the thin film depends on its length L, its width W and its thickness d_{film}. Here, the film consists of a carbon nanotube/polycation (CNT/PDADMA) multilayer.

ellipsometry (Multiskop, Optrel GbR, Sinzing, Germany). A He-Ne laser (power 4 mW, wavelength $\lambda = 632.8$ nm) serves as light source. A CNT/PDADMA film is described by a homogeneous film thickness as well as its complex refractive index $n_{film} - i \cdot \kappa_{film}$. Here, n_{film} is the real part of the refractive index, i the imaginary unit and κ_{film} is the extinction coefficient indicating the light attenuation while passing the non-transparent CNT/PDADMA film. Effects of surface roughness are neglected. By measuring the ellipsometric angles Ψ and Δ of a CNT/PDADMA film the three film parameters d_{film}, n_{film} and κ_{film} are fitted using a slab model [28]. However, determining three film parameters based on two independently measured values (Ψ and Δ) may leave the resulting values vulnerable to parameter cross-coupling. Therefore, all ellipsometric measurements were carried out at several angles of

incidence (66° to 72° in 1° steps) [29]. Moreover, for each sample condition light absorption A_{film} was measured independently by Vis-NIR absorption spectroscopy (Lambda 900, Perkin-Elmer, Wiesbaden, Germany) at the wavelength 635 nm. According to Beer-Lambert law the absorption A_{film} is connected to the attenuation coefficient $\alpha = \ln(10) \cdot A_{film}/d_{film}$ which is in turn connected to the extinction coefficient $\kappa_{film} = \alpha \cdot \lambda/(4\pi)$. Thus, for ellipsometric data analysis κ_{film} was always determined by the condition $\kappa_{film}(A_{film}, d_{film}) = \ln(10) \cdot A_{film} \lambda/(4\pi \cdot d_{film})$ reducing the effective number of free fitting parameters to two (d_{film} and n_{film}). d_{film} is required to quantify the sheet resistance R_S. Therefore, the reliability of d_{film} determination by ellipsometry is confirmed by AFM. AFM-based thickness determination is purely mechanically and serves as an independent method to gain the film surface height distribution
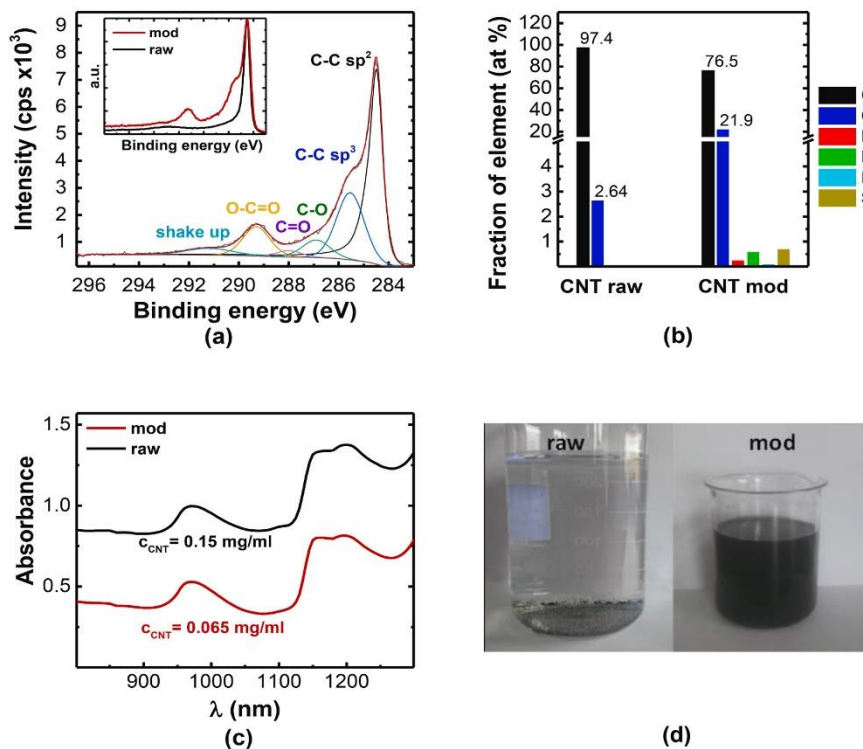

Fig. 1. Characterization of CNTs before and after acid treatment, indicated "raw" and "mod", respectively. **(a)** XPS: Peak-fit of the high-resolution C1s peak of CNT after acid treatment. Note the large fraction of C—C bonds in sp³ hybridization. Inset: the original normalized data, both for raw (black) and modified (red) CNTs (normalized with respect to the C—C sp² peak). **(b)** Fraction of atoms found in XPS before and after acid treatment, as indicated. **(c)** Optical absorption data of CNTs dissolved in water before and after acid treatment. CNT concentration was 0.15 mg/ml (before treatment, and 2 wt% SDS) and 0.065 mg/ml (after treatment). Note the absorption peak at 970 nm. **(d)** CNT dispersion before (raw, without SDS) and after (mod) modification.

relative to the substrate. Ellipsometry derived film thickness (with neglected roughness) matches the mean value of the surface height distribution within 1 nm error.

2.6. Electrical conductivity

Electrical properties of CNT/PDADMA films at ambient conditions (10% to 15% r.h.) were measured with an ELNEOS FIVE multimeter (Ernst Fischer GmbH + Co.KG, Freudenstadt, Germany). The device includes a waveform generator and a digital ampere– and voltmeter. The set-up is shown in Scheme 1: a glass slide is covered by an electrically conductive film. Measured is the ohmic resistance $R = \frac{U}{I}$ which will then be normalized to determine the sheet resistance ($R_S = \frac{1}{\sigma} \frac{L}{W \cdot d_{\text{film}}}$ with L the length, W the width, d_{film} the film thickness and σ the conductivity) [30,31]. For data analysis, the resistivity ρ is determined which is the inverse of the conductivity, $\sigma = 1/\rho$.

2.7. X-ray photoelectron spectroscopy (XPS)

Surface elemental composition was determined by high resolution scanning XPS [32,33]. Charge neutralization was implemented by low energy electrons, injected in the magnetic field of the lens from a filament located directly atop the sample. Spectra were acquired using an Axis Supra DLD electron spectrometer (Kratos Analytical, Manchester, UK) with a monochromatic Al Kα source (1486.6 eV). The instrument was set to the medium magnification lens mode and by selecting the slot mode, providing an analysis area of approximately 250 μm in diameter. Core level spectra of F1s, O1s, N1s, C1s, Na1s and S2p were collected at an analyser pass energy of 80 eV and for the highly resolved measured C1s peak the pass energy was set to 10 eV. Data acquisition and processing were carried out using Casa XPS software, version 2.3.22PR1.0 (Casa Software Ltd., Teignmouth, UK). Concentrations are given in atomic percent (at %). Curve-fitting procedure of the C1s high-resolution spectrum was performed after Shirley background subtraction to characterize the chemical structure of the surface. Peak positions of the carbon species, based on literature data [34], were: aromatic carbon (C—C sp^2, 284.5 eV), aliphatic carbon (C—C sp^3, 285.5 eV), hydroxyl (C—OH, 286.9 eV), epoxy (C—OC, 286.9 eV), carbonyl (C=O, 288.0 eV) and carboxyl (O—C=O, 289.3 eV). The full width at half maximum of the C1s components was 0.5 eV to 1.3 eV for high energy resolution measurements.

3. Results and discussion

3.1. X-ray photoelectron spectroscopy

XPS measurements were performed to obtain information on the chemical composition and the nature of chemical bonds of the CNTs. The peak fit of the high-resolution C1s XPS spectra of untreated and chemically modified CNTs are shown in Fig. 1(a). Changes in the peak shape of the modified CNT show that a lot of oxygen has been bound to the surface of the CNT. The C1s spectrum of the untreated CNTs is characterized by a main peak at 284.5 eV with an asymmetric shape attributed to graphitic carbon sp^2. Also, a π-π* satellite peak at a binding energy of 288 eV to 294 eV is observed, typical for CNTs [35–37]. Amorphous carbon is expected within 284.5 eV to 284.7 eV, indicating mainly sp^3 hybridization, carbon with sp^2 hybridization and defect sites in a non-aromatic form [38]. The C1s spectrum of the modified sample were fitted with 6 peaks (cf. Fig. 1(a)) at binding energies of 284.5 eV, 285.5 eV, 286.9 eV, 288 eV, 289.3 eV and 291 eV, respectively. Again, the main peak at 284.5 eV corresponds to graphitic carbon sp^2. The peaks at 286.9 eV, 288 eV and 289.3 eV correspond to three different oxygen-containing environments, in particular C—O, C=O and O—C=O. The position of the peaks is expected since strong and covalent bonds of oxidative carbon lead to lower electron densities at the carbon
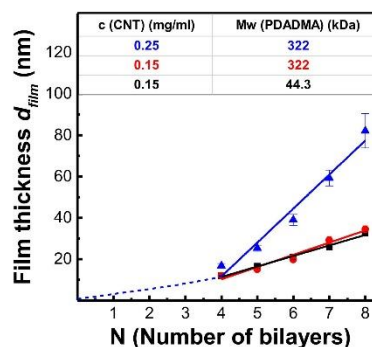

Fig. 2. PEI/PSS/PDADMA/(CNT/PDADMA)$_N$ films, with N the number of CNT/PDADMA BL. Varied was the molecular weight of the polycation PDADMA and the concentration of the CNTs in the adsorption solution as indicated. The measurements were performed in air with ellipsometry. PDADMA, PSS and PEI were adsorbed from 0.1 M NaCl solution. All thicknesses are average values determined from three different films. The error bars indicate the standard deviation.

atom, which lead to positive chemical shifts (286.1 eV to 291 eV). The elemental surface composition of CNT before and after acid treatment is shown in Fig. 1(b).

After the treatment an increase of the oxygen content from 2.6 at.% to 21.9 at.% was determined. Furthermore, contaminations of F, Si and Na originating from the wet chemical process were detected by XPS. Even if every C atom is oxidized at the exposed ends of the CNTs, this would correspond to a much lower oxygen percentage than observed (cf. Fig. 1(b)).

Based on the XPS results, the majority of the oxygen atoms must be bound to the defective sites on the CNT sidewalls [23,24]. The acidic oxidative treatment of the CNTs can change its structural properties considerably. Note that the peak at 291 eV (cf. Fig. 1(a)) corresponding to the π-π* shake-up transition is reduced considerably after treatment, indicating a disturbance of the π electron system and thus to a change in the electronic structure of the CNT side walls [23].

Additionally, the defects on the CNT structure have increased dramatically compared to the untreated sample (at 285.5 eV) [38–41]. Therefore, we assume that not only an oxidative attack on existing carbon defect sites occurred, but also CNTs were shortened and additional defects were generated, which could be further oxidized [38]. In summary XPS data revealed that the acid treatment introduced hydroxyl, aldehyde and carboxyl groups, all of them hydrophilic and weakly negatively charged in water (pH$_{\text{modified CNTs in water}}$ = 3.8).

3.2. Absorption in solution

Absorption measurements in the near IR (cf. Fig. 1(c)) of fine dispersed raw CNT in aqueous solution (with the help of SDS) show two peaks; one at ≈ 970 nm and the other at ≈ 1140 nm. These peaks are related to large-diameter single-walled and/or double-walled CNTs [12]. Interestingly, the acid treatment causing the addition of negatively charged groups renders the CNTs and allowed a fine dispersion in water (cf. Fig. 1(d)), yet the peaks attributed to the delocalized π-electrons and the CNTs remain the same.

From the absorption spectrum of CNTs in solution (cf Fig. 1(c)), the extinction coefficient ε was calculated ($\varepsilon \approx 8 \, \text{l g}^{-1}\text{cm}^{-1}$ at 970nm). Therefore, the CNTs can now be described as polyanions. They were integrated in the LbL preparation process instead of classical polyanions like PSS.
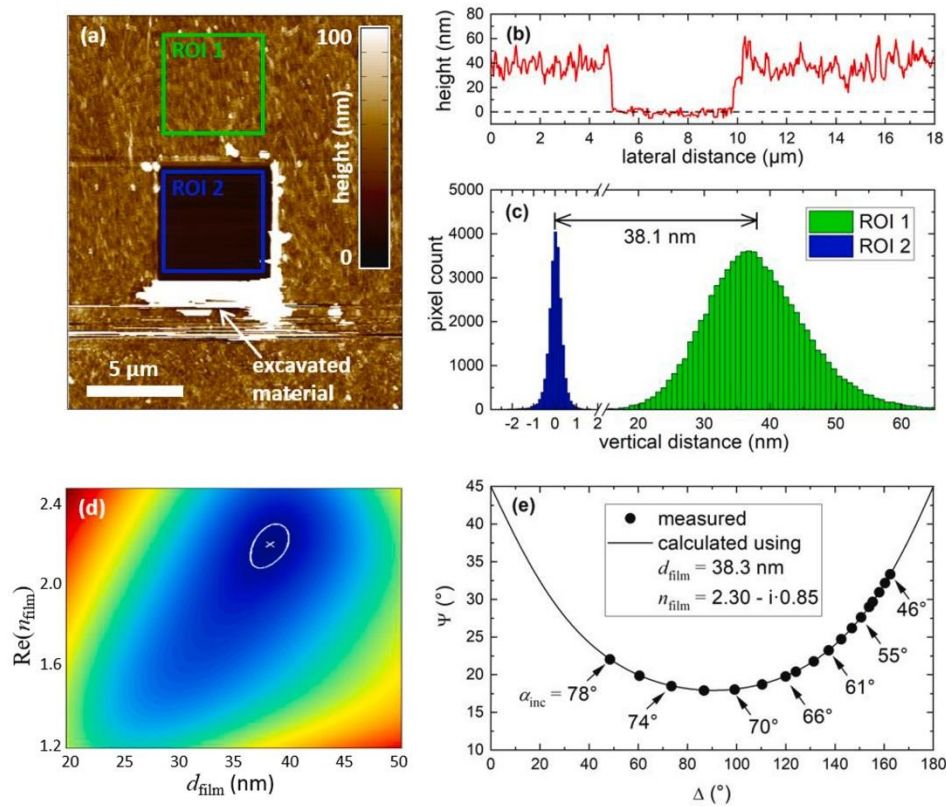
4

Fig. 3. Comparison of AFM-based and ellipsometric thickness determination. **(a)** AFM tapping mode image of PDADMA/CNT multilayer film (8 bilayers, $M_{w,PDADMA}$ = 44.3 kDa) treated by the AFM 'furrow method' [42]. Prior to imaging in AFM tapping mode, a 6 µm × 6 µm subarea was scanned several times in AFM contact mode with a vertical force of 1.5 µN (region of interest ROI 2, blue frame). The contact force is sufficient to displace the multilayer material, but too low to damage the underlying Si substrate. The ROI 1 region (green frame) is a typical multilayer region that is not affected by the contact mode process (scratching). **(b)** Exemplary sample height profile along a section line through the trench region ROI 2 shown in (a). **(c)** Histograms of the height distributions of ROI 1 and ROI 2, respectively, as depicted in (a). The root mean square (RMS) roughness within the trench (ROI 2) is about 1 nm, as is typical for a bare Si wafer, suggesting complete multilayer ablation. In contrast, ROI 1 is characterized by an RMS roughness of 8 nm and a mean height of 38.1 nm. This value deviates slightly from the distribution peak (at 36.8 nm) due to the skewness of the height distribution. **(d)** Color-coded least mean squared residuum of the ellipsometric fitting procedure. Systematic variation of the fitting parameters d_{film} and $Re(n_{film})$ results either in good agreement (dark blue region) or significant discrepancy (red and yellow regions) with the experimental ellipsometric data. The best agreement is indicated by a white cross (d_{film} = 38.3nm and $Re(n_{film})$ = 2.30) and the closed white line indicates the confidence interval of the parameters. The sample studied is the same as shown in (a)-(c). **(e)** Measured ellipsometric angles Δ and Ψ at various angles of incidence α_{inc} (black circles) and the calculated trajectory (black line) determined by least square regression as shown in (d).

3.3. Film deposition monitored by ellipsometry

The film growth of CNT/PDADMA multilayers was monitored with null-ellipsometry, in air at ambient conditions (cf. Fig. 2) [28,29]. All measurements were obtained from three films of the same structure, each built under the same conditions. Averages of these measurements are shown. In order to verify the thickness measured by ellipsometry we compared the results with AFM measurements as a cross check (cf. Fig. 3). For all films studied, the thickness of the first three CNT/PDADMA bilayers (BL) did grow non-linearly with the number N of deposited BL. Varied was the molecular weight of PDADMA and the concentration of the CNTs in the deposition solution.

Starting at four bilayers, the film thickness increased linearly with the number of deposited CNT/PDADMA BL (cf. Fig. 2). Films which were produced with a high CNT concentration of 0.25mg/ml were the thickest, those with a concentration of 0.15mg/ml CNTs were the thinnest. The variation of the PDADMA molecular weight from 322kDa down to 44.3kDa did not have any significant effect on the film growth,

respectively thickness. The thickness for each deposited CNT/PDADMA BL prepared with a CNT concentration of 0.15mg/ml is (5.5 ± 0.5) nm, independent of the PDADMA molecular weight (to be exact: (5.9 ± 0.6) nm for $M_{w,PDADMA}$ = 322kDa and (5.1 ± 0.3) nm for $M_{w,PDADMA}$ = 44.3kDa). After increasing the CNT concentration up to 0.25mg/ml, the thickness for each deposited CNT/PDADMA BL also increased to (16.5 ± 1.7) nm, which is about a factor of three larger. All investigated films appeared stable and homogeneous.

3.4. Vis-NIR absorbance spectroscopy

Ellipsometric measurements showed that the average thickness of a deposited CNT/PDADMA BL depends on the concentration of CNTs in suspension. To find out whether the CNT coverage depends on the polycation molecular weight, the films were investigated by Vis-NIR absorbtion spectroscopy (cf. Fig. 4). The absorption spectra of individual CNT/PDADMA films show qualitatively similar single peaks at 1100nm. However, in comparison, the CNT suspension showed two
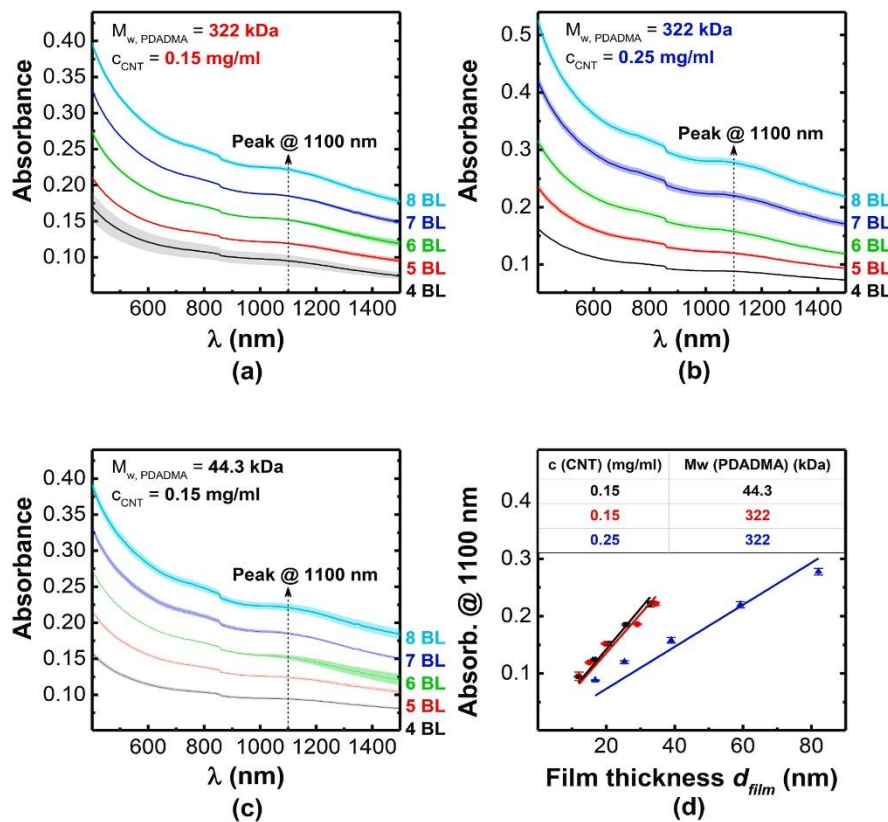
S. Neuber et al.

Fig. 4. Vis-NIR absorbance spectra in air of PEI/PSS/PDADMA/(CNT/PDAD-MA)$_N$ films in dependence of N, the number of deposited CNT/PDADMA BL. Varied is the concentration of CNTs in the adsorption dispersion and the molecular weight of PDADMA: **(a)** $M_{w,PDADMA} = 322$kDa and $c_{CNT} = 0.15$mg/ml, **(b)** $M_{w,PDADMA} = 322$kDa and $c_{CNT} = 0.25$mg/ml and **(c)** $M_{w,PDADMA} = 44.3$kDa and $c_{CNT} = 0.15$mg/ml. **(d)** Dependence of absorbance at 1100 nm on the film thickness. All absorption measurements are the average obtained from three different films; in (d), the error bars represent the standard deviation.

distinct absorption peaks slightly above and below 1100nm, respectively (cf. Fig. 1(c)). The position and shape of the absorption peak are within the expected range, as a broad absorbtion peak between ≈ 900nm to 1300nm has been described for mixtures of CNTs and amorphous carbon [12,43]., The single peaks at 1100nm are independent of the polycation molecular weight, CNT concentration and film thickness. With each additional BL deposited, the peak intensity increased, as did the background.

Fig. 4(a) shows the Vis-NIR-absorption spectra for the CNT/PDADMA films prepared with the heavy PDADMA ($M_{w,PDADMA} = 322$kDa and $c_{CNT} = 0.15$mg/ml). For films with 8 BL a maximum absorbance of 0.2211 at 1100nm was achieved. The same maximum absorbance (of 0.2211) was observed for CNT/PDADMA films with the same CNT concentration (0.15mg/ml) but decreased PDADMA molecular weight (44.3kDa, cf. Fig. 4(c)). Thus, it appears that the change of the PDADMA molecular weight does not influence the adsorption of the CNTs. In contrast, if the CNT concentration is increased up to 0.25mg/ml, ($M_{w,PDADMA} = 322$kDa), the absorbance for 8 BL increases up to 0.2775, which is shown in Fig. 4(b).

The results are quantified and summarized in Fig. 4(d). The absorbance at the peak wavelength increases linearly with the film thickness for all CNT/PDADMA films. The constant slope demonstrates that CNT amount deposited at each adsorption step is the same, but the exact value depends on the CNT concentration used.

Whereas the slope for CNT/PDADMA films prepared from $c_{CNT} = 0.15$mg/ml is within error independent of the molecular weight of PDADMA, $0.0057 \pm 3 \cdot 10^{-4}$ (to be exact: $0.0053 \pm 4 \cdot 10^{-4}$ for $M_{w,PDADMA} = 322$kDa and $0.0061 \pm 2 \cdot 10^{-4}$ for $M_{w,PDADMA} = 44.3$kDa) the slope for films prepared with an increased CNT concentration of

0.25mg/ml is halved ($0.0028 \pm 9 \cdot 10^{-5}$).

3.5. Surface topography

AFM was applied to study the arrangement of the CNTs and the surface morphology. Images of CNT/PDADMA films for N = 1, 4 and 8 BL with a PDADMA molecular weight of 322 kDa and a CNT concentration of 0.15 mg/ml are shown in Fig. 5(a) to (c). In all cases flatly adsorbed CNTs are observed. They are randomly oriented and form a network, which resembles fallen jackstraws. Single-/double-walled and also bundles of CNTs can be identified. When only one CNT/PDADMA BL is deposited, one recognizes isolated CNTs, with very few cross-overs. A film consisting of four CNT/PDADMA BL shows a network of CNTs. The network is even more pronounced when the film consists of eight bilayers, additionally an increased roughness can be observed.

By changing the molecular weight and CNT concentration no significant difference was observed (data not shown). In Fig. 5(d) the development of the film/air roughness σ_{RMS} is shown for 1, 4 and 8 BL of deposited CNT/PDADMA BL. Films consisting of one CNT/PDADMA BL have all the same σ_{RMS}. With increasing BL number, for all CNT/PDADMA films investigated a linear increase in roughness is found. CNT/PDADMA films built with a PDADMA molecular weight of 44.3kDa and a low CNT concentration (0.15mg/ml) showed the lowest increase, with a slope of σ_{RMS} (nm) = $0.89N \pm 0.03$. CNT/PDADMA films prepared with an increased carbon nanotube concentration (0.25mg/ml) have the lowest CNT content per nm-thickness according to NIR absorption (cf. Fig. 3(d)). For films prepared with a higher PDADMA molecular weight, the roughness shows a larger increase with each additional layer, independent of the CNT concentration ($\sigma_{RMS, 322kDa, 0.15mg/ml}$ (nm) = 1.51N +
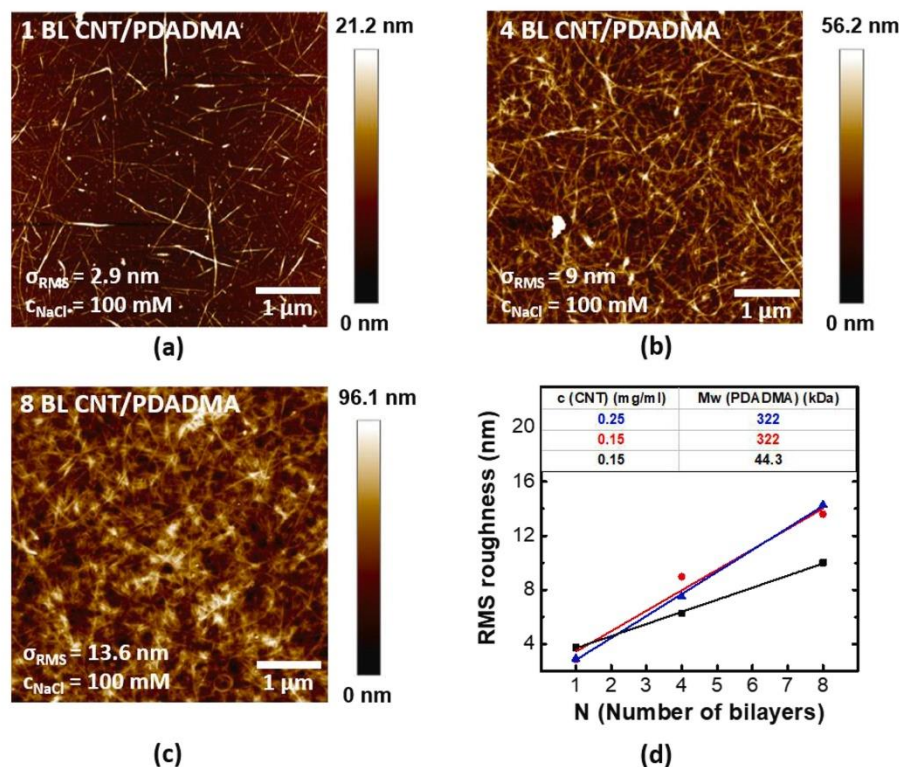
Fig. 5. AFM images ($5 \times 5 \, \mu m^2$) in air of PEI/PSS/PDADMA/(CNT/PDADMA)$_N$ films, in dependence of N the number of CNT/PDADMA BL: **(a)** 1 BL, **(b)** 4 BL and **(c)** 8 BL ($M_{w,PDADMA} = 322$kDa, $c_{CNT} = 0.15$mg/ml. **(d)** RMS roughness in dependence of the number of depositedBL.

0.25 and $\sigma_{RMS, \, 322kDa, \, 0.25 mg/ml}$ (nm) $= 1.63N + 0.05$). Furthermore, all films were stable and homogeneous. The thickness of a CNT/PDADMA BL ((5.5 ± 0.5) nm for $c_{CNT} = 0.15$mg/ml and (16.5 ± 1.7) nm for $c_{CNT} = 0.25$mg/ml) exceeds the diameter of a carbon nanotube (1nm to 2nm). Since the AFM images show horizontal alignment of the CNTs, the thickness is presumably due to a single layer of CNTs covered by a polycation layer.

It is advantageous that the PDADMA were adsorbed from 0.1 M NaCl. At this ion concentration, PDADMA adsorbs in a coiled conformation which can be thicker than the diameter of the molecules (1 nm for PDADMA). Additionally, the NaCl ions in the deposition solution screen the electrical charges on the polycation chains, causing a low persistence length and allowing the PDADMA chains to adjust their conformation for optimum coverage of the CNTs. The variation of the parameters $M_{w,PDADMA}$ (44.3kDa and 322kDa) and CNT concentration in suspension (0.15mg/ml and 0.25mg/ml) showed that only changing the CNT concentration influenced the BL thickness (Δd_{BL}) of the films. The increase of c_{CNT} from 0.15mg/ml up to 0.25mg/ml results in an increase of Δd_{BL} by a factor of three (from $\Delta d_{BL} = 6$nm up to $\Delta d_{BL} = (17)$nm.). When the CNT concentration was kept constant (in adsorption suspension) and the PDADMA molecular weight was varied, we expected a similar influence on the thickness per deposited BL. However, we got exactly the same BL thickness ($\Delta d_{BL} = (5.5 \pm 0.5)$nm for $c_{CNT} = 0.15$mg/ml). The thickness of PDADMA monolayers depends on the selected deposition conditions on PDADMA molecular weight [18,39]. We conclude that the thickness of a CNT/PDADMA BL depends on the thickness of the CNT network only. PDADMA adsorbed onto CNTs provides a positively charged shell. Thick PDADMA monolayers were always observed on flat homogeneous substrates. CNTs do not provide these kinds of flat surfaces. Also, the absorption measurements show that the surface coverage

per deposited CNT layer is independent of the PDADMA molecular weight. The only effect of the larger PDADMA molecular weight is the increase of the film/air roughness. The roughness is due to the CNT network. Each additional CNT layer adds more crisscrossing points; thus, the roughness increases. The thickness of the adsorption layer of the light PDADMA on flat surfaces is small [44], thus the increase in roughness is less pronounced. On increase of c_{CNT}, the thickness of a CNT/PDADMA BL gets thicker.

We assume that an increased CNT concentration leads to a fast adsorption process, without the possibility of the CNTs to rearrange. When in the next adsorption step PDADMA adsorbs on the disordered CNTs, the average thickness of the polymer layer is thick, thicker than on the low-coverage CNT layer. This leads to a factor three thicker CNT/PDADMA adsorption layer ($\Delta d_{BL} = (16.5 \pm 1.7)$nm for $c_{CNT} = 0.25$mg/ml). To understand this process further experiments are necessary in the future.

3.6. Electrical properties

The resistance of each film was measured using the set-up depicted in Scheme 1. For each film, the dependence between applied voltage and measured current could be described by Ohm's law (cf. Fig. 6(a)). As expected, with every additional CNT layer the sheet resistance decreases. The sheet resistance could be varied by one order of magnitude (factor 15), between ≈ 120 kΩ and ≈ 8 kΩ (data from 1 BL CNT/PDADMA and 8 BL CNT/PDADMA, respectively, $M_{w,PDADMA} = 322$ kDa, $c_{CNT} = 0.15$ mg/ml). Since the sheet resistance decreases inversely proportional to the film thickness d_{film}, the resistivity ρ is constant for a CNT/PDADMA system and was determined according to $\rho = R \cdot \frac{W \cdot d_{film}}{L}$,
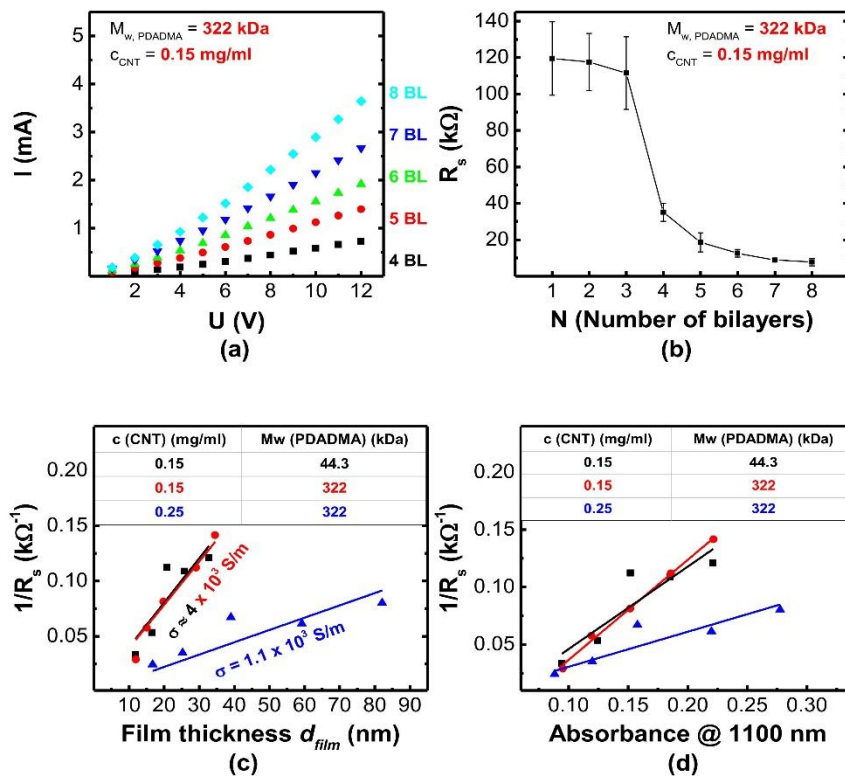
7

Fig. 6. Electrical properties of PEI/PSS/PDADMA/(CNT/PDADMA)$_N$ films consisting from N = 4 BL up to N = 8 BL. **(a)** Linear current I vs voltage U characteristics of a representative film prepared as indicated. All CNT/PDADMA films investigated exhibit ohmic behavior. From the slope the resistance was determined (5 kΩ to 20 kΩ). **(b)** Sheet resistance R_S in dependence of the number of deposited CNT/PDADMA BL ($M_{w,PDADMA}$ = 322kDa and c_{CNT} = 0.15mg/ml). Each R_S value shown is the average of three different films, error bars indicate the standard deviation. **(c)** The inverse sheet resistance increases linearly with the film thickness; from the slope of the linear fits the conductivity σ is determined. **(d)** The inverse sheet resistance increases linearly with the absorbance at 1100nm. Investigated were PEI/PSS/PDADMA/(CNT/PDADMA)$_N$ films, with N the number of CNT/PDADMA BL. All polyelectrolytes were adsorbed from a solution containing 0.1 M NaCl.

with film thickness d_{film} determined by ellipsometry. Fig. 6(b) also shows that four CNT/PDADMA BL are necessary to obtain a CNT network which is able to transport the electrons effectively through the film. Between three and four BL, the resistance drops by almost an order of magnitude. It looks like a percolation transition, after the deposition of four BL the lateral density of crossing points between CNTs is constant, and so is the conductivity. In dependence of the film composition, the measured conductivity varies by a factor of four.

The lowest conductivity $\sigma = \frac{1}{\rho} = 1.11 \cdot 10^3$ S/m was obtained for the CNT/PDADMA films with c_{CNT} = 0.25mg/ml, whereas films built with c_{CNT} = 0.15mg/ml had four times higher conductivity ($\approx 3.97 \cdot 10^3$ S/m). This conductivity ($\approx 3.97 \cdot 10^3$ S/m) is the largest that has been achieved in polyelectrolyte multilayers. But it is still two orders of magnitude smaller than that of films of pure CNTs [45].

Our results are consistent with the initial hypothesis: Charge transport from one CNT to the next is the main source of resistance. Since the CNTs are the conducting elements in the film we compare also the inverse sheet resistance with the optical absorbance at 1100nm (cf. Fig. 6 (d)). The dependence is linear, which is expected, since both the inverse of R_S and the film thickness increase linearly with the absorbance at 1100nm. It is remarkable that both the CNT coverage per layer and the conductivity are independent of the molecular weight of PDADMA and identical. This observation suggests that the scaffold formed by the CNTs determines the positions where PDADMA adsorbs, whereas the polymer length has no influence on scaffold formation.

Surprisingly, the CNT concentration in the deposition suspension has an influence, not only on the film thickness but also on the electrical conductivity. Panel (a) of Fig. 7 shows the linear growth region of CNT/PDADMA multilayers. The thickness increase per deposited CNT/PDADMA bilayer is three times larger when the CNTs are adsorbed from a more concentrated suspension. But for the thicker films, the increase in

absorbance at 1100nm is only slightly larger than for the thinner films (see panel b of Fig. 7), so the CNT content in the thicker bilayers is only slightly increased. Therefore, the increased thickness of the CNT/PDADMA bilayers is caused by additional PDADMA content. Thus, the film composition is changed, the ratio PDADMA monomers/CNT is increased. The lower CNT content in the film leads to fewer crossing points of CNT rods, less charge transfer and thus increase in the sheet resistance and a concommitant decrease in the conductivity, as shown in panel (c) of Fig. 7.

We can only speculate why the increased CNT concentration in the suspension led to a larger thickness of the PDADMA adsorption layer in each adsorptin step. The increased thickness of the PDADMA adsorption layer indicates that the CNT conformation at the surface is different. We suggest that the increased concentration in the deposition suspension led to more tilted CNT rods, providing more adsorption sites for the PDADMA molecules. However, the changes have to be very subtle because we did not observe any differences in the AFM images of the films prepared from the different CNT suspensions. In summary, the higher the monomer/CNT ratio, the lower the conductivity is, as shown in Fig. 7.

4. Conclusions

With the aim of fabricating ultrathin electrically conductive layers for biological applications [46], multilayers of different PDADMA molecular weights and CNT concentrations were built using the LbL assembly method. Films were prepared by sequential adsorption of oxidized CNTs (from water) and PDADMA (from 0.1 M NaCl solution). The sheet resistance was highest for one CNT/PDADMA BL, and decreased monotonously with each added CNT/PDADMA BL. The electrical conductivity increased during the depositon of the first four
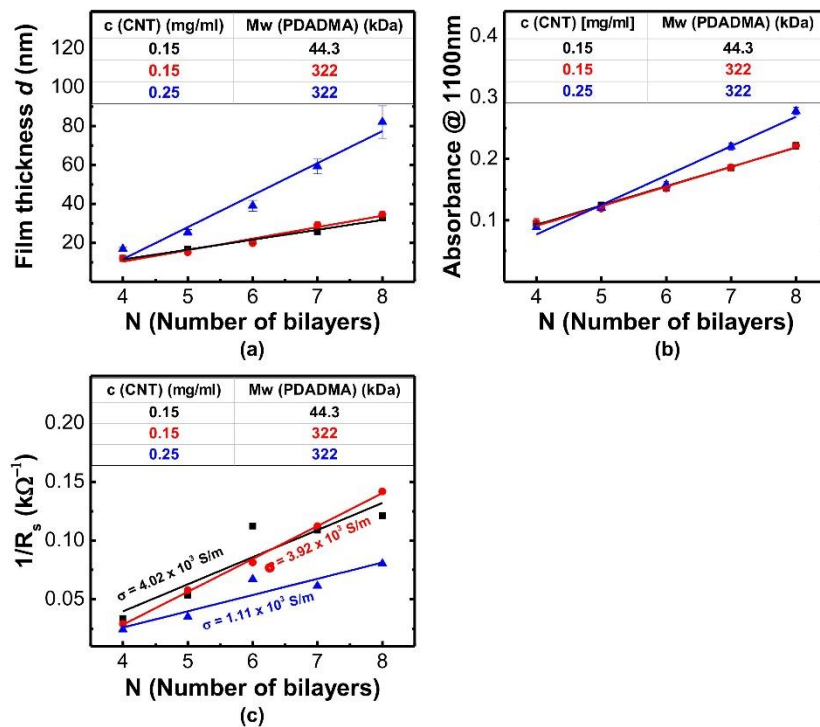
Fig. 7. PEI/PSS/PDADMA/(CNT/PDADMA)$_N$ films, where N denotes the number of CNT/PDADMA bilayers. The molecular weight of the polycation PDADMA and the concentration of the CNTs in the adsorption solution were varied as indicated. **(a)** Film thickness as a function of the number of BL measured by ellipsometry. **(b)** Dependence of absorbance at 1100nm and **(c)** inverse sheet resistance $1/R_S$ on the number of bilayers N.

CNT/PDADMA BL, then it was constant. This finding suggests that four CNT/PDADMA BL are necessary to obtain a constant coverage of CNT crossing points or nodes. With more than four CNT/PDADMA BL the sheet resistance depends only on the number of deposited BL. In our experiments, the sheet resistance could be varied by a factor of six, in dependence of the number of CNT/PDADMA BL. The thickness of each CNT/PDADMA BL was constant, as determined ellipsometrically [47]. Furthermore, the molecular weight of PDADMA was varied, by almost an order of magnitude. Even though the thickness of one adsorbed PDADMA monolayer depends on the molecular weight [2,39], the PDADMA molecular weight did not affect the thickness of a CNT/PDADMA BL, nor the electrical conductivity. We conclude that the polycations adsorb to the CNTs and the shape of the CNT network determines the thickness of a CNT/PDADMA BL, not the PDADMA molecular weight.

Two different CNT concentrations were used in the absorption suspension. A higher CNT concentration in the suspension correlated with an increased film thickness. It is suggested that the fast adsorption process of the CNTs led to more adsorption sites for the polycation. The lower CNT coverage per nm thickness increase (by a factor two) demonstrated that the ratio PDADMA monomer/CNT was increased, which led to a lower electrical conductivity.

AFM images of one CNT/PDADMA BL showed isolated CNTs, while AFM images of four or more BL showed flatly absorbed CNTs that lay crisscross on top of each other. They form a flat network, with many crossing points or nodes, which make electron transfer between CNTs possible. A percolation transition occurs when four BL are deposited, leading to the highest electrical conductivity reported so far for LbL films made with CNTs ($\approx$ 4000 S/m) was achieved.

Author contributions

S.N. oxidized the CNTs, built the multilayers and characterized them. He also performed the statistical analysis of the data. K.F. performed the XPS measurements and analyzed them. A.S. planned the chemical modification of the CNTs and validated it . P.N. analyzed the ellipsometric data. I.E. performed ellipsometric measurements. CAH planned the experiments. S.N., A.S., and C.A.H. wrote the manuscript, and all authors read and approved it.

Declaration of Competing interest

The authors declare that they have no known competing financial interests or personal relationships that could have appeared to influence the work reported in this paper.

Acknowledgement

References

[1] E. Gongadze, D. Kabaso, S. Bauer, T. Slivnik, P. Schmuki, U. van Rienen, A. Iglic, Adhesion of osteoblasts to a nanorough titanium implant surface, Int. J. Nanomed. 6 (2011) 1801–1816.

[2] A.R. Farooqi, J. Zimmermann, R. Bader, U. van Rienen, Numerical simulation of electroactive hydrogels for cartilage-tissue engineering, Materials (Basel) 12 (2019) 18.

[3] Y. Hanein, L. Bareket-Keren, Carbon nanotube-based multi electrode arrays for neuronal interfacing: progress and prospects, Front. Neural. Circ. 6 (2013) 122.

[4] L. Inzelberg, Y. Hanein, Electrophysiology meets printed electronics: the beginning of a beautiful friendship, Front. Neurosci. 12 (2019) 992.

[5] M.A. Sousa, J.R. Siqueira, A. Vercik, M.J. Schöning, O.N. Oliveira, Determining the optimized layer-by-layer film architecture with dendrimer/carbon nanotubes for field-effect sensors, IEEE Sens. J. 17 (2017) 1735–1740.

[6] P.V. Morais, V.F. Gomes, A.C. Silva, N.O. Dantas, M.J. Schöning, J.R. Siqueira, Nanofilm of ZnO nanocrystals/carbon nanotubes as biocompatible layer for enzymatic biosensors in capacitive field-effect devices, J. Mater. Sci. 52 (2017) 12314–12325.

[7] V.O. Fávero, D.A. Oliveira, J.L. Lutkenhaus, J.R. Siqueira, Layer-by-layer nanostructured supercapacitor electrodes consisting of ZnO nanoparticles and multi-walled carbon nanotubes, J. Mater. Sci. 53 (2018) 6719–6728.

[8] G. Decher, Fuzzy nanoassemblies: toward layered polymeric multicomposites, Science 277 (1997) 1232–1237.

[9] L. Fernández-Peña, E. Guzmán, F. Ortega, L. Bureau, F. Leonforte, D. Velasco, R. G. Rubio, G.S. Luengo, Physico-chemical study of polymer mixtures formed by a polycation and a zwitterionic copolymer in aqueous solution and upon adsorption onto negatively charged surfaces, Polymer (Guildf) 217 (2021) 123442.

[10] J. de Grooth, B. Haakmeester, C. Wever, J. Potreck, W.M. de Vos, K. Nijmeijer, Long term physical and chemical stability of polyelectrolyte multilayer membranes, J. Memb. Sci. 489 (2015) 153–159.

[11] W. Cheng, C. Liu, T. Tong, R. Epsztein, M. Sun, R. Verduzco, J. Ma, M. Elimelech, Selective removal of divalent cations by polyelectrolyte multilayer nanofiltration membrane: role of polyelectrolyte charge, ion size, and ionic strength, J. Memb. Sci. 559 (2018) 98–106.

[12] A.A. Green, M.C. Hersam, Processing and properties of highly enriched double-wall carbon nanotubes, Nat. Nanotechnol. 4 (2009) 64.

[13] N.W.S. Kam, E. Jan, N.A. Kotov, Electrical stimulation of neural stem cells mediated by humanized carbon nanotube composite made with extracellular matrix protein, Nano Lett. 9 (2009) 273–278.

[14] T.W. Ebbesen, Wetting, filling and decorating carbon nanotubes, J. Phys. Chem. Solids 57 (1996) 951–955.

[15] Z. Wu, Z. Chen, X. Du, J.M. Logan, J. Sippel, M. Nikolou, K. Kamaras, J. R. Reynolds, D.B. Tanner, A.F. Hebard, Transparent, conductive carbon nanotube films, Science 305 (2004) 1273–1276.

[16] M. Gu, W.-J. Song, J. Hong, S.Y. Kim, T.J. Shin, N.A. Kotov, S. Park, B.-S. Kim, Stretchable batteries with gradient multilayer conductors, Sci. Adv. 5 (2019) eaaw1879.

[17] Y. Akgöl, C. Cramer, C. Hofmann, Y. Karatas, H.-D. Wiemhöfer, M. Schönhoff, Humidity-dependent DC conductivity of polyelectrolyte multilayers: protons or other small ions as charge carriers? Macromolecules 43 (2010) 7282–7287.

[18] B.S. Shim, Z. Tang, M.P. Morabito, A. Agarwal, H. Hong, N.A. Kotov, Integration of conductivity, transparency, and mechanical strength into highly homogeneous layer-by-layer composites of single-walled carbon nanotubes for optoelectronics, Chem. Mater. 19 (2007) 5467–5474.

[19] A.R. Farooqi, J. Zimmermann, R. Bader, U. van Rienen, Numerical simulation of electroactive hydrogels for cartilage–tissue engineering, Materials (Basel) 12 (2019) 2913.

[20] S.W. Lee, B.S. Kim, S. Chen, Y. Shao-Horn, P.T. Hammond, Layer-by-layer assembly of all carbon nanotube ultrathin films for electrochemical applications, J. Am. Chem. Soc. 131 (2009) 671–679.

[21] P. Nestler, M. Paßvogel, C.A. Helm, Influence of polymer molecular weight on the parabolic and linear growth regime of PDADMAC/PSS multilayers, Macromolecules 46 (2013) 5622–5629.

[22] A. López-Oyama, R. Silva-Molina, J. Ruíz-García, R. Gámez-Corrales, R. Guirado-López, Structure, electronic properties, and aggregation behavior of hydroxylated carbon nanotubes, J. Chem. Phys. 141 (2014) 174703.

[23] K.A. Wepasnick, B.A. Smith, K.E. Schrote, H.K. Wilson, S.R. Diegelmann, D. H. Fairbrother, Surface and structural characterization of multi-walled carbon nanotubes following different oxidative treatments, Carbon 49 (2011) 24–36.

[24] X. Li, J. Niu, J. Zhang, H. Li, Z. Liu, Labeling the defects of single-walled carbon nanotubes using titanium dioxide nanoparticles, J. Phys. Chem. B 107 (2003) 2453–2458.

[25] L. Yue, W. Li, F. Sun, L. Zhao, L. Xing, Highly hydroxylated carbon fibres as electrode materials of all-vanadium redox flow battery, Carbon 48 (2010) 3079–3090.

[26] W. Kern, The evolution of silicon wafer cleaning technology, J. Electrochem. Soc. 137 (1990) 1887–1892.

[27] G. Decher, M. Eckle, J. Schmitt, B. Struth, Layer-by-layer assembled multicomposite films, Curr. Opin. Colloid Interface Sci. 3 (1998) 32–39.

[28] R.M. Azzam, N.M. Bashara, S.S. Ballard, Ellipsometry and polarized light, Phys. Today 31 (1978) 72.

[29] P. Nestler, S. Block, C.A. Helm, Temperature-induced transition from odd–even to even–odd effect in polyelectrolyte multilayers due to interpolyelectrolyte interactions, J. Phys. Chem. B 116 (2012) 1234–1243.

[30] S. Runde, H. Ahrens, F. Lawrenz, A. Sebastian, S. Block, C.A. Helm, Stable 2D conductive Ga/Ga (OxHy) multilayers with controlled nanoscale thickness prepared from gallium droplets with oxide skin, Adv. Mater. Interfaces 5 (2018), 1800323.

[31] J.G. Webster, Electrical Measurement, Signal Processing, and Displays, CRC Press, 2003.

[32] J.C. Vickerman, I.S. Gilmore, Surface Analysis: The Principal Techniques, John Wiley & Sons, 2011.

[33] C. Cushman, S. Chatterjee, G.H. Major, N. Smith, A. Roberts, M. Linford, Trends in advanced XPS instrumentation. 1. Overview of the technique, automation, high sensitivity, imaging, snapshot spectroscopy, gas cluster ion beams, and multiple analytical techniques on the instrument, Vac. Technol. Coat. (2016) 1–9.

[34] L. Stobinski, B. Lesiak, A. Malolepszy, M. Mazurkiewicz, B. Mierzwa, J. Zemek, P. Jiricek, I. Bieloshapka, Graphene oxide and reduced graphene oxide studied by the XRD, TEM and electron spectroscopy methods, J. Electron. Spectros Relat. Phenomena 195 (2014) 145–154.

[35] H. Estrade-Szwarckopf, XPS photoemission in carbonaceous materials: a "defect" peak beside the graphitic asymmetric peak, Carbon 42 (2004) 1713–1721.

[36] G. Moraitis, Z. Špitalský, F. Ravani, A. Siokou, C. Galiotis, Electrochemical oxidation of multi-wall carbon nanotubes, Carbon 49 (2011) 2702–2708.

[37] A. Theodosiou, B.F. Spencer, J. Counsell, A.N. Jones, An XPS/UPS study of the surface/near-surface bonding in nuclear grade graphites: a comparison of monatomic and cluster depth-profiling techniques, Appl. Surf. Sci. 508 (2020), 144764.

[38] V. Datsyuk, M. Kalyva, K. Papagelis, J. Parthenios, D. Tasis, A. Siokou, I. Kallitsis, C. Galiotis, Chemical oxidation of multiwalled carbon nanotubes, Carbon 46 (2008) 833–840.

[39] H. Ago, T. Kugler, F. Cacialli, W.R. Salaneck, M.S. Shaffer, A.H. Windle, R. H. Friend, Work functions and surface functional groups of multiwall carbon nanotubes, J. Phys. Chem. B 103 (1999) 8116–8121.

[40] V. Datsyuk, C. Guerret-Piécourt, J.-.C. Dupin, E. Flahaut, A. Peigney, C. Laurent, Double walled carbon nanotube/polymer composites via in-situ nitroxide mediated polymerisation of amphiphilic block copolymers, (2004).

[41] N. Zhang, J. Xie, V.K. Varadan, Functionalization of carbon nanotubes by potassium permanganate assisted with phase transfer catalyst, Smart Mater. Struct. 11 (2002) 962.

[42] R. Lobo, M. Pereira-da-Silva, M. Raposo, R. Faria, O. Oliveira Jr., In situ thickness measurements of ultra-thin multilayer polymer films by atomic force microscopy, Nanotechnology 10 (1999) 389.

[43] A. Ryabenko, T. Dorofeeva, G. Zvereva, UV–VIS–NIR spectroscopy study of sensitivity of single-wall carbon nanotubes to chemical processing and Van-der-Waals SWNT/SWNT interaction. Verification of the SWNT content measurements by absorption spectroscopy, Carbon 42 (2004) 1523–1535.

[44] M. Porus, P. Maroni, M. Borkovec, Structure of adsorbed polyelectrolyte monolayers investigated by combining optical reflectometry and piezoelectric techniques, Langmuir 28 (2012) 5642–5651.

[45] S.W. Lee, B.-.S. Kim, S. Chen, Y. Shao-Horn, P.T. Hammond, Layer-by-layer assembly of all carbon nanotube ultrathin films for electrochemical applications, J. Am. Chem. Soc. 131 (2009) 671–679.

[46] N.A. Kotov, J.O. Winter, I.P. Clements, E. Jan, B.P. Timko, S. Campidelli, S. Pathak, A. Mazzatenta, C.M. Lieber, M. Prato, Nanomaterials for neural interfaces, Adv. Mater. 21 (2009) 3970–4004.

[47] P Nestler, C.A. Helm, Determination of refractive index and layer thickness of nm-thin films via ellipsometry, Optics Express 25 (22) (2017) 27077–27085.

10

Article 2

Influence of Different Solutions on Electrically Conductive Films Composed of Carbon Nanotubes and Polydimethyldiallylammonium

Neuber, S., Sill, A., Ahrens, H., Quade, A., & Helm, C. A.

Influence of Different Solutions on Electrically Conductive Films Composed of Carbon Nanotubes and Polydimethyldiallylammonium

Sven Neuber, Annekatrin Sill, Heiko Ahrens, Antje Quade, and Christiane A. Helm*

Cite This: *ACS Appl. Eng. Mater.* 2023, 1, 1493−1503   Read Online

ACCESS | Metrics & More   Article Recommendations   Supporting Information

ABSTRACT: For engineering and biomedical applications, nanometer-thin films with high electrical conductivity in aqueous solutions are desirable. Multilayers of polydimethyldiallylammonium chloride (PDADMA) and oxidized carbon nanotubes (CNTs) were built using the layer-by-layer technique. CNTs with a low linear charge density were used. The surface coverage of the CNTs was monitored with optical absorption. The film thickness and the surface coverage of the CNTs increased linearly with the number of CNT/PDADMA bilayers deposited. On immersion into aqueous solutions, the film thickness decreased or remained constant. This finding is attributed to the hydrophobic character of the CNTs and the backbone of PDADMA. The films showed ohmic behavior, both in air and in solutions. The electrical conductivity was 0.95×10^4 S/m in air and increased to 1.36×10^4 S/m in solution, provided the thickness of the CNT/PDADMA bilayers was as low as 1.9 nm. We suggest that high electrical conductivity can be achieved by flat adsorption of the CNTs.

KEYWORDS: *LbL films, carbon nanotubes, electrical conductivity, ultrathin films, hydrophobic interaction, electrostatic interactions*
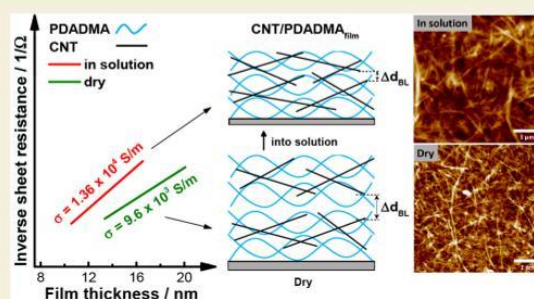
■ INTRODUCTION

Electrically active implants are isolators covered by an electrically conducting coating.[1,2] These coatings must have several properties: (i) high in-plane electrical conductivity in aqueous solution,[3] (ii) low and adjustable sheet resistance,[2] (iii) thickness in the 10−100 nm range, (iv) biomedical compatibility, i.e., cells have to adhere and proliferate on them. We are investigating whether polyelectrolyte multilayers are suitable for such coating. Polyelectrolyte multilayer films are built by the layer-by-layer (LbL) technique.[4,5] The sequential adsorption of oppositely charged polyions allows the formation of thin organic coatings. By selecting the top adsorption layers appropriately, polyelectrolyte multilayers can be prepared on which the desired type of cell will grow.[6−9] Chemically modified, electrically conducting carbon nanotubes (CNTs) were used as polyanions to achieve electrical conductivity. Due to freely moving electrons, the electrical conductivity of a multiwalled carbon nanotube is large (10^6−10^7 S/m).[10] A hopping process between touching CNTs transfers electrons. This electron transfer between CNTs reduces the electrical conductivity within that film by a few orders of magnitude.[3,11] Therefore, flatly adsorbed CNTs are advantageous to obtain many in-plane contacts.

Controlling the electrical conductivity in air and in an aqueous solution is challenging. It is known that polyelectrolyte multilayers swell by 30−120% when placed in an aqueous environment, due to increased hydration of the hydrophilic molecular groups.[12−14] Swelling poses a problem for electron transfer, which relies on contact between CNTs. The separation between CNTs increases, when a polyelectrolyte multilayer swells. It has been shown, that the electrical conductivity of polyelectrolyte multilayers with electrically conductive gold nanoparticles as polyanions decreased drastically in humid air when swelling occurred because electron transfer between gold nanoparticles was no longer possible.[15] Since we want to make LbL films that are electrically conductive in aqueous solutions, swelling in solution is an issue.

To that end, it is helpful to consider the intra- and intermolecular interactions in LbL films. It is well-known that the built-up of layer-by-layer coatings is based on electrostatic interactions. In addition, alternatives have been investigated, such as hydrogen-bonded LbL films[16] or the influence of hydrophobicity.[14] Hydrophobic regions in molecular assem-

1493

blies do not incorporate water molecules, and therefore their thickness is the same in air and in water.[17]

CNTs consist of a carbon network, are hydrophobic, and cannot be dissolved in water.[18] The CNTs were chemically modified to introduce negative charges. We ensured the CNTs had a low linear charge density to reduce swelling. Hydrophobic carbon atoms in the sp^2 configuration separate the negative charges bound to defects of the CNTs. The fewer negative charges bound to the CNTs, the more hydrophobic the CNTs are. The polycation, the strong polyelectrolyte polydimethyldiallylammonium chloride (PDADMA), has a hydrophobic backbone. For film buildup, we started from the following approach: the opposite charges of CNTs and PDADMA should cause the cohesion of the polyelectrolyte multilayer. The hydrophobic forces support the cohesion and prevent the incorporation of water molecules. Thus, film swelling should be reduced. The proportion of uncharged C atoms in sp^2 conformation was quantified with X-ray photoelectron spectroscopy.

Two additional features also determine the thickness of a CNT/PDADMA bilayer (BL): the orientation of the CNTs (flat or tilted with respect to the substrate) and the resulting conformations of the PDADMA chains. Furthermore, parallel alignment of the CNTs leads to many contact points between the CNTs and high electrical conductivity. We cannot measure the orientation of the CNTs directly, but we can measure the film/air roughness of a film with the atomic force microscope (AFM). A very low roughness suggests the formation of an orientation parallel to the substrate.

In previous work, we found that four CNT/polycation layers were required for homogeneous film formation and constant electrical conductivity.[19] Therefore, we investigate films consisting of four or more CNT/PDADMA bilayers. The lower the CNT concentration in the deposition suspension, the thinner the resulting films.[19] The film thickness is determined by ellipsometry;[20] varied were the number of layers deposited and the environment (air and biologically relevant solutions).

Specifically, we used the following aqueous solutions: (i) phosphate-buffered saline (PBS), which has an osmolarity and ion concentration similar to that of the human body (isotonic) and is often used in biological research; (ii) Dulbecco's modified Eagle's medium (DMEM), a synthetic culture medium used for the cultivation of human and animal cells, that contains (among other things) a high concentration of glucose; and (iii) a 0.2 M sodium chloride solution to study the influence of monovalent ions on the films. Images of the film surfaces and the film/air roughness were obtained by AFM. CNTs absorb light in the visible and near-infrared.[21] The increase in the absorption peak intensity with the film thickness provides information on the CNT:PDADMA ratio. The film composition was varied by different CNT concentrations in the suspension and by the use of freshly prepared and aged CNT suspensions.

■ EXPERIMENTAL SECTION

Materials

Poly(ethylenimine) (PEI, branched, M_w = 750 kDaA, PDI = 12.5) was purchased from Sigma-Aldrich Chemistry GmbH (Steinheim, Germany). Poly(styrenesulfonate) sodium salt (PSS, M_w = 666 kDa, PDI < 1.2) and polydimethyldiallylammonium chloride (PDADMA, Mw = 322 kDa, PDI = 2.19) were purchased from Polymer Standard Service (Mainz, Germany).

The unmodified carbon nanotubes (CNT, single-walled/double-walled mixture; CNT ratio >90%, diameter 1−2 nm, length 5−30 μm) were provided by abcr (Karlsruhe, Germany). Microscope slides (76 mm × 26 mm, Carl Roth GmbH + Co. KG, Karlsruhe, Germany) and single side polished silicon wafer (Silicon Materials, Kaufering, Germany) served as substrates. For measurements in solution, NaCl and StableCell DMEM (Merck KGaA, Darmstadt, Germany), Roti-CELL PBS (Carl Roth GmbH + Co. KG, Karlsruhe, Germany), and synthetic resin (Meffert AG Farbwerke, Bad Kreuznach, Germany) as isolator were used. Copper stripes (10 m × 25 mm, Conrad Electronic SE, Hirschau, Germany) were used as current entrance points into the film.

Film preparation

As substrates, microscope slides and silicon wafers were used. Both substrates were cleaned via a RCA treatment protocol.[22] The films were prepared using the layer-by-layer (LbL) method:[23] sequential adsorption of oppositely charged polyelectrolytes (PE) and negatively charged modified CNTs from solution. The preparation process was automated using a dipping robot (Riegler & Kirstein GmbH, Potsdam, Germany). A temperature-controlled circulation thermostat (Carl Roth GmbH + Co. KG, Karlsruhe, Germany) was used for temperature control during the preparation process.

Each deposition step lasted 30 min with three washing steps with ultrapure water in between (each 1 min) to remove loosely bonded polycations and polyanions.

The film build-up always started with a PEI/PSS base layer to provide a homogeneous negatively charged surface. Subsequently, PDADMA was used as polycation and modified CNTs as polyanion. The concentration of the polyelectrolyte solution (PEI, PSS, and PDADMA) is 1 mM with respect to the monomer weight and the solutions contain a NaCl concentration of 100 mM.

To achieve a negative charge of the CNTs and make them dispersible in water, a CNT modification was carried out using volume/volume acid treatment according to López-Oyama.[24] For film preparation, the concentration of modified CNT was 0.15 or 0.25 mg/mL suspended in ultrapure water (Sartorius Lab Instruments, Göttingen, Germany). Then, film build-up occurred by sequential adsorption of oppositely charged PDADMA and CNTs. The rinsing solution was pure water. After preparation, the dried multilayers were characterized and placed in an aqueous solution (0.2 M NaCl, PBS, or DMEM). Different films were used for each solution. To ensure accuracy, we conducted measurements on at least three independent films prepared under the same conditions to characterize the film's thickness, electrical properties, absorption, and more. The data presented reflect the average values, including the standard deviation as indicated.

Ellipsometry and Vis−NIR Absorption Spectroscopy

The film thickness d_{film} of each CNT/PDADMA film was determined using null ellipsometry (Multiskop, Optrel GbR, Sinzing, Germany) in a PCSA (polarizer−compensator−sample−analyzer) configuration. The light source is a He−Ne laser (power 4 mW, wavelength λ = 632.8 nm).

A CNT/PDADMA film is described by its homogeneous film thickness and its complex refractive index $n_{film} - i \kappa_{film}$. Here, n_{film} is the real part of the refractive index, and i is the imaginary unit. The extinction coefficient κ_{film} indicates the light attenuation when passing through the nontransparent CNT/PDADMA film.

By measuring the ellipsometric angles Ψ and Δ of a CNT/PDADMA film, the three film parameters d_{film}, n_{film}, and κ_{film} are determined using a slab model.[25] All ellipsometric measurements were performed at different angles of incidence (66° to 72° in 1° steps).[20] Thus, six different values for d_{film} and n_{film} were obtained and averaged. Additionally, for each sample condition, light absorption was measured independently using vis−NIR absorption spectroscopy (Lambda 900, PerkinElmer, Wiesbaden, Germany) at the wavelength of 635 nm. This allowed κ_{film} to be determined by the condition $\kappa_{film}(A_{film}, d_{film}) = \ln(10) A_{film} \cdot \lambda / (4\pi \cdot d_{film})$ when analyzing ellipsometric data, reducing the effective number of free fitting parameters to two (n_{film} and d_{film}). Here A_{film} is the absorption.[19]

Scheme 1. (a, b) Top and (c) Front View of Resistance Measurements on an Electrically Conductive Film on a Nonconductive Support[a]
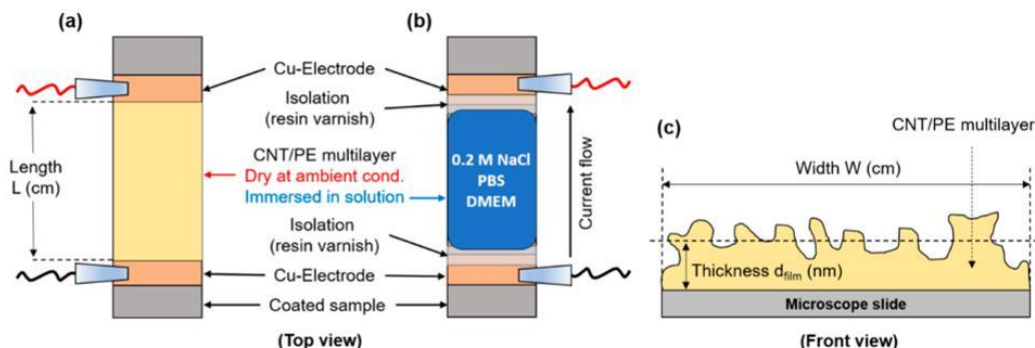
[a]The set-up is used (a) in air and (b) in solution. The resistivity of the thin film depends on its length L, its width W, and its thickness d_{film}. Here, the film consists of a carbon nanotube/polycation (CNT/PDADMA) multilayer.

In order to determine the thickness of the films, their refractive indices were determined and kept constant ($n_{film, air} = 1.65 - i\,0.619$ and $n_{film, solution} = 2.19 - i\,0.4092$). The reliability of d_{film} determination by ellipsometry was validated by AFM (scratching test).

The method described by Benjamins et al.[26] was used to perform measurements at a liquid/solid interface at a variable angle of incidence. For this purpose, special cylindrical cuvettes (Hellma, Müllheim, Germany) are attached to the laser and detector arms, and the sample is fixed to the bottom of a homemade liquid-filled Teflon trough. Prior to each measurement, the cuvettes are aligned so that their front plates are perpendicular to the laser beam. The two cuvettes serve as windows for coupling the laser beam into and out of the liquid volume. Regardless of the selected angle of incidence α_{inc}, the light emitted by the laser arm strikes the glass of the first cuvette perpendicular to the air/glass/solution interface and then strikes the solution/sample interface at the angle α_{inc}. The reflected light finally leaves the solution again perpendicularly across the glass of the second cuvette in the direction of the detector arm.

A perpendicular transition of the light from air into the solution volume (and vice versa) ensures that the two cuvettes themselves have no influence on the polarization state of the light. The CNT/PDADMA films were first measured at ambient conditions in air. Then the thicknesses of the films were measured in different solutions (0.2 M NaCl, PBS, and DMEM) after 5 min of equilibration time.

Furthermore, vis–NIR spectra of the dry films were recorded at 30% relative humidity (r.h.). The films on the microscopic slides were measured at ambient conditions (≈ 21 °C and relative humidity $\approx$ 30%). The slide was covered on both sides due to preparation conditions. To obtain the absorbance of one film, the obtained values were divided by two. The extinction coefficient was determined with a CNT suspension in a cuvette (Rotilabo-single-use cells, 4 mL, Carl Roth GmbH + Co. KG, Karlsruhe, Germany).

According to the Beer–Lambert law the absorbance is given by $A = -\log(I/I_0) = \varepsilon \cdot d \cdot c$. The incident intensity is I_0 (at a particular wavelength), I is the transmitted intensity after passing through a sample with a thickness d, containing a concentration c of the absorbing species with a wavelength-dependent extinction coefficient ε. Absorption was measured from 400 to 1800 nm with 5 nm/s steps and an integration time of 1 s per step. The absorption spectra of individual CNT/PDADMA films show single peaks at 1100 nm.[19] The position and shape of the absorption peak are within the expected range, as a broad absorption peak between ~900 and 1300 nm has been described for mixtures of CNTs and amorphous carbon.[21,27]

X-ray Photoelectron Spectroscopy

To analyze the surface chemistry, the CNT suspension was concentrated using a rotary evaporator (Heidolph Instruments GmbH Co. KG, Schwabach, Germany) and the residue was dried via vacuum lyophilization (Alpha 3–4 LSCbasic, Martin Christ Gefriertrocknungsanlagen GmbH, Osterode am Harz, Germany). The elemental composition of the sample surfaces was carried out with a Kratos Axis Supra spectrometer (Kratos Analytical, Manchester, UK) using a monochromatic Al Kα source (1486.6 eV). The Kratos charge neutralizer system was applied for all specimens.

Survey scans were acquired with an analysis area of 300 μm × 700 μm and a pass energy of 160 eV. Core level spectra of Na 1s, F 1s, O 1s, N 1s, C 1s, Cl 2p, S 2p, and Si 2p were collected at a pass energy of 80 eV. Survey and core level spectra were acquired using an X-ray power of 150 W (10 mA, 15 kV). For the highly resolved measured C 1s peak, the pass energy was set to 10 eV and the X-ray power to 225 W (15 mA, 15 kV). Three spots at different positions were analyzed and averaged. Data acquisition and processing were performed using CasaXPS software, version 2.3.15 (Casa Software Ltd., Teignmouth, UK). The concentrations are given in atomic percent (at %).

After subtraction of Shirley background, the high-resolution C 1s peaks were fitted using Gaussian–Lorentzian GL (30) peak shape; for the sp^2 component, an asymmetric line shape was used. The peak positions of the carbon species, based on literature data,[28] were aromatic carbon (C–C sp^2, 284.5 eV), aliphatic carbon (C–C sp^3, 285.5 eV), hydroxyl (C–OH, 286.9 eV), epoxy (C–O–C, 286.9 eV), carbonyl (C=O, 288.0 eV), and carboxyl (O–C=O, 289.3 eV). The full width at half-maximum (fwhm) of the C 1s components ranged from 0.6 to 1.3 eV for the high-resolution measurements.[19]

Atomic Force Microscopy (AFM)

Surface imaging was done by a BioScope Resolve AFM using NanoScope 9.7 software (BRUKER, Billerica, MA, USA). FESP-V2 cantilever models (BRUKER, Billerica, MA, USA) were used for air and liquid measurements. All recordings in air were carried out via AFM *TappingMode in Air*, dry and at ambient conditions. *TappingMode in Fluid* was used for the liquid measurements, where the sample is covered with 1 mL of 0.2 M NaCl, PBS, or DMEM solutions.

For statistics, at least 3 different sample positions were imaged at a scan size of 100 μm^2. Data analysis was done via NanoScope Analysis (Version 2.0) software from BRUKER (Billerica, MA, USA).

Additionally, to surface imaging AFM was also used to determine surface roughness, calculated via root-mean-square (RMS) deviation from the average height. In order to have a cross-check of the ellipsometric thickness measurements, AFM surface scratching was performed as described before.[19]
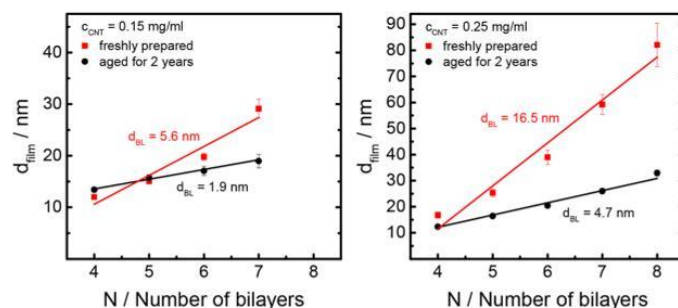
Figure 1. Thickness of PEI/PSS/PDADMA(CNT/PDADMA)$_N$ films built with freshly prepared CNTs (red) and aged CNTs (black), which were kept for two years in solution, in dependence of N, the number of CNT/PDADMA bilayers. The CNT concentration in the suspension was varied, 0.15 mg/mL (left) and 0.25 mg/mL (right). All measurements were performed in air (at ambient conditions) using ellipsometry. We adapted some data from freshly prepared solutions from previous work.[19] The straight lines are linear fits. From the slopes of the linear fits, d_{BL}, the thickness of a CNT/PDADMA bilayer, is determined. R-values of the fits are 0.98 (both films from aged CNT suspensions), 0.94, and 0.97 (films from 0.15 and 0.25 mg/mL freshly prepared CNT suspension, respectively). Note the different scaling of the y-axis.

Electrical Conductivity Measurements

Electrical PE/CNT film properties at ambient conditions (r.h. ≈ 20%, T = 22 °C) and in solution (0.2 M NaCl, PBS, DMEM) were investigated with an ELNEOS FIVE multimeter (Ernst Fischer GmbH + Co.KG, Freudenstadt, Germany). This device included a waveform generator in combination with an ampere- and a voltmeter. Scheme 1 shows the setup: a glass slide covered with a CNT/PE film at ambient conditions (a) and in combination with solution (b). The ohmic resistance $R = U/I$ was determined and then normalized to determine the sheet resistance ($R_s = \frac{U}{I} \cdot \frac{L}{W}$ with L the length and W the width).[19,29,30]

With known film thickness d_{film}, the resistivity $\rho = \left(\frac{R_S}{d_{film}}\right)$ and the conductivity $\sigma = 1/\rho$ can be determined at ambient conditions and in solution. After the sample was transferred to a new environment, 5 min elapsed before starting the electrical measurement.

■ RESULTS AND DISCUSSION

Comparison of CNT/PDADMA Films from Freshly Prepared and Two Year Old CNT Suspensions

To make the hydrophobic CNTs accessible for the preparation of CNT/PDADMA films, hydrophilic functional groups were introduced by chemical modification (see Experimental Section). These modified CNTs were suspensible in water. We used two different suspensions: freshly prepared and two years old. Two different CNT concentrations were used (c_{CNT} = 0.15 mg/mL, 0.25 mg/mL).

The LbL films were prepared using the dipping method. The silicon substrate was first coated with a PEI/PSS layer pair. PDADMA and modified CNTs were then alternately adsorbed, resulting in the film structure PEI/PSS/PDADMA/(CNT/PDADMA)$_N$, with N as the number of CNT/PDADMA bilayers. Varied was the concentration of CNTs in the deposition suspension. Film thickness was measured with null-ellipsometry in air at ambient conditions.[20,31] To verify the thickness measured via ellipsometry, results were compared with AFM measurements as cross-checks (AFM scratching method). Our previous work has shown that four CNT/PDADMA bilayers are required to build a stable conductive CNT network structure with a continuously linearly increasing film thickness up to 8 BL.[19] Therefore, we consider only multilayers consisting of four or more bilayers.

Figure 1 left shows the film thickness dependence on the number of CNT/PDADMA bilayers deposited for films prepared from CNT suspensions with c_{CNT} = 0.15 mg/mL. The films prepared two years ago from the then-fresh suspension were thicker than those prepared recently from the aged CNT suspension (provided the film consisted of more than five CNT/PDADMA bilayers), also the thickness per CNT/PDADMA bilayer was larger (d_{BL} = 5.6 and 1.9 nm).

The film became unstable when more than seven bilayers were adsorbed. A new CNT suspension with c_{CNT} = 0.15 mg/mL was prepared to verify the results. This film had the same thickness as the films built two years earlier[19] when the aged CNT suspension was fresh.

With a higher CNT concentration in the adsorption suspension (c_{CNT} = 0.25 mg/mL), the thickness of a CNT/PDADMA bilayer increased.[19] However, the film thickness is lower when an aged CNT suspension was used for film preparation (cf. Figure 1, right).

For all films, extrapolation to low numbers of bilayers yields a negative film thickness. Therefore, the thickness increase of the first bilayers was less than the average bilayer thickness of films consisting of four or more bilayers. (Furthermore, for the films prepared from freshly prepared suspension, the thickness increment per bilayer increases with increasing number of bilayers, suggesting a nonlinear increase in thickness. In fact, fits of nonlinear functions such as power or exponential functions yield better R-values.[32] But we want to compare the average bilayer thickness of the different films. Therefore, we use a suboptimal linear fit.)

For the films prepared from fresh CNT suspensions, the error bars increase with the number of bilayers deposited. As shown by the AFM images in our last publication,[19] the film/air roughness increases with each CNT/PDADMA bilayer deposited. The increase in roughness leads to decreased film-to-film reproducibility, as the increasing error bars demonstrate.

With each adsorption step, the difference in the film thicknesses increases since the mean bilayer thickness d_{BL} of the film from the fresh suspension exceeds that from the aged one by a factor of about three (16.5 to 4.7 nm, and 5.6 to 1.9 nm, respectively). Comparing films prepared from an aged or a fresh suspension, one finds that a higher CNT concentration results in a thicker film.

To figure out what happened to the modified CNTs that were stored in water for two years, the CNT suspension was concentrated using a rotary evaporator, and the residue was dried under a vacuum. The dried CNTs were analyzed by XPS and compared with the data of unmodified CNTs and freshly modified CNTs (cf. Figure S1 shows the XPS spectra). High-resolution C 1s peak fits yielded the fraction of different C-atoms in different chemical states and to which elements or functional groups the C-atoms are bonded.

By acid treatment, polar functional groups, such as hydroxyl or carboxyl groups, were introduced at the ends and defective sites of the CNTs, as was demonstrated by XPS.[19] Comparison of XPS results of freshly modified and aged modified CNTs (which were stored two years in suspension) showed that the percentage of functional groups decreased (cf. Figure 2 and
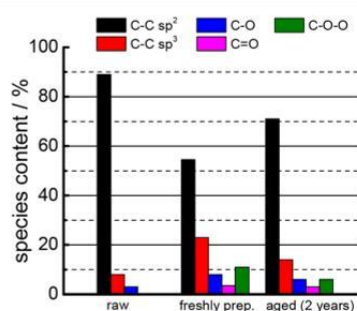

Figure 2. XPS determination of the fraction of C-atoms of different CNTs bond to atoms/functional groups as indicated: CNTs as provided by the supplier (raw), after acid treatment (freshly prep.), and after additional two-year storage in a suspension (aged (2 years)). The highly resolved measured XPS C 1s spectra with peakfits are shown in Figure S1 (SI).

Table 1. Relative Percentage of Different Species As Determined by XPS[a]

	C−C sp^2 (%)	C−C sp^3 (%)	C−O (%)	C=O (%)	C−O−O (%)
Raw	89	8	3	—	—
Freshly prepared	54.5	23	8	3.5	11
Aged for 2 years	71	14	6	3	6

[a]The parameter assignment is the same as in Figure 2.

Table 1). Since the portion of C−C sp^3 signals has also decreased, we hypothesize that the functional groups have left the CNTs as CO_2, CO, or CH_2O. Thus, fewer negative charges exist on the aged CNTs.

The XPS results explain the thicker films obtained with freshly modified CNTs which have more negatively charged functional groups and thus a larger linear charge density. To achieve charge compensation, more PDADMA adsorbs. Therefore, CNT/PDADMA bilayers are thicker when prepared from freshly modified CNTs (cf. Figure 1).

Furthermore, Figure 1 shows that the films made from the suspension with the higher CNT concentration are thicker. This observation applies to both freshly modified and aged CNT suspensions. The next question concerns the composition of a CNT/PDADMA bilayer, more precisely, the ratio

between CNT and PDADMA. A broad absorption peak between 900 and 1300 nm has been described for CNTs and amorphous carbon mixtures.[21] Films containing modified CNT and PDADMA have a broad absorption peak at 1100 nm. The vis−NIR-absorption spectra of the different films are shown in Figure S2 in the Supporting Information. Again, one finds an absorption peak at 1100 nm.

Figure 3 shows the dependence of the absorbance at 1100 nm on the film thickness. The absorbance at 1100 nm increases linearly with the addition of CNT/PDADMA bilayers. Comparing the films built from freshly prepared and aged CNT suspensions, one finds that the absorption per nm film thickness is more significant for films made from aged CNT suspensions, even though the films from aged suspensions are much thinner. Therefore, the CNT:PDADMA ratio is larger for the films from aged suspensions. By comparing the slopes of the lines in Figure 3, i.e., the increase in absorption per nanometer of film thickness, it is possible to quantify the effect.

For films built from c_{CNT} = 0.15 mg/mL, the difference in the slopes is almost a factor of 3 (0.012 nm^{-1} and 0.0045 nm^{-1}, respectively). For a concentration of c_{CNT} = 0.25 mg/mL, the slope difference is a factor of 6 (0.018 nm^{-1} and 0.003 nm^{-1}). The respective influence of the age and the CNT concentration of the suspension is not straightforward and needs to be further explored.

The more significant increase in the absorption per nm film thickness shows that there is less PDADMA between the CNT layers in films built from the aged CNT suspension. The decreased thickness of the PDADMA adsorption layer is due to the lower linear charge density of the aged CNTs. This means that less PDADMA is required to reverse the negative surface charge density of the CNT-covered surface.

It was impossible to prepare more than seven bilayers from the aged CNT suspension with a concentration of 0.15 mg/mL. This film has a large CNT:PDADMA ratio. Furthermore, the bilayer thickness is 1.9 nm, more than the diameter of a single-walled CNT (1 nm) and less than that of a double-walled CNT (2 nm). These numbers suggest that a bilayer consists mainly of flatly adsorbed CNTs with interspersed PDADMA. The high CNT:PDADMA ratio, combined with the small thickness of an adsorbed bilayer, makes it difficult for PDADMA to form the network that usually stabilizes LbL films. Note that the film from an aged CNT suspension with c_{CNT} = 0.25 mg/mL has an even higher CNT:PDADMA ratio, but the bilayer thickness is a factor of 2 larger, allowing PDADMA to act as an adhesive network between the CNTs.

The decreased linear charge density of the CNTs in the aged suspensions enhances the hydrophobicity of the CNTs. So far, we have only considered the electrostatic forces as the cause of multilayer cohesion. However, the hydrophobic nature of the PDADMA backbone and the CNTs is also important. Since contacting hydrophobic groups do not intercalate water, the next step is to examine the swelling of films prepared from aged solutions.

Properties of Films Built with CNTs with a Low Linear Charge Density in Solution

In our previous publication[19] films from freshly prepared CNTs were characterized thoroughly. Therefore, we concentrate now on films prepared from aged CNT solutions. We want to find out how the CNT density influences the film properties. After determining the thickness of CNT/PDADMA
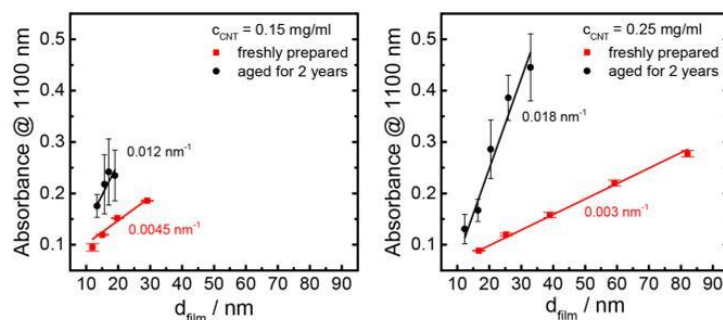
Figure 3. Dependence of absorbance at 1100 nm on the film thickness for films with freshly prepared CNTs and aged CNTs, which were kept for two years in suspension. The CNT concentration in the suspension, 0.15 mg/mL (left) and 0.25 mg/mL (right), was varied. The straight lines are linear fits. The slope corresponds to the absorbance per nm film thickness and is indicated. R-values of the fits are 0.91 and 0.96 (prepared from c_{CNT} = 0.15 mg/mL of an aged and freshly prepared suspension, respectively), and 0.95 (films from c_{CNT} = 0.25 mg/mL). The corresponding absorption spectra are shown in Figure S2 in the SI.
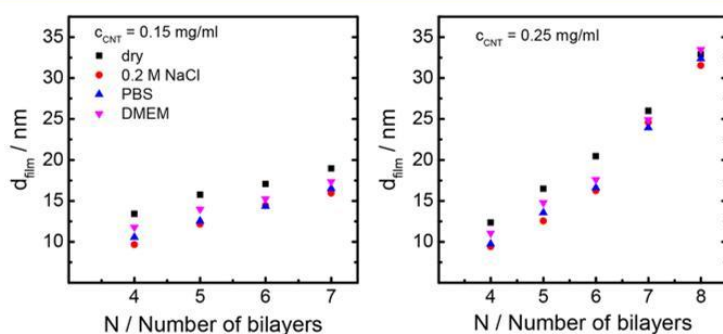

Figure 4. Thickness of multilayer films in air and in different aqueous solutions (0.2 M NaCl, PBS, and DMEM) as a function of the number of CNT/PDADMA bilayers, determined by ellipsometry. All films were built from aged CNT suspensions, with the CNT concentration 0.15 mg/mL (left) and 0.25 mg/mL (right). The legend of the left plot also applies to the right plot.

multilayers with null-ellipsometry in air (at ambient conditions), the films with the low linear charge density were immersed in different solutions, (cf. Figure 4).[20,31] and their thickness was determined again. The influence of the different solutions only results in a slight but constant decrease in the film thickness of ~2 nm, independent of the number of bilayers (cf. Figure 4 left). Neither the 0.2 M NaCl, PBS, nor DMEM solutions have a significant effect on the film thickness. Note that the shrinkage does not depend on the number of deposited bilayers. The constant decline indicates that the shrinkage occurs in the first bilayers next to the substrate, which are laterally inhomogeneous as is evidenced by the ohmic resistance.[19] Films prepared with c_{CNT} = 0.25 mg/mL immersed in solution showed for four to six bilayers the same shrinkage behavior as those prepared from the lower CNT concentration. After six bilayers, the difference decreased and vanished nearly completely at eight bilayers (cf. Figure 4 right). This behavior is consistent with the shrinkage occurring primarily in the bilayers adjacent to the substrate. When the film thickness exceeds 20 nm, the films maintain their thickness in the various solutions. We assume that the solutions cannot penetrate the film to cause shrinkage. Note that shrinkage is weakest in the DMEM solution. This is attributed to the glucose dissolved in DMEM. Like many small molecules, glucose adsorbs onto the positive charges of PDADMA,

intercalates into the film, and brings a large amount of water with it.[36]

Normally, polyelectrolyte multilayers tend to swell by around 30–120% when placed in an aqueous environment, due to increased hydration of the hydrophilic molecular groups.[12–14] Therefore, the thickness of CNT/PDADMA films is expected to increase when they are placed in a solution (0.2 M NaCl, PBS, DMEM), which is due to the interaction between the polymer and the solution.[33] In our case, we observed the opposite effect, even if only slightly. The reason for this effect may lie in the nature of the CNTs themselves, which are highly hydrophobic. They can only be suspended in water by the addition of a few negatively charged groups. However, the aggregates consisting of PDADMA and CNTs with low linear charge density do not intercalate water molecules, and the composition of the solution has little influence (0.2 M NaCl, PBS, and DMEM solution). Thus, the film thickness does not increase. The slight decrease could be due to the structure of the film itself near the substrate. In a solution, small voids or holes created during the preparation process are closed or filled. This would imply that the solution is able to soften the network structure slightly, allowing the film to get denser by closing possible voids and holes. The result would be a slight decrease in the film thickness, as in our case with a $\Delta d_{film} \approx 2$ nm.
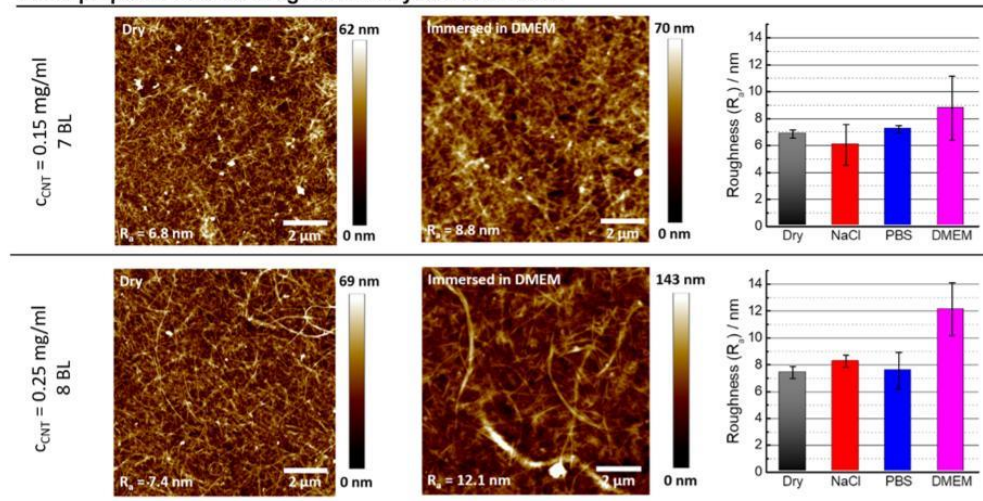
Figure 5. AFM images ($10\,\mu m \times 10\,\mu m$) of PEI/PSS/PDADMA(CNT/PDADMA)$_N$ films in air (left) and immersed in DMEM solution (center). The surface roughness of films in different environments is shown in the bar chart (right), including standard deviation. CNT preparation concentration was 0.15 mg/mL (top row) and 0.25 mg/mL (bottom row). Additional AFM images are in the SI (cf. Figure S3). Note the difference in height scales.

It also appears that a different CNT concentration, in our case c_{CNT} = 0.15 mg/mL (cf. Figure 4, left) or c_{CNT} = 0.25 mg/mL (cf. Figure 4, right) in the suspension, only affects the base thickness (dry state). Concerning the interaction between the film and the surrounding solutions, we have more or less the same results in both cases, namely a slight decrease in film thickness.

AFM was used to further investigate the influence of the different solutions (0.2 M NaCl, PBS, and DMEM solution) on the surface morphology and the possible changes in CNT arrangement. Figure 5 shows AFM images of film surfaces and their derived roughness R_a for both dry and DMEM immersed CNT/PDADMA films consisting of eight bilayers (prepared from CNT solutions with c_{CNT} = 0.15 mg/mL and also c_{CNT} = 0.25 mg/mL). Additional images of films immersed in 0.2 M NaCl and PBS solution are shown in Figure S3.

We cannot measure the orientation of the CNTs directly, but we can measure the film/air roughness. When the films are built from aged CNT suspensions, it is 7.25 ± 0.25 nm. Films made from freshly prepared CNT suspensions are thicker (cf. Figure 1) and the roughness is 14 nm.[19] The decreased roughness strongly suggests a flatter orientation of the CNTs for films made from aged CNT suspensions.

The CNTs are always flatly adsorbed and randomly oriented. The CNT network, which resembles fallen straws, also remains the same. No significant change was observed when comparing the surface morphology of the film in the dry and immersed states.

While there is no significant effect of 0.2 M NaCl and PBS solution on the film surface roughness and overall structure of the film, independent of c_{CNT}, DMEM seems to slightly affect the film morphology. Comparing the height scales of the images of dry with those of the immersed films, only the films immersed in DMEM and prepared from 0.25 mg/mL show a significant change in roughness and a larger peak-to-valley distance. In this case, the height scale increased by a factor of 2

from 69 to 143 nm, whereas the height scales in all the other cases (films in air or immersed in 0.2 M NaCl and PBS) did not change significantly and remained more or less constant about 70 nm.

Comparing the surface roughness of the films in the dry and immersed state (cf. Figure 5, right), only DMEM appears to have an influence. For films prepared from a CNT suspension with c_{CNT} = 0.15 mg/mL, the roughness R_a remains stable at ~7 nm in the dry state and when immersed in 0.2 M NaCl and PBS solutions. For films immersed in DMEM, R_a increased by 2 nm up to 9 nm (cf. Figure 5, right), which is attributed to glucose intercalation.

Increasing c_{CNT} in the suspension to 0.25 mg/mL resulted in a slight increase of σ_{RMS} up to ~8 nm for the dry films and while immersed in 0.2 M NaCl and PBS. Films immersed in DMEM showed a significant increase in the roughness by 4 nm up to 12 nm in total (cf. Figure 5 right, bottom row).

The part of the film, which is interacting with the solution, is the polycation due to the hydrophilic character of the charged groups. Due to the structure of the film, a change in R_a would be expected when the films are placed into solution. Of the 0.2 M NaCl, PBS, and DMEM solutions, only DMEM can interact with the film so that the polymers begin to swell slightly. (This is also only the case if the film consists of at least 8 CNT/PDADMA bilayers.) The result is an increase in R_a of ≈2 nm for films built from CNT suspensions with c_{CNT} = 0.15 mg/mL compared to the dry state. Increasing the CNT concentration in the suspension to 0.25 mg/mL also leads to increased CNT/PDADMA bilayer thickness. The increased bilayer thickness suggests a more network-like structure of the PDADMA and results in higher peak-to-valley values measured by a larger σ_{RMS} of ~4 nm. Locally, the top PDADMA layer swelled and moved laterally and vertically even though the film thickness did not change (cf. Figure 4).

Film resistance R and sheet resistance R_S were measured using the setup shown in Scheme 1 at ambient conditions
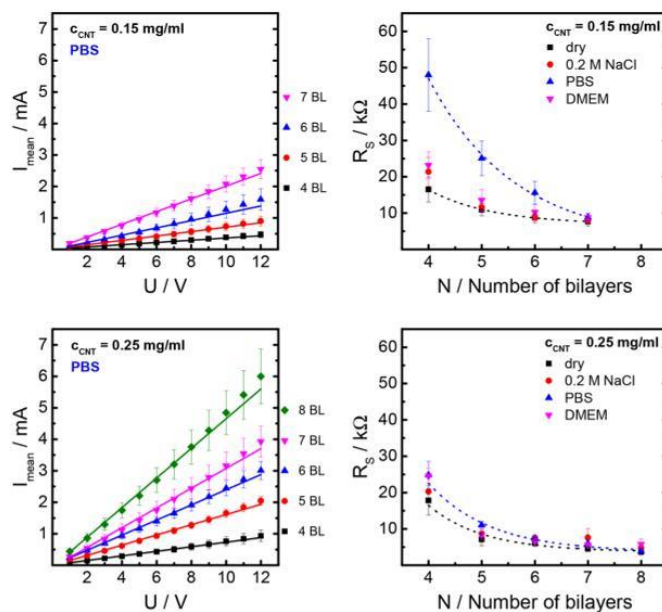
Figure 6. Current–voltage characteristics of a representative series of multilayers in PBS solution (left) and sheet resistance in different environments as a function of the number N of CNT/PDADMA bilayers (right). PEI/PSS/PDADMA/(CNT/PDADMA)$_N$ films were prepared from aged suspensions with c_{CNT} = 0.15 mg/mL (top) and c_{CNT} = 0.25 mg/mL (bottom).
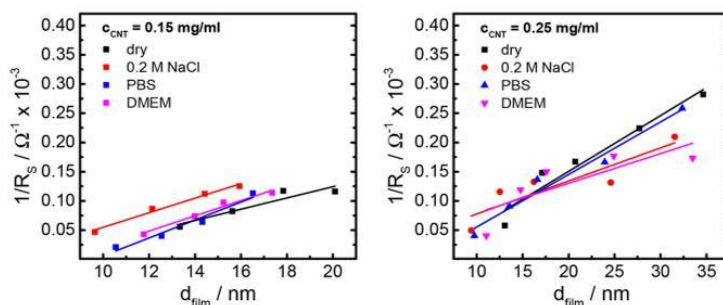

Figure 7. Inverse sheet resistance $1/R_S$ versus film thickness d_{film} of PEI/PSS/PDADMA/(CNT/PDADMA)$_N$ films immersed in air and in different solutions as indicated. For film build-up, the CNT concentration in the aged suspensions was 0.15 mg/mL (left) and 0.25 mg/mL (right). Since $1/R_S = \sigma_{film}d_{film}$, the conductivity σ is determined from the slope of the linear fits of $1/R_S$ versus d_{film}. The R-values of the least-squares fits are listed in Table S2.

(dry) and immersed in a solution. For both CNT concentrations (c_{CNT} = 0.15 mg/mL and c_{CNT} = 0.25 mg/mL), all dry films showed ohmic behavior with respect to the dependence between the applied voltage and the measured current (cf. Figure S4 in the SI). This behavior was also found for films from freshly prepared CNT solutions.[19] Moreover, as expected, the sheet resistance decreases with each additional CNT layer.

Figure 6 left shows the ohmic behavior of CNT/PDADMA multilayers in PBS solution depending on the number of CNT/PDADMA bilayers. The corresponding measurements for films immersed in 0.2 M NaCl and DMEM are presented in Figure S5. In each environment, the sheet resistance R_S decreases with the increasing number of CNT/PDADMA bilayers (cf. Figure 6 right). For films prepared from an CNT suspension with c_{CNT} = 0.15 mg/mL, the sheet resistance in air

is the smallest. The values in 0.2 M NaCl and in DMEM solution are very similar (the decrease is from ~20 kΩ at $N = 4$ to 8 kΩ at $N = 7$). The sheet resistance in PBS and for films consisting of four CNT/PDADMA bilayers is the largest ($\approx$ 50 kΩ). However, the influence of PBS diminishes with each additional bilayer until the impact of PBS completely disappears at 7 BL.

CNT/PDADMA films in air, 0.2 M NaCl, and DMEM solution show similar ohmic behavior to films in PBS (see Figures S4 and S5 in SI). All I_{mean} and R_S values shown are the average of three different films with the standard deviation indicated. Straight lines are least-squares fits to Ohm's law, dotted lines are guides to the eye.

Increasing c_{CNT} to 0.25 mg/mL (cf. Figure 6 bottom row right) resulted in a decreased influence of the solutions on the sheet resistance. Here R_S varied between ~25 kΩ (4 BL CNT/

PDADMA immersed in PBS) and ~8 kΩ (8 BL CNT/ PDADMA immersed in PBS). In summary, it appears that only PBS has a significant effect on the CNT/PDADMA films in terms of their sheet resistance, whereas the influence of the 0.2 M NaCl and DMEM solution is small. However, these observations are only qualitative. Note that not only the sheet resistance changes but also the film thickness d_{film} (cf. Figure 4).

The electrical conductivity σ is defined as $1/\sigma_{film} = R\frac{W \cdot d_{film}}{L} = R_S \cdot d_{film}$, which leads to $1/R_S = \sigma_{film} \cdot d_{film}$. Assuming that the electric conductivity of a CNT/PDADMA film is independent of the number of CNT/PDADMA bilayers, plots of $1/R_S$ as a function of d_{film} yield the conductivity σ. Figure 7 shows the linear dependence between the inverse sheet resistance and the film thickness for films prepared with aged CNT suspensions (c_{CNT} = 0.15 mg/mL, 0.25 mg/mL) in air and immersed in 0.2 M NaCl, PBS, and DMEM solutions, respectively. The deduced conductivity values are shown in Table 2.

Table 2. Electrical Conductivity of Films Prepared with Aged CNTs (Kept Two Years in Solution) in Air and Immersed in Different Solutions As Indicated

	σ_{film} (× 10^4 S m^{-1})	
	c_{CNT} = 0.15 mg/mL	c_{CNT} = 0.25 mg/mL
dry	0.96 ± 0.24	0.95 ± 0.13
immersed		
0.2 M NaCl	1.25 ± 0.11	0.57 ± 0.16
PBS	1.53 ± 0.22	0.89 ± 0.09
DMEM	1.30 ± 0.15	0.51 ± 0.21
average of solutions	1.36 ± 0.13	0.66 ± 0.17

The electrical conductivity of the dry films showed no dependence on c_{CNT} (cf. Figure 7 and Table 2) and amounted to 0.95 × 10^4 S/m. This value is a factor two to nine higher than obtained from compacted multiwalled carbon nanotubes (MWCNT) or graphene[11] in the in-plane direction (0.1–0.5) × 10^4 S/m). Yet, the electrical conductivity is an order of magnitude less than that of graphene monolayers in the in-plane direction ((20–30) × 10^4 S/m).[34] When films prepared from the aged suspension with c_{CNT} = 0.15 mg/mL were immersed into solution, the conductivity increased significantly by a factor of ~1.5 (average in solution 1.36 × 10^4 S/m). The highest value was observed in PBS solution (1.53 × 10^4 S/m).

When films prepared from an aged suspension with c_{CNT} = 0.25 mg/mL were immersed into solution, the conductivity decreased by a factor of ~1.5 (0.66 × 10^4 S/m). The lowest conductivity was obtained in combination with DMEM (0.51 × 10^4 S/m)

This is a surprising result. The films prepared from the aged CNT suspension with the higher concentration (0.25 mg/mL) also showed the highest CNT:PDADMA ratio (cf. Figure 3). Nevertheless, the electrical conductivity in air was the same as for the films prepared with the lower CNT concentration. The conductivity dropped down by a factor of ≈1.5 when these films were placed in solution. This is unexpected. In solution, the film thickness shrank or remained constant (for films made of seven or eight bilayers; cf. Figure 4).

The only parameter that differs significantly in the films from the more concentrated CNT suspension is the thickness of the

CNT/PDADMA bilayers; it is larger (4.7 instead of 1.9 nm; cf. Figure 1). Considering that the diameter of a CNT is 1–2 nm, and that of PDADMA is 0.1–0.2 nm, in a CNT/PDADMA bilayer the CNT are not arranged ideally parallel to the substrate, but more like jackstraws. This hinders the in-plane contacts of the CNTs, which are necessary for electron conduction. In solution, the film thickness decreases due to the hydrophobic attraction of the CNTs; obviously, the shrinkage did not promote in-plane contacts. Probably, the PDADMA wrapped around the CNTs hindered the electron transfer. The lowest electrical conductivity was observed in DMEM, which showed an increased roughness (cf. Figure 5).

The opposite occurred for films prepared with the lower c_{CNT} = 0.15 mg/mL concentration in the aged suspension. Here, the conductivity increases by a factor of ~1.5 up to 1.36 × 10^4 S/m (dry state: 0.96 × 10^4 S/m). The ellipsometry measurements show a thickness decrease which suggests a higher film density (cf. Figure 4). Also, the thickness of a CNT/PDADMA bilayer is 1.9 nm, a value that is very similar to the diameter of a CNT. The CNTs are more flatly arranged, and more in-plane contacts occur. As the films are immersed in the solution, they seem to become denser, which progressively reduces the distances between the single CNTs and creates more CNT contact points. This results in a more effective electron transfer, whereby the electrical conductivity increases.

CONCLUSION

CNT/PDADMA multilayers were built from CNTs with a low linear charge density. The cohesion of the multilayer was achieved on the one hand by electrostatic attraction between oppositely charged functional groups of modified CNTs and PDADMA, and on the other hand by the hydrophobic attraction of the PDADMA backbone and the nonfunctionalized carbon atoms in the CNTs. Remarkably, the CNT/ PDADMA multilayers do not swell in aqueous solutions, as always observed previously,[35] but shrink (on average by Δd = 2 nm for films made from a solution with c_{CNT} = 0.15 mg/mL), or retain their thickness. We achieved the low linear charge density of the CNTs by using aged suspensions; obviously, there are other, more effective ways to control the linear charge density.

Intuitively, one might think that the highest electrical conductivity is achieved with the highest CNT:PDADMA ratio within the film. This was not the case; the highest electrical conductivity was achieved with films having a high CNT:PDADMA ratio, and additionally a CNT/PDADMA bilayer thickness (1.9 nm) that was very similar to the diameter of a carbon nanotube (1–2 nm). Therefore, the CNTs adsorbed flat, as did the PDADMA chains. In biological research-relevant solutions, the film thickness decreased and the electrical conductivity increased. The electrical conductivity σ increased from σ_{air} = 0.96 ± 0.24 × 10^4 S/m in air to $\sigma_{wet, mean}$ = 1.36 ± 0.13 × 10^4 S/m in solution. The highest value was $\sigma_{wet, PBS}$ = 1.53 ± 0.22 × 10^4 S/m.

In conclusion, we have shown that tuning the interpolyelectrolyte forces can suppress the swelling of LbL films in aqueous solutions. The films were stable, and on immersion into biological relevant solutions, the electrical conductivity increased at selected preparation conditions. For biological applications, one can cover the CNT/PDADMA multilayer with a few additional biocompatible polyelectrolyte layers.[7,9]

■ ASSOCIATED CONTENT

Ⓢ Supporting Information

The Supporting Information is available free of charge at https://pubs.acs.org/doi/10.1021/acsaenm.3c00085.

Constant parameters used to fit the ellipsometric data; R-values of the least-squares fits shown for inverse sheet resistance $1/R_S$ vs film thickness d_{film}; XPS spectra and peak-fit of the highly resolved measured C 1s peaks; Vis/NIR absorbance spectra for PEI/PSS/PDADMA/(CNT/PDADMA)$_N$ films; additional AFM images (10 μm × 10 μm) of PEI/PSS/PDADMA(CNT/PDADMA)$_8$ films immersed in 0.2 M NaCl and PBS; current I vs voltage U of PEI/PSS/PDADMA/(CNT/PDADMA)$_N$ films at ambient conditions; current I vs voltage U of PEI/PSS/PDADMA/(CNT/PDADMA)$_N$ films immersed in 0.2 M NaCl and DMEM; inverse sheet resistance vs the number of bilayers N of films built with freshly prepared CNTs and aged CNTs (PDF)

■ AUTHOR INFORMATION

Corresponding Author

Christiane A. Helm − University of Greifswald, Institute of Physics, Greifswald 17489, Germany; Ⓞ orcid.org/0000-0001-5181-1688; Phone: +49 3834 420 4710; Email: helm@uni-greifswald.de

Authors

Sven Neuber − University of Greifswald, Institute of Physics, Greifswald 17489, Germany

Annekatrin Sill − University of Greifswald, Institute of Physics, Greifswald 17489, Germany; Ⓞ orcid.org/0000-0002-5454-1289

Heiko Ahrens − University of Greifswald, Institute of Physics, Greifswald 17489, Germany

Antje Quade − Leibniz Institute for Plasma Science and Technology (INP), Greifswald 17489, Germany

Complete contact information is available at:
https://pubs.acs.org/10.1021/acsaenm.3c00085

Notes

The authors declare no competing financial interest.

■ ACKNOWLEDGMENTS

■ REFERENCES

(1) Gongadze, E.; Rienen, U.; Iglic, A. Generalized stern models of the electric double layer considering the spatial variation of permittvity and finite size of ions in saturation regime. *Cell. Mol. Biol. Lett.* **2011**, *16*, 576−594.

(2) Farooqi, A. R.; Bader, R.; van Rienen, U. Numerical study on electromechanics in cartilage tissue with respect to its electrical properties. *Tissue Engineering Part B: Reviews* **2019**, *25* (2), 152−166.

(3) Zhang, H.; Patel, P. R.; Xie, Z.; Swanson, S. D.; Wang, X.; Kotov, N. A. Tissue-compliant neural implants from microfabricated carbon nanotube multilayer composite. *ACS Nano* **2013**, *7* (9), 7619−7629.

(4) Decher, G. Fuzzy Nanoassemblies: Toward Layered Polymeric Multicomposites. *Science* **1997**, *277*, 1232−1237.

(5) Wågberg, L.; Erlandsson, J. The use of layer-by-layer self-assembly and nanocellulose to prepare advanced functional materials. *Adv. Mater.* **2021**, *33* (28), 2001474.

(6) Mendelsohn, J. D.; Yang, S. Y.; Hiller, J. A.; Hochbaum, A. I.; Rubner, M. F. Rational design of cytophilic and cytophobic polyelectrolyte multilayer thin films. *Biomacromolecules* **2003**, *4* (1), 96−106.

(7) Picart, C. Polyelectrolyte multilayer films: from physico-chemical properties to the control of cellular processes. *Curr. Med. Chem.* **2008**, *15* (7), 685−697.

(8) Gregurec, D.; Wang, G.; Pires, R. H.; Kosutic, M.; Lüdtke, T.; Delcea, M.; Moya, S. E. Bioinspired titanium coatings: self-assembly of collagen-alginate films for enhanced osseointegration. *J. Mater. Chem. B* **2016**, *4* (11), 1978−1986.

(9) Gruening, M.; Neuber, S.; Nestler, P.; Lehnfeld, J.; Dubs, M.; Fricke, K.; Schnabelrauch, M.; Helm, C. A.; Muller, R.; Staehlke, S.; Nebe, J. B. Enhancement of intracellular calcium ion mobilization by moderately but not highly positive material surface charges. *Frontiers in Bioengineering and Biotechnology* **2020**, *8*, 1016.

(10) Ebbesen, T. W. Carbon nanotubes. *Annual review of materials science* **1994**, *24* (1), 235−264.

(11) Marinho, B.; Ghislandi, M.; Tkalya, E.; Koning, C. E.; de With, G. Electrical conductivity of compacts of graphene, multi-wall carbon nanotubes, carbon black, and graphite powder. *Powder technology* **2012**, *221*, 351−358.

(12) Dodoo, S.; Balzer, B. N.; Hugel, T.; Laschewsky, A.; Klitzing, R. v. Effect of ionic strength and layer number on swelling of polyelectrolyte multilayers in water vapour. *Soft Mater.* **2013**, *11* (2), 157−164.

(13) Koehler, R.; Steitz, R.; Von Klitzing, R. About different types of water in swollen polyelectrolyte multilayers. *Adv. Colloid Interface Sci.* **2014**, *207*, 325−331.

(14) Sadman, K.; Wang, Q.; Chen, Y.; Keshavarz, B.; Jiang, Z.; Shull, K. R. Influence of hydrophobicity on polyelectrolyte complexation. *Macromolecules* **2017**, *50* (23), 9417−9426.

(15) Ostendorf, A.; Cramer, C.; Decher, G.; Schönhoff, M. Humidity-tunable electronic conductivity of polyelectrolyte multi-layers containing gold nanoparticles. *J. Phys. Chem. C* **2015**, *119* (17), 9543−9549.

(16) Hlushko, R.; Ankner, J. F.; Sukhishvili, S. A. Layer-by-Layer hydrogen-bonded antioxidant films of linear synthetic polyphenols. *Macromolecules* **2020**, *53* (3), 1033−1042.

(17) Israelachvili, J. N. *Intermolecular and Surface Forces*; Academic Press: 2011.

(18) Moya, S. E.; Ilie, A.; Bendall, J. S.; Hernandez-Lopez, J. L.; Ruiz-García, J.; Huck, W. T. Assembly of polyelectrolytes on CNTs by Van der Waals interactions and fabrication of LBL polyelectrolyte/CNT composites. *Macromol. Chem. Phys.* **2007**, *208* (6), 603−608.

(19) Neuber, S.; Sill, A.; Efthimiopoulos, I.; Nestler, P.; Fricke, K.; Helm, C. A. Influence of molecular weight of polycation polydimethyldiallylammonium and carbon nanotube content on electric conductivity of layer-by-layer films. *Thin Solid Films* **2022**, *745*, 139103.

(20) Nestler, P.; Helm, C. A. Determination of refractive index and layer thickness of nm-thin films via ellipsometry. *Opt. Express* **2017**, *25* (22), 27077−27085.

(21) Green, A. A.; Hersam, M. C. Processing and properties of highly enriched double-wall carbon nanotubes. *Nat. Nanotechnol.* **2009**, *4* (1), 64−70.

(22) Kern, W. The evolution of silicon wafer cleaning technology. *J. Electrochem. Soc.* **1990**, *137* (6), 1887.

(23) Decher, G.; Eckle, M.; Schmitt, J.; Struth, B. Layer-by-layer assembled multicomposite films. *Curr. Opin. Colloid Interface Sci.* **1998**, *3*, 32−39.

(24) López-Oyama, A.; Silva-Molina, R.; Ruíz-García, J.; Gámez-Corrales, R.; Guirado-López, R. Structure, electronic properties, and

aggregation behavior of hydroxylated carbon nanotubes. *J. Chem. Phys.* **2014**, *141* (17), 174703.

(25) Azzam, R. M.; Bashara, N. M.; Ballard, S. S. Ellipsometry and polarized light. *Phys. Today* **1978**, *31* (11), 72.

(26) Benjamins, J.-W.; Jönsson, B.; Thuresson, K.; Nylander, T. New experimental setup to use ellipsometry to study liquid- liquid and liquid- solid interfaces. *Langmuir* **2002**, *18* (16), 6437−6444.

(27) Ryabenko, A.; Dorofeeva, T.; Zvereva, G. UV-VIS-NIR spectroscopy study of sensitivity of single-wall carbon nanotubes to chemical processing and Van-der-Waals SWNT/SWNT interaction. Verification of the SWNT content measurements by absorption spectroscopy. *Carbon* **2004**, *42* (8−9), 1523−1535.

(28) Stobinski, L.; Lesiak, B.; Malolepszy, A.; Mazurkiewicz, M.; Mierzwa, B.; Zemek, J.; Jiricek, P.; Bieloshapka, I. Graphene oxide and reduced graphene oxide studied by the XRD, TEM and electron spectroscopy methods. *J. Electron Spectrosc. Relat. Phenom.* **2014**, *195*, 145−154.

(29) Runde, S.; Ahrens, H.; Lawrenz, F.; Sebastian, A.; Block, S.; Helm, C. A. Stable 2D Conductive Ga/Ga(OxHy) Multilayers with Controlled Nanoscale Thickness Prepared from Gallium Droplets with Oxide Skin. *Adv. Mater. Interfaces* **2018**, *5* (16), 1800323.

(30) Webster, J. G. *Electrical measurement, signal processing, and displays*. CRC Press: 2003.

(31) Bittrich, E.; Furchner, A.; Koenig, M.; Aulich, D.; Uhlmann, P.; Hinrichs, K.; Eichhorn, K.-J., Polymer brushes, hydrogels, polyelectrolyte multilayers: Stimuli-responsivity and control of protein adsorption. In *Ellipsometry of Functional Organic Surfaces and Films*; Springer: 2018; pp 115−143.

(32) Cini, N.; Tulun, T. l.; Decher, G.; Ball, V. Step-by-step assembly of self-patterning polyelectrolyte films violating (almost) all rules of layer-by-layer deposition. *J. Am. Chem. Soc.* **2010**, *132* (24), 8264−8265.

(33) Schönhoff, M.; Ball, V.; Bausch, A. R.; Dejugnat, C.; Delorme, N.; Glinel, K.; Klitzing, R. v.; Steitz, R. Hydration and internal properties of polyelectrolyte multilayers. *Colloids Surf., A* **2007**, *303* (1−2), 14−29.

(34) *Handbook of Chemistry and Physics*, 67th ed.; CRC Press: Cleveland, OH, 2005.

(35) Volodkin, D.; Von Klitzing, R. Competing mechanisms in polyelectrolyte multilayer formation and swelling: Polycation-polyanion pairing vs. polyelectrolyte-ion pairing. *Curr. Opin. Colloid Interface Sci.* **2014**, *19* (1), 25−31.

(36) Müller, M.; Rieser, T.; Dubin, P. L.; Lunkwitz, K. *Macromolecular Rapid Communications* **2001**, *22* (6), 390−395.

Article 3

Self-Patterning Polyelectrolyte Multilayer Films: Influence of Deposition Steps and Drying in a Vacuum

Azinfar, A., **Neuber, S.**, Vancova, M., Sterba, J., Stranak, V., & Helm, C. A.

Langmuir

Volume 37 (2021) 10490 - 10498

LANGMUIR

Article

Self-Patterning Polyelectrolyte Multilayer Films: Influence of Deposition Steps and Drying in a Vacuum

Amir Azinfar, Sven Neuber, Marie Vancova, Jan Sterba, Vitezslav Stranak, and Christiane A. Helm*

Cite This: *Langmuir* 2021, 37, 10490–10498

Read Online

ACCESS | Metrics & More | Article Recommendations | Supporting Information

ABSTRACT: Typically, laterally patterned films are fabricated by lithographic techniques, external fields, or di-block copolymer self-assembly. We investigate the self-patterning of polyelectrolyte multilayers, poly(diallyldimethylammonium) $(PDADMA)/poly(styrenesulfonate)$ $(PSS)_{short}$. The low PSS molecular weight $(M_w(PSS_{short}) = 10.7$ kDa) is necessary because PSS_{short} is somewhat mobile within a $PDADMA/PSS_{short}$ film, as demonstrated by the exponential growth regime at the beginning of the $PDADMA/PSS_{short}$ multilayer build-up. No self-patterning was observed when the PDADMA/PSS film consisted of only immobile polyelectrolytes. Atomic force microscopy images show that self-patterning begins when the film consists of seven deposited $PDADMA/PSS_{short}$ bilayers. When more bilayers are added, the surface ribbing evolved into bands, and circular domains were finally observed. The mean distance between the surface structures increased monotonously with the film thickness, from 70 to 250 nm. Scanning electron microscopy images showed that exposure to vacuum resulted in thinning of the film and an increase in the mean distance between domains. The effect is weaker for PSS_{short}-terminated films than for PDADMA-terminated films. The mechanism leading to domain formation during film build-up and the effect of post-preparation treatment are discussed.
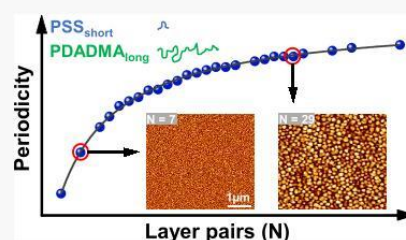
INTRODUCTION

Layer-by-layer films (LbL films) are prepared by sequential deposition of alternating layers of oppositely charged polyelectrolytes (PEs) (synthetic PEs, proteins, DNA, or nanoparticles).[2–4] The targeted integration of suitable building blocks enables many technological and biomedical applications.[5,6] The vertical structures of LbL films have been studied in detail, especially the respective influence of the layer sequence and interdiffusion.[2,7–9] Their lateral structure is poorly understood; the focus has been on the film/air roughness because that limits their usefulness for applications. In some cases, scanning electron microscopy has been used to demonstrate the formation of surface domains.[10] Understanding self-assembly during layer-by-layer growth allows controlled fabrication of nano-patterned films.

Micro- or nano-patterned films are used in applications such as nanolithography,[11,12] nanotemplating, nanoporous membranes,[13] or surface functionalization to improve cell growth.[14,15] For surface patterning, one can modify the polymer films by external fields,[16] or one can use self-assembly.[17–19] Ten years after the discovery of LbL films, it was recognized that the film surface could be rough.[10] The increasing roughness could have two reasons: film destabilization or pattern formation.[10,20,21] In the first case, only films with limited thickness can be formed because increasing roughness limits the number of deposition steps which can be achieved. We investigate the second case, increased roughness due to pattern formation during film build-up.

Spontaneous pattern formation was also observed in PEMs before,[22,23] but it was never investigated systematically. More work on pattern formation has been done with gel films adhering to a surface. The freshly prepared gel film was homogeneous, and the pattern formed only during drying. The decrease in film volume due to drying caused asymmetric stresses, since the film could only shrink vertically, but not laterally.[24] This observation was explained by calculations considering the film thickness, and the elastic moduli of the film and the substrate. These calculations predict that the average distance between domains increases linearly with the film thickness. The formation of the surface pattern of drying gels was enabled by the movement of water molecules.[24] In LbL films, the asymmetric stress is dictated by the conformation of the adsorbed PEs. Just like a drying gel film, a LbL film can only expand in the direction perpendicular to the substrate during its fabrication. The PEs adsorb in a non-equilibrium conformation: If the PEs have a low diffusion coefficient, the original conformation is further immobilized as subsequent layers adsorb.[25–27] The water content is much

10490

lower than in gels, it stands to reason that the mobile species must also be a polyelectrolyte.

To obtain mobility within the film that is necessary for surface patterning, a mobile PE species is required. The diffusion coefficient increases as the polymer length (i.e., molecular weight) is reduced.[28,29] As the domains form, PE movement occurs not only within the film but also on the surface and the sides of the domains. As the average distance between domains increases when additional layers are deposited, not only mobile PEs in the bulk, but also PEs with an adsorption/desorption equilibrium at the surface may be involved.[27,30]

Additional stresses are applied to the LbL film post-preparation when the film is exposed to vacuum. Then, not only the weakly bound water leaves the film, but also the tightly bound water.[31,32] The absence of water molecules between the PEs and at the film/vacuum interface allows the chains to rearrange themselves to produce an energetically more favorable conformation. It was often observed that flat films deswell when moved from water to air as the weakly bound water evaporates. When the film is placed in a vacuum, tightly bound water leaves the film and changes the interaction between PE chains.[31,32] We will show that the additional stress caused by exposure to vacuum changes the surface pattern.

The polycation poly(diallyldimethylammonium) chloride (PDADMA), and polyanion poly(styrenesulfonate) sodium salt (PSS) were used to prepare the LbL films. This system was chosen because it is a well characterized system[1,3,4] with a wide range of biomedical applications.[33−35] The linear charge density of PSS is twice that of PDADMA, therefore, the system grows asymmetrically.[3] To reverse the surface charge, the PDADMA coverage must be larger than the PSS coverage at each deposition step. Therefore, the film growth is nonlinear, i.e., the film thickness increases nonlinearly with the number of PDADMA/PSS bilayers deposited. After PDADMA adsorption, the film is positively charged, and subsequent PSS adsorption leads to charge neutralization.

Finally, after the deposition of N_{trans} bilayers, the film growth changes from nonlinear to linear, i.e., the film thickness increase per deposited PDADMA/PSS bilayer is constant. In the linear growth regime, PSS adsorption no longer leads to charge compensation within the film. As a result, there are more positive than negative monomers in the film[3,36] and electroneutrality within the film is achieved by the incorporation of monovalent anions from the deposition solution.

The exact nature of the nonlinear growth regime at the beginning of the LbL film build-up depends on the mobility of the PSS molecules. After N_{trans} deposited PDADMA/PSS bilayers, a transition from a nonlinear towards a linear growth regime always occurs. However, for PSS with a molecular weight below $M_{w}(PSS_{short}) < M_{w}^{threshold}(PSS)$,[1,27] film growth starts with an exponential growth regime, followed by a parabolic one. Neutron reflectivity measurements show that in the exponential growth regime, PSS_{short} is freely mobile within the film bulk, in a direction perpendicular to the film surface,[37] as expected for an exponential growth regime.[38] In situ monitoring of multilayer build-up indicated that fast adsorption of short PSS is followed by slow desorption of the PDADMA/PSS complexes.[27] In contrast to PSS, in all studies with low molecular weight PDADMA, the polycation was immobile within the film, even though the film thickness increase in the linear growth region was significantly decreased due to the low molecular weight of PDADMA.[37]

The picture is simpler for PSS_{long} with $M_{w}(PSS_{long}) > M_{w}^{threshold}(PSS) \approx 25$ kDa. The smaller diffusion constant of PSS_{long} hinders the exponential growth. The remaining nonlinear growth regime is parabolic. Furthermore, no desorption of PSS_{long}/PDADMA complexes was observed. Although the mobility of PSS_{long} and PSS_{short} is dramatically different, the elastic modulus of the LbL film is assumed to be independent of the PSS molecular weight.[28]

We hypothesize that mobile PSS molecules are necessary for pattern formation. To evaluate this idea, PSS_{short} and PSS_{long} were used in the current study, with $M_{w}(PSS_{short}) = 10.7$ kDa and $M_{w}(PSS_{long}) = 130$ kDa. The other parameters characterizing film growth were kept constant: the molecular weight of the positively charged polyelectrolyte ($M_{w}(PDADMA) = 322$ kDa) and the ion concentration in the adsorption solution (0.1 M). To demonstrate that the chains must not only be short but also mobile, the surface structure of a film of $PDADMA_{short}$ (23.6 kDa) and PSS_{long} was examined. $PDADMA_{short}$ is found to be immobile by neutron reflectometry.[37] The film thickness was determined by X-ray reflectivity and ellipsometry. The evolution of surface patterning as a function of film thickness was followed by atomic force microscopy (AFM) images in air and in pure water. Surface domains in a vacuum were studied from different tilt angles using scanning electron microscopy (SEM).

■ MATERIALS AND METHODS

Materials. Branched poly(ethylenimine) (PEI; $M_{w} = 750$ kDa) was purchased from Sigma-Aldrich (Munich, Germany). Poly-(styrenesulfonate) sodium salt (PSS) with two different molecular weights was used as the polyanion, PSS_{short} with the polymer weight $M_{w}(PSS_{short}) = 10.7$ kDa and PSS_{long} with $M_{w}(PSS_{long}) = 130$ kDa and 666 kDa (all PSS polymers with a PDI < 1.20). The polycation was poly(diallyldimethylammonium) chloride (PDADMA) with the polymer weight $M_{w}(PDADMA_{long}) = 322$ kDa and a PDI of 2.19 and $M_{w}(PDADMA_{short}) = 23.6$ kDa (PDI ≈ 2). PSS and PDADMA polymers were purchased from PSS (Polymer Standard Service, Mainz, Germany). Sodium chloride (NaCl) was obtained from Merck KGaA (Darmstadt, Germany). All solutions were prepared with ultrapure water, using a reverse osmosis system (Sartorius Arium Advance, Göttingen, Germany) which was followed by a millipore purification system (Millipore, Milli-Q synthesis, Molsheim, France, nominal conductivity 0.054 μS/cm). Each polyelectrolyte (PE) deposition solution was prepared at a concentration of 1 mmol/L with respect to the monomer unit. The NaCl concentration of the deposition solution was 100 mM. Single side polished silica wafers were used as substrates (⟨100⟩, Silicon Materials, Kaufering, Germany and Andrea Holm GmbH, Tann, Germany). Prior to sample preparation, silicon wafers were cleaned according to the RCA cleaning protocol.[39]

Preparation of Multilayer Films. Polyelectrolyte multilayers were fabricated via a dipping self-assembly technique[40] using a dipping robot (Riegler & Kirstein, Berlin, Germany). Each adsorption step lasted 30 min, followed by three washing steps in salt free ultrapure water for 1 min each. Branched PEI was always used as the first layer, which reverses the surface charge of the silicon wafers and serves as substrate anchoring layer. All adsorption solutions contained 0.1 M NaCl and 1 mM polyelectrolyte with respect to the monomer concentration. During the adsorption process, all solutions were maintained at 20 °C using a thermostat (Thermo Fisher Scientific, Haake A25, Haake AC200).

X-Ray Reflectometry. The X-ray measurements were performed with a Seifert XRD 3003 TT diffractometer (GE Sensing and Instrument Technology, Ahrensburg, Germany) using Cu Kα radiation (wavelength λ = 1.54 Å). This technique measures the interference between the light reflected from the nanometer-thick surface layer and the light reflected from the substrate/layer interface.
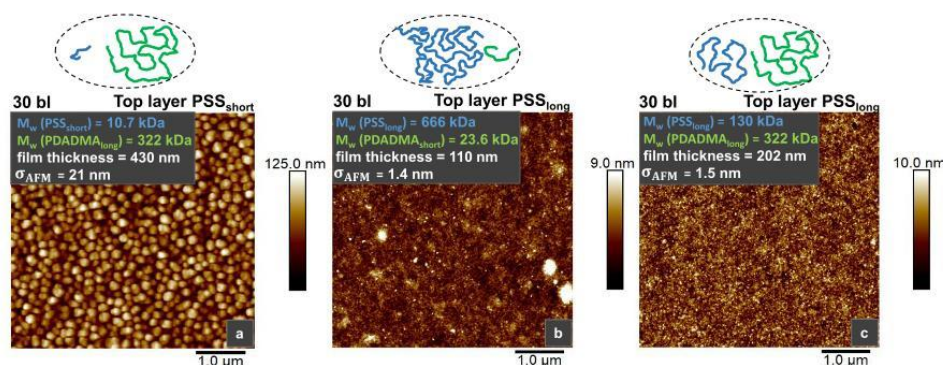
Figure 1. AFM images (5 μm × 5 μm) of three different PEI/PSS/(PDADMA/PSS)$_{29}$ films in air (in water cf. Figure S1). The polyelectrolyte molecular weight is varied as indicated. (a): PSS$_{short}$ (10.7 kDa) and PDADMA$_{long}$ (322 kDa); (b): PSS$_{long}$ (666 kDa) and PDADMA$_{short}$ (23.6 kDa); (c): PSS$_{long}$ (130 kDa) and PDADMA$_{long}$ (322 kDa). All AFM measurements were performed under ambient conditions (r.h. = 40%). Note the different height scales of the images.

With this small wavelength, the index of refraction $n = 1 - \delta$ depends linearly on the electron density of the constituting molecules. Since n deviates a little from 1 ($\delta \leq 3 \times 10^{-5}$), approximations are possible, and the measured reflectivity R can be normalized with respect to the Fresnel reflectivity R_F of an infinitely sharp interface modulated by interference effects from the surface layer. Above about two critical angles of total external reflection ($\alpha_c = \sqrt{2\delta}$) the reflectivity is given by the kinematic approximation[50]

$$\frac{R(Q_z)}{R_F(Q_z)} = \left| \frac{1}{\rho_\infty} \int dz \frac{d\rho(z)}{dz} \exp(-iQ_z z) \right|^2$$

where ρ_∞ is the electron density of the substrate, $\frac{d\rho(z)}{dz}$ is the gradient of the electron density along the surface normal, and $Q_z = \frac{4\pi}{\lambda}\sin\alpha$ is the wave vector transfer normal to the surface (α is the incident angle that is equal to the exit angle in a specular scattering geometry), $R_F(Q_z)$ is the Fresnel reflectivity of an ideally smooth surface. To quantify the molecular parameters, the exact, optical matrix formalism (dynamical approach) is used. The surface layer is parametrized as consisting of different slabs (each with a density and a thickness parameter, as well as a roughness parameter). In all cases, the simulated reflectivity is convoluted with the angular divergence of the respective spectrometer (0.012°).

The structure of the sample perpendicular to the surface is represented by a stack of three slabs, each with a constant refractive index (Si substrate with electron density 0.7 e$^-$/Å^3, PEM, and air with electron density 0 e$^-$/Å^3. The parameters to be determined are thickness d_{PEM} and electron density $\rho_{e,PEM}$ of the PEM. In a good approximation, d_{PEM} can be determined from the separation of two interference minima of the X-ray reflectivity curve (cf. Figure S3) according to

$$d_{PEM} = \frac{2\pi}{\Delta Q_z}$$

The relative humidity varied slightly (3–5%) during one measurement. The low humidity in the chamber was achieved by inserting a small dish with P$_2$O$_5$ (Merck KGaG, Darmstadt, Germany).

Ellipsometry. For thicker films ($\geq$130 nm), the thickness was determined by null-ellipsometry. The measurements are performed with an ellipsometer (Multiskop; Optrel GbR, Sinzing, Germany) in the PCSA configuration (polarizer-compensator-sample-analyzer). A He−Ne laser (power = 4 mW; wavelength λ = 632.8 nm) is used as the light source. The measured quantities were the ellipsometric angles Ψ and Δ, which correspond to the ratio of amplitude and phase shift of light due to reflection at the sample, respectively.

The ellipsometric angles are related to the ratio of the Fresnel reflection coefficients by $r_p/r_s = \tan(\Psi)e^{i\Delta}$, where r_p and r_s are the reflection coefficients of the parallel and normal components of the electric vector $\vec{E}$ (with respect to the plane of incidence). The relative humidity within the laboratory averaged around 18% during the measurements.

The structure of the sample perpendicular to the surface is represented by a stack of four slabs, each with a constant refractive index (Si substrate, SiO$_2$ layer, PEM, and air). The roughnesses between different slabs are set to zero. In this model the refractive indices of the Si wafer and the SiO$_2$ layer are fixed to 3.882 − 0.02i and 1.457.[41] The index of refraction of air is 1. Before the preparation of a PEM, the thickness of the native oxide layer was determined, it was usually about 1 nm. The only remaining unknown sample parameters are the PEM film thickness and refractive index (d, n_{PEM}).

The angle of incidence traverses during the measurement, the range from 66 to 72° (with respect to the surface normal) in 1° steps. In each position the corresponding ellipsometric angles of the sample are measured. The resulting angles Ψ and Δ are particularly sensitive to changes caused by the PEM film. d and n_{PEM} are determined by a least mean square algorithm.

Atomic Force Microscopy (AFM). AFM imaging in air was performed using a Multimode microscope (Veeco/Digital Instruments, Santa Barbara, CA) equipped with a Nanoscope IIIa controller. For measurements in liquids, a Bioscope Resolve microscope (Bruker, Karlsruhe, Germany) was used. The images were recorded using AFM tapping-mode in air with standard cantilevers (OMCL-AC160TS, $k \approx$ 40 N/m, $f \approx$ 320 kHz, tip curvature radius < 10 nm as specified by the manufacturer; Olympus Inc., Hamburg, Germany), while for imaging in pure water, FESP-V2 rectangular cantilevers ($k \approx$ 1−5 N/m, $f \approx$ 50−100 kHz, tip curvature radius $\approx$ 8 nm as specified by the manufacturer; Bruker AFM Probes, Palaiseau, France) were used. AFM images were processed using Bruker NanoScope Analysis 1.9; with this program also the surface roughness $\sigma_{AFM} \triangleq \sigma_{RMS}$, root-mean-square roughness was determined. To determine the average domain separation, two-dimensional fast Fourier transform (2D FFT) of the images was performed, leading to a 2D power spectrum. In the case of images that exhibit a coarse structure, the 2D power spectrum shows radial symmetry with a preferred spatial wavelength. The directional information on the 2D power spectrum was removed by radial averaging.[42]

Scanning Electron Microscopy (SEM). SEM was performed using a field emission scanning electron microscope (FESEM, JSM-7401F, JEOL, Japan) incorporating a cold cathode field emission gun, ultra-high vacuum, and sophisticated digital technologies for high resolution, high-quality imaging of micro structures. Using SEM, high-quality imaging depends on the film conductivity. Therefore, all PEMs
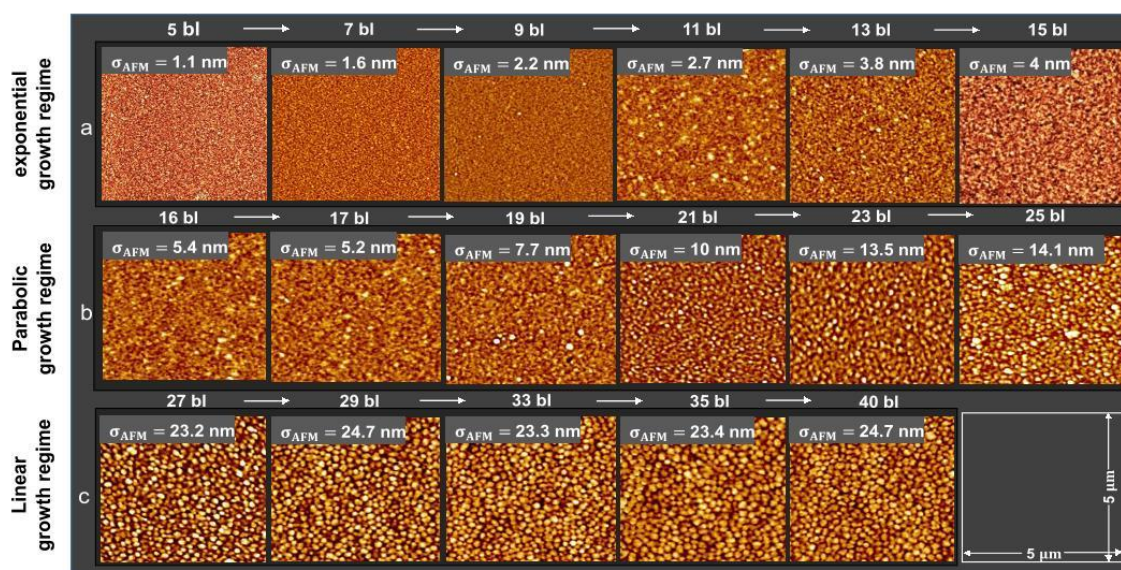
Figure 2. AFM images (5 μm $\times$ 5 μm) in air of the topography development of PEI/PSS$_{short}$ /(PDADMA/PSS$_{short}$)$_{N-1}$ films from N = 5 up to N = 40 bl. Shown is the surface structure and roughness (σ_{AFM}) as the films progress through the three different growth regimes: (a) exponential, (b) parabolic and (c) linear. The height scales are also constantly increasing with increasing number of deposited bilayers. Therefore, only nine representative examples for the height scale are given: 8 nm for 5 bl, 20 nm for 9 bl, 27.7 nm for 13 bl, 41.6 nm for 16 bl, 63.4 nm for 19 bl, 99.0 nm for 23 bl, 152 nm for 27 bl, 175 nm for 33 b and 167 nm for 40 bl (at r.h. = 40%).

had to be coated (30 s) with a thin gold layer (~6 nm) via plasma sputtering using a SCD 050 sputter coater (Bal-Tec, Los Angeles, CA). Measurements from three selected tilt angles (0, 45, 90°) were taken to acquire a highly and detailed demonstration of the PEM surfaces. The PEM micrographs were taken at selected options: Voltage 1−8 kV, working distance (WD) 8.0 mm. To determine the mean domain distance, a 2D FFT was performed using the Gwyddion 2.56 program.

■ RESULTS AND DISCUSSION

The theories about pattern formation predict that the separation of the surface domains increases with film thickness.[24,43] Experimentally, large patterns are easier to resolve than small ones. Therefore, we started the investigation with thick films. PSS-terminated films consisting of 30 polycation/polyanion bilayers (bl) were imaged with atomic force microscopy (cf. Figure 1). The film consisting of PSS$_{long}$ was flat. The same surface roughness (σ_{AFM} = 1.5 nm) was obtained as that with X-ray and neutron reflectometry.[27,44] In contrast, the film consisting of PSS$_{short}$ shows domains with an average distance exceeding 100 nm. The surface roughness was almost an order of magnitude larger (σ_{AFM} = 21 nm). The domains were also observed in pure water (cf. Figure S1). However, in pure water, the surface roughness was smaller. These results indicate that the domains of PDADMA/PSS$_{short}$ films were formed during the LbL film self-assembly.

To demonstrate that it is not sufficient to use a long and a short polyelectrolyte, films made of PDADMA$_{short}$/PSS$_{long}$ were also investigated (cf. Figure 1b). As expected,[1] these films are only half as thick as the films from PDADMA$_{long}$ and PSS$_{long}$. Furthermore, they are flat and show the same film/air roughness as the PDADMA/PSS$_{long}$ films. It is not sufficient that the polyelectrolyte is short, it has also to be mobile.

The forces which led to the domain formation are mechanical stresses within the film, similar to those which led to wrinkling in gel films.[24,43] However, only the films consisting of PSS$_{short}$ show a surface pattern. Therefore, while the stresses are probably similar, domain formation is made possible by the increased mobility of PDADMA/PSS$_{short}$ complexes.[27]

To monitor the formation of domains during film growth, the surface topology of different LbL films was imaged in dependence on the number of deposited PDADMA/PSS$_{short}$ bl. The obtained AFM images are shown in Figure 2. When the first polyelectrolyte layers are deposited, the film thickness increases exponentially with the number of deposited layers, i.e., the film is in the exponential growth regime. PDADMA/PSS$_{short}$ films consisting of up to five bl appear smooth. However, films consisting of seven bl start to show corrugations on the surface. Eventually, when the film consists of 15 bl, the corrugations turn into ribbons. Concomitantly, the surface roughness increases from 1.1 nm up to $\approx$ 4 nm. Now, at 15 bl, the transition from the exponential to the parabolic growth regime occurs. In the beginning of the parabolic growth regime, a similar trend was observed as in the exponential growth regime: the ribbons get more distinct and their separation increases (from 72.5 to 209 nm according to FFT), simultaneously the roughness increases further. Eventually, the ribbons change into small circular domains. At the end of the parabolic growth regime the film consists of 25 bl, and the surface shows circular domains only.

During the subsequent linear growth regime, the circular domains persist. Their separation increases further on the addition of PDADMA/PSS$_{short}$ bilayers (from 209 to 226 nm when the number of bl is increased from 25 to 40). However,
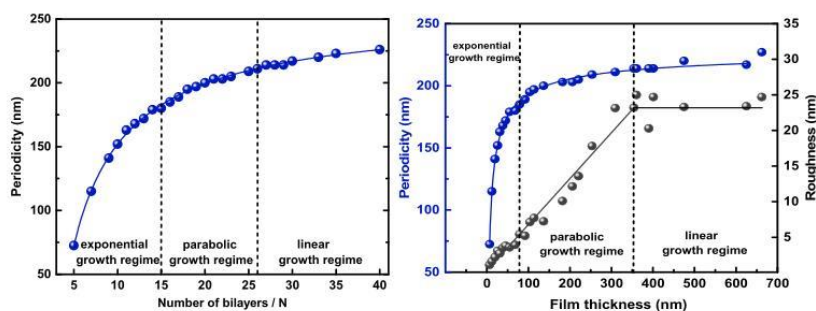
Figure 3. Average distance of PDADMA/PSS$_{short}$ surface patterns as calculated by the FFT power spectrum from AFM images in Figure 2. The average distance of domains is shown in dependence of the number of PDADMA/PSS$_{short}$ bilayers deposited (left) and of film thickness (right). Additionally, the film/air roughness (σ_{AFM}) is shown (right). Film thickness was measured with X-ray reflectivity up to thicknesses of 125 nm, then ellipsometry was used. Different growth regimes of the LbL film are indicated.
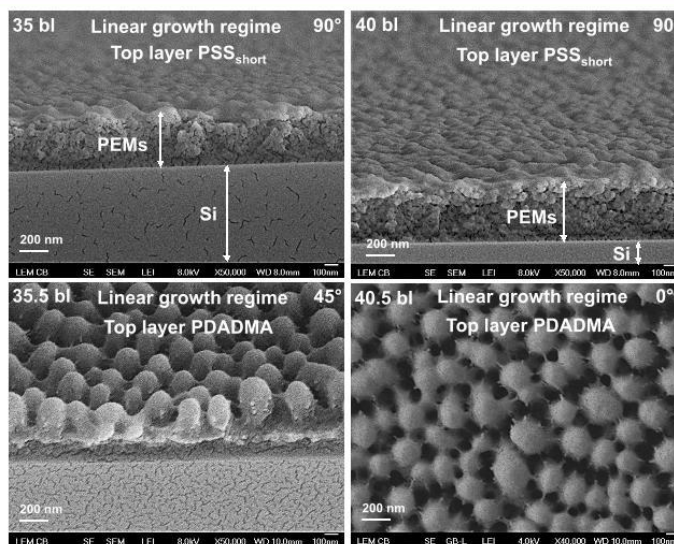
Figure 4. Scanning electron microscopy images of PEMs made from PSS$_{short}$ (10.7 kDa) at different tilt angles and magnifications. PSS-terminated (top) and PDADMA-terminated (bottom) films are shown. The number of PDADMA/PSS$_{short}$ bilayers (bl) and the tilt angle (0, 45, 90°) are indicated in each panel.

the roughness is basically independent of the number of deposited bilayers (σ_{AFM} = 23.6 ± 1.4 nm).

The average distance between the surface corrugations was determined by fast Fourier transform (FFT) in two-dimensions. Only one peak is observed, showing a well-defined average distance between domains (cf. Figure S2), but no crystalline order. As Figure 3 shows, the average distance increases monotonously with the number of deposited bilayers. First the average distance increases steeply, and then it gets flatter. The influence of different growth regimes on domain formation can be better discerned when the average distance is plotted against the film thickness (cf. Figure 3, right; X-ray reflectivity measurements of the film thickness are shown in Figure S3 and the film thickness vs the number of PDADMA/PSS$_{short}$ bl in Figures S4). When the domains (or rather the corrugations) form, the initial very pronounced growth of the average domain distance can be discerned. With each deposited bilayer, the average distance increases by a smaller amount. Eventually, in the linear growth regime, the increase in

domain separation is small. In other words, as predicted theoretically,[24] the domain separation increases linearly with the film thickness.

The surface area of the domains could be determined when the film consisted of 20 bl (i.e., is in the middle of the parabolic growth regime) or more. Both the diameter of domain area and the mean separation of the domains increase monotonically. However, the diameter of the domain area is always smaller (cf. Figure S7).

The predictive power of the theory is limited if one calculates in the linear growth regime the elastic modulus of the film from the domain separation, one gets elastic moduli on the order of MPa as was found experimentally.[45] However, at the beginning of the film build-up the calculated elastic modulus is on the order of GPa, which is unrealistic. These observations illustrate that the domains are not necessarily equilibrium structures but formed during the PDADMA adsorption process due to the lateral movement of the PDADMA/PSS$_{short}$ complexes. The surface roughness σ_{AFM}

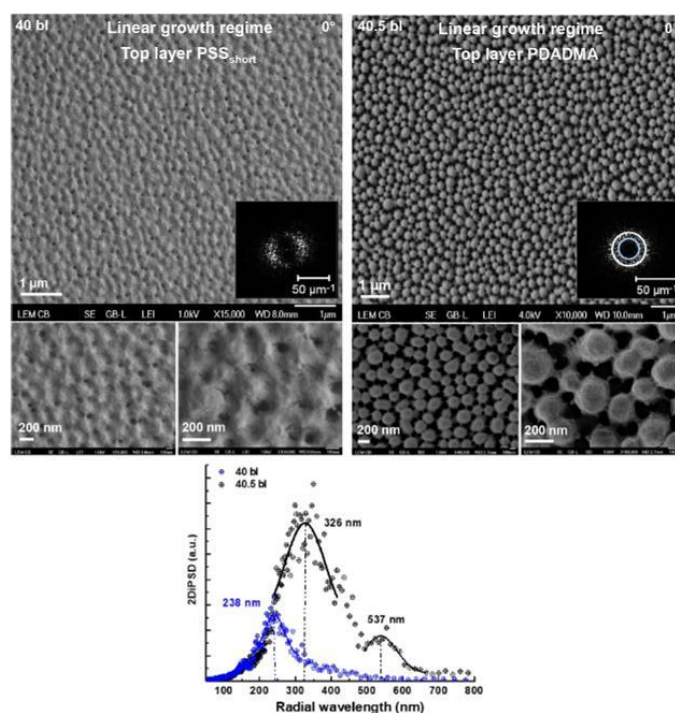**Figure 5.** Top: Scanning electron microscopy images of PSS_{short} (left) and PDADMA (right)-terminated multilayers consisting of 40 or 40.5 bilayers (top view). Different magnifications are shown. Insets: FFT power spectrum of the images. For the 40 bl film, the angle-averaged peak position is 26.38 μm^{-1} (white ring) and for the 40.5 bl film 11.69 μm^{-1} (blue ring) and 19.2 μm^{-1} (white ring). Bottom: Radially averaged power spectral density spectra obtained from the PSS_{short}-terminated (blue symbols) and the PDADMA-terminated film (black symbols). The lines are fits to Gaussian functions.

as determined by AFM can be taken as a measure of the height of the surface structures. It increases linearly in the exponential and parabolic growth regimes with the film thickness, and it is constant in the linear growth regime, suggesting that the domain height is constant in this growth regime. Since the domains are so tunable and well-defined, we examine the domains in the linear growth regime in more detail.

The films were investigated by scanning electron microscopy (SEM). For investigation with an electron microscope, the films were placed in a vacuum chamber, and water within the LbL film was extracted using a vacuum pump system (all water molecules), not only the weakly bound ones which desorb when the film is brought from aqueous solution into air.[31] Scanning electron microscopy images of $PDADMA/PSS_{short}$ films under different angles of PSS_{short}- and PDADMA-terminated films are shown in Figure 4, top views with different magnifications are shown in Figure 5. In the side view, the films do not look homogeneous, but grainy. The grainy structure is attributed to polyelectrolyte clustering during drying. PSS_{short} terminated films have corrugations which are separated by shallow trenches. For films consisting of 35 bl, these trenches are about 83 nm deep, with a film thickness of about 336 ± 27 nm. The SEM images of PDADMA-terminated films differ dramatically from those of PSS_{short}-terminated films. Instead of corrugations with shallow trenches, pillars surrounded by deep trenches are found. The side view shows that the pillars are homogeneous with similar heights (341 ± 22 nm). Some pillars are connected by thin and short

filaments. These thin filaments are attributed to $PDADMA/PSS_{short}$ complexes which shuttled between the domains during PDADMA adsorption and adjusted the domain separation.[27]

The very different lateral structure of PDADMA and PSS_{short} terminated films is attributed to the different configuration of PSS and PDADMA on PDADMA/PSSfilms: PSS with its large linear charge density adsorbs flatly, it compensates positive charges at the film surface. One PSS chain can adsorb on adjacent domains. Earlier experiments showed that upon a decrease in the ion concentration of the surrounding solution, PSS remains flatly adsorbed.[36] This flat adsorption is due to many electrostatic bonds between the monomers of PSS_{short} and the film surface.[36]

PDADMA adsorbs in a coiled structure since PDADMA has a low linear charge density. To overcompensate or balance the charges at the film surface, a flat adsorption is sterically not possible. This leads to fewer electrostatic monomer/monomer bonds between the PDADMA chain and the substrate. If a PDADMA-terminated film is immersed in a solution containing a low salt concentration, one finds that PDADMA chains protrude into the solution and form pseudo-brushes, which scale with the ion concentration as is known for polyelectrolyte brushes.[36,46,47] The occurrence of pseudo-brushes shows that a substantial part of the PDADMA chain is not bound to the surface of the film. If a PDADMA-terminated film forms three-dimensional domains, then it is to be expected that not only the top but also the sides of the domains are covered by polyelectrolyte pseudo-brushes. Two opposing

10495

surfaces covered with polyelectrolyte brushes repel each other.[48] Therefore, a PDADMA-terminated film shrinks vertically and laterally on drying. We suggest that this is the reason why SEM images of PDADMA-terminated films are very different from those of PSS_{short}-terminated films.

To further analyze the SEM images, the mean distance between the domains is determined by a two-dimensional fast Fourier transform (FFT) just as that for the AFM images. As representative examples, the analysis of films consisting of 40 and 40.5 PDADMA/PSS_{short} bilayers are shown (cf. Figure 5). The average distance between the domains of a PSS_{short} terminated film (40 bl) was 238 nm. If an additional PDADMA layer is added (40.5 bl) the average distance between pillars increased to 326 nm. For the PDADMA-terminated film a second, weaker peak can be discerned at 537 nm, which is a factor of $\sim\sqrt{3}$ larger than the first peak. This factor is consistent with the pair correlation function of a fluid, provided each particle in the fluid has about 6 nearest neighbors.[49] The difference between PSS_{short}- and PDADMA-terminated films is substantial, and is attributed to polymer movement during drying, and exposure to vacuum.

To better describe the changes that the films undergo under exposure to vacuum, Figure 6 shows the film thickness
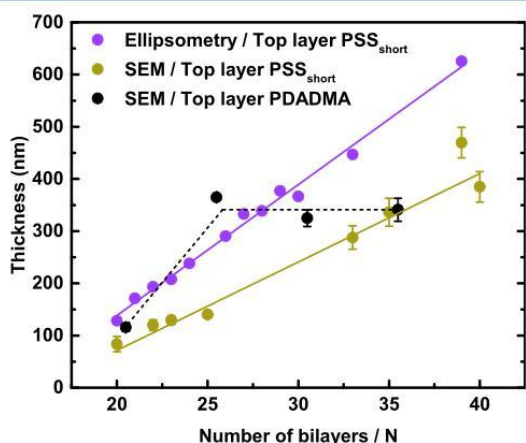

Figure 6. Film thickness (in linear growth regime) depending on the number of deposited PDADMA/PSS_{short} bilayers. Values obtained by ellipsometry in air (18% r.h.) and from tilted SEM images are shown (original data in Figures S4–S6). The lines are least-square fits assuming a linear thickness increase (slopes are 25 and 17 nm/bl, respectively). The dotted line connects the SEM data obtained from PDADMA-terminated films and is a guide to the eye.

obtained from SEM images (original data are shown in Figure 4 at a tilt angle of 90° and Figure S5) together with the results of ellipsometric measurements in air. As expected for the linear growth regime and confirmed with ellipsometry, the thickness of PSS_{short}-terminated films in a vacuum increases linearly with the number of deposited PDADMA/PSS_{short} bilayers. At 18% relative humidity (r.h.) the film is 32% thicker than in a vacuum. Shrinkage by ≈6% is expected when r.h. is changed from 18 to 0% r.h. Additional shrinking is not found when a non-structured film is brought from 0% r.h. to vacuum.[32]

Removal of tightly bound water molecules (8 vol % as deduced from the change in the refractive index) leads to voids within the film. For PDADMA/PSS_{short} films with surface

domains, lateral and vertical movement of polymer molecules lead to additional thinning when tightly bound water molecules are removed. The thickness of the PDADMA-terminated films as measured with SEM does not increase linearly but in steps (cf. Figure 6), a finding which is attributed to the inhomogeneous shrinking of the films when exposed to vacuum. Apparently, not only the trenches which separate the domains broaden and deepen, but also the pillars shrink. Note that even when the roughness is two times bigger for PSS_{short}-terminated films measured by AFM (~24 nm), it is much less than the depth of trenches observed with SEM (~150 nm). Note that PDADMA-terminated films swell more,[32] therefore it is not unexpected that these films change drastically.

To further quantify the changes in PSS_{short}-terminated during exposure to vacuum, the average distance between domains is compared for films in a vacuum, in air, and in pure water (cf. Figure 7). The data obtained in air and in pure water
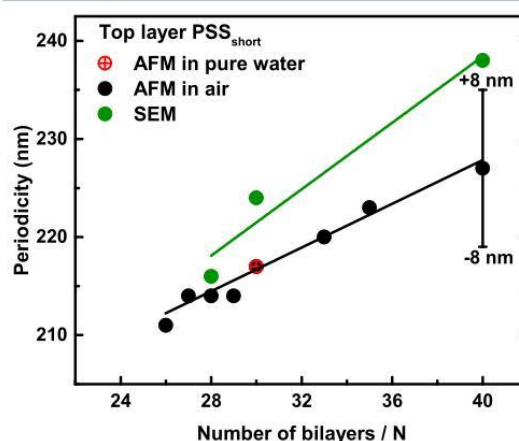
Figure 7. Mean distance of domains of PSS_{short}-terminated films in the linear growth regime as a function of the number of PDADMA/PSS_{short} bilayers deposited. The average distance was determined from AFM images in air, in water, and from SEM experiments (original data in Figures 4, 5, and S1, respectively). A representative error bar for the AFM measurements in air is shown; it results from the imaging of various films at different locations.

coincide and the inter-domain distance under these conditions is smaller than that in a vacuum. It is noteworthy that the average distance increases more in a vacuum than in air, 1.7 and 1.1 nm/bl, respectively. Dehydration in a vacuum increases the elastic modulus of the film which should lead according to theory to an increased distance.[24] Finally, the simultaneous extraction of tightly bound water molecules and the increase in elastic modulus allows for an increased polymer mobility leading not only to film shrinking but also to an increase in the mean distance between the domains which is in qualitative agreement with theoretical predictions.

■ CONCLUSIONS

The morphology of PDADMA/PSS multilayers was studied by AFM in air and in pure water as a function of the number of PDADMA/PSS bilayers deposited. Films made from PSS_{short} showed a patterned surface, the pattern changed during film growth. As the number of deposited PDADMA/PSS_{short} bilayers increased, surface grooves, then stripes, and finally

circular domains were observed. The morphology of the surface patterns correlated with the growth regime of the PDADMA/PSS$_{short}$ film (exponential, parabolic, linear). The average distance between adjacent patterns increased with the number of deposited PDADMA/PSS$_{short}$ bilayers. The pattern formation was attributed to vertical and lateral mechanical stress in the film[24] and the ability of PSS$_{short}$ and/or PDADMA/PSS$_{short}$ complexes to move laterally to release the stress. In the linear growth regime, a linear relationship was observed between the mean distance of circular domains and the film thickness.

PSS$_{short}$ has a high diffusion constant, which resulted in an exponential growth regime at the beginning of the multilayer build-up. In this process, the adsorbing PSS$_{short}$ molecules diffuse through the entire multilayer, and the thickness of the top PDADMA/PSS$_{short}$ bilayer is proportional to the film thickness. Films made from PSS$_{long}$ do not show an exponential growth regime which is attributed to the small diffusion constant of PSS$_{long}$. Furthermore, films made from PSS$_{long}$ did not show any surface pattern and were always flat. Similarly, films built with immobile PDADMA$_{short}$ do not show self-patterning. We conclude that self-patterning films with tunable inter-domain spacing require at least one mobile polyelectrolyte.

Scanning electron microscopy was used to image the films and to see whether and how the morphology changed when placed in a vacuum. The images were very different depending on whether the films were PSS$_{short}$- or PDADMA-terminated. PSS$_{short}$-terminated films were vertically shrunk and the average distance between domains was slightly increased, which was attributed to the adaptation to the increased elastic modulus caused by dehydration. PDADMA-terminated films showed tall pillars (the pillar height exceeded the roughness determined by AFM by a factor of 10) and the average distance between domains was increased by a factor 1.4.

In summary, the self-patterning of the films and the appearance of circular domains were enabled by polymer mobility. Their average spacing can be adjusted by the number of deposition steps. The self-patterning changes further when the films are exposed to vacuum. We assume that the changes of the film in vacuum depend on whether many (as in PSS$_{short}$-terminated films) or not so many (as in PDADMA-terminated films) electrostatic monomer–monomer bonds are present in the film. Furthermore, the conformation of the top polyelectrolyte layer may have an influence.

■ ASSOCIATED CONTENT

ⓢ Supporting Information

The Supporting Information is available free of charge at https://pubs.acs.org/doi/10.1021/acs.langmuir.1c01409.

> AFM images of the self-patterned and flat films measured in water (Figure S1); power spectral-density profiles obtained by the FFT analysis of the images shown in Figure 2 (Figure S2); X-ray reflectivity curves and deduced electron density profiles of different films (Figure S3); the film thickness and surface roughness in dependence of the number of deposited polycation/polyanion bilayers (Figure S4); vertical profiles of various films imaged by electron microscopy, both PSS$_{short}$- and PDADMA-terminated (Figures S5 and S6, respectively); and the diameter of the cross-sectional area of the domains (Figure S7) (PDF)

■ AUTHOR INFORMATION

Corresponding Author

Christiane A. Helm − *Institute of Physics, University of Greifswald, D-17489 Greifswald, Germany;* ● orcid.org/0000-0001-5181-1688; Phone: +49 3834 420 4710; Email: helm@uni-greifswald.de; Fax: +49 3834 420 4712

Authors

Amir Azinfar − *Institute of Physics, University of Greifswald, D-17489 Greifswald, Germany*

Sven Neuber − *Institute of Physics, University of Greifswald, D-17489 Greifswald, Germany*

Marie Vancova − *Institute of Parasitology, Biology Centre of the Czech Academy of Sciences, 37005 Ceske Budejovice, Czech Republic; Faculty of Science, University of South Bohemia, 37005 Ceske Budejovice, Czech Republic*

Jan Sterba − *Faculty of Science, University of South Bohemia, 37005 Ceske Budejovice, Czech Republic*

Vitezslav Stranak − *Faculty of Science, University of South Bohemia, 37005 Ceske Budejovice, Czech Republic*

Complete contact information is available at: https://pubs.acs.org/10.1021/acs.langmuir.1c01409

Notes

The authors declare no competing financial interest.

■ ACKNOWLEDGMENTS

■ REFERENCES

(1) Nestler, P.; Paßvogel, M.; Helm, C. A. Influence of polymer molecular weight on the parabolic and linear growth regime of PDADMAC/PSS multilayers. *Macromolecules* **2013**, 46, 5622−5629.

(2) Hong, J. D.; Lowack, K.; Schmitt, J.; Decher, G. Layer-by-layer deposited multilayer assemblies of polyelectrolytes and proteins: from ultrathin films to protein arrays. *Prog. Colloid Polym. Sci.* **1993**, 93, 98−102.

(3) Ghostine, R. A.; Markarian, M. Z.; Schlenoff, J. B. Asymmetric growth in polyelectrolyte multilayers. *J. Am. Chem. Soc.* **2013**, 135, 7636−7646.

(4) Fu, J.; Schlenoff, J. B. Driving forces for oppositely charged polyion association in aqueous solutions: enthalpic, entropic, but not electrostatic. *J. Am. Chem. Soc.* **2016**, 138, 980−990.

(5) Costa, R. R.; Mano, J. F. Polyelectrolyte multilayered assemblies in biomedical technologies. *Chem. Soc. Rev.* **2014**, 43, 3453−3479.

(6) Richardson, J. J.; Björnmalm, M.; Caruso, F. Technology-driven layer-by-layer assembly of nanofilms. *Science* **2015**, 348, No. aaa2491.

(7) Picart, C.; Mutterer, J.; Richert, L.; Luo, Y.; Prestwich, G.; Schaaf, P.; Voegel, J.-C.; Lavalle, P. Molecular basis for the explanation of the exponential growth of polyelectrolyte multilayers. *Proc. Natl. Acad. Sci., U.S.A.* **2002**, 99, 12531−12535.

(8) Schönhoff, M. Layered polyelectrolyte complexes: physics of formation and molecular properties. *J. Phys.: Condens. Matter* **2003**, *15*, R1781−R1808.

(9) Gopinadhan, M.; Ivanova, O.; Ahrens, H.; Günther, J.-U.; Steitz, R.; Helm, C. A. The influence of secondary interactions during the formation of polyelectrolyte multilayers: Layer thickness, bound water and layer interpenetration. *J. Phys. Chem. B* **2007**, *111*, 8426−8434.

(10) Dubas, S. T.; Schlenoff, J. B. Swelling and smoothing of polyelectrolyte multilayers by salt. *Langmuir* **2001**, *17*, 7725−7727.

(11) Ginger, D. S.; Zhang, H.; Mirkin, C. A. The evolution of dip-pen nanolithography. *Angew. Chem., Int. Ed.* **2004**, *43*, 30−45.

(12) Acikgoz, C.; Hempenius, M. A.; Huskens, J.; Vancso, G. J. Polymers in conventional and alternative lithography for the fabrication of nanostructures. *Eur. Polym. J.* **2011**, *47*, 2033−2052.

(13) Jackson, E. A.; Hillmyer, M. A. Nanoporous membranes derived from block copolymers: from drug delivery to water filtration. *ACS Nano* **2010**, *4*, 3548−3553.

(14) Mörke, C.; Rebl, H.; Finke, B.; Dubs, M.; Nestler, P.; Airoudj, A.; Roucoules, V.; Schnabelrauch, M.; Körtge, A.; Anselme, K.; Helm, C. A.; Nebe, J. B. Abrogated cell contact guidance on amino-functionalized microgrooves. *ACS Appl. Mater. Interfaces* **2017**, *9*, 10461−10471.

(15) Chen, L.; Yan, C.; Zheng, Z. Functional polymer surfaces for controlling cell behaviors. *Mater. Today* **2018**, *21*, 38−59.

(16) Rodríguez-Hernández, J. Wrinkled interfaces: Taking advantage of surface instabilities to pattern polymer surfaces. *Prog. Polym. Sci.* **2015**, *42*, 1−41.

(17) Bates, F. S. Polymer-polymer phase behavior. *Science* **1991**, *251*, 898−905.

(18) Halperin, A.; Tirrell, M.; Lodge, T. Tethered Chains in Polymer Microstructures. In *Macromolecules: Synthesis, Order and Advanced Properties*; Springer, 1992; pp 31−71.

(19) Luo, M.; Epps, T. H., III Directed block copolymer thin film self-assembly: emerging trends in nanopattern fabrication. *Macromolecules* **2013**, *46*, 7567−7579.

(20) Cini, N.; Tulun, T.; Decher, G.; Ball, V. Step-by-step assembly of self-patterning polyelectrolyte films violating (almost) all rules of layer-by-layer deposition. *J. Am. Chem. Soc.* **2010**, *132*, 8264−8265.

(21) Chen, X.-c.; Ren, K.-f.; Chen, J.-y.; Wang, J.; Zhang, H.; Ji, J. Self-wrinkling polyelectrolyte multilayers: construction, smoothing and the underlying mechanism. *Phys. Chem. Chem. Phys.* **2016**, *18*, 31168−31174.

(22) Ghostine, R. A.; Jisr, R. M.; Lehaf, A.; Schlenoff, J. B. Roughness and salt annealing in a polyelectrolyte multilayer. *Langmuir* **2013**, *29*, 11742−11750.

(23) Witt, M. A.; Valenga, F.; Blell, R.; Dotto, M. E.; Bechtold, I. H.; Felix, O.; Pires, A. T. J.; Decher, G. Layer-by-layer assembled films composed of "charge matched" and "length matched" polysaccharides: self-patterning and unexpected effects of the degree of polymerization. *Biointerphases* **2012**, *7*, 64.

(24) Tanaka, T.; Sun, S.-T.; Hirokawa, Y.; Katayama, S.; Kucera, J.; Hirose, Y.; Amiya, T. Mechanical instability of gels at the phase transition. *Nature* **1987**, *325*, 796−798.

(25) Rubinstein, M.; Semenov, A. N. Dynamics of entangled solutions of associating polymers. *Macromolecules* **2001**, *34*, 1058−1068.

(26) Seo, J.; Lutkenhaus, J. L.; Kim, J.; Hammond, P. T.; Char, K. Effect of the layer-by-layer (LbL) deposition method on the surface morphology and wetting behavior of hydrophobically modified PEO and PAA LbL films. *Langmuir* **2008**, *24*, 7995−8000.

(27) Sill, A.; Nestler, P.; Weltmeyer, A.; Paßvogel, M.; Neuber, S.; Helm, C. A. Polyelectrolyte Multilayer Films from Mixtures of Polyanions: Different Compositions in Films and Deposition Solutions. *Macromolecules* **2020**, *53*, 7107−7118.

(28) Akkaoui, K.; Yang, M.; Digby, Z. A.; Schlenoff, J. B. Ultraviscosity in entangled polyelectrolyte complexes and coacervates. *Macromolecules* **2020**, *53*, 4234−4246.

(29) Sill, A.; Nestler, P.; Azinfar, A.; Helm, C. A. Tailorable Polyanion Diffusion Coefficient in LbL Films: The Role of Polycation

Molecular Weight and Polymer Conformation. *Macromolecules* **2019**, *52*, 9045−9052.

(30) Hoogeveen, N.; Stuart, M. C.; Fleer, G.; Böhmer, M. Formation and stability of multilayers of polyelectrolytes. *Langmuir* **1996**, *12*, 3675−3681.

(31) Dodoo, S.; Steitz, R.; Laschewsky, A.; von Klitzing, R. Effect of ionic strength and type of ions on the structure of water swollen polyelectrolyte multilayers. *Phys. Chem. Chem. Phys.* **2011**, *13*, 10318−10325.

(32) Zerball, M.; Laschewsky, A.; von Klitzing, R. Swelling of polyelectrolyte multilayers: The relation between, surface and bulk characteristics. *J. Phys. Chem. B* **2015**, *119*, 11879−11886.

(33) de Grooth, J.; Oborný, R.; Potreck, J.; Nijmeijer, K.; de Vos, W. M. The role of ionic strength and odd−even effects on the properties of polyelectrolyte multilayer nanofiltration membranes. *J. Membr. Sci.* **2015**, *475*, 311−319.

(34) Han, L.; Mao, Z.; Wu, J.; Zhang, Y.; Gao, C. Influences of surface chemistry and swelling of salt-treated polyelectrolyte multilayers on migration of smooth muscle cells. *J. R. Soc., Interface* **2012**, *9*, 3455−3468.

(35) Kim, B. J.; Choi, I. S.; Yang, S. H. Cytocompatible Coating of Yeast Cells with Antimicrobial Chitosan through Layer-by-Layer Assembly. *Bull. Korean Chem. Soc.* **2016**, *37*, 1850−1853.

(36) Mohamad, H. S.; Neuber, S.; Helm, C. A. Surface Forces of Asymmetrically Grown Polyelectrolyte Multilayers: Searching for the Charges. *Langmuir* **2019**, *35*, 15491−15499.

(37) Paßvogel, M.; Nestler, P.; Köhler, R.; Soltwedel, O.; Helm, C. A. Influence of Binary Polymer Mixtures on the Nonlinear Growth Regimes of Polyelectrolyte Multilayer Films. *Macromolecules* **2016**, *49*, 935−949.

(38) Lavalle, P.; Picart, C.; Mutterer, J.; Gergely, C.; Reiss, H.; Voegel, J.-C.; Senger, B.; Schaaf, P. Modeling the buildup of polyelectrolyte multilayer films having exponential growth. *J. Phys. Chem. B* **2004**, *108*, 635−648.

(39) Kern, W. The evolution of silicon wafer cleaning technology. *J. Electrochem. Soc.* **1990**, *137*, 1887−1892.

(40) Decher, G.; Eckle, M.; Schmitt, J.; Struth, B. Layer-by-layer assembled multicomposite films. *Curr. Opin. Colloid Interface Sci.* **1998**, *3*, 32−39.

(41) Palik, E. D. *Handbook of Optical Constants of Solids*; Academic Press, 1998; Vol. 3.

(42) Cornelsen, M.; Helm, C. A.; Block, S. Destabilization of polyelectrolyte multilayers formed at different temperatures and ion concentrations. *Macromolecules* **2010**, *43*, 4300−4309.

(43) Wu, Z.; Bouklas, N.; Huang, R. Swell-induced surface instability of hydrogel layers with material properties varying in thickness direction. *Int. J. Solids Struct.* **2013**, *50*, 578−587.

(44) Soltwedel, O.; Ivanova, O.; Nestler, P.; Müller, M.; Köhler, R.; Helm, C. A. Interdiffusion in polyelectrolyte multilayers. *Macromolecules* **2010**, *43*, 7288−7293.

(45) Collin, D.; Lavalle, P.; Garza, J. M.; Voegel, J.-C.; Schaaf, P.; Martinoty, P. Mechanical properties of cross-linked hyaluronic acid/poly-(L-lysine) multilayer films. *Macromolecules* **2004**, *37*, 10195−10198.

(46) Ahrens, H.; orster, S. F.; Helm, C. A. Charged polymer brushes: counterion incorporation and scaling relations. *Phys. Rev. Lett* **1998**, *81*, 4172−4175.

(47) Ballauff, M.; Borisov, O. Polyelectrolyte brushes. *Curr. Opin. Colloid Interface Sci.* **2006**, *11*, 316−323.

(48) Raviv, U.; Giasson, S.; Kampf, N.; Gohy, J.-F.; Jérôme, R.; Klein, J. Lubrication by charged polymers. *Nature* **2003**, *425*, 163−165.

(49) Gorelik, T. E. *Electron Pair-Distribution Function (ePDF) Analysis.* https://www.uni-ulm.de/fileadmin/website_uni_ulm/hrem/Outreach/ePDF_lecture_notes.pdf.

(50) Als-Nielsen, J.; Jacquemain, D.; Kjaer, K.; Leveiller, F.; Lahav, M.; Leiserowitz, L. Principles and applications of grazing incidence x-ray and neutron scattering from ordered molecular monolayers at the air-water interfac. *Phys. Rep.* **1994**, *246* (5), 251−313.

Surface Forces of Asymmetrically Grown Polyelectrolyte Multilayers: Searching for the Charges

Mohamad, H. S., **Neuber, S.**, & Helm, C. A

Surface Forces of Asymmetrically Grown Polyelectrolyte Multilayers: Searching for the Charges

Heba S. Mohamad, Sven Neuber, and Christiane A. Helm*

Institute of Physics, University of Greifswald, Felix-Hausdorff-Straße 6, D-17489 Greifswald, Germany

S *Supporting Information*

ABSTRACT: Surface forces are used to investigate the polymer conformation and the surface charge of polyelectrolyte multilayers. Films are prepared from strong polyelectrolytes with low and high linear charge density at 0.1 M NaCl, namely poly(diallyldimethylammonium) (PDADMA) and poly(styrenesulfonate) (PSS). The multilayer has two growth regimes: in the beginning, the film can contain as many positive as negative monomers. After about 15 deposited layer pairs, a linear growth regime characterized by an excess of cationic PDADMA monomers occurs. Independent of the film composition, at preparation conditions, the film surface is flat, uncharged and partially hydrophobic. Surface force measurements at decreased ionic strength provide insight. For PSS-terminated films electrostatic forces are found. At the beginning of multilayer formation, the surface charge density is negative. However, in the linear growth regime it is positive and low (one charge per 200−400 nm^2). This reversal of surface charge density of PSS-terminated films is attributed to excess PDADMA-monomers within the film. PDADMA terminated films show steric forces, chains protrude into the solution and form a pseudobrush, which scales as a polyelectrolyte brush with a low grafting density (1900 nm^2 per chain). We suggest a model of polyelectrolyte multilayer formation: PDADMA with its low linear charge density adsorbs with weakly bound chains. Monovalent anions within the film compensate PDADMA monomer charges. When PSS adsorbs onto a PDADMA-terminated multilayer, PSS monomers replace monovalent anions. While electrostatic bonds are formed and dissolved within the polyelectrolyte multilayer, the surface charge density remains zero.
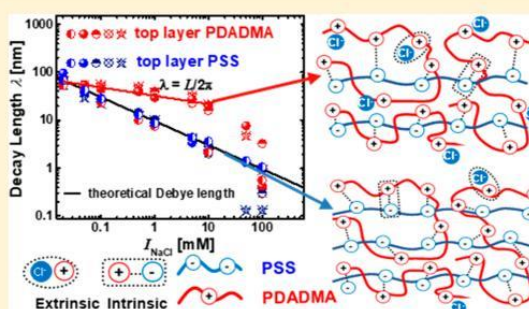
■ INTRODUCTION

The layer-by-layer assembly of polyelectrolyte multilayers (PEMs)[1,2] from natural or synthetic polyelectrolytes is a versatile and simple strategy to modify surfaces.[3−6] Yet the use of PEMs is empirically optimized, since little is known about the surface charge density and polyelectrolyte conformation at the PEM surface. Surface force measurements can shed some light on the issue. Synthetic polyelectrolytes have a hydrophobic backbone, charged functional groups, and are hydrated. Thus, one might expect that electrostatic forces, hydration forces, and hydrophobic forces contribute to the surface forces. Last, but not least, polyelectrolytes are polymers, if they are anchored at one end, steric forces are expected.

Jacob N. Israelachvili was instrumental in establishing surface forces as a function of the composition of both the surface and the aqueous solution. In their pioneering work in Australia, Jacob N. Israelachvili and G. Adams characterized the electrostatic repulsion of flat charged surfaces[7] in dependence of the ion concentration in solution. The electrostatic forces increase exponentially on the decrease of the surface separation, and the inverse decay length (the so-called Debye length) is described by $\kappa^{-1} = 0.3 I_{NaCl}^{-1/2}$ nm (with I_{NaCl} being the concentration of monovalent ions in mol/L).

Careful analysis of the amplitude and the detailed shape of surface forces yields the surface potential and the surface charge density.[8] Additionally, bound water molecules may cause a repulsive hydration force.[9] Like the electrostatic forces, the repulsive hydration forces depend exponentially on the surface separation; however, the decay length is very short, causing a steep increase of the repulsive force. Another cause of repulsion is the steric forces due to polymer chains protruding into solution.[8,10,11] Approximately, this repulsion increases exponentially on the decrease of the surface separation. The decay length λ^{-1} is a measure of the brush thickness. The grafting density of the polymer chains determines the amplitude of the steric forces. Jacob Israelachvili worked with steric forces mainly in connection with biological materials. He also characterized the attractive hydrophobic forces, both in Australia[12] and Santa Barbara.[13] He identified the distance dependence and pointed out the limits of our understanding.

Langmuir

PEMs are prepared by subsequent deposition of oppositely charged polyelectrolytes.[1,2] Early surface forces measurements[14] showed charge reversal whenever a layer was adsorbed to the film. Thus, the surface charge density depended on the top polyelectrolyte layer; it was positive if the top layer was a polycation and negative when the top layer was a polyanion. These early measurements used polyelectrolytes adsorbed from salt-free solution; the polyelectrolytes adsorbed flatly due to large electrostatic forces.[15−17] However, for practical applications adsorption from salt solution is preferred since the thickness increase per deposition step is larger (electrostatic forces are screened) and, thus, fewer deposition steps are necessary to achieve a desired film thickness. From a biological point of view, a salt solution akin to the one in the body is preferred (0.15 M). From a surface forces point of view a large thickness increase per deposition step indicates a coiled polymer conformation, thus steric forces are expected. Since polymer chains are charged, the scaling of polyelectrolyte brushes is likely. Actually, the thickness of polyelectrolyte brushes increases on dilution of the measuring solution; the brush thickness d scales according to $d \propto I_{NaCl}^{-\alpha}$ with a scaling exponent $n \approx 0.33$.[18−25]

For the polyelectrolyte multilayers, we chose two strong polyelectrolytes, poly(diallyldemethylammonium) (PDADMA) and poly(styrenesulfonate) (PSS). PEMs from these polyelectrolytes are often used; thus, a thorough characterization is available in the literature.[26,27] Important is the fact that the line charge density of the polyanion PSS (4 nm^{-1}) is larger than the one of the polycation PDADMA (2.22 nm^{-1}). This imbalance leads to asymmetric film growth.

First, the thickness of a polyelectrolyte multilayer grows parabolically with the number of deposited PDADMA/PSS bilayers (BL).[26−28] To achieve charge compensation, a higher surface coverage of PDADMA is necessary than of PSS. Charge overcompensation at the surface occurs only on the addition of the polycation, whereas PSS merely compensates the PDADMA, as was found with radioactive labeling. Multilayers in the parabolic growth regime are characterized by intrinsic charge compensation, that is, for PSS-terminated films, the ratio of positive to negative monomers is 1. After a defined number of deposited BLs, a transition to a linear growth regime takes place (cf. Figure 1). After how many deposited PDADMA/PSS BL the transition occurs depends sensitively on the molecular weight of PDADMA and PSS (between 7 and 30, provided the films are grown from 100 mM NaCl).[28] In the linear growth regime there is an excess of positive monomers. Within the film, electroneutrality is achieved by the incorporation of monovalent anions (i.e., Cl$^-$). The monovalent anions are distributed evenly within the film.[26]

We are interested in the polymer conformation and the surface charge of the polyelectrolyte multilayers. Therefore, we measure the surface forces in different salt concentrations. Both flatly adsorbed and polymers with chains protruding into solution cause a repulsive force. These forces can be approximated as exponentially decaying with the surface separation. The decay length λ depends on the salt concentration, but the relationships are different for electrostatic ($\lambda \propto I_{NaCl}^{-1/2}$), steric ($\lambda \propto I_{NaCl}^{-\alpha}$, $\alpha \approx 0.33$ for polyelectrolyte brushes),[18,19] or hydration forces (0.3 nm $\leq \lambda \leq$ 2 nm). The latter can be either repulsive (i.e., hydrophilic surfaces) or attractive (i.e., hydrophobic surfaces).[13]

Surface forces shown in this paper are measured on approach, if not indicated otherwise. We will demonstrate
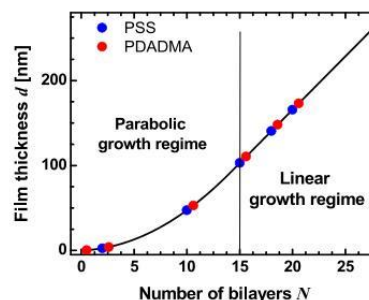
Figure 1. Thickness of a PDADMA/PSS multilayer as a function of number of deposited PDADMA/PSS bilayers N built from a solution containing 100 mM NaCl (ellipsometric measurements in air; M_w(PDADMA) = 322 kDa, M_w(PSS) = 76 kDa).[28] Marked are films whose surface forces were examined with the Colloidal Probe Technique, both PSS-terminated (blue) and PDADMA-terminated (red) films. The line indicates the transition from parabolic to linear growth regime.

that PSS-terminated films always are flat, and at the ionic strength of deposition (100 mM) most multilayers are neutral, provided the multilayer consists of more than 10 PDADMA/PSS BL (i.e., in the linear growth regime). On decrease of the ionic strength, the PSS-terminated multilayers are flat and either negatively or positively charged, depending on the growth regime. In contrast, only the first PDADMA-terminated multilayers are flat and positively charged. When many layers are deposited, PDADMA forms a pseudobrush, which scales as a polyelectrolyte brush for ion concentrations ≤0.01 M and collapses on approaching the deposition conditions. If the multilayer is flat and uncharged at 0.1 M NaCl, then it is partially hydrophobic, with a distinctive pull-off force.

■ MATERIALS AND METHODS

Multilayer Preparation. Polyelectrolyte multilayers are deposited on polished Si (100) wafers (Wacker Siltronic AG, Burghausen, Germany) by dip-coating. The wafers are cleaned according to the RCA standard (which is a mixture of 25% ammonia solution (VWR, Hannover, Germany), 35% hydrogen peroxide (VWR), and ultrapure water in a ratio of 1:1:5, heated for 15 min to 75 °C) and freshly used. All deposition solutions contain a polyelectrolyte concentration of 1 mM (with respect to the monomer concentration) and 0.1 mM NaCl (Merck, Darmstadt, Germany). Always the branched polycation poly(ethylenimine) (PEI; M_w(PEI) = 750 kDa, Sigma-Aldrich, Taufkirchen, Germany) served as substrate anchoring layer. Subsequently, the linear polyanion poly(styrenesulfonate) sodium salt (PSS; M_w(PSS) = 75.6 kDa, degree of polymerization N(PSS) = 367, contour length l_c = 92 nm with PDI < 1.2) and the linear polycation poly(diallyldimethylammonium) chloride (PDADMA; M_w(PDADMA) = 322 kDa, N(PDADMA) = 1994, contour length l_c = 1077 nm with PDI = 2.19) were sequently deposited. PDADMA and PSS were purchased from Polymer Standard Service (Mainz, Germany).

Ultrapure water is from a Milli-Q unit (Millipore, Eschborn, Germany). PEM preparation is performed for all polyelectrolytes in the same way via a dipping robot (Riegler and Kirstein, Berlin, Germany) with 30 min for each adsorption step, followed by three washing steps with pure water for 1 min each. All solutions are kept at 20 °C, which is adjusted externally by a thermostat (Haake, Karlsruhe, Germany).

Surface Preparation. Colloidal probes (CPs) were created by gluing silica spheres (Bangs Laboratories, Fishers, IN; diameter 5−6 μm; root-mean-square roughness 1.5−2 nm, as determined from AFM images) onto the tipless cantilevers (CSC12, MicroMash,
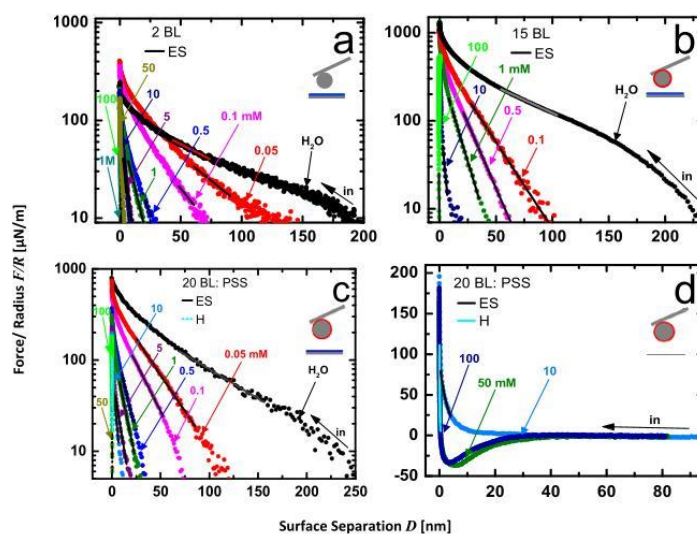
Figure 2. Representative normalized force between PSS-terminated multilayer films and (a) negatively charged bare and (b, c, d) a positively charged PEI-covered colloidal probes. Varied is the NaCl concentration in the aqueous solution as indicated. The film investigated in (a) consists of two polycation/polyanion bilayers (2 BL) and is in the parabolic growth regime, while the films in (b) and (c, d) consist of 15 BL and 20 BL, respectively. They are at the transition between the growth regimes (15 BL) and in the linear growth regime (20 BL). The lines are best fits either to electrostatic repulsion (indicated ES) or to hydration repulsion/attraction (indicated H).

Tallinn, Estonia, spring constant $k = 0.005-0.06$ N/m) using a UV curable epoxy (NOA68, Norland Adhesives, Cranbury, NJ). Colloidal probes were cleaned with argon-plasma at 35 W for 1 min (Harrick Scientific, NY, U.S.A.) and used immediately.

Force Measurements. We perform asymmetric measurements (one polyelectrolyte multilayer covered surface against a bare silica CP or a silica CP with adsorbed PEI). The force measurements are performed in NaCl solutions of different ionic strengths I_{NaCl}: starting with deionized water, then enriching up to 1 M NaCl. Sometimes, the solution was subsequently diluted. The force curves were reproducible and did not change after enriching. The recording of force curves started not later than 5 min after change of the solution. Measuring approach curves, we did not find any relaxation effects.

The minimum distance between two surfaces cannot be measured directly by colloidal probe technique. The interaction between a CP and a flat surface is measured. From the deflection of the cantilever (with spring constant k), the force acting on the CP is calculated with Hooke's law. Contact is defined as the point when the displacements of the cantilever and the piezo are equal (constant compliance).

For steric forces, the force profile exhibits at least one point of inflection, so the minimum surface separation can be determined. If the surface is covered with a polymer brush, the distance 0 will not be reached even with the highest experimentally accessible compressive force. There will always be a displacement δ between the surface separation calculated from the experimentally measured D_{CP} and the true surface separation $D = D_{CP} + \delta$. The determination of this displacement δ is crucial as the fitted value of the grafting density strongly depends on it. Fortunately, the shape of a steric force profile is only determined by the brush thickness L, and the displacement δ can be determined from the inflection point.[8,23,25]

During one experiment we record at least 200 force curves for each salt concentration at different positions on the surface, with one approach/separation cycle per 5 s. Shown are only the averaged force curves on approach. After the measurement spring constants are determined using the methods of Butt, Sader, and Cleveland,[29] all in all, more than 60000 force curves were recorded.

Afterward, the distance-dependent force curves $F(D)$ are normalized by the radius of the CP to give (according to Derjaguin's approximation) the interaction energy per unit area $W(D)$ of two flat

surfaces: $W(D) = F(D)/(2\pi R)$.[8] This allows an easy quantification of the force curves with the theoretical models, which are often calculated for the interaction of two infinitely extended flat surfaces. A commercial DI Multimode AFM (Nanoscope IIIa Controller, Veeco, Santa Barbara, CA, U.S.A.) was used.

■ RESULTS

Top Layer PSS. The polyelectrolyte multilayers were investigated using asymmetric surfaces (a colloidal probe interacts with the surface of a polyelectrolyte multilayer). We started with a PSS-terminated surface of multilayers in the parabolic growth regime. In Figure 2a, the interaction forces between a bare negatively charged colloidal probe and a multilayer consisting of two polycation/polyanion films (abbreviated 2 BL) are shown. The repulsive surface forces are described by the DLVO theory.

Since asymmetric surfaces were used, the surface potential of the bare colloidal probe $\psi_{0,SiO_2} = \psi_{0,probe}$ in dependence of the NaCl concentration needed to be determined (cf. Table S1 in the Supporting Information). Then, the surface potential $\psi_{0,PSS} = \psi_{0,film}$ could be determined from the electrostatic surface forces $F_{ES}(D)$,[8,30] using the weak overlap approximation:

$$\frac{F_{ES,asymm}(D)}{2\pi R} = 64 k_B T \varrho_\infty \tanh\left(\frac{e\psi_{0,probe}}{4k_B T}\right)\tanh\left(\frac{e\psi_{0,film}}{4k_B T}\right)e^{-\kappa D}$$

$$= 0.0482\sqrt{I_{NaCl}}\,\tanh\left(\frac{e\psi_{0,probe}}{103\text{ mV}}\right)\tanh\left(\frac{e\psi_{0,film}}{103\text{ mV}}\right)e^{-\kappa D}$$

$$[\text{mN/m}] \tag{1}$$

Here, R denotes the radius of the colloidal probe, ϱ_∞ is the number density of the ions in the bulk solution, k_B is the Boltzmann constant, T is the temperature, D is the surface separation, and κ is the inverse Debye length. The measured Debye length agreed with theoretical predictions and Jacob Israelachvili's classical measurements.[7] To further characterize PSS-terminated multilayers in the parabolic growth regime,

Langmuir

also the surface forces of films consisting of 10 BL were determined (cf. Figure S2 in Supporting Information). The results coincided with those of films consisting of 2 BL (cf. Figure 2a), with one exception: at 1 M, an adhesive force was observed; on approach, the minimum force was −5 μN/m. The adhesive force decayed exponentially with the surface separation.

In the next step, PSS terminated multilayers in the linear growth regime were investigated (cf. Figure 2b,c). Again, asymmetric surfaces were used. However, we found that in clean water the polyanion-terminated multilayers were positively charged. With the aim to measure repulsive surface forces, PEI was adsorbed on the colloidal probe. For the probe characterization, the dependence of the surface potential $\psi_{0,PEI}$ = $\psi_{0,probe}$ on the NaCl concentration was determined for symmetric surfaces (cf. Table S2 in the SI). With the PEI covered probe, repulsive electrostatic interactions were observed (cf. eq 1). The surface potential $\psi_{0,film}$ decreased on increase of the NaCl concentration (cf. Figure 3). Again, it
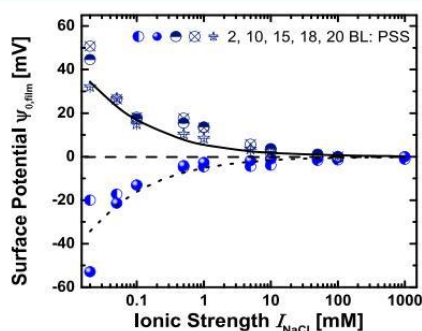

Figure 3. Surface potential $\Psi_{0,film}$ of PSS terminated PDADMA/PSS multilayers consisting of different number of PDADMA/PSS bilayers (BL). Films consisting of up to 10 BL exhibit a negative surface potential, then a charge reversal occurs, which is concomitant with the transition from parabolic to linear growth at 15 ± 2 BL. The lines show $\Psi_{0,film}$ calculated with eq 2 assuming a constant surface charge.

was independent of the number of deposited PDADMA/PSS bilayers. Adhesive forces, which could not be described by the DLVO theory, occurred with increasing bilayer number N at NaCl concentrations above 50 mM and will be discussed in more detail below.

From the surface potential $\psi_{0,film}$, the surface charge density $\sigma_{0,film}$ was calculated according to the Graham equation

$$\sigma_{0,film} = \sqrt{8k_BT\varepsilon_0\varepsilon\varrho_\infty}\,\sinh\left(\frac{e\psi_{0,film}}{2k_BT}\right) = 0.118\sqrt{I_{NaCl}}\,\sinh\left(\frac{e\psi_{0,film}}{51.5\,mV}\right)$$
$$[C \cdot m^{-2}] \tag{2}$$

Unexpectedly, the surface charge density was constant for each film (cf. Figures 3 and S2 in the Supporting Information), both for films in the parabolic and linear growth regimes, even though it was different in each growth regime (changed sign, actually). For films in the parabolic growth regime consisting of 2 or 10 polycation/polyanion BL, the average surface charge density was −0.44 ± 0.28 mC m⁻², corresponding to one elementary charge per 360 nm² (for each film alone, the standard deviation was smaller, however, there was film-to-film variation). For the films in the linear growth regime (15, 18, and 20 BL), the surface charge density was positive, and also

constant (0.62 ± 0.22 mC m⁻²). This corresponds to one charge per 260 nm². Concluding, at the low ion concentrations, when the multilayers were charged, the surface charge density was always low.

At high NaCl concentrations (≥50 mM), attractive surface forces as shown in Figure 2d for a film consisting of 20 BL were observed. Table 1 summarizes those films which showed

Table 1. Parameters Characterizing the Surface Forces of Different PSS-Terminated Multilayers Consisting of the Numbers of Bilayers as Indicated at Salt Concentrations I_{NaCl} close to the Preparation Conditions (I_{NaCl} = 100 mM)[a]

multilayer		2 BL	10 BL	15 BL	20 BL
I_{NaCl} (mM)	Debye length κ^{-1} (nm)	κ^{-1} (nm)	κ^{-1} or D_H (nm)	κ^{-1} or D_H (nm)	κ^{-1} or D_H (nm)
50	1.3	1.44	1.3		**0.24**
100	0.96	1.06	0.97	**0.39**	**0.88**
1000	0.3	0.4	**0.52**		

[a]In the second column, the theoretical Debye length κ^{-1} is given. If an attractive force on approach (and no evidence of an electrostatic force) is found, the decay length D_H of the hydration or hydrophobic force is given in **bold**.

attractive forces. For 2 BL, we found only repulsive electrostatic forces; for 10 BL, attractive forces were only observed at the highest ion concentration used in this paper, 1000 mM. With increasing bilayer number, attractive forces occur at lower ion concentrations: for 15 BL already at 100 mM, for 20 BL even at 50 mM. We tried to fit these attractive forces with (i) van der Waals forces,[8] as well as patch-charge attraction.[17] However, the distance dependence of the attractive force was not consistent with van der Waals- or patch charge attraction. Since the backbones of both polyelectrolytes, PDADMA and PSS, are hydrophobic, it is possible that the surfaces are partially hydrophobic. The contact angle of PSS terminated films is between 30° and 60°, depending on the layer number.[6] For the hydrophobic attraction, the distance dependence on approach is strongly influenced by the gas content of the aqueous solution. In case of nondegassed water (which we used), the hydrophobic interactions are rather long-ranged.[13] We found that the range of the attraction varied from film to film. The contact angle needs to be investigated further before adhesive forces can be understood.

The hydration forces are described by the general interaction potential for hydrophobic and hydrophilic interactions:[13]

$$\frac{F_{H,asymm}(D)}{2\pi R} = -\frac{2Hy}{2\pi R}e^{-D/D_H} \tag{3}$$

D_H denotes the decay length ($D_H \approx 0.3–2$ nm), whose exact value depends on the system, and Hy is the Hydra parameter characterizing the hydration or hydrophobic interaction, respectively. Often, surfaces are charged and partially hydrophobic. Then, the surface forces are described by the sum of electrostatic and attractive hydration (i.e., hydrophobic) interactions.[13] However, we find only partially hydrophobic surfaces when the decay length of the hydration forces and electrostatic forces are very similar, and it is difficult to distinguish them. Therefore, we describe the surface forces of PSS-terminated polyelectrolyte multilayers as partially hydro-

phobic when (i) the decay length is smaller than the Debye length and (ii) an attractive force is observed.

For some surfaces at NaCl concentrations close to the preparation conditions (15 BL at 100 mM, and 20 BL at 50 and 100 mM), D_H is significantly smaller than the Debye length κ^{-1}. For these films, we do not find any evidence of a surface charge and conclude that the surfaces of the PEMs are uncharged. These neutral surfaces are only found in the linear growth regime, when there is an excess of positively charged PDADMA monomers in the film, and the polyanion-terminated polyelectrolyte multilayer exhibited a positive surface charge density at low salt concentrations.

To gauge the strength of the hydrophobic interaction, the pull-off force was measured repeatedly (cf. Figure 4). On
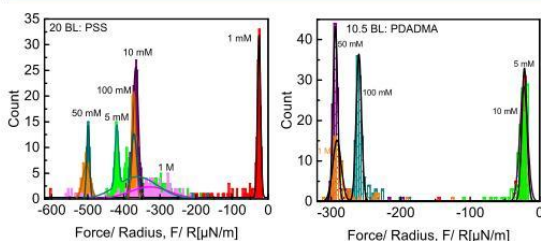

Figure 4. Top: Pull-off force for multilayers terminated by PSS (left) and PDADMA (right) in dependence of the ionic strength in the measuring solution. Bottom: Representative force distance profiles for adhesive forces in the order of 0.1−0.4 mN/m.

increase of the ionic strength, the pull-off force generally increases, and shrinks at 1 M NaCl (cf. Figure 4, left). Also, there is a pronounced film-to-film variation, which is stronger than the effects of PSS- or PDADMA-termination. An additional caveat is the fact that adhesive minima deeper than 500 μN/m could not be resolved and the pull-off forces are estimated (the set-point was chosen in a way that repulsive forces could be measured with great accuracy, not adhesive forces). Figure 4 demonstrates that each film yielded reproducible pull-off forces (with the exception of films in 1 M NaCl, when electrostatic monomer−monomer bonds are partially replaced by monomer-ion bonds), as is expected from partially hydrophobic surfaces.

Approach/retreat force distance profiles are also shown in Figure 4. Table S4 in Supporting Information gives an overview. The force profiles show pronounce hysteresis. Note that hysteresis was always found when the measuring solution contained 50−100 mM. However, hysteresis was never observed when the solution was diluted to 1 mM NaCl. When the salt concentration is increased to about 5 mM, few force profiles show approach/retreat hysteresis. On further increase of the ionic strength to 10−50 mM, most force profiles show hysteresis. Table S4 suggests that with increasing layer number, the onset of hysteresis occurs at lower layer numbers. These statements are valid both when PSS and when PDADMA form the top layer.

If one considers the hysteresis in detail, two effects are obvious: (i) when the surface separation starts, the force is more short-ranged, suggesting film compression caused by deswelling. However, the surfaces relax quickly, the approach curves superimpose. (ii) On approach, there is no long-ranged attraction, even when there is a pronounced and long-ranged pull-off force. The polymers do not stretch out and cause a

jump-in as described in the literature for neutral brushes.[31] Here, we deal with charged polymers, and the opposite surfaces have the same charge. The electrostatic repulsion hinders the polymers to stretch out. However, when the surfaces are in contact, the polyelectrolyte molecules rearrange and form local bonds. Separating the surfaces causes the polymers to stretch out. The surface roughness, as determined by AFM images, was the same before and after the repeated force profiles, suggesting that the films are stable.

Top Layer PDADMA. The polycation PDADMA has a lower line charge density than the polyanion PSS. In the parabolic growth regime there is intrinsic charge compensation, that is, the ratio between PDADMA and PSS monomers is one. Surface forces are measured between the multilayer surface and a colloidal probe covered with physisorbed PEI. Two films in the parabolic growth regime were investigated, one consists of 2.5 BL and the other consists of 10.5 BL (cf. Figure 5).

The surface forces between the polyelectrolyte multilayer consisting of 2.5 BL film and the positively charged colloidal probe are repulsive, they increase exponentially on approach of the surfaces (cf. Figure 5a). The dependence of the decay length on I_{NaCl} is the one of a Debye length ($=0.3/\sqrt{I_{NaCl}}$ nm), as is shown in Figure 6. The repulsion between the surfaces can be described as electrostatic (cf. eq 1). This leads to the conclusion that a PDADMA-terminated multilayer consisting of 2.5 BL is a flat surface; PDADMA has been adsorbed flatly in the first deposition steps.

The multilayer consisting of 10.5 BL is also in the parabolic growth regime; however, the force curves differ from those obtained from a multilayer consisting of 2.5 BL (cf. Figure 5a,b). Again, the force curves are repulsive, and they increase approximately exponentially on approach of the surfaces. However, the range in deionized water is almost doubled, and the amplitude of the forces at low ion concentrations has a 10-fold increase. The former leads to a larger decay length (cf. Figure 6).

These observations suggest steric forces. Some chain fragments (tails or loops) protrude from the surface and form a pseudobrush. Steric forces were established to describe the forces between brush-layers end-grafted to a surface. The repulsive force is due to a subtle interplay of an osmotic repulsion between the coils, which favors their stretching, and an elastic energy of the chains, which opposes stretching. To describe these steric forces, the Alexander de Gennes theory[8,10,11] is used for the asymmetric case, the forces between a flat surface and a surface covered with a polymer brush.

$$\frac{F_{AdG,asymm}(D)}{2\pi R} = \frac{2k_B TL}{35s^3}\left[7\left(\frac{L}{D}\right)^{5/4} + 5\left(\frac{D}{L}\right)^{7/4} - 12\right] \text{ for } D < L \tag{4}$$

Here, s^2 is the average grafting area per chain and L is the brush thickness. We use eq 4 to fit the measured force profiles. However, to find the origin of the repulsive interaction forces characterizing the different multilayer surfaces, decay lengths were compared (cf. Figure 6). For D/L in the range of 0.2 to 0.9, the surface force is roughly exponential.[8] Thus, we extracted from the fitted force profile a decay length. Both from the least-squares fits to eq 4 and from the decay length, the brush thickness L was calculated, and the same result was obtained. The decay length is $\lambda = \frac{L}{2\pi}$.
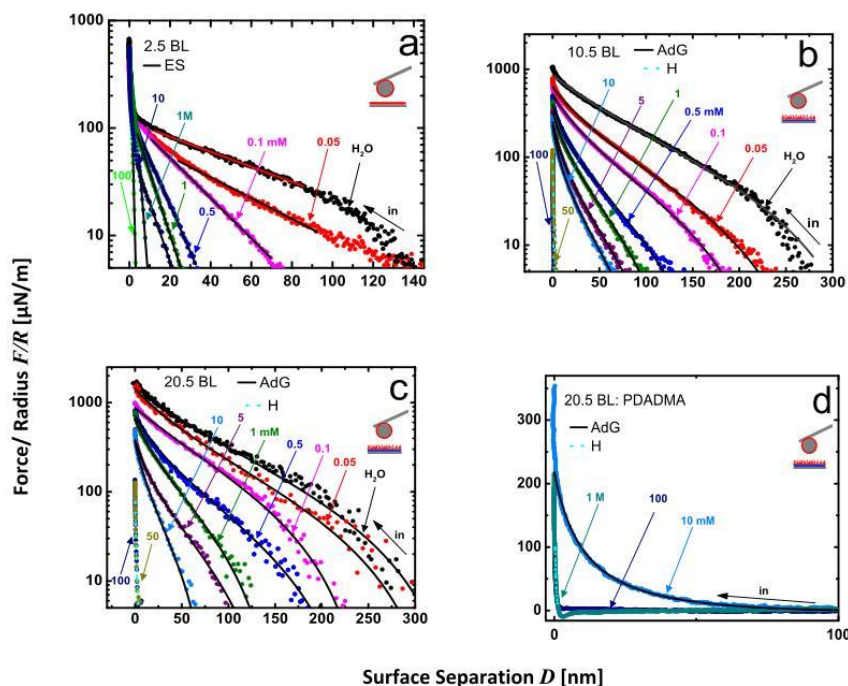
Figure 5. Representative normalized force profiles between PDADMA-terminated multilayer films and positively charged PEI-covered colloidal probes. Varied is the NaCl concentration in the aqueous solution as indicated. The film investigated in (a) consists of 2.5 polycation/polyanion bilayers (2.5 BL) and is in the parabolic growth regime, as is the film in (b) (10.5 BL; note the rescaled x-axis). The film shown in (c) and (d) consists of 20.5 BL and is in the linear growth regime. The black and colored lines are best fits to electrostatic repulsion, the Alexander de Gennes theory (indicated by ES and AdG, respectively), the dashed lines to the hydration interaction (indicated by H).
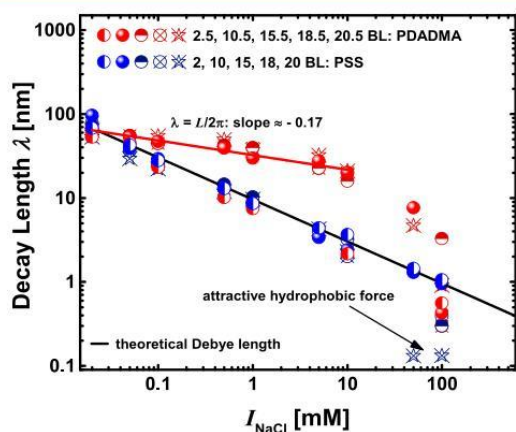
Figure 6. Decay length λ of exponentially decaying repulsive force profiles in dependence of the NaCl concentration in the measuring solution. The polyelectrolyte multilayers consist of different numbers of PDADMA/PSS bilayers (BL), as indicated. For measurements from PSS and PDADMA terminated multilayers blue and red symbols are used, respectively. The straight black line is the theoretically predicted Debye length (power to −0.5), the straight red line a weaker power law (power to −0.17), which was obtained by least-squares fits to describe the thickness of polyelectrolyte pseudobrushes of those PDADMA-terminated polyelectrolyte multilayers, which consist of 10.5 or more BL.

The surface forces obtained from the 10.5 BL film are consistent with forces expected from polyelectrolyte brushes, but only at low salt concentrations up to 10 mM NaCl. On increase of the salt concentration I_{NaCl}, the brush length L shrinks. The brush length follows a power law ($L \propto I_{NaCl}^{-\alpha}$). The power ($\alpha \approx 0.17$) is lower than theoretically predicted ($\alpha = 0.33$).[18,19] Yet, the theory was developed for ideal polyelectrolyte brushes, and the monomer volume was neglected. Pseudobrushes with a finite monomer size may affect the scaling. The thickness of the pseudobrush is at most 450 nm (in pure water), this is about 42% of the contour length of PDAMA. Pronounced swelling is observed for both anchored and adsorbed polyelectrolyte brushes.[21,23−25,32] In the quoted literature, the maximum swelling was between 30 and 60% of the contour length. These brushes were either chemically anchored or physisorbed at one end. The strong swelling of the PDADMA pseudobrush suggests that it consists mostly of end-physisorbed chains. On increase of I_{NaCl}, the anchoring density of the pseudobrush remains constant ($s = 43.2$ nm, cf. Figure 7). The anchoring density is low, 1866 nm² per chain. This number can be compared with the average area per PDADMA molecule, 125 nm² (calculated from degree of polymerization N(PDADMA) = 1994, the mean thickness of the 10th PDADMA layer, 4.5 nm, the monomer volume of PDAMA and PSS, 0.206 and 0.200 nm³, respectively, and 5.5 water molecules per monomer pair with a volume of 0.03 nm³ each[28,33]). Only 7.5% of the adsorbed PDADMA molecules in the top layer supply a train to protrude into the water and form a pseudobrush.

Figure 7. Average distance s between PDADMA pseudotails in dependence of the brush thickness for a multilayer consisting of 10.5 layer pairs. The straight line shows the average value (43.2 nm) obtained from the polyelectrolyte pseudobrush. The dependence of the brush thickness on I_{NaCl} is shown in Figure 6.

If the salt concentrations are larger than 10 mM, then the brush shrinks faster than the scaling law predicts (cf. Figure 6). At 100 mM, the decay length (0.25 nm) of the exponential force is very short, even shorter than the Debye length known from the electrostatic double layer theory. The short decay length describes a surface that shows only hydration forces, neither steric nor electrostatic forces. When the brush thickness shrinks faster than a polyelectrolyte brush (brush thickness < 100 nm, at I_{NaCl} = 50 and 100 mM), then the measured separation between two chains also shrinks (from the average value of 43.2 to 30 nm, cf. Figure 7), but we are not sure how meaningful the grafting density values are that were obtained from a collapsing brush.

PDADMA-terminated multilayers described so far were in the parabolic growth regime. Force curves obtained in the linear growth regime from a multilayer consisting of 20.5 BL are shown in Figure 5. As for the 10.5 BL film, steric forces are found (cf. Figure 6). The thickness of the pseudobrush and its dependence on I_{NaCl} are identical within error to the film consisting of 10.5 BL, again only for low ion concentrations (i.e., for $I_{NaCl} \leq 10$ 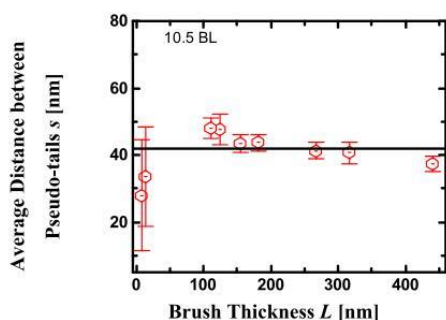mM). The same polyelectrolyte pseudobrush was observed if the film consisted of 15.5 or 18.5 BL. Also, s, the separation of the brush-forming chains did not very much for the different PDADMA-terminated polyelectrolyte multilayers, 41.1 ± 3.0 nm (cf. Table S3 in the Supporting Information). Note that the grafting density for each film was constant within 2%; however, between two nominally identical films, the grafting density could change by 20%. In the linear growth regime, the PDADMA coverage per deposition step is larger than in the parabolic growth regime (average thickness per PDADMA layer: 6 nm). Thus, the mean area per deposited PDADMA molecule is decreased (94 nm^2 instead of 125 nm^2). Since the grafting density of the pseudobrush is unchanged, one has to conclude that only 5% of the PDADMA molecules in the top layer provide the chains that form the pseudobrush.

In the parabolic growth regime, PDADMA-terminated films and PSS-terminated films showed similar force profiles at the ionic strength of film preparation (100 mM): a short-ranged attraction with a decay length shorter than the Debye length. At this ionic strength, the pseudobrush of PDADMA-terminated films consisting of 10.5 or more polycation/polyanion bilayers was collapsed (cf. Figure 6). The decay

length of the hydration force showed film-to-film variation (0.60 ± 0.23 nm, cf. Figure 6 and Tables 1 and 2). Note that

Table 2. Parameters Characterizing the Surface Forces of Different PDADMA-Terminated Multilayers Consisting of the Numbers of Bilayers, as Indicated at Salt Concentrations I_{NaCl} close to the Preparation Conditions (I_{NaCl} = 100 mM)[a]

multilayer		2.5 BL	10.5 BL	18.5 BL	20.5 BL
I_{NaCl} (mM)	Debye length κ^{-1} (nm)	κ^{-1} (nm)	κ^{-1} or D_H (nm)	κ^{-1} or D_H (nm)	κ^{-1} or D_H (nm)
100	0.96	0.96	0.25	**0.68**	0.45
1000	0.3		**0.52**		**0.37**

[a]In the second column, the theoretical Debye length κ^{-1} is given. If an attractive force on approach (and no evidence of an electrostatic or steric force) is found, the decay length D_H of the hydration or hydrophobic force curves is given in **bold**.

surface energy of an uncharged surface is less than that of a charged surface or of a pseudobrush. We wonder if this low surface energy is typical for asymmetrically grown polyelectrolyte multilayers.

■ DISCUSSION

The surface forces of polyelectrolyte multilayers consisting of strong polyelectrolytes, polycation PDADMA, and polyanion PSS were described. The system is intriguing and was subject to many studies.[26−28,34] Due to the smaller linear charge density of PDADMA (in absolute values), the PDADMA coverage per deposition step is larger than the one of PSS. Therefore, these polyelectrolyte multilayers grow asymmetrically. A few observations in our work are unexpected: (i) the surface charge density of a PSS terminated multilayer is −0.44 ± 0.28 mC m^{-2}, corresponding to one elementary charge per 360 nm^2. This is low compared to other data: PSS monolayer adsorbed onto latex particles showed a surface charge density of 2.6 mC m^{-2},[17] about 1 order of magnitude larger than the results presented here. There are two main reasons for the larger surface charge density of PSS: (i) PSS was adsorbed from salt-free solution (ii) and the surface charge density of latex particles was large (5.9 mC m^{-2}). Furthermore, polyelectrolyte multilayers grown of poly(allylamine) hydrochloride) (PAH) and PSS from ion-free solution showed similar large surface charge density, 2−3 mC m^{-2} (absolute values).[14,35] Note that PAH and PSS have the same linear charge density; thus, the surface coverage is the same and each adsorption step is accompanied by charge overcompensation.

The unusually small surface charge density discussed in the last paragraph occurs only when the salt concentration is low, beneath 50 mM NaCl. If the film consists of more than 10 BL, the polyelectrolyte multilayer is electrically neutral at 100 mM NaCl (preparation ionic strength). The force curves are reproducible after increasing/decreasing the salt concentration; therefore, the change in the surface charge is attributed to binding/unbinding of monovalent ions only. The conformation of the polymers in the film is not affected by the change of the measuring solution. At 50 mM NaCl and below, some bound Na$^+$ ions are dissolved, and the film is negatively charged, with a low surface charge density.

During multilayer preparation, at 15 ± 2 BL the transition from parabolic to linear growth regime occurs. Also, in the linear growth regime, at preparation conditions, the surface of

Langmuir

the film is electrically neutral. Only on decrease of the NaCl concentration below 50 mM, a surface charge is observed. Now, at lower salt concentrations, Cl^- ions are dissolved from the multilayer which is now positively charged. The surface charge density is again unusually low, 0.62 ± 0.22 mC m^{-2} (corresponding to one elementary charge per 260 nm^2).

This low surface charge density is attributed to the conformation of the PDADMA chains, which have a large surface coverage and form polyelectrolyte pseudobrushes on decrease of the ionic strength. We did not find a description of formation and structural characteristics of the complex between a polyelectrolyte brush and oppositely charged linear polyelectrolytes. The interaction of polyelectrolyte brushes and surfactants[36] is described, which is accompanied by a strong shrinking of the polyelectrolyte brush and by a decrease of the effective charge of the complexes, which may induce partial collapse of the brush, depending on the surfactant concentration and ionic strength. Similarly, the interaction of proteins and polyelectrolyte brushes is based on electrostatic attraction between the proteins and brush forming polyelectrolytes. The interaction is not only electrostatically driven, but also entropically driven, due to the release of monovalent ions from the brush.[37,38]

We suggest that PSS adsorption can be described as PSS uptake into a PDADMA layer with many loosely bound chains, which leads to a solidification of the multilayer surface. This is consistent with the observation of PDADMA-terminated multilayers: they are uncharged at preparation conditions; only hydration forces are observed. On the decrease of the ionic strength, a polyelectrolyte brush is found whose thickness can be varied by a factor of 4, following the expected scaling law. As observed before with the surface forces apparatus, the polyelectrolyte brush itself is uncharged.[21−23,32] Only a small fraction (5−7.5%) of the adsorbed polymers actually form the brush; most chains remain flatly adsorbed. The ends of the polymers are weakly bound; they form the brush.[23,32,39] On PSS adsorption, the surface charge density remains zero; however, within the brush, the composition is changed and many anions are released.

In the parabolic growth regime, PSS replaces all monovalent anions. However, in the linear growth regime, some monovalent anions remain. The composition of the multilayer does not affect the surface forces at preparation conditions (0.1 M). As the ionic strength decreases, monovalent ions are released from the film. Under these conditions, one can see which type of monomer is predominantly present on the surface.

The multilayer formation described in our experiments is reminiscent of a phenomenological description of the polyelectrolyte multilayer growth by Joseph B. Schlenoff and co-workers.[40] Film formation was characterized by two parameters, an overcompensation level and its decay length into the multilayer region, to describe the excess charge of the terminating layer, as distributed over several layers beneath. However, we find no excess charge at the surface; the overcompensation region is within the film. PSS, which adsorbs to the weakly bound PDADMA chains, is rather localized (a finding consistent with neutron reflectometry measurements[33]); possibly, the PDADMA chains burrow deeper into the film surface.

■ CONCLUSION AND OUTLOOK

Usually, the formation of electrostatically bound polyelectrolyte multilayers is described as "subsequent adsorption of oppositely charged polyelectrolytes", which in turn is accompanied by charge reversal after each adsorption step, as was indicated by streaming potential measurements.[2,14] Here we used an asymmetric system, where polycation and polyanion have different linear charge densities. Both polycation and polyanion are strong polyelectrolytes, but we did not observe charge reversal after each adsorption step. At high layer numbers (more than 10 BL) the multilayer surface was electrically neutral. Based on our observations, we suggest another mechanism: the polycation with its low linear charge density adsorbs with few loosely bound chains (which may form a polyelectrolyte brush on decrease of the ionic strength). When in the next step the polyanion layer adsorption occurs, the polyanion replaces monovalent anions, and the surface remains electrically neutral. Thus, on each adsorption step, many electrostatic monomer−monomer bonds are formed. The bond formation does not affect the surface charge, but the composition of the polyelectrolyte multilayer.

It is not clear if this mechanism is limited to asymmetric polycation/polyanion systems, such as PDADMA/PSS, or if it also happens if multilayers of symmetric polycation/polyanion systems are formed at high ionic strengths. Change of the pH causes a different linear charge density of polycation and polyanion, which in turn may induce a similar growth mechanism of the multilayer, as observed for PDADMA/PSS.

■ ASSOCIATED CONTENT

Ⓢ Supporting Information

The Supporting Information is available free of charge on the ACS Publications website at DOI: 10.1021/acs.langmuir.9b01787.

> The dependence of the surface potential of bare silica surfaces and PEI-coated silica surfaces on the NaCl concentration is shown in Tables S1 and S2, respectively. Table S3 gives the grafting density of those PDADMA chains that form a pseudobrush; Table S4 gives an overview about the occurrence of an approach/retreat hysteresis in force profiles. Figure S1 shows force profiles of a multilayer consisting 10 BL. Figure S2 shows the dependence of the surface charge density on the NaCl concentration for all PSS-terminated multilayers investigated (PDF)

■ AUTHOR INFORMATION

Corresponding Author

*E-mail: helm@uni-greifswald.de.

ORCID Ⓞ

Christiane A. Helm: 0000-0001-5181-1688

Notes

The authors declare no competing financial interest.

■ ACKNOWLEDGMENTS

■ DEDICATION

This article is dedicated to the memory of Jacob N. Israelachvili.

■ REFERENCES

(1) Decher, G. Fuzzy Nanoassemblies: Toward Layered Polymeric Multicomposites. *Science* **1997**, *277*, 1232−1237.

(2) Schönhoff, M. Self-assembled polyelectrolyte multilayers. *Curr. Opin. Colloid Interface Sci.* **2003**, *8*, 86−95.

(3) Szweda, R.; Tschopp, M.; Felix, O.; Decher, G.; Lutz, J. F. Sequences of Sequences: Spatial Organization of Coded Matter through Layer-by-Layer Assembly of Digital Polymers. *Angew. Chem., Int. Ed.* **2018**, *57* (48), 15817−15821.

(4) Mutschler, A.; Betscha, C.; Ball, V.; Senger, B.; Vrana, N. E.; Boulmedais, F.; Schroder, A.; Schaaf, P.; Lavalle, P. Nature of the Polyanion Governs the Antimicrobial Properties of Poly(arginine)/Polyanion Multilayer Films. *Chem. Mater.* **2017**, *29* (7), 3195−3201.

(5) Guillot, R.; Pignot-Paintrand, I.; Lavaud, J.; Decambron, A.; Bourgeois, E.; Josserand, V.; Logeart-Avramoglou, D.; Viguier, E.; Picart, C. Assessment of a polyelectrolyte multilayer film coating loaded with BMP-2 on titanium and PEEK implants in the rabbit femoral condyle. *Acta Biomater.* **2016**, *36*, 310−322.

(6) Borges, J.; Mano, J. F. Molecular Interactions Driving the Layer-by-Layer Assembly of Multilayers. *Chem. Rev.* **2014**, *114* (18), 8883−8942.

(7) Israelachvili, J. N.; Adams, G. E. Measurement of Forces between 2 Mica Surfaces in Aqueous-Electrolyte Solutions in Range 0−100 nm. *J. Chem. Soc., Faraday Trans. 1* **1978**, *74*, 975.

(8) Israelachvili, J. N. *Intermolecular and Surface Forces.*, 3rd ed.; Academic Press: London, 2011.

(9) Israelachvili, J. N.; Wennerstrom, H. Role of hydration and water structure in biological and colloidal interactions. *Nature* **1996**, *379* (6562), 219.

(10) Alexander, S. Adsorption of chain molecules with a polar head: a scaling description. *J. Phys. (Paris)* **1977**, *38* (8), 983−987.

(11) de Gennes, P. Conformations of polymers attached to an interface. *Macromolecules* **1980**, *13* (5), 1069−1075.

(12) Israelachvili, J. N.; Pashley, R. M. Measurement of the Hydrophobic Interaction between Two Hydrophobic Surfaces in Aqueous Electrolyte Solutions. *J. Colloid Interface Sci.* **1984**, *98*, 500−514.

(13) Donaldson, S. H.; Royne, A.; Kristiansen, K.; Rapp, M. V.; Das, S.; Gebbie, M. A.; Lee, D. W.; Stock, P.; Valtiner, M.; Israelachvili, J. Developing a General Interaction Potential for Hydrophobic and Hydrophilic Interactions. *Langmuir* **2015**, *31* (7), 2051−2064.

(14) Lowack, K.; Helm, C. Molecular mechanisms controlling the self-assembly process of polyelectrolyte multilayers. *Macromolecules* **1998**, *31* (3), 823−833.

(15) Van de Steeg, H. G. M.; Cohen Stuart, M. A.; De Keizer, A.; Bijsterbosch, B. H. Polyelectrolyte adsorption: a subtle balance of forces. *Langmuir* **1992**, *8*, 2538−2546.

(16) Berndt, P.; Kurihara, K.; Kunitake, T. Adsorption of Poly(styrenesulfonate) onto an Ammonium Monolayer on Mica: A Surface Forces Study. *Langmuir* **1992**, *8* (10), 2486−2490.

(17) Szilágyi, I.; Trefalt, G.; Tiraferri, A.; Maroni, P.; Borkovec, M. Polyelectrolyte adsorption, interparticle forces, and colloidal aggregation. *Soft Matter* **2014**, *10* (15), 2479−2502.

(18) Borisov, O. V.; Zhulina, E. B.; Birshtein, T. M. Diagram of the States of a Grafted Polyelectrolyte Layer. *Macromolecules* **1994**, *27* (17), 4795−4803.

(19) Zhulina, E. B.; Birshtein, T. M.; Borisov, O. V. Theory of Ionizable Polymer Brushes. *Macromolecules* **1995**, *28* (5), 1491−1499.

(20) Ahrens, H.; Förster, S.; Helm, C. A. Charged Polymer Brushes: Counterion Incorporation and Scaling Relations. *Phys. Rev. Lett.* **1998**, *81*, 4172−4175.

(21) Balastre, M.; Li, F.; Schorr, P.; Yang, J.; Mays, J. W.; Tirrell, M. V. A study of polyelectrolyte brushes formed from adsorption of amphiphilic diblock copolymers using the surface forces apparatus. *Macromolecules* **2002**, *35* (25), 9480−9486.

(22) Liberelle, B.; Giasson, S. Friction and normal interaction forces between irreversibly attached weakly charged polymer brushes. *Langmuir* **2008**, *24* (4), 1550−1559.

(23) Block, S.; Helm, C. A. Conformation of poly (styrene sulfonate) layers physisorbed from high salt solution studied by force measurements on two different length scales. *J. Phys. Chem. B* **2008**, *112* (31), 9318−9327.

(24) Block, S.; Helm, C. A. Equilibrium and nonequilibrium features in the morphology and structure of physisorbed polyelectrolyte layers. *J. Phys. Chem. B* **2011**, *115* (22), 7301−7313.

(25) Block, S.; Helm, C. A. Measurement of long-ranged steric forces between polyelectrolyte layers physisorbed from 1 M NaCl. *Phys. Rev. E* **2007**, *76* (3), 030801.

(26) Fu, J.; Schlenoff, J. B. Driving forces for oppositely charged polyion association in aqueous solutions: enthalpic, entropic, but not electrostatic. *J. Am. Chem. Soc.* **2016**, *138* (3), 980−990.

(27) Ghostine, R. A.; Markarian, M. Z.; Schlenoff, J. B. Asymmetric Growth in Polyelectrolyte Multilayers. *J. Am. Chem. Soc.* **2013**, *135* (20), 7636−7646.

(28) Nestler, P.; Passvogel, M.; Helm, C. A. Influence of Polymer Molecular Weight on the Parabolic and Linear Growth Regime of PDADMAC/PSS Multilayers. *Macromolecules* **2013**, *46* (14), 5622−5629.

(29) Butt, H.-J.; Kappl, M. *Surface and Interfacial Forces*; Wiley-VCH, 2010.

(30) Hunter, R. J. *Foundations of Colloid Science*; Oxford Science Publications: New York, 1992; Vols. I and II.

(31) Kulcsar, A.; Lavalle, P.; Voegel, J. C.; Schaaf, P.; Kekicheff, P. Interactions between two polyelectrolyte multilayers investigated by the surface force apparatus. *Langmuir* **2004**, *20* (2), 282−286.

(32) Block, S.; Helm, C. A. Single polyelectrolyte layers adsorbed at high salt conditions: Polyelectrolyte brush domains coexisting with flatly adsorbed chains. *Macromolecules* **2009**, *42* (17), 6733−6740.

(33) Soltwedel, O.; Ivanova, O.; Nestler, P.; Müller, M.; Köhler, R.; Helm, C. A. Interdiffusion in polyelectrolyte multilayers. *Macromolecules* **2010**, *43* (17), 7288−7293.

(34) Lappan, U.; Rau, C.; Naas, C.; Scheler, U. Odd-Even Effect on Rotational Dynamics of Spin-Labeled Polyacid Chain Segments in Polyelectrolyte Multilayers. *Macromolecules* **2019**, *52* (6), 2384−2392.

(35) Donath, E.; Walther, D.; Shilov, V. N.; Knippel, E.; Budde, A.; Lowack, K.; Helm, C. A.; Möhwald, H. The Nonlinear Hairy Layer Theory of Electrophoretic Fingerprinting Applied to Concecutive Layer by Layer Polyelectrolyte Adsorption onto Charged Polystyrene Latex Particles. *Langmuir* **1997**, *13*, 5294−5305.

(36) Samokhina, L.; Schrinner, M.; Ballauff, M.; Drechsler, M. Binding of oppositely charged surfactants to spherical polyelectrolyte brushes: A study by cryogenic transmission electron microscopy. *Langmuir* **2007**, *23* (7), 3615−3619.

(37) Cooper, C. L.; Dubin, P. L.; Kayitmazer, A. B.; Turksen, S. Polyelectrolyte-protein complexes. *Curr. Opin. Colloid Interface Sci.* **2005**, *10* (1−2), 52−78.

(38) Wang, X.; Zheng, K.; Si, Y.; Guo, X.; Xu, Y. Protein−Polyelectrolyte Interaction: Thermodynamic Analysis Based on the Titration Method. *Polymers* **2019**, *11* (1), 82.

(39) Johansson, E.; Blomberg, E.; Wågberg, L. Adhesive interaction between polyelectrolyte multilayers of polyallylamine hydrochloride and polyacrylic acid studied using atomic force microscopy and surface force apparatus. *Langmuir* **2009**, *25* (5), 2887−2894.

(40) Dubas, S. T.; Schlenoff, J. B. Factors controlling the growth of polyelectrolyte multilayers. *Macromolecules* **1999**, *32*, 8153−8160.

Article 5

Enhancement of Intracellular Calcium Ion Mobilization by Moderately but Not Highly Positive Material Surface Charges

Gruening, M., **Neuber, S.**, Nestler, P., Lehnfeld, J., Dubs, M., Fricke, K., & Nebe, J. B.

Frontiers in bioengineering and biotechnology

Volume 8 (2020) Article 1016

The article was originally published in Frontiers in bioengineering and biotechnology: Gruening, M., **Neuber, S.**, Nestler, P., Lehnfeld, J., Dubs, M., Fricke, K., ... & Nebe, J. B. (2020). Enhancement of Intracellular Calcium Ion Mobilization by Moderately but Not Highly Positive Material Surface Charges. *Frontiers in bioengineering and biotechnology*, *8*, 1016.

Enhancement of Intracellular Calcium Ion Mobilization by Moderately but Not Highly Positive Material Surface Charges

Martina Gruening[1], Sven Neuber[2], Peter Nestler[2], Jutta Lehnfeld[3], Manuela Dubs[4], Katja Fricke[5], Matthias Schnabelrauch[4], Christiane A. Helm[2], Rainer Müller[3], Susanne Staehlke[1] and J. Barbara Nebe[1,6]*

[1] Department of Cell Biology, Rostock University Medical Center, Rostock, Germany, [2] Soft Matter and Biophysics, Institute of Physics, University of Greifswald, Greifswald, Germany, [3] Colloid and Interface Chemistry, Institute of Physical and Theoretical Chemistry, University of Regensburg, Regensburg, Germany, [4] Department of Biomaterials, INNOVENT e.V., Jena, Germany, [5] Leibniz Institute for Plasma Science and Technology e.V. (INP), Greifswald, Germany, [6] Department Science and Technology of Life, Light and Matter, Faculty of Interdisciplinary, University of Rostock, Rostock, Germany

Electrostatic forces at the cell interface affect the nature of cell adhesion and function; but there is still limited knowledge about the impact of positive or negative surface charges on cell-material interactions in regenerative medicine. Titanium surfaces with a variety of zeta potentials between -90 mV and $+50$ mV were generated by functionalizing them with amino polymers, extracellular matrix proteins/peptide motifs and polyelectrolyte multilayers. A significant enhancement of intracellular calcium mobilization was achieved on surfaces with a moderately positive ($+1$ to $+10$ mV) compared with a negative zeta potential (-90 to -3 mV). Dramatic losses of cell activity (membrane integrity, viability, proliferation, calcium mobilization) were observed on surfaces with a highly positive zeta potential ($+50$ mV). This systematic study indicates that cells do not prefer positive charges in general, merely moderately positive ones. The cell behavior of MG-63s could be correlated with the materials' zeta potential; but not with water contact angle or surface free energy. Our findings present new insights and provide an essential knowledge for future applications in dental and orthopedic surgery.

Keywords: human osteoblasts, calcium ion signaling, titanium surface modification, amino polymer, polyelectrolyte multilayer, zeta potential, surface charge, wettability

INTRODUCTION

Bone defects due to fractures, infections or tumor resections are one of the main causes of disability in an aging society, leading to a loss of quality of life (Akter and Ibanez, 2016). In orthopedic applications, titanium (Ti) has been and still is the material of choice due to properties such as high strength and corrosion resistance (Hanawa, 2019). To improve the bioactivity of Ti-based materials, several strategies are used, including physical treatments to modify the topography (Wennerberg and Albrektsson, 2009; Nikkhah et al., 2012; Kumar et al., 2019) or chemical treatments to modify the bioactivity (Kokubo and Yamaguchi, 2015; Muderrisoglu et al., 2018; Devgan and Sidhu, 2019) all aiming to optimize the interaction with osteoblastic cells.

Surface properties are one of the main factors influencing the cells' fate by guiding cellular processes at the interface from the very beginning (Felgueiras et al., 2018; Ferrari et al., 2019). As a result, the advanced cell-material interaction is a pivotal step determining the success of osseointegration, ultimately, the success of implants. Initial processes driven by the surface properties involve cellular attachment, adhesion and spreading (von der Mark and Park, 2013), which further affect other cell activities such as proliferation, differentiation (Bacakova et al., 2011), and intracellular signaling (Anselme et al., 2010; Staehlke et al., 2015, 2018). Stimulating cellular behavior at the interface by acting on surface physico-chemical properties, especially roughness, stiffness, wettability, and surface charge via surface functionalization can be an effective way to improve bone regeneration (Ferrari et al., 2019).

Previous research has shown that osteoblasts favor a certain range of roughness, pore size, wettability, specific biomacromolecules or their biomimetic motifs (Chen et al., 2018) and also stiffness (Abalymov et al., 2020). It could be demonstrated that cells prefer moderately hydrophilic surfaces displaying contact angles between 40° and 65° (Bacakova et al., 2011; Rebl et al., 2012; Mörke et al., 2017). However, other studies have shown that this is not always the case; for instance MG-63 osteoblasts exhibited increased cell attachment and spreading on methylated silicon surfaces with decreasing wettability (Padial-Molina et al., 2011). Similarly, Kennedy et al. (2006) reported that MC3T3-E1 cells displayed improved cell proliferation with increased hydrophobicity and the lowest spreading on the most hydrophilic SAM (self-assembled monolayers) surface. Thus, the contact angle is not a good predictor of cell behavior (Gentleman and Gentleman, 2014).

Furthermore, it has been proven that extracellular matrix (ECM) proteins (mainly collagen, fibronectin, laminin and vitronectin) (Müller et al., 2006; Rico et al., 2009; Chen et al., 2018), their RGD sequence (Arg-Gly-Asp) (Mörke et al., 2017) and cytokines [e.g., basic fibroblast growth factor (bFGF)] (Cao et al., 2015) have the capacity to promote cell attachment.

Some explanations have also been suggested for the surface charge and its effect on the cell-material interaction. Surface charges can generate electrical cues necessary to regulate cell function (De Aza et al., 2003; Finke et al., 2007; Fernández-Yagüe et al., 2019). As human osteoblasts are negatively charged

(Rebl et al., 2016), positive surface charges significantly influence cell adhesion (Rebl et al., 2010; Dhowre et al., 2015; Mörke et al., 2017), spreading and proliferation (Staehlke et al., 2019), particularly in the early stages of cell responses. The most detailed study on the effect of surface charges to date is that of Metwally and Stachewicz (2019), indicating a great importance in the development of functionally implantable biomaterials. They reviewed that surface charges determine protein adsorption and thus the subsequent cell adhesion process. Referring to Goldenberg and Steinberg (2010) surface charge seems to be also important for the correct protein localization of signaling molecules in the cell membrane; it has been documented that proteins like GTPases of the Ras, Rho, Arf, and Rab protein families target the plasma membrane through electrostatic interactions (Heo et al., 2006).

The measurement of zeta (ζ) potentials is a suitable technique for characterizing the charging behavior at the solid-liquid interface of modified biomaterial surfaces (Ferraris et al., 2018). There are few papers that address materials such as hydrogels (Schulz et al., 2018), polyelectrolyte multilayers (PEM) (Guo et al., 2018) or metals (Ponsonnet et al., 2003; Nebe et al., 2007) exhibiting a positive ζ-potential enhancing cell processes like cell adhesion, spreading, viability and proliferation. And yet present understanding of the mechanism involved in controlling cell activities via surface charge in tissue engineering is still limited.

In order to gain deeper insights into the impact of surface charges on the cell-material interaction, systematic experiments are required. Our previous work has shown that a plasma polymerized nanolayer of allylamine (PPAAm) provides positive charges on an otherwise negatively charged Ti surface that can boost cell behavior (reviewed in Nebe et al., 2019). The question arose whether a positive ζ-potential is generally considered to be a decisive factor for the cellular outcome.

In the present study, we generated a broad range of surface charges to investigate in detail their influence on osteoblastic cell response via intracellular calcium ion (Ca^{2+}) mobilization, cell viability and proliferation. For this purpose, we deposited nine different top layers on Ti substrates from the following three categories: (i) amino polymers, (ii) ECM/peptide motifs, and (iii) PEM. We determined the physico-chemical characterization of these surfaces via water contact angles (WCA), surface free energies (SFE), X-ray photoelectron spectroscopy (XPS) and layer thicknesses, and employed ζ-potential measurements to determine surface charges.

We hypothesize that cell physiology can be improved by material surfaces featuring a certain range of positive ζ-potential.

MATERIALS AND METHODS

Functionalization of Titanium Arrays

The following section describes the methods for the diverse Ti surface modifications used for surface charge determination and in the cell biological experiments shown in **Figure 1**. They are categorized in modifications with amino polymers, ECM/peptide motifs, as well as in PEM. As base material and negative control we used planar silicon arrays sputtered

FIGURE 1 | Chemical surface modifications of plane Ti arrays. The modifications can be classified into three groups: amino polymers, extracellular matrix (ECM)/peptide motifs and polyelectrolyte multilayers (PEM). Please note that the molecular structures are schematic formula drawings (created using the freeware ACD/ChemSkretch 2018.2.5, Advanced Chemistry Development, Toronto, ON, Canada), which do not necessarily allow conclusions about the molecular length of the individual layers. Ti, titanium; Col I, collagen-type I; RGD, peptide sequence Arg-Gly-Asp; PPAAm, plasma polymerized allylamine; PEI, poly(ethylene imine); PPI-G4, poly(propylene imine) dendrimer generation 4; APTES, (3-aminopropyl)triethoxysilan; PSS, poly(styrene sulfonate); PDADMA, poly(diallyldimethylammonium chloride); HSPG, heparan sulfate proteoglycans; Lam, laminin; Ent, entactin; Col IV, collagen-type IV; PAH, poly(allylamine hydrochloride).

with 100 nm Ti particles obtained from the Center for Microtechnologies (ZFM, University of Technology Chemnitz, Germany) at $1 \times 1 \times 0.075$ cm in size (length $\times$ width $\times$ depth) for cell analysis, or $2 \times 1 \times 0.075$ cm for ζ-potential analysis as previously reported (Staehlke et al., 2018).

Amino Polymers
Plasma polymerized allylamine (PPAAm)
As it is known that the positively charged plasma polymerized allylamine (PPAAm) layer can improve several cell functions (Rebl et al., 2012; Mörke et al., 2017; Staehlke et al., 2018;

Nebe et al., 2019), this plasma functionalization of Ti was used as a positive control in all experiments. The specimens were coated with the PPAAm nanolayer by using a low-pressure plasma reactor (V55G, Plasma Finish, Germany) (Rebl et al., 2012) with the following parameters: continuous wave oxygen/argon plasma (500 W, 50 Pa, 1000-sccm O_2, 5 sccm Ar, 60 s), 480 s PPAAm deposition time. PPAAm films have proven to be very robust according to DIN EN 582 (1993), mechanically stable (Fritsche et al., 2009) and can be used for cell experiments for up to 200 days when stored in ambient air (Finke et al., 2014).

(3-Aminopropyl)triethoxysilane (APTES)

Ti surfaces were modified with the linker (3-aminopropyl)triethoxysilane (APTES) (Mörke et al., 2017). Prior to modification, the substrates were cleaned and pre-activated by water vapor plasma treatment for 15 s at 0.1 mbar in a microwave. Then, Ti surfaces were coated with 100 mM APTES (abcr, Karlsruhe, Germany) in toluene (Alfa Aesar/Fisher Scientific, Kandel, Germany) for 3 h at 60°C in an incubator (GFL 3032, Burgwedel, Germany) turning at 35 rpm. After carefully washing with ultrapure water, the samples were dried under a stream of pure nitrogen (ultra-high purity 5.0 grade) in a laminar flow box (Herasafe KS 12, Kendro, Langenselbold, Germany). APTES layers are stable up to 1 year when stored under exclusion of light and oxygen.

Poly(ethylene imine) (PEI)

Before functionalization, contaminants were removed from the substrate surface by sonicating in acetone (p.a., Sigma-Aldrich Chemie, Taufkirchen, Germany), followed by oxidation of the substrates in a semi-concentrated HNO_3 solution (38%, 1:1 v/v from concentrated ($\geq$ 65%) nitric acid, obtained from Carl Roth, Karlsruhe, Germany) for 1 week. The wafers were rinsed with ultrapure and sterile water multiple times until a neutral pH was obtained, then dried in a vacuum desiccator (Carl Roth). As described in previous publications, further modification steps were performed under an argon atmosphere in anhydrous solvents (dried with a molecular sieve from Carl Roth) (Eichler et al., 2011; Katzur et al., 2012). The synthesis of carboxylic acid-terminated SAM (SAM-COOH) is based on the protocol by Liu et al. (2002) and was described previously (Katzur et al., 2012). Here, the silanization in a 7-octenyltrichlorosilane solution was carried out for 2 h, the conversion of the terminal alkene groups in a $KMnO_4$ solution for 15 min.

For the immobilization of the poly(ethylene imine) (PEI) polymer, the SAM-COOH-modified substrates were first activated via immersion in a solution containing 100 mmol/l N-(3-dimethylaminopropyl)-N'-ethylcarbodiimide hydrochloride (EDC) and 100 mmol/l N-hydroxysuccinimide (NHS) in 0.1 mol/l 2-(N-morpholino) ethanesulfonic acid (sodium salt) (MES) buffer (pH adjusted to 5.4) for 2 h at room temperature (RT). EDC, NHS and MES were purchased from Sigma-Aldrich Chemie of analytical grade. After rinsing once with MES buffer, twice with water and once with methanol (p.a., Fischer Scientific, Schwerte, Germany), the immobilization of the polymer was carried out in a 10 mg/ml PEI solution (linear, Mw = 25 kDa, abcr, Karlsruhe, Germany) in a methanol/water mixture (9:1 v/v) for 1.5 h at RT. Excess polymer was removed by rinsing twice with the methanol/water mixture and once with methanol before the specimens were dried in a desiccator. PEI layers are stable for up to 8 weeks when stored in the dark and under argon atmosphere.

Poly(propylene imine) dendrimer (PPI-G4)

In respect to the functionalization with PEI described above, the surfaces were first cleaned by sonication and then oxidized for 1 week. Then a silanization of substrates with 3-(triethoxysilyl)propyl succinic acid anhydride (TESPSA, abcr,

Karlsruhe, Germany) was performed according to previously published protocols (Eichler et al., 2011) at elevated temperatures (110°C for 30 min, followed by 130°C for 10 min) under an argon atmosphere. Excess silane was removed by rinsing twice with dry toluene. The specimens were sonicated once with dry dimethyl sulfoxide (DMSO, Fisher Scientific, Schwerte, Germany) and immersed in a 0.5 mmol/l poly(propylene imine) dendrimer generation 4 (PPI-G4, SyMO-Chem, Eindhoven, Netherlands) solution in anhydrous DMSO. The reaction was performed for at least 40 h at RT. Rinsing was performed by sonicating once with DMSO and at least three times with methanol before drying the wafers in a desiccator. PPI-G4 layers are stable for up to 8 weeks when stored in the dark and under argon atmosphere.

Extracellular Matrix (ECM) Proteins and Peptide Motifs

Collagen type-I (Col I)

Ti substrates were chemically wet-coated with 40 µg/cm² collagen type-I (Col I; rat tail, Corning, Discovery Labware, Bedford, MA, United States) and dried overnight at RT (Rebl et al., 2010). Residues of acetic acid were removed by rinsing twice with sterile ultrapure water. Col I coatings were produced prior to cell experiments and used directly.

Basement membrane matrix (Matrigel)

Ti arrays were coated with basement membrane matrix (Matrigel) containing laminin, collagen type-IV, heparan sulfate proteoglycans, entactin and growth factors (Corning, Discovery Labware, Bedford, MA, United States) using a thin-film coating method. For this purpose, Matrigel was thawed on ice and diluted to a concentration of 1 mg/ml using serum-free ice-cold Dulbecco's Modified Eagle Medium (DMEM, 21063-029, Life Technologies Limited, Paisley, United Kingdom). 200 µl of the solution was added to the Ti substrates (200 µg/cm²) with pre-cooled pipette tips and incubated at RT for 1 h under sterile conditions. Unbound material was aspirated and substrates were rinsed gently using serum-free DMEM. Matrigel coatings were produced prior to cell experiments and used directly.

Arginine-glycine-aspartic sequence (RGD)

Ti surfaces were modified with a nonapeptide containing the arginine-glycine-aspartic acid (RGD)-tripeptide (complete amino acid sequence C-Y-G-G-R-G-D-T-P, kindly provided by Dr. K. Rischka, Fraunhofer IFAM Institute Bremen, Germany) as reported in Mörke et al. (2017). Prior to peptide coupling Ti substrates was coated with APTES as described above. RGD layers are stable up to 1 year when stored under exclusion of light and oxygen.

Polyelectrolyte Multilayers (PEM)

Polyelectrolyte multilayer films were created by dip-coating of oppositely charged polyelectrolytes with a deposition robot (Riegler & Kirstein, Potsdam, Germany) according to Mohamad et al. (2019). Here, we used PEI [branched, Mw = 750 kDa, polydispersity (PDI) = 12.5], polyallylamine hydrochloride (PAH, Mw = 50–60 kDa) and poly(diallyldimethylammonium chloride) (PDADMA, Mw = 322 kDa, PDI = 2.19) as polycations and

poly(styrene sulfonate) sodium salt (PSS, M_w = 666 kDa, PDI < 1.2) as polyanion.

PSS-terminated PEM consisted of three double layers with the sequence PEI/PSS/(PAH/PSS)₂. PDADMA-terminated polyelectrolyte brushes were composed of 10.5 double layers with the sequence PEI/PSS/(PDADMA/PSS)₉/PDADMA. The layer stability of prepared PEM was verified by AFM measurements [DI Multimode AFM using NanoScope IIIa software from Veeco (Santa Barbara, CA, United States)]. Layers are stable in the range of pH 3–11, in solutions up to 1 M NaCl and after storage in ambient air up to 1 year unchanged.

Surface Characterization
Zeta Potential
ζ-potentials were assessed with the SurPASS™ system (Anton Paar, Ostfildern, Germany) and the associated software Attract 2.1 as previously published (Staehlke et al., 2018). Streaming potentials were measured at pH 6.5–8.0 in a 1 mM KCl solution (VWR International, Darmstadt, Germany) and ζ-potentials at pH 7.4 were calculated via a linear regression using the software GraphPad Prism version 6.05 (n = 3, three pairs of samples).

Surface Wettability
Surface free energies of the substrate/air interface and WCA were determined by the sessile drop method using the Drop Shape Analyzer—DSA25 (Krüss, Hamburg, Germany) (Staehlke et al., 2018). One µl drops of distilled water and diiodomethane (Sigma-Aldrich Chemie, Taufkirchen, Germany) were deposited on the sample surface (n = 3 at 3 drops each). WCA values were calculated with the supplied software (ADVANCE, V.1.7.2.1, Krüss, Hamburg, Germany) via the Young's equation and the SFE according to Owens, Wendt, Rabel und Kaelble (OWRK).

Layer Thickness
Layer thickness was measured with null ellipsometry (Multiskop; Optrel GbR, Sinzing, Germany) as described before (Mörke et al., 2017). Each sample was modeled by 6 slabs in order to account for oxide layers (Si, SiO₂, Ti, TiO₂, layer of interest and ambient air). The thickness of the Ti and TiO₂ layer was determined independently prior to deposition of the layer of interest. Additionally, uncoated samples were measured and served as a reference. Each measurement was carried out at several angles of incidence (50°−80° in 1° steps) in two different ellipsometric zones (Nestler et al., 2012).

Chemical Composition
The elemental composition of the modified surfaces was analyzed by using an AXIS Supra X-ray photoelectron spectrometer from Kratos Analytical Ltd. (Manchester, United Kingdom). Measurements were performed using a monochromatic Al Kα X-ray source (1486.6 eV) operated at 150 W. Survey and core-level spectra were acquired using a pass energy of 80 eV. For each sample, an area of 250 µm was analyzed in duplicates on three different positions. During the analysis, the integrated charge neutralization system was activated for charge compensation. XPS measurements for PEI and PPI-G4 were performed with a PHI 5700 (Physical Electronics, United States). Here, survey and core-level spectra were acquired using pass energies of 117–187 eV. Charge neutralization was not necessary.

Cell Biological Investigations
Cell Culture
Human osteoblast-like MG-63 cells (American Type Culture Collection ATCC®, CRL1427™, Bethesda, MD, United States) were used; this cell line has been successfully applied as a model for studying cell-material interactions (Staehlke et al., 2019) and has similar characteristics to primary human osteoblasts (Clover and Gowen, 1994; Czekanska et al., 2014). The cells were cultured in Dulbecco's Modified Eagle Medium (DMEM, 31966-021, Life Technologies Limited, Paisley, United Kingdom), with 10% fetal calf serum (FCS, Biochrom FCS Superior, Merck, Darmstadt, Germany) and 1% antibiotics (gentamicin, Ratiopharm, Ulm, Germany) at 37°C with 5% CO₂/95% air atmosphere (Staehlke et al., 2018). All experiments were performed in passages 5–30, as the MG-63 cell physiology is known to remain stable over the entire range of these passages (Staehlke et al., 2019).

Cell Morphology
Scanning electron microscopy (SEM)
MG-63s (15,000 cells/cm²) were cultured for 24 h on the Ti arrays, washed three times with phosphate buffered saline (PBS, Sigma-Aldrich Chemie, Taufkirchen, Germany), fixed with 2.5% glutardialdehyde (Merck, Darmstadt, Germany) at 4°C overnight and rinsed with 0.1% sodium phosphate buffer (according to Sørensen, Merck, Darmstadt, Germany). The samples were then dehydrated through an ethanol series of 30, 50, 75, 90 and twice 100% (for 5, 5, 15, 10, and 10 min, respectively) and dried in a critical point dryer (K 850, EMITECH, Taunusstein, Germany). The samples were sputtered with gold for 50 s (15 nm, SCD 004, BAL-TEC, Wetzlar, Germany) and field emission scanning electron microscopy (FE-SEM, ZEISS Merlin VP compact, Carl Zeiss, Oberkochen, Germany) observations were taken with an acceleration voltage of 5 kV, a working distance of 5.6 mm and a high efficiency secondary electron detector (InlenseDuo for 2,000x, HE-SE2 detector for 100, 500x, and 5,000x).

Circularity
The circularity of the cells after 24 h could be evaluated with Photoshop CC 2017 using fluorescence microscopic images of fluoro-3-acetoxymethyl ester (fluo-3) stained cells ($n \geq 3$ independent experiments á 15 cells). These images were also used for determining the cell area as basic values for the Ca²⁺ mobilization experiments (**Supplementary Table S1**). For the staining procedure see section "Intracellular Ca²⁺ mobilization." A circularity value of 1.0 represents a perfect circle, whereas a value converging toward 0 indicates an elongated polygon.

Cell Viability
Cell viability was analyzed by an MTS assay, flow cytometry (both described in the **Supplementary Material**) and live/dead staining for selective surfaces representing negative, moderately and 2x highly positive surface charges (Ti, PPAAm, PPI-G4, and PDADMA, respectively). For live/dead staining a cell viability kit (L3224, Molecular Probes, Eugene, OR, United States)

was used. This two-color fluorescence assay is based on the measurement of intracellular esterase activity of living cells (Calcein-acetoxymethyl ester, Calcein-AM) and the abrogation of the plasma membrane integrity of dead cells (Ethidium homodimer-1, EthD-1). While EthD-1 is excluded by the intact plasma membrane of living cells, it can enter cells with damaged cell membrane and binds to nucleic acids. After a cultivation period of 24 h MG-63s (80,000 cells/cm²) were washed carefully with PBS and incubated with a Calcein-AM/EthD-1 solution (1:1, 2 µM Calcein-AM, 4 µM EthD-1) for 20 min at 37°C in the dark. The cells were then rinsed with PBS and fixed with 4% paraformaldehyde (PFA, Sigma-Aldrich Chemie, Taufkirchen, Germany) at RT for 10 min. Samples were embedded on a coverslip with mounting medium Fluoroshield$^{\text{TM}}$ (Sigma-Aldrich Chemie, Taufkirchen, Germany) containing 4′,6-diamidino-2-phenylindole (DAPI) and examined using the confocal laser scanning microscope LSM780 (Carl Zeiss, Jena, Germany) with a Plan-Apochromat 63x oil immersion objective (Carl Zeiss; zoom 1 and 2.5) and the ZEN software (ZEISS efficient navigation, ZEN 2011 SP4, black edition, Carl Zeiss).

Intracellular Ca²⁺ Mobilization

Pre-screening study

The Ca²⁺ mobilization process in MG-63s was specified with respect to the adenosine 5′-triphosphate (ATP) concentration for cell stimulation, Ca²⁺ origin and the presence of ATP receptors as provided in the **Supplementary Material**. The basal Ca²⁺ signal of MG-63s on Ti and PPAAm controls was validated by immunofluorescence. Therefore, 50,000 cells/cm² were stained after 1 h with the Ca²⁺ indicator fluo-3 (5 µM, Life Technologies Corporation, Eugene, OR, United States) (Staehlke et al., 2015, 2018), Hoechst 33342 (1:1000, Life Technologies Corporation) and for images after 24 h additionally with 20 µl BacMam 2.0 reagent (CellLight$^{\text{TM}}$ actin-RFP, Life Technologies Corporation) at 37°C in isotonic 4-(2-hydroxyethyl)-1-piperazineethanesulfonic acid buffer (HEPES) (Staehlke et al., 2015, 2018). Confocal laser scanning microscopy (LSM780, Carl Zeiss, Jena, Germany) was carried out with a Plan-Apochromat 63x oil immersion objective (Carl Zeiss, 1.40. Oil DIC M27) and the ZEN software (ZEISS efficient navigation, ZEN 2011 SP4, black edition, Carl Zeiss).

Ca²⁺ mobilization

Ca²⁺ mobilization experiments on different Ti surface modifications were performed according to Staehlke et al. (2015, 2018). In brief, 80,000 cells/cm² were seeded onto the samples for 24 h and then loaded with 5 µM fluo-3 in Ca²⁺ containing HEPES buffer via a hypo-osmotic shock treatment. Ca²⁺ fluorescence signals of 10 single cells per surface over a time span of 480 s were recorded with a confocal laser scanning microscope LSM780 and the ZEN software (ZEN 2011 SP4, black edition) with the following settings: scan mode 'time series' (1 frame every 2 s, 240 frames in total), maximum pinhole (15 airy unit, 13.5 µm section), gain 632, digital offset −3. First, the basal Ca²⁺ signal was recorded for 180 s. Then, the cells were stimulated with ATP (0.5 mM, SERVA Electrophoresis, Heidelberg, Germany), which indicates the reactivity of vital

cells in dependence of the underlying chemical layer. At least three independent experiments per modification with 10 cells each for 240 analysis points per cell were investigated (=7,200 records per surface modification). The mean fluorescence intensity of the single cells (MFI$_{\text{C}}$) was evaluated with the ZEN2 software (blue edition, version 2.0.0.0, Carl Zeiss). For this purpose, ten defined boxes were positioned on randomly chosen cells in the first image of the time series (one box per cell). Using the function 'mean ROI' (region of interest), the software analyzed the MFI of the boxes (MFI$_{\text{ROI}}$) for 240 time points per cell. However, the MFI$_{\text{ROI}}$ represents only a small sub-area of a cell (**Supplementary Figure S4**). Compared with a flat expanded cell, the Ca²⁺ signal of a spherical cell (more cell volume under limited area as cell height is larger) is concentrated on a smaller area, which leads to increased MFI$_{\text{ROI}}$ values. Therefore, the MFI$_{\text{ROI}}$ values were normalized to the mean area of cells after 24 h (A$_{\text{C}}$) and the defined area of ROI (A$_{\text{ROI}}$), assuming that MFI$_{\text{ROI}}$ is independent of the ROI position in the cell. Accordingly, the A$_{\text{C}}$ of 15 fluo-3 stained cells per surface were measured with the software Photoshop CC 2017 (*n* = 3 independent experiments, **Supplementary Table S1**). The MFI$_{\text{C}}$ is described in the form:

$$MFI_c = MFI_{ROI} \times \frac{A_c}{A_{ROI}}$$

where MFI$_{\text{C}}$ is the mean fluorescence intensity of cells at 0–480 s, MFI$_{\text{ROI}}$ is the mean fluorescence intensity of the region of interest (ROI), A$_{\text{C}}$ is the mean area of cells after 24 h (µm²), and A$_{\text{ROI}}$ is the defined area of ROI (100 µm²). To calculate the mean *basal* fluorescence intensity of a cell (MFI$_{\text{B}}$), MFI$_{\text{ROI}}$ values of 0–170 s were used. In order to determine the MFI *after* ATP stimulation (MFI$_{\text{A}}$), MFI$_{\text{ROI}}$ values of 190–240 s were employed. The Ca²⁺ mobilization (increase of the Ca²⁺ signal = slope) was calculated by subtracting the MFI$_{\text{B}}$ from MFI$_{\text{A}}$.

Statistics

Non-parametric Kruskal–Wallis followed by Dunn's multiple comparisons test (or non-parametric Wilcoxon matched pairs signed-rank test) with the software GraphPad Prism version 6.05 for Windows (GraphPad Software, La Jolla, CA, United States) was conducted on the *p*-values < 0.05. Results are presented in (i) mean ± sem (standard error of the mean) for MFI$_{\text{C}}$ values of the Ca²⁺ mobilization, (ii) in mean ± SD (standard deviation) for proliferation and cell area values, as well as for WCA, SFE, ζ-potential and XPS analyses, and (iii) in median with interquartile ranges (IQR) for cell circularity and MTS values.

RESULTS

Physico-Chemical Characterization of Ti Surface Coatings

Results regarding layer thickness, wettability and surface charge (deduced from ζ-potentials) are given in **Table 1**. The chemical surface composition determined by XPS measurements is listed in **Supplementary Table S2**.

TABLE 1 | Surface characteristics of chemically modified Ti (mean ± SD, $n = 3$).

Surface		Layer thickness [nm]	WCA [°]	SFE [mN/m] dispersive polar	ζ at pH 7.4 [mV]
Controls	Ti	9.0 + TiO$_2$ (5.0)	87.4 ± 0.8	37.6 ± 1.4 / 35.6 ± 1.1 / 2.1 ± 0.3	**−87.5 ± 1.6**
	PPAAm	24.5	66.9 ± 1.7	46.2 ± 1.5 / 36.2 ± 0.6 / 10.0 ± 1.0	**+7.1 ± 2.7**
Amino Polymers	APTES	5.0	88.1 ± 4.1	37.0 ± 2.7 / 35.1 ± 1.6 / 1.9 ± 1.0	**+1.9 ± 1.5**
	PEI	18.0	27.6 ± 2.4	74.3 ± 2.1 / 48.8 ± 0.9 / 25.5 ± 1.1	**+9.1 ± 2.6**
	PPI-G4	23.0	47.2 ± 4.3	62.4 ± 3.6 / 45.0 ± 1.2 / 17.4 ± 2.4	**+50.2 ± 6.2**
ECM and Peptides	Col I	165.0	50.5 ± 4.3	58.6 ± 3.5 / 41.6 ± 1.1 / 17.0 ± 2.5	**−2.8 ± 1.5**
	Matrigel	5.5	69.6 ± 6.9	46.7 ± 5.4 / 38.9 ± 2.1 / 7.8 ± 3.3	**−43.3 ± 1.0**
	RGD	5.6	74.9 ± 1.2	43.0 ± 1.8 / 37.0 ± 1.2 / 6.0 ± 0.6	**+1.7 ± 1.0**
Polyelectrolyte Multilayers	PSS	7.0	62.3 ± 2.7	49.3 ± 2.3 / 37.2 ± 0.8 / 12.1 ± 1.5	**−88.8 ± 11.8**
	PDADMA	38.0	38.7 ± 3.2	62.0 ± 3.3 / 34.6 ± 1.3 / 27.3 ± 2.0	**+51.4 ± 3.6**

Layer Thickness

The layer thickness of all modifications was less than or equal to 165 nm. The oxide layer of titanium surfaces was found to be 5 nm. The thinnest layer was achieved with RGD (0.6 nm) with an underlying APTES layer of 5.0 nm (in total 5.6 nm). The thickest layer was measured for Col I at 165 nm.

Wettability

The analysis demonstrated a change to more hydrophilic surfaces for all modifications except APTES, indicated by a decrease in WCA and an increase in SFE. Uncoated Ti surfaces as well as APTES-functionalized surfaces showed the highest WCA (with Ti 87.4° < APTES 88.1°), the lowest SFE under 40 mN/m and the lowest content of polar interactions with ≤2 mN/m. PEI-functionalized surfaces displayed the lowest WCA (27.6°) and consequently were the most hydrophilic surfaces showing the highest SFE values (74.3 mN/m) with polar interactions of 25.5 mN/m.

Zeta Potential

A less negative ζ-potential was achieved on almost all surfaces compared with uncoated Ti at −87.5 mV. Only the ζ-potential of PSS (−88.8 mV) was slightly lower. Further negative surface potentials were found for Matrigel (−43.3 mV). Col I substrates exhibit only a slightly negative ζ-potential (−2.8 mV). All other surfaces present a positive ζ-potential and can be classified as moderately and highly positive. Moderately positively charged surfaces include PPAAm, APTES, PEI and RGD (+7.1, +1.9, +9.1, and +1.7 mV, respectively), whereas highly positively charged surfaces comprise PPI-G4 and PDADMA (+50.2 and +51.4 mV, respectively). Here we sorted the investigated surfaces starting with the most negative ζ-potential: PSS < Ti < Matrigel < Col I < RGD < APTES < PPAAm < PEI < PPI-G4 < PDADMA.

Cell Biological Investigations

The effect of positive and negative ζ-potential of chemically modified Ti surfaces on MG-63s behavior was observed and correlated.

Cell Morphology

The cell morphology on highly positively charged PPI-G4 and PDADMA surfaces was significantly changed to a more round shape (circularity 0.74 and 0.77, respectively) compared to

FIGURE 2 | Morphology of MG-63s after 24 h on bare and functionalized Ti with negative (–), moderately positive (+) and highly positive (++) ζ-potential. **(A)** The cell circularity on highly positive surface charges reveals a morphologically significant difference to the other surfaces (*). A circularity value of 1.0 represents a perfect circle. (Statistics: Kruskal–Wallis and Dunn's multiple comparison test, *$p < 0.05$; median ± IQR; $n = 3$ independent experiments). **(B)** Note the enormous decrease in cell area (from black arrowhead to white) on PPI-G4 and PDADMA. The PPI-G4 image (right) shows filopodia residues after the cell has retracted (arrow). On PDADMA different membrane structures with and without microvilli are visible (right image). (SEM images, magnification from left to right 100, 500, 2,000 and 5,000x, scale bars 50, 10, 4, and 2 μm, respectively, FE-SEM Merlin VP compact; mean cell area, $n = 3$ independent approaches, fluo-3 staining, LSM780).

Table A (Circularity):

Surface	Ti	PPAAm	APTES	PEI	PPI-G4	Col I	Matrigel	RGD	PSS	PDADMA
Median	0.36	0.44	0.45	0.38	**0.74 ***	0.37	0.50	0.46	0.50	**0.77 ***
25th Quartile	0.28	0.37	0.36	0.32	0.67	0.26	0.38	0.40	0.36	0.74
75th Quartile	0.45	0.54	0.66	0.49	0.77	0.50	0.65	0.64	0.57	0.81

FIGURE 3 | Cell viability of MG-63s after 24 h on Ti and PPAAm arrays representing negatively and moderately positive surface charges, as well as PPI-G4 and PDADMA, representing highly positive surface charges. Cells on PPI-G4 and PDADMA surfaces are stained with both calcein and EthD-1, indicating damaged plasma membranes. (Immunofluorescence images of live/dead staining; 63x objective with 1x and 2.5x zoom, scale bar 10 and 5 μm; nucleus in blue (DAPI), esterase activity of living cells in green (calcein), DNA of cells with abrogated membrane integrity in red (EthD-1); LSM780).

all other surfaces with a polygonal shape (**Figure 2A**). High resolution SEM images revealed a decrease in cell area of MG-63s on PPI-G4 and PDADMA (**Figure 2B**, indicated by arrowheads), showing impaired cell morphology in contrast to well spread phenotypes on Ti and PPAAm. At 5,000x magnification, filopodia and membrane residues of cells on PPI-G4 are visible (arrow), whereas cells on PDADMA also show an altered membrane structure, as no microvilli are presented in individual cells.

Cell Viability

Fluorescence live/dead images displayed several cells on highly positively charged PPI-G4 and PDADMA surfaces that were positive for both Calcein and EthD-1 in contrast to Ti and PPAAm, suggesting a damaged plasma membrane (**Figure 3**). These images also confirmed the reduced cell area and circular shape on PPI-G4 and PDADMA after 24 h. In addition, we observed a decreased relative cell viability (**Supplementary Figure S1**) and cell proliferation (**Supplementary Figure S2**) on

these surfaces compared with Ti and PPAAm, with a greater extent on PDADMA surfaces. While the amount of proliferative cells declined (with 64.1, 66.8, 51.8, and 24.6% for Ti, PPAAm, PPI-G4 and PDADMA, respectively), the cells increasingly remained in the G1 phase (34.0, 32.2, 47.5, and 73.7% for Ti, PPAAm, PPI-G4 and PDADMA, respectively).

Intracellular Ca²⁺ Mobilization

The intracellular basal Ca²⁺ signals on the control surfaces Ti and PPAAm are depicted in **Figure 4**. The fluorescence images reveal an increased cell area on PPAAm after 1 h compared with the uncoated Ti control (white dotted lines), while cells are equally spread after 24 h (insert top right). The basal Ca²⁺ level was found elevated after 1 h as well as after 24 h on PPAAm compared with Ti. Consequently, these control surfaces were consistently included in the following Ca²⁺ mobilization experiments.

The influence of the individual Ti modifications on Ca²⁺ mobilization in vital cells is presented in **Figure 5** (an overview

FIGURE 4 | Basal Ca^{2+} signals in living MG-63s after 1 h and 24 h on the control surfaces Ti **(left)** and PPAAm **(right)**. The intracellular basal Ca^{2+} level on PPAAm is increased both after 1 and 24 h, suggesting higher cell function. While cells on PPAAm exhibit a larger cell area after 1 h (white dotted line), the area is balanced after 24 h. (Immunofluorescence images; 63x objective, scale bar 10 μm; nucleus in blue (Hoechst), Ca^{2+} ions in green (fluo-3), cytoskeleton in red (actin-RFP); LSM780).

of the time series with fluorescence images can be found in the **Supplementary Figure S5**). Shown are the whole time series of Ca^{2+} mobilization in MG-63 osteoblasts cultured 24 h on Ti modifications (blue curves) and the corresponding controls (gray curves = Ti, green/red curves = PPAAm). The exact values for MFI_B, MFI_A and slope can be found in **Table 2**. Stimulation with ATP after 180 s resulted in a significantly lower Ca^{2+} mobilization in cells on PSS and PDADMA compared with their Ti controls, whereas the MFI_A of cells on Col I and PEI exceeded the Ti control significantly (**Figure 5**). Cells on Matrigel could not display a significantly different Ca^{2+} level upon stimulation than Ti. The MFI_A in cells on RGD-functionalized surfaces was significantly elevated compared with Ti, but below PPAAm. The highest Ca^{2+} mobilization after ATP stimulation was found in cells on APTES. Cells cultured on PDADMA surfaces exhibited the lowest mobilization rate, while cells on PPI-G4 surfaces could not mobilize Ca^{2+} ions at all.

These results could be correlated with the ζ-potential of the substrates, as shown in **Figure 6**. Here, the sections 5A-C are classified into negative, moderately and highly positive according to ζ-potential values, starting with the most negative and ending with the most positive value. With this alignment the diminished Ca^{2+} mobilization in cells on surfaces with negative (**Figure 6A**) and highly positive ζ-potential (**Figure 6C**) compared with surfaces with moderately positive ζ-potential (**Figure 6B**) could be clearly demonstrated. Cells on surfaces with negative ζ-potentials of −88.8 to −43.3 mV displayed significantly lower Ca^{2+} levels after ATP stimulation than PPAAm, the positively charged control (red line in highlighted area = MFI_A of PPAAm) (**Figure 6A**). Exclusively, Col I-functionalized surfaces with an almost neutral ζ-potential of −2.8 mV lacked significance to PPAAm. The absolute slope from basal Ca^{2+} level to the level

after ATP stimulation reached a maximum of 594.9 MFI_C on negatively charged surfaces (**Table 2**).

Materials revealing a moderately positive ζ-potential of ∼1 to 10 mV consistently exhibited significantly higher Ca^{2+} levels after stimulation than Ti, the negatively charged control (black line in highlighted area = MFI_A of Ti, **Figure 6B**). Here, the Ca^{2+} mobilization ranged between 800.7 and 1392.4 MFI_C (**Table 2**).

On substrates presenting highly positive ζ-potentials (∼ + 50 mV), MG-63s indicated an impaired Ca^{2+} mobilization with MFI_A values significantly lower than PPAAm and Ti (**Figure 6C**). The maximum Ca^{2+} level increase was 79.1 MFI_C (**Table 2**).

Furthermore, a correlation of Ca^{2+} mobilization data with the measured surface properties for wettability (WCA and SFE) could not be identified (**Table 2**). There were both less and more hydrophilic surfaces in the range of cells showing a stronger ability to mobilize intracellular Ca^{2+} (e.g., ∼90° for APTES and ∼30° for PEI) as well as a lower ability for Ca^{2+} mobilization (e.g., ∼90° for Ti and ∼40° for PDADMA). However, osteoblasts behave differently with respect to their Ca^{2+} dynamics. A similar statement can be formulated regarding the SFE values. Here, the highest SFE values (Col I < PDADMA < PPI-G4 < PEI with 58.6, 62.0, 62.4, and 74.3 mN/m, respectively) did not automatically lead to the best Ca^{2+} mobilization results, especially noticeable for PPI-G4 and PDADMA, which displayed the lowest slope.

DISCUSSION

Cells in living bone tissue are surrounded by an electrically charged, organic/inorganic solid that is permeated by a flow of ionic solution through an intricate channel system

FIGURE 5 | Dynamic Ca^{2+} mobilization in vital fluo-3 loaded MG-63s growing on amino polymers, extracellular matrix (ECM)/peptide motifs and polyelectrolyte multilayers (PEM) in the time frame 0–480 s. The positive control PPAAm (also an amino polymer) and the negative control Ti are embedded for the respective experiment. Shown are time courses of the mean fluorescence intensity of cells (MFI$_C$) over 8 min: First, the basal Ca^{2+} signal is recorded for 180 s. At 180 s the cells are stimulated with ATP (arrowheads) and the Ca^{2+} signal is detected (LSM780, Carl Zeiss; ZEN-software). For statistical analyses of the basal MFI, values of the time points 0–170 s are used. For analyses of the MFI after ATP stimulation, values of the time points 190–240 s are used (highlighted in grey). MFI$_C$ values are normalized to the mean cell area after 24 h. (Statistics: Kruskal–Wallis and Dunn's multiple comparison test, $p < 0.05$; mean ± sem; $n \geq 3$ independent approaches, per time point $\geq$ 30 cells; * indicates significance of modification x to Ti and [#] significance to PPAAm).

(Chakkalakal, 1989). Consequently, it is not surprising that bone cell physiology is also affected by electrical cues when cultivating cells on artificial material surfaces. Cell-material interactions are highly complex and require more systematic investigations regarding surface charge. It is certain that electrostatic forces are crucial for cellular attachment via focal adhesion to material

TABLE 2 | Ca^{2+} mobilization results related to surface characteristics of chemically modified Ti (mean ± SD, $n = 3$ for surface characteristics; mean ± sem, $n \leq 3$ for Ca^{2+} values).

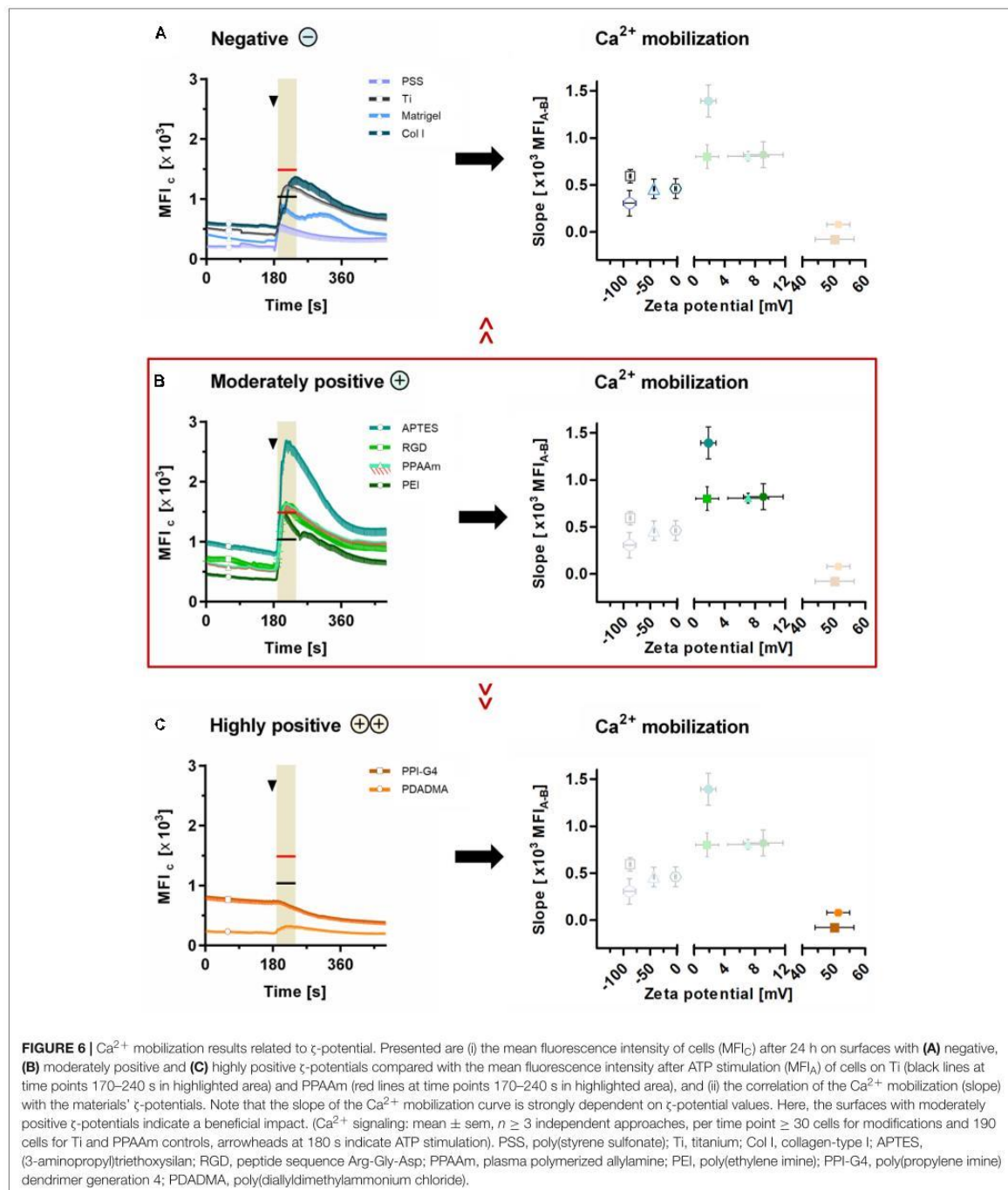| Surface	PSS	Ti	Matrigel	Col I	RGD	APTES	PPAAm	PEI	PPI-G4	PDADMA
ζ [mV]	−88.8 ± 12	−87.5 ± 2	−43.3 ± 1	−2.8 ± 1	1.7 ± 1	1.9 ± 1	7.1 ± 3	9.1 ± 3	50.2 ± 6	51.4 ± 4
MFI$_B$	216.4 ± 40	445.1 ± 18	329.6 ± 20	575.3 ± 44	683.6 ± 60	918.5 ± 72	656.6 ± 32	412 ± 35	769.8 ± 63	221.5 ± 28
MFI$_A$	523.4 ± 107	1040 ± 53	791 ± 72	1037.5 ± 97	1484.3 ± 123	2310.9 ± 157	1461.4 ± 58	1232.4 ± 104	691.8 ± 54	300.6 ± 37
Slope	307.1 ± 134	594.9 ± 71	461.3 ± 104	462.2 ± 105	800.7 ± 126	1392.4 ± 169	804.8 ± 53	820.4 ± 138	−78.0 ± 17	79.1 ± 18
WCA [°]	62.3 ± 3	87.4 ± 1	69.6 ± 7	50.5 ± 4	74.9 ± 1	88.1 ± 4	66.9 ± 2	27.6 ± 2	47.2 ± 4	38.7 ± 3
SFE [mN/m]	49.3 ± 2	37.6 ± 1	46.7 ± 5	58.6 ± 3	43.0 ± 2	37.0 ± 3	46.2 ± 1	74.3 ± 2	62.4 ± 4	62.0 ± 3

surfaces (Metwally and Stachewicz, 2019) influencing the further fate of cells. Earlier studies have mostly dealt with a limited number of surface charges [e.g., only negative surfaces (Altankov et al., 2003), one positive compared with several negative surfaces (Chang et al., 2014), or only one negative, neutral and positive surface charge (Iwai et al., 2013)] disallowing detailed statements. It has been reported that materials with positive surface potentials have a beneficial effect on cell viability as well as on adhesion and spreading. But most studies lacked a clear determination of the surface potential (Lee et al., 1994; Bacakova et al., 1996; Webb et al., 1998; Lesný et al., 2006). Hence, the underlying mechanism controlling cell activities using the materials' surface charge is still not fully understood in bone tissue engineering.

In the present study, the behavior of osteoblastic MG-63s via intracellular Ca^{2+} mobilization was systematically investigated on different Ti modifications and correlated with the materials' ζ-potential as a parameter for the electric surface property. We used unmodified Ti (−87.5 mV) and PPAAm coated Ti (+7.1 mV) as controls with negative and positive ζ-potential, respectively, as published before (Mörke et al., 2017; Nebe et al., 2019), knowing that the PPAAm surface modification enhances cell physiology concerning adhesion, spreading, motility (Rebl et al., 2010), actin filament network (Rebl et al., 2016), viability and Ca^{2+} mobilization (Moerke et al., 2018; Staehlke et al., 2018), as well as the implant osseointegration (Hoene et al., 2010). Cells bind to this positively charged plasma polymer layer via electrostatic forces, as it is known that osteoblasts (Finke et al., 2007), epithelial cells and chondrocytes (Cohen et al., 2004) express i.a. the negatively charged hyaluronan as a spherical shell around the cells (Zimmerman et al., 2002). However, the question arose whether positive ζ-potentials generally lead to a beneficial cellular outcome.

Physico-Chemical Characterization of Ti Surface Coatings

Therefore, we successfully prepared nine chemical modifications of Ti substrates with (i) amino polymers, (ii) ECM/peptide motifs, and (iii) PEM, resulting in a broad range of ζ-potentials. The materials' characteristic ζ-potential, WCA, SFE, layer thickness (**Table 1**) and chemical composition (**Supplementary Table S2**) were evaluated.

The layer thickness was in the nanometer range (max. 165 nm). The APTES-modified surface layer was similar in thickness to the PEI and PPI-G4 layers. These layers are SAM arrangements, whereby the smaller thickness of the APTES layer correlates with the shorter molecular length of the APTES molecule compared with both the PEI and PPI-G4 molecule lengths. The molecular length of the RGD-conjugated APTES molecule is slightly longer than the APTES molecule itself. However, it is unlikely that an RGD molecule is coupled to every amino group on APTES. It therefore seems possible that individual RGD molecules are not necessarily aligned completely orthogonal to the surface as it is the case in a perfect SAM arrangement. In addition, interactions like hydrogen bonding between amino groups on APTES and residual amino acids of the RGD may possibly lead to a "bending" of the RGD molecules and consequently to a

FIGURE 6 | Ca²⁺ mobilization results related to ζ-potential. Presented are (i) the mean fluorescence intensity of cells (MFI$_C$) after 24 h on surfaces with **(A)** negative, **(B)** moderately positive and **(C)** highly positive ζ-potentials compared with the mean fluorescence intensity after ATP stimulation (MFI$_A$) of cells on Ti (black lines at time points 170–240 s in highlighted area) and PPAAm (red lines at time points 170–240 s in highlighted area), and (ii) the correlation of the Ca²⁺ mobilization (slope) with the materials' ζ-potentials. Note that the slope of the Ca²⁺ mobilization curve is strongly dependent on ζ-potential values. Here, the surfaces with moderately positive ζ-potentials indicate a beneficial impact. (Ca²⁺ signaling: mean ± sem, $n \geq 3$ independent approaches, per time point ≥ 30 cells for modifications and 190 cells for Ti and PPAAm controls, arrowheads at 180 s indicate ATP stimulation). PSS, poly(styrene sulfonate); Ti, titanium; Col I, collagen-type I; APTES, (3-aminopropyl)triethoxysilan; RGD, peptide sequence Arg-Gly-Asp; PPAAm, plasma polymerized allylamine; PEI, poly(ethylene imine); PPI-G4, poly(propylene imine) dendrimer generation 4; PDADMA, poly(diallyldimethylammonium chloride).

reduction of the overall layer thickness. Regarding PPAAm coatings, it must be emphasized that PPAAm is a very complex, highly cross-linked structure, which was presented here only in a very simplified and model-like schematic manner (see **Figure 1**). The thickness of PPAAm, as well as Col I, Matrigel, and the polyelectrolyte multilayer coatings is mainly

determined by the individual material properties and the process parameters.

The wettability analysis demonstrated a change to more hydrophilic surfaces. There is evidence that mammalian cells favor modestly hydrophilic surfaces displaying water contact angles between 40° and 65° (Rebl et al., 2012; Ahn et al., 2014; Gentleman and Gentleman, 2014). However, Gentleman and Gentleman (2014) reviewed that studies often lack a clear trend of cell behavior with wettability. They rather assumed SFE to be the more relevant feature for cellular behavior. This could not, however, be confirmed here. We could neither find a connection between WCA and SFE to the surface charge which is consistent with Olsson et al. (1995), nor a correlation with the cell behavior.

The ζ-potential could rather be the pivotal parameter for controlling cell physiology in osteoblasts, as our results indicate. In whole bone tissue negative ζ-potentials could be determined (Skalak and Shu, 1986; Otter et al., 1988; Chakkalakal, 1989). In this study, ζ-potentials of the investigated surface modifications were identified in the range of -90 to -3 mV (PSS < Ti < Matrigel < Col I), $+1$ to $+10$ mV (RGD < APTES < PPAAm < PEI) and $\sim+50$ mV (PPI-G4 < PDADMA). For the first time, we were able to classify the ζ-potential into three categories with regard to an improved cell response on the respective surfaces and introduce the following terms: negative < moderately positive > highly positive.

ζ-Potential – A Parameter for Surface Charge – Can Strongly Influence Cellular Behavior

It is known that physiology features of MG-63s such as actin cytoskeleton organization (Staehlke et al., 2015), viability (Staehlke et al., 2018) or proliferation (Labelle et al., 2007) are reflected by intracellular Ca²⁺ dynamics. However, to our knowledge there is no literature on intracellular Ca²⁺ dynamics in the context of the ζ-potential of biomaterials other than our previously published study comparing surfaces with negative ζ-potential with positive charges of plasma polymer nanolayers (PPAAm). The question remained, if positive charges in general promote the cellular outcome.

In order to gain deeper insights into the effect of surface charges on Ca²⁺ dynamics, we analyzed the intracellular Ca²⁺ signals before (MFI$_B$) and after ATP stimulation (MFI$_A$) on surface modifications with various charges using confocal laser scanning microscopy (**Figure 5** and **Supplementary Figure S5**). Additionally, cell morphology (**Figure 2**), cell viability (**Figure 3** and **Supplementary Figure S1**) and cell proliferation (**Supplementary Figure S2**) were investigated on selected surfaces. In the following, our results are discussed regarding negative, moderately and highly positive ζ-potentials.

Negative ζ-Potential (-90 to -3 mV)

On our surfaces with negative ζ-potential we found evidence of reduced Ca²⁺ mobilization after 24 h compared with surfaces with moderately positive ζ-potential. On PSS terminated PEM surfaces, MG-63s showed one of the lowest Ca²⁺ slopes after 24 h. Other studies documented that hMSC cell numbers after 2, 5, and 7 days were consistently lower on PSS terminated PEM films than on control surfaces (Liao et al., 2010). However, PSS ending

films exhibited good biocompatibility, as shown for SaOS-2 cells (cytokine IL-8 production) (Tryoen-Tóth et al., 2002), at least for films consisting of not more than six polyelectrolyte layers (Arias et al., 2016).

Moderately Positive ζ-Potential ($+1$ to $+10$ mV)

Surfaces in the moderately positively charged range were found to promote the cell physiology via Ca²⁺ mobilization. Cells can access their intracellular Ca²⁺ stores more effectively after an external stimulus (here: ATP) than cells on negatively charged substrates, suggesting higher cell activities.

Ravenscroft-Chang et al. (2010) loaded primary cardiac myocytes growing on (3-trimethoxysilylpropyl) diethylenetriamine (DETA) silane modified and fluorinated glass substrates with fura-2 AM and induced a Ca²⁺ signal by electrical stimulation (1 HZ, 6 V, 5 ms/pulse). Cells exhibited a significantly higher Ca²⁺ level, as shown in higher amplitude and duration. However, the authors did not determine the ζ-potential of their surfaces. But a slightly positive ζ-potential at pH 7.4 of such DETA amino silane treated glass surfaces was measured earlier by Metwalli et al. (2006) supporting the idea of higher cellular activity on the basis of moderately positive charges.

For PEI functionalized surfaces it is known that cytotoxicity can exist depending on the molecular weight and concentration (Brunot et al., 2007). However, in studies with surfaces derived from low molecular weight PEI, as used here (25 kDa), no cytotoxic effects were reported for fibroblasts up to 7 days (Hernandez-Montelongo et al., 2017). PEI modification could further improve proliferation and function of MG-63s (Liu et al., 2009), as indicated here by an increased Ca²⁺ slope.

RGD peptide motifs covalently bonded to Ti surfaces promote osteoblast attachment and survival (Secchi et al., 2007). El-Ghannam et al. (2004) showed that APTES-RGD coatings provided the optimal surface for cell adhesion, spreading, and cytoskeletal organization for MC3T3-El cells, better than RGD and APTES alone. It must be taken into consideration that surfaces modified with RGD (as well as Col I and Col IV and laminin containing Matrigel) can trigger Ca²⁺ mobilization through integrin mediated "outside-in" signal transduction during cell adhesion (Sjaastad and Nelson, 1997; Boraschi-Diaz et al., 2017). After 24 h cultivation, however, integrin signaling may no longer be that influential in this case, as no additional stimulus such as mechanical stress (Pommerenke et al., 2002) was applied. Otherwise an increased Ca²⁺ mobilization on these ECM coated surfaces would be expected. Here, we found that APTES alone was capable of mobilizing Ca²⁺ in MG-63s even more than PPAAm – surfaces that do not present integrin ligands.

Lee et al. (2018) presented ATPES-treated PDMS concave microwell surfaces to cortical neurons which revealed optimal surface conditions additionally supporting a spheroid formation. The authors also stimulated the cells with KCl for spontaneous calcium transients (fluo-4 AM), observing typical temporal Ca²⁺ responses in all chemically modified microwells based on APTES (APTES, APTES-Laminin, APTES-poly-L-lysine, APTES-carbon nanotubes).

Highly Positive ζ-Potentials (∼+50 mV)

On PPI-G4 and PDADMA surfaces with highly positive ζ-potentials we discovered a restricted cell viability, reflected in an impaired Ca^{2+} mobilization and a disturbed cell morphology and proliferation after 24 h, indicating that cells cannot tolerate such ζ-potentials.

Koch et al. (2018) produced the 11-amino acid self-assembling peptides P11-8 and P11-28/29 hydrogels exhibiting ζ-potentials of ∼ + 20 mV and ∼ + 60 mV at pH 7.0, respectively. HPDLF and HCO cells on highly positive P11-28/29 surfaces showed reduced cell area after 24 h, while cells on P11-8 displayed also enhanced osteogenic differentiation (ALP activity) compared with hydrogels containing negatively charged glutamic acids. Similarly, Kidambi et al. (2004) reported that primary hepatocytes were unable to remain attached to PEM films with PDADMA as the outermost layer. Inactive cells completely lifted off the surface by day 7 where liver-specific functions approached zero. In our previous study (Gruening et al., 2020) we found an impeded cell spreading dynamic on PDADMA surfaces after an initial tendency to spread better than Ti. The longer the influence of strongly positive charges on the cells, the more the cells were hampered.

Guo et al. (2018) pointed out that on positively charged non-cross-linked PEI films (ζ-potential: +50 and +62 mV) more fibroblasts could adhere within the first 24 h compared with negatively charged polymer films. But, on the second day, cells on the negatively charged surfaces proliferated well, in contrast to those on samples with high ζ-potentials. The authors argued that this was due to the reported cytotoxicity of PEI. But by cross-linking these PEI films, the high ζ-potential was reduced to ∼ + 20 mV and cells proliferated on all surfaces.

During the cell cycle, checkpoints in G1 and G2 (gap) phases prevent cells from entering into the next phase in case of cell injury e.g., due to accumulation of reactive oxygen species (ROS) (Muller et al., 2007) or inadequate environmental conditions such as bacterial infection (Kato et al., 2008), hypoxia (Zou et al., 2015) or withdrawal of nutrition (Blagosklonny, 2011). Cells which do not pass the safety controls proceed with the non-proliferative G0/G1 phase in quiescence (cell cycle arrest) or even permanent senescence (Blagosklonny, 2011; Terzi et al., 2016). We found an increasing cell amount in the G1 phase on highly positive surfaces, leading to a decline of cellular proliferation. In further experiments it is to be examined whether the high surface charges lead to an elevated ROS production as stress response and thus to a cell cycle arrest, allowing cells to cope with their environment.

However, the high surface charge leads to an intense interaction with the negatively charged cell surface (Rebl et al., 2016), which is further considered to cause damaged lipid bilayers due to new vesicular structures around the cationic molecules which create holes in the cell membrane (Mecke et al., 2005). This could be supported by the live/dead staining, demonstrating an abolished membrane integrity in still vital cells on PPI-G4 and PDADMA.

The adverse effects of highly positive surface charges deduced from the ζ-potential might also be indirectly linked to protein adsorption, since it has been published that the protein adsorption is strongly affected by the ζ-potential (Krajewski et al., 1998; Lehnfeld et al., 2020) influencing the protein population (Shelton et al., 1988) and orientation (Norde and Lyklema, 1991; Antonini et al., 2014). Therefore, a further correlation between protein adsorption and ζ-potential of different surface modifications with well-defined effects on the cell behavior is of great interest.

CONCLUSION

This is the largest systematic study so far documenting the importance of the materials' surface charge deduced from ζ-potential for the intracellular Ca^{2+} dynamics and viability of human osteoblasts. Positive charges offer unique cues that induce an intensive cell response. But interestingly, we identified that cells favor only a certain range of moderately positive surface charges and not a positively charged surface in general. The ζ-potential appears to be a key property of biomaterial surfaces dominating the relevance of wettability (WCA, SFE), and should be considered in biomaterial coating design in tissue engineering and dental and orthopedic implantology.

DATA AVAILABILITY STATEMENT

The datasets presented in this study can be found in online repositories. The names of the repository/repositories and accession number(s) can be found below: Mendeley data doi: 10.17632/h8rs6v4dgt.1.

AUTHOR CONTRIBUTIONS

MG: conceptualization, investigation, validation, visualization, and original draft preparation. SN: PEM preparation. PN: layer thickness measurement and review and editing. KF: XPS measurement and PPAAm preparation. MD: APTES and RGD preparation. JL: PEI and PPI-G4 preparation and review and editing. MS: visualization and review and editing. CH and RM: review and editing and funding acquisition. SS: ATP receptor immunofluorescence and review and editing. JBN: conceptualization, review and editing, project administration, and funding acquisition. All authors contributed to the article and approved the submitted version.

FUNDING

SUPPLEMENTARY MATERIAL

The Supplementary Material for this article can be found online at: https://www.frontiersin.org/articles/10.3389/fbioe.2020.01016/full#supplementary-material

REFERENCES

Abalymov, A., Van der Meeren, L., Skirtach, A. G., and Parakhonskiy, B. V. (2020). Identification and analysis of key parameters for the ossification on particle functionalized composites hydrogel materials. *ACS Appl. Mater. Interf.* 2020:acsami.0c06641. doi: 10.1021/acsami.0c06641

Ahn, H., Lee, I., Lee, H., and Kim, M. (2014). Cellular behavior of human adipose-derived stem cells on wettable gradient polyethylene surfaces. *Int. J. Mol. Sci.* 15, 2075–2086. doi: 10.3390/ijms15022075

Akter, F., and Ibanez, J. (2016). Bone and cartilage tissue engineering. *Tissue Eng. Made Easy* 2016, 77–97. doi: 10.1016/B978-0-12-805361-4.00008-4

Altankov, G., Richau, K., and Groth, T. (2003). The role of surface zeta potential and substratum chemistry for regulation of dermal fibroblasts interaction. *Materwiss. Werksttech.* 34, 1120–1128. doi: 10.1002/mawe.200300699

Anselme, K., Ponche, A., and Bigerelle, M. (2010). Relative influence of surface topography and surface chemistry on cell response to bone implant materials. Part 2: biological aspects. *Proc. Inst. Mech. Eng. H* 224, 1487–1507. doi: 10.1243/09544119JEIM901

Antonini, V., Torrengo, S., Marocchi, L., Minati, L., Serra, M. D., Bao, G., et al. (2014). Combinatorial plasma polymerization approach to produce thin films for testing cell proliferation. *Coll. Surf. B Biointerf.* 113, 320–329. doi: 10.1016/J.COLSURFB.2013.09.020

Arias, C. J., Surmaitis, R. L., and Schlenoff, J. B. (2016). Cell adhesion and proliferation on the "living" surface of a polyelectrolyte multilayer. *Langmuir* 32, 5412–5421. doi: 10.1021/acs.langmuir.6b00784

Bacakova, L., Filova, E., Parizek, M., Ruml, T., and Svorcik, V. (2011). Modulation of cell adhesion, proliferation and differentiation on materials designed for body implants. *Biotechnol. Adv.* 29, 739–767. doi: 10.1016/J.BIOTECHADV.2011.06.004

Bacakova, L., Svorcik, V., Rybka, V., Micek, I., Hnatowicz, V., Lisa, V., et al. (1996). Adhesion and proliferation of cultured human aortic smooth muscle cells on polystyrene implanted with N+, F+ and Ar+ ions: correlation with polymer surface polarity and carbonization. *Biomaterials* 17, 1121–1126. doi: 10.1016/0142-9612(96)85914-X

Blagosklonny, M. V. (2011). Cell cycle arrest is not senescence. *Aging* 3, 94–101. doi: 10.18632/aging.100281

Boraschi-Diaz, I., Wang, J., Mort, J. S., and Komarova, S. V. (2017). Collagen Type I as a Ligand for receptor-mediated signaling. *Front. Phys.* 5:12. doi: 10.3389/fphy.2017.00012

Brunot, C., Ponsonnet, L., Lagneau, C., Farge, P., Picart, C., and Grosgogeat, B. (2007). Cytotoxicity of polyethyleneimine (PEI), precursor base layer of polyelectrolyte multilayer films. *Biomaterials* 28, 632–640. doi: 10.1016/J.BIOMATERIALS.2006.09.026

Cao, C., Song, Y., Yao, Q., Yao, Y., Wang, T., Huang, B., et al. (2015). Preparation and preliminary *in vitro* evaluation of a bFGF-releasing heparin-conjugated poly(ε-caprolactone) membrane for guided bone regeneration. *J. Biomater. Sci. Polym. Edn.* 26, 600–616. doi: 10.1080/09205063.2015.1049044

Chakkalakal, D. A. (1989). Mechanoelectric transduction in bone. *J. Mater. Res.* 4, 1034–1046. doi: 10.1557/JMR.1989.1034

Chang, H.-Y., Huang, C.-C., Lin, K.-Y., Kao, W.-L., Liao, H.-Y., You, Y.-W., et al. (2014). Effect of surface potential on NIH3T3 cell adhesion and proliferation. *J. Phys. Chem. C* 118, 14464–14470. doi: 10.1021/jp504662c

Chen, S., Guo, Y., Liu, R., Wu, S., Fang, J., Huang, B., et al. (2018). Tuning surface properties of bone biomaterials to manipulate osteoblastic cell adhesion and the signaling pathways for the enhancement of early osseointegration. *Coll. Surf. B Biointerf.* 164, 58–69. doi: 10.1016/J.COLSURFB.2018.01.022

Clover, J., and Gowen, M. (1994). Are MG-63 and HOS TE85 human osteosarcoma cell lines representative models of the osteoblastic phenotype? *Bone* 15, 585–591. doi: 10.1016/8756-3282(94)90305-0

Cohen, M., Joester, D., Geiger, B., and Addadi, L. (2004). Spatial and temporal sequence of events in cell adhesion: from molecular recognition to focal adhesion assembly. *Chembiochem* 5, 1393–1399. doi: 10.1002/cbic.200400162

Czekanska, E. M., Stoddart, M. J., Ralphs, J. R., Richards, R. G., and Hayes, J. S. (2014). A phenotypic comparison of osteoblast cell lines versus human primary osteoblasts for biomaterials testing. *J. Biomed. Mater. Res. Part A* 102, 2636–2643. doi: 10.1002/jbm.a.34937

De Aza, P. N., Luklinska, Z. B., Santos, C., Guitian, F., and De Aza, S. (2003). Mechanism of bone-like formation on a bioactive implant in vivo. *Biomaterials* 24, 1437–1445. doi: 10.1016/S0142-9612(02)00530-6

Devgan, S., and Sidhu, S. S. (2019). Evolution of surface modification trends in bone related biomaterials: a review. *Mater. Chem. Phys.* 233, 68–78. doi: 10.1016/J.MATCHEMPHYS.2019.05.039

Dhowre, H. S., Rajput, S., Russell, N. A., and Zelzer, M. (2015). Responsive cell-material interfaces. *Nanomedicine* 10, 849–871. doi: 10.2217/nnm.14.222

Eichler, M., Katzur, V., Scheideler, L., Haupt, M., Geis-Gerstorfer, J., Schmalz, G., et al. (2011). The impact of dendrimer-grafted modifications to model silicon surfaces on protein adsorption and bacterial adhesion. *Biomaterials* 32, 9168–9179. doi: 10.1016/J.BIOMATERIALS.2011.08.063

El-Ghannam, A. R., Ducheyne, P., Risbud, M., Adams, C. S., Shapiro, I. M., Castner, D., et al. (2004). Model surfaces engineered with nanoscale roughness and RGD tripeptides promote osteoblast activity. *J. Biomed. Mater. Res.* 68A, 615–627. doi: 10.1002/jbm.a.20051

Felgueiras, H. P., Antunes, J. C., Martins, M. C. L., and Barbosa, M. A. (2018). Fundamentals of protein and cell interactions in biomaterials. *Pept. Proteins Biomater. Tissue Regen. Repair* 88, 956–970. doi: 10.1016/B978-0-08-100803-4.00001-2

Fernández-Yagüe, M., Antoñanzas, R. P., Roa, J. J., Biggs, M., Gil, F. J., and Pegueroles, M. (2019). Enhanced osteoconductivity on electrically charged titanium implants treated by physicochemical surface modifications methods. *Nanomed. Nanotechnol. Biol. Med.* 18, 1–10. doi: 10.1016/J.NANO.2019.02.005

Ferrari, M., Cirisano, F., and Morán, M. C. (2019). Mammalian cell behavior on hydrophobic substrates: influence of surface properties. *Colloids Interf.* 3:48. doi: 10.3390/colloids3020048

Ferraris, S., Cazzola, M., Peretti, V., Stella, B., and Spriano, S. (2018). Zeta potential measurements on solid surfaces for in vitro biomaterials testing: surface charge, reactivity upon contact with fluids and protein absorption. *Front. Bioeng. Biotechnol.* 6:60. doi: 10.3389/fbioe.2018.00060

Finke, B., Luethen, F., Schroeder, K., Mueller, P. D., Bergemann, C., Frant, M., et al. (2007). The effect of positively charged plasma polymerization on initial osteoblastic focal adhesion on titanium surfaces. *Biomaterials* 28, 4521–4534. doi: 10.1016/J.BIOMATERIALS.2007.06.028

Finke, B., Rebl, H., Hempel, F., Schäfer, J., Liefeith, K., Weltmann, K.-D., et al. (2014). Aging of plasma-polymerized allylamine nanofilms and the maintenance of their cell adhesion capacity. *Langmuir* 30, 13914–13924. doi: 10.1021/la5019778

Fritsche, A., Haenle, M., Zietz, C., Mittelmeier, W., Neumann, H.-G., Heidenau, F., et al. (2009). Mechanical characterization of anti-infectious, anti-allergic, and bioactive coatings on orthopedic implant surfaces. *J. Mater. Sci.* 44, 5544–5551. doi: 10.1007/s10853-009-3776-1

Gentleman, M. M., and Gentleman, E. (2014). The role of surface free energy in osteoblast-biomaterial interactions. *Int. Mater. Rev.* 59, 417–429. doi: 10.1179/1743280414Y.0000000038

Goldenberg, N. M., and Steinberg, B. E. (2010). Surface charge: a key determinant of protein localization and function. *Cancer Res.* 70, 1277–1280. doi: 10.1158/0008-5472.CAN-09-2905

Gruening, M., Neuber, S., Fricke, K., Helm, C. A., and Nebe, B. (2020). Cell-material interaction - spreading course correlates with surface charge. *Am. J. Biomed. Sci. Res.* 9, 4–6. doi: 10.34297/AJBSR.2020.09.001341

Guo, S., Kwek, M. Y., Toh, Z. Q., Pranantyo, D., Kang, E.-T., Loh, X. J., et al. (2018). Tailoring polyelectrolyte architecture to promote cell growth and inhibit bacterial adhesion. *ACS Appl. Mater. Interf.* 10, 7882–7891. doi: 10.1021/acsami.8b00666

Hanawa, T. (2019). Titanium-tissue interface reaction and its control with surface treatment. *Front. Bioeng. Biotechnol.* 7:170. doi: 10.3389/fbioe.2019.00170

Heo, W., Do Inoue, T., Park, W. S., Kim, M. L., Park, B. O., Wandless, T. J., et al. (2006). PI(3,4,5)P3 and PI(4,5)P2 lipids target proteins with polybasic clusters to the plasma membrane. *Science* 314, 1458–1461. doi: 10.1126/SCIENCE.1134389

Hernandez-Montelongo, J., Lucchesi, E. G., Nascimento, V. F., França, C. G., Gonzalez, I., Macedo, W. A. A., et al. (2017). Antibacterial and non-cytotoxic ultra-thin polyethylenimine film. *Mater. Sci. Eng. C* 71, 718–724. doi: 10.1016/J.MSEC.2016.10.064

Hoene, A., Walschus, U., Patrzyk, M., Finke, B., Lucke, S., Nebe, B., et al. (2010). In vivo investigation of the inflammatory response against allylamine plasma polymer coated titanium implants in a rat model. *Acta Biomater.* 6, 676–683. doi: 10.1016/J.ACTBIO.2009.09.003

Iwai, R., Nemoto, Y., and Nakayama, Y. (2013). The effect of electrically charged polyion complex nanoparticle-coated surfaces on adipose-derived stromal progenitor cell behaviour. *Biomaterials* 34, 9096–9102. doi: 10.1016/J.BIOMATERIALS.2013.08.027

Kato, T., Tsuda, T., Inaba, H., Kawai, S., Okahashi, N., Shibata, Y., et al. (2008). Porphyromonas gingivalis gingipains cause G(1) arrest in osteoblastic/stromal cells. *Oral Microbiol. Immunol.* 23, 158–164. doi: 10.1111/j.1399-302X.2007.00405.x

Katzur, V., Eichler, M., Deigele, E., Stage, C., Karageorgiev, P., Geis-Gerstorfer, J., et al. (2012). Surface-immobilized PAMAM-dendrimers modified with cationic or anionic terminal functions: physicochemical surface properties and conformational changes after application of liquid interface stress. *J. Coll. Interf. Sci.* 366, 179–190. doi: 10.1016/J.JCIS.2011.09.029

Kennedy, S. B., Washburn, N. R., Simon, C. G., and Amis, E. J. (2006). Combinatorial screen of the effect of surface energy on fibronectin-mediated osteoblast adhesion, spreading and proliferation. *Biomaterials* 27, 3817–3824. doi: 10.1016/J.BIOMATERIALS.2006.02.044

Kidambi, S., Ilsoon, L., and Chan, C. (2004). Controlling primary hepatocyte adhesion and spreading on protein-free polyelectrolyte multilayer films. *J. Am. Chem. Soc.* 126, 16286–16287. doi: 10.1021/JA046188U

Koch, F., Wolff, A., Mathes, S., Pieles, U., Saxer, S., Kreikemeyer, B., et al. (2018). Amino acid composition of nanofibrillar self-assembling peptide hydrogels affects responses of periodontal tissue cells in vitro. *Int. J. Nanomed.* 13, 6717–6733. doi: 10.2147/IJN.S173702

Kokubo, T., and Yamaguchi, S. (2015). Growth of novel ceramic layers on metals via chemical and heat treatments for inducing various biological functions. *Front. Bioeng. Biotechnol.* 3:176. doi: 10.3389/fbioe.2015.00176

Krajewski, A., Piancastelli, A., and Malavolti, R. (1998). Albumin adhesion on ceramics and correlation with their Z-potential. *Biomaterials* 19, 637–641. doi: 10.1016/S0142-9612(97)00153-1

Kumar, P. S., Sathesh, K., Grandhi, V. V., and Gupta, V. (2019). The effects of titanium implant surface topography on osseointegration: literature review. *JMIR Biomed. Eng.* 4:e13237. doi: 10.2196/13237

Labelle, D., Jumarie, C., and Moreau, R. (2007). Capacitative calcium entry and proliferation of human osteoblast-like MG-63 cells. *Cell Prolif.* 40, 866–884. doi: 10.1111/j.1365-2184.2007.00477.x

Lee, G., Lim, J., Park, J., Lee, W., Yoon, D. S., Kim, S. H., et al. (2018). Construction of neurospheroids via surface modified concave microwells. *J. Ind. Eng. Chem.* 62, 341–351. doi: 10.1016/J.JIEC.2018.01.014

Lee, J. H., Jung, H. W., Kang, I.-K., and Lee, H. B. (1994). Cell behaviour on polymer surfaces with different functional groups. *Biomaterials* 15, 705–711. doi: 10.1016/0142-9612(94)90169-4

Lehnfeld, J., Gruening, M., Kronseder, M., and Mueller, R. (2020). Comparison of protein-repellent behavior of linear versus dendrimer-structured surface-immobilized polymers. *Langmuir* 2020:acs.langmuir.0c00625. doi: 10.1021/acs.langmuir.0c00625

Lesný, P., Přádný, M., Jendelová, P., Michálek, J., Vacík, J., and Syková, E. (2006). Macroporous hydrogels based on 2-hydroxyethyl methacrylate. Part 4: growth of rat bone marrow stromal cells in three-dimensional hydrogels with positive and negative surface charges and in polyelectrolyte complexes. *J. Mater. Sci. Mater. Med.* 17, 829–833. doi: 10.1007/s10856-006-9842-1

Liao, T., Moussallem, M. D., Kim, J., Schlenoff, J. B., and Ma, T. (2010). N-isopropylacrylamide-based thermoresponsive polyelectrolyte multilayer films for human mesenchymal stem cell expansion. *Biotechnol. Prog.* 26, 1705–1713. doi: 10.1002/btpr.471

Liu, Q., Ding, J., Mante, F. K., Wunder, S. L., and Baran, G. R. (2002). The role of surface functional groups in calcium phosphate nucleation on titanium foil: a self-assembled monolayer technique. *Biomaterials* 23, 3103–3111. doi: 10.1016/S0142-9612(02)00050-9

Liu, Z.-M., Lee, S.-Y., Sarun, S., Peschel, D., and Groth, T. (2009). Immobilization of poly (ethylene imine) on poly (l-lactide) promotes MG63 cell proliferation and function. *J. Mater. Sci. Mater. Med.* 20, 2317–2326. doi: 10.1007/s10856-009-3806-1

Mecke, A., Majoros, I. J., Patri, A. K., Baker, J. R., Banaszak Holl, M. M., and Orr, B. G. (2005). Lipid bilayer disruption by polycationic polymers:? the roles of size and chemical functional group. *Langmuir* 21, 10348–10354. doi: 10.1021/la050629l

Metwalli, E., Haines, D., Becker, O., Conzone, S., and Pantano, C. G. (2006). Surface characterizations of mono-, di-, and tri-aminosilane treated glass substrates. *J. Coll. Interf. Sci.* 298, 825–831. doi: 10.1016/J.JCIS.2006.03.045

Metwally, S., and Stachewicz, U. (2019). Surface potential and charges impact on cell responses on biomaterials interfaces for medical applications. *Mater. Sci. Eng. C* 104:109883. doi: 10.1016/J.MSEC.2019.109883

Moerke, C., Staehlke, S., Rebl, H., Finke, B., and Nebe, J. B. (2018). Restricted cell functions on micropillars are alleviated by surfacenanocoating with amino groups. *J. Cell Sci.* 131:jcs207001. doi: 10.1242/jcs.207001

Mohamad, H. S., Neuber, S., and Helm, C. A. (2019). Surface forces of asymmetrically grown polyelectrolyte multilayers: searching for the charges. *Langmuir* 35, 15491–15499. doi: 10.1021/acs.langmuir.9b01787

Mörke, C., Rebl, H., Finke, B., Dubs, M., Nestler, P., Airoudj, A., et al. (2017). Abrogated cell contact guidance on amino-functionalized microgrooves. *ACS Appl. Mater. Interf.* 9, 10461–10471. doi: 10.1021/acsami.6b16430

Muderrisoglu, C., Saveleva, M., Abalymov, A., Van der Meeren, L., Ivanova, A., Atkin, V., et al. (2018). Nanostructured biointerfaces based on bioceramic calcium carbonate/hydrogel coatings on titanium with an active enzyme for stimulating osteoblasts growth. *Adv. Mater. Interf.* 5:1800452. doi: 10.1002/admi.201800452

Muller, F. L., Lustgarten, M. S., Jang, Y., Richardson, A., and Van Remmen, H. (2007). Trends in oxidative aging theories. *Free Radic. Biol. Med.* 43, 477–503. doi: 10.1016/J.FREERADBIOMED.2007.03.034

Müller, R., Abke, J., Schnell, E., Scharnweber, D., Kujat, R., Englert, C., et al. (2006). Influence of surface pretreatment of titanium- and cobalt-based biomaterials on covalent immobilization of fibrillar collagen. *Biomaterials* 27, 4059–4068. doi: 10.1016/J.BIOMATERIALS.2006.03.019

Nebe, B., Finke, B., Lüthen, F., Bergemann, C., Schröder, K., Rychly, J., et al. (2007). Improved initial osteoblast functions on amino-functionalized titanium surfaces. *Biomol. Eng.* 24, 447–454. doi: 10.1016/J.BIOENG.2007.07.004

Nebe, J. B., Rebl, H., Schlosser, M., Staehlke, S., Gruening, M., Weltmann, K.-D., et al. (2019). Plasma polymerized allylamine—the unique cell-attractive nanolayer for dental implant materials. *Polymers* 11:1004. doi: 10.3390/polym11061004

Nestler, P., Block, S., and Helm, C. A. (2012). Temperature-induced transition from odd-even to even-odd effect in polyelectrolyte multilayers due to

interpolyelectrolyte interactions. *J. Phys. Chem. B* 116, 1234–1243. doi: 10.1021/jp208837m

Nikkhah, M., Edalat, F., Manoucheri, S., and Khademhosseini, A. (2012). Engineering microscale topographies to control the cell-substrate interface. *Biomaterials* 33, 5230–5246. doi: 10.1016/J.BIOMATERIALS.2012.03.079

Norde, W., and Lyklema, J. (1991). Why proteins prefer interfaces. *J. Biomater. Sci. Polym. Edn.* 2, 183–202. doi: 10.1080/09205063.1991.9756659

Olsson, J., Carlén, A., Burns, N. L., and Holmberg, K. (1995). Modified pellicle formation and reduced in vitro bacterial adherence after surface treatment with different siloxane polymers. *Coll. Surf. B Biointerf.* 5, 161–169. doi: 10.1016/0927-7765(95)01212-2

Otter, M., Goheen, S., and Williams, W. S. (1988). Streaming potentials in chemically modified bone. *J. Orthop. Res.* 6, 346–359. doi: 10.1002/jor.1100060306

Padial-Molina, M., Galindo-Moreno, P., Fernández-Barbero, J. E., O'Valle, F., Jódar-Reyes, A. B., Ortega-Vinuesa, J. L., et al. (2011). Role of wettability and nanoroughness on interactions between osteoblast and modified silicon surfaces. *Acta Biomater.* 7, 771–778. doi: 10.1016/J.ACTBIO.2010.08.024

Pommerenke, H., Schmidt, C., Dürr, F., Nebe, B., Lüthen, F., Muller, P., et al. (2002). The mode of mechanical integrin stressing controls intracellular signaling in osteoblasts. *J. Bone Miner. Res.* 17, 603–611. doi: 10.1359/jbmr.2002.17.4.603

Ponsonnet, L., Reybier, K., Jaffrezic, N., Comte, V., Lagneau, C., Lissac, M., et al. (2003). Relationship between surface properties (roughness, wettability) of titanium and titanium alloys and cell behaviour. *Mater. Sci. Eng. C* 23, 551–560. doi: 10.1016/S0928-4931(03)00033-X

Ravenscroft-Chang, M. S., Stohlman, J. M., Molnar, P., Natarajan, A., Canavan, H. E., Teliska, M., et al. (2010). Altered calcium dynamics in cardiac cells grown on silane-modified surfaces. *Biomaterials* 31, 602–607. doi: 10.1016/J.BIOMATERIALS.2009.09.084

Rebl, H., Finke, B., Ihrke, R., Rothe, H., Rychly, J., Schroeder, K., et al. (2010). Positively charged material surfaces generated by plasma polymerized allylamine enhance vinculin mobility in vital human osteoblastss. *Adv. Eng. Mater.* 12, B356–B364. doi: 10.1002/adem.200980070

Rebl, H., Finke, B., Lange, R., Weltmann, K.-D., and Nebe, J. B. (2012). Impact of plasma chemistry versus titanium surface topography on osteoblast orientation. *Acta Biomater.* 8, 3840–3851. doi: 10.1016/J.ACTBIO.2012.06.015

Rebl, H., Finke, B., Schmidt, J., Mohamad, H. S., Ihrke, R., Helm, C. A., et al. (2016). Accelerated cell-surface interlocking on plasma polymer-modified porous ceramics. *Mater. Sci. Eng. C* 69, 1116–1124. doi: 10.1016/J.MSEC.2016.08.016

Rico, P., Hernández, J. C. R., Moratal, D., Altankov, G., Pradas, M. M., and Salmerón-Sánchez, M. (2009). Substrate-induced assembly of fibronectin into networks: influence of surface chemistry and effect on osteoblast adhesion. *Tissue Eng. Part A* 15, 3271–3281. doi: 10.1089/ten.tea.2009.0141

Schulz, A., Katsen-Globa, A., Huber, E. J., Mueller, S. C., Kreiner, A., Pütz, N., et al. (2018). Poly(amidoamine)-alginate hydrogels: directing the behavior of mesenchymal stem cells with charged hydrogel surfaces. *J. Mater. Sci. Mater. Med.* 29:105. doi: 10.1007/s10856-018-6113-x

Secchi, A. G., Grigoriou, V., Shapiro, I. M., Cavalcanti-Adam, E. A., Composto, R. J., Ducheyne, P., et al. (2007). RGDS peptides immobilized on titanium alloy stimulate bone cell attachment, differentiation and confer resistance to apoptosis. *J. Biomed. Mater. Res. Part A* 83A, 577–584. doi: 10.1002/jbm.a.31007

Shelton, R. M., Rasmussen, A. C., and Davies, J. E. (1988). Protein adsorption at the interface between charged polymer substrata and migrating osteoblasts. *Biomaterials* 9, 24–29. doi: 10.1016/0142-9612(88)90065-8

Sjaastad, M. D., and Nelson, W. J. (1997). Integrin-mediated calcium signaling and regulation of cell adhesion by intracellular calcium. *Bioessays* 19, 47–55. doi: 10.1002/bies.950190109

Skalak, R., and Shu, C. (1986). *Electromechanical Effects in Bone. Handb. Bioeng.* Available online at: https://www.ideals.illinois.edu/handle/2142/25222 (accessed April 14, 2020).

Staehlke, S., Koertge, A., and Nebe, B. (2015). Intracellular calcium dynamics dependent on defined microtopographical features of titanium. *Biomaterials* 46, 48–57. doi: 10.1016/J.BIOMATERIALS.2014.12.016

Staehlke, S., Rebl, H., Finke, B., Mueller, P., Gruening, M., and Nebe, J. B. (2018). Enhanced calcium ion mobilization in osteoblasts on amino group containing plasma polymer nanolayer. *Cell Biosci.* 8:22. doi: 10.1186/s13578-018-0220-8

Staehlke, S., Rebl, H., and Nebe, B. (2019). Phenotypic stability of the human MG-63 osteoblastic cell line at different passages. *Cell Biol. Int.* 43, 22–32. doi: 10.1002/cbin.11073

Terzi, M. Y., Izmirli, M., and Gogebakan, B. (2016). The cell fate: senescence or quiescence. *Mol. Biol. Rep.* 43, 1213–1220. doi: 10.1007/s11033-016-4065-0

Tryoen-Tóth, P., Vautier, D., Haikel, Y., Voegel, J.-C., Schaaf, P., Chluba, J., et al. (2002). Viability, adhesion, and bone phenotype of osteoblast-like cells on polyelectrolyte multilayer films. *J. Biomed. Mater. Res.* 60, 657–667. doi: 10.1002/jbm.10110

von der Mark, K., and Park, J. (2013). Engineering biocompatible implant surfaces: Part II: cellular recognition of biomaterial surfaces: lessons from cell-matrix interactions. *Prog. Mater. Sci.* 58, 327–381. doi: 10.1016/J.PMATSCI.2012.09.002

Webb, K., Hlady, V., and Tresco, P. A. (1998). Relative importance of surface wettability and charged functional groups on NIH 3T3 fibroblast attachment, spreading, and cytoskeletal organization. *J. Biomed. Mater. Res.* 41, 422–430. doi: 10.1002/(SICI)1097-4636(19980905)41:3<422::AID-JBM12>3.0.CO;2-K

Wennberg, A., and Albrektsson, T. (2009). Effects of titanium surface topography on bone integration: a systematic review. *Clin. Oral Implants Res.* 20, 172–184. doi: 10.1111/j.1600-0501.2009.01775.x

Zimmerman, E., Geiger, B., and Addadi, L. (2002). Initial stages of cell-matrix adhesion can be mediated and modulated by cell-surface hyaluronan. *Biophys. J.* 82, 1848–1857. doi: 10.1016/S0006-3495(02)75535-5

Zou, W., Yang, S., Zhang, T., Sun, H., Wang, Y., Xue, H., et al. (2015). Hypoxia enhances glucocorticoid-induced apoptosis and cell cycle arrest via the PI3K/Akt signaling pathway in osteoblastic cells. *J. Bone Miner. Metab.* 33, 615–624. doi: 10.1007/s00774-014-0627-1

9.2 Further scientific achievements

9.2.1 Publications published in peer-reviewed journals

Gruening, M., **Neuber, S.**, Fricke, K., Helm, C. A., & Nebe, B. (2020). Cell-material interaction-spreading course correlates with surface charge. *Am. J. Biomed. Sci. Res*, *9*(9), 4-6.
(DOI: 10.34297/AJBSR.2020.09.001341)

Gruening, M., Dawson, J. E., Voelkner, C., **Neuber, S.**, Fricke, K., van Rienen, U., ... & Nebe, J. B. (2021). Automatic Actin Filament Quantification and Cell Shape Modeling of Osteoblasts on Charged Ti Surfaces. *Applied Sciences*, *11*(12), 5689.
(DOI: 10.3390/app11125689)

Sill, A., Nestler, P., Weltmeyer, A., Paßvogel, M., **Neuber, S.**, & Helm, C. A. (2020). Polyelectrolyte Multilayer Films from Mixtures of Polyanions: Different Compositions in Films and Deposition Solutions. *Macromolecules*, *53*(16), 7107-7118.
(DOI: 10.1021/acs.macromol.0c01089)

Voelkner, C., Assi, I., Karberg, W., Lange, R., **Neuber, S.**, Helm, C. A., ... & Speller, S. (2022). Response of Osteoblasts to Electric Field Line Patterns Emerging from Molecule Stripe Landscapes. *Applied Sciences*, *12*(14), 7329.
(DOI: 10.3390/app12147329)

9.2.2 Manuscripts in preparation

Sill, Annekatrin; Ahrens, Heiko; Soltwedel, Olaf; Gutfreund, Philipp; **Neuber, Sven**; Nestler, Peter; Helm, Christiane. In-situ neutron reflectometry measurements of polyelectrolyte diffusion in Layer-by-Layer films in an aqueous solution.

Khurram, Muhammad; **Neuber, Sven**; Sill, Annekatrin; and Helm, Christiane. High electrically conductive PEDOT/PSS films via layer – by – layer self – assembly.

9.2.3 Conference talk

Neuber S., Sill A., Nestler P., Ahrens H., And Helm C. A.: Influence of molecular weight of polycation polydimethyldiallylammonium and carbon nanotube content on the electric conductivity of layer-by-layer films; DPG, Spring Meeting, Regensburg, September 4th – 9th 2022

9.2.4 Poster presentations

Mohammad H., **Neuber S.**, Sill A., & Helm C. A.: A wide range of surface forces of PSS terminated polyelectrolyte multilayers; DPG Spring Meeting, Technische Universität Berlin, Germany, March 11th – 16th, 2018

Azinfar A., **Neuber S.**, Vanecek J., Vancova M., Stranak V., & Helm C. A.: Roughness and Salt annealing in a polyelectrolyte Multilayer; DPG, Spring Meeting, Technische Universität Berlin, Germany, March 11th – 16th, 2018

Neuber S., Sill A., Ahrens H., & Helm C. A.: Electrically conductive multilayer films from carbon nanotubes and polyelectrolytes; DPG, Spring Meeting, Universität Regensburg, Germany, March 31st – April 5th, 2019

Azinfar A., **Neuber S.**, Vanecek J., Vancova M., Streba J., Stranak V., & Helm C. A.: Buckling patterns and their elastic response on the surface of polyelectrolyte multilayer films with short PSS chains; DPG, Spring Meeting, Universität Regensburg, Germany, March 31st – April 5th, 2019

Neuber S., Sill A., Nestler P., Ahrens H., & Helm C. A.: Electrically conductive multilayer films from carbon nanotubes and polyelectrolytes; 9th International Colloids Conference, Sitges, Spain, June 16th – 19th, 2019

Sill A., Paßvogel M., Azinfar A., **Neuber S.**, Nestler P., & Helm C. A.: Molecular properties and growth conditions associated with PSS diffusion during annealing in polyelectrolyte multilayers; 9th International Colloids Conference, Sitges, Spain, June 16th – 19th, 2019

Sill A., Weltmeyer A., Nestler P., Paßvogel M., **Neuber S.**, & Helm C. A.: Polyelectrolyte multilayer films from mixtures of polyanions: different composition in film and preparation solution; 11th Joint BER II and Bessy User Meeting, Berlin, Germany, December 4th – 6th, 2019